WL-TR-97-2083

MICRO/MINIATURE HEAT PIPE TECHNOLOGY FOR ELECTRONIC COOLING

AMIR FAGHRI, PH.D.
DMITRY KHRUSTALEV, PH.D.

DEPARTMENT OF MECHANICAL AND
MATERIALS ENGINEERING
WRIGHT STATE UNIVERSITY
DAYTON, OH 45435

JULY 1997

FINAL REPORT FOR 6/1/92-6/25/97

AEROPROPULSION AND POWER DIRECTORATE
WRIGHT LABORATORY
AIR FORCE MATERIEL COMMAND
WRIGHT PATTERSON AFB OH 45433-7251

19980410 070

DTIC QUALITY INSPECTED 8

NOTICE

When Government drawings, specifications, or other data are used for any purpose other than in connection with a definitely Government-Related procurement, the United States Government incurs no responsibility or any obligation whatsoever. The fact that the government may have formulated or in any way supplied the said drawings, specifications, or other data, is not to be regarded by implication, or otherwise in any manner construed, as licensing the holder, or any other person or corporation; or as conveying any rights or permission to manufacture, use, or sell any patented invention that may in any way be related thereto.

This report is releasable to the National Technical Information Service (NTIS). At NTIS, it will be available to the general public, including foreign nations.

This technical report has been reviewed and is approved for publication.
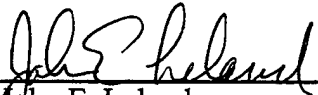
John E. Leland
Project Engineer
Mechanical Branch

Phillip G. Colegrove
Chief
Mechanical Branch

MICHAEL A. MARCINIAK, Major, USAF
Deputy Chief
Aerospace Power Division
Aero Propulsion and Power Directorate

Publication of this report does not constitute approval or disapproval of the ideas or findings. It is published in the interest of scientific and technical information exchange.

If you address has changed, if you wish to be removed from our mailing list, or if the addressee is no longer employed by your organization, please notify WL/POOS, WPAFB, OH 45433-7251 to help us maintain a current mailing list.

Copies of this report should not be returned unless return is required by security considerations, contractual obligations, or notice on a specific document.

REPORT DOCUMENTATION PAGE

Form Approved
OMB No. 0704-0188

1. AGENCY USE ONLY *(Leave blank)*	2. REPORT DATE July 1997	3. REPORT TYPE AND DATES COVERED FINAL 06/01/92 – 06/25/97

4. TITLE AND SUBTITLE
MICRO/MINIATURE HEAT PIPE TECHNOLOGY FOR ELECTRONIC COOLING

6. AUTHOR(S)

AMIR FAGHRI, PH.D.
DMITRY KHRUSTALEV

5. FUNDING NUMBERS
C: F33615-92-C-2276
PE: 63218C
PR: 1601
TA: 05
WU: 05

7. PERFORMING ORGANIZATION NAME(S) AND ADDRESS(ES)
Department of Mechanical and Materials Engineering
Wright State University
Dayton, Ohio 45435

8. PERFORMING ORGANIZATION REPORT NUMBER

9. SPONSORING/MONITORING AGENCY NAME(S) AND ADDRESS(ES)
AEROPROPULSION AND POWER DIRECTORATE
WRIGHT LABORATORY
AIR FORCE MATERIEL COMMAND
WRIGHT-PATTERSON AFB OH 45433-7251
POC: JOHN LELAND, WL/POOS, 937-255-2922

10. SPONSORING/MONITORING AGENCY REPORT NUMBER

WL-TR-97-2083

11. SUPPLEMENTARY NOTES

12a. DISTRIBUTION AVAILABILITY STATEMENT

APPROVED FOR PUBLIC RELEASE; DISTRIBUTION IS UNLIMITED

12b. DISTRIBUTION CODE

13. ABSTRACT *(Maximum 200 words)*

Detailed analysis and experimental data presented in this report show that longitudinal groove designs are crucial to increase the heat transport capacity of miniature heat pipes. The steady-state mathematical models of a miniature axially grooved heat pipe with micro grooves are developed where the importance of the interfacial phenomena at the surfaces of the ultra-thin is emphasized. The predicted capillary and boiling limitations as well as thermal resistance are compared to detailed in-house experimental data on miniature and conventional axially-grooved heat pipes. It is found that flat miniature heat pipes are easily capable of withstanding heat fluxes on the order of 100 W/cm2 at the evaporator wall. Advanced flat miniature heat pipes are suggested and modeled to further increase the maximum heat flux at the evaporator wall. Additional experiments carried out for the heat pipe evaporators with forced convection and heat fluxes in excess of 200 W/cm2 proved that capillary limitation is the limiting one for flat miniature heat pipes with micro grooves.

14. SUBJECT TERMS
Miniature heat pipe; Micro grooves; Evaporation; Condensation; High heat flux

15. NUMBER OF PAGES
180

16. PRICE CODE

17. SECURITY CLASSIFICATION OF REPORT	18. SECURITY CLASSIFICATION OF THIS PAGE	19. SECURITY CLASSIFICATION OF ABSTRACT	20. LIMITATION OF ABSTRACT
UNCLASSIFIED	UNCLASSIFIED	UNCLASSIFIED	SAR

DTIC QUALITY INSPECTED 3

Contents

List of Figures

List of Tables

NOMENCLATURE

a, b	constants
B, C	constants
A	cross sectional area, [m^2], or Hamaker constant ($6\pi\overline{A}$)
A'	dispersion constant [J]
c_p	specific heat at constant pressure [J/(kg-K)]
c_v	specific heat at constant volume [J/(kg-K)]
C	vapor channel thickness-width ratio
D_h	hydraulic diameter [m]
f	friction factor
f_l	friction factor of liquid flow
f_{lo}	friction factor with no vapor interaction
f_{TP}	two-phase friction factor
g	gravity constant [m/s^2]
h	heat transfer coefficient [W/(m^2-K)]
h_{fg}	latent heat of vaporization [J/kg]
H	meniscus height or elevation [m]
i, j	indices of grid point
k	thermal conductivity [W/(m-K)]
k_{eff}	thermal conductivity of dry porous structure
k_w	thermal conductivity of solid wall or fin
K	permeability [m^2]
K	curvature [1/m]
L	length [m]
L_t	total length of the heat pipe [m]
L_{eff}	effective heat pipe length [m]
L_1	half-width of the top of the fin [m]
L_2	length of condensate film [m]
L_p	width of porous plate [m]
$\dot{m}$	mass flow rate [kg/s]
M	molecular weight, [kg/kmol], or mass [kg]
Ma	$\overline{w}_{v,a}/\sqrt{\gamma_0 R_g T_v}$, Mach number
N	number of grooves
n'	number of active sites per square centimeter
p	pressure [Pa]
p_d	disjoining pressure [Pa]
P	perimeter
q	heat flux [W/m^2]
Q	axial heat flow through heat pipe [W]
Q_a	total heat load [W]
Q'	heat flow rate per unit length [W/m]
r	thermal resistance [K/W]
r_h	hydraulic radius [m]

r_{eff}	effective capillary radius of the wick pores at the liquid-vapor interface [m]
R	gas constant, [J/(kg-K)], or radius [m]
Re	Reynolds number, UD_h/ν or $\overline{w}_v D_{h,v}/\nu_v$, vapor axial Reynolds number
Re_r	$\overline{v}_{v,\delta} D_{h,v}/\nu_v$, radial Reynolds number
R_g	gas constant [J/(kg-K)]
R_m	radius of curvature of the meniscus [m]
R_o	outer pipe radius [m]
R_r	characteristic roughness size [m]
R_v	vapor space radius [m]
s	coordinate along the solid-liquid interface [m]
t	heat pipe thickness [m]
t_g	groove depth [m]
t_t	height of the curved top of the fin [m]
t_w	wall thickness [m]
T	temperature [K]
T_w	temperature of the solid-liquid thin film interface [K]
T_{sat}	saturation vapor temperature at liquid vapor interface [K]
u	velocity of microfilm flow along the x-coordinate [m/s]
v	radial velocity or vapor velocity along the η-coordinate [m/s]
$\overline{v}$	mean radial velocity [m/s]
V	velocity vector [m/s]
w	axial velocity [m/s]
$\overline{w}$	mean axial velocity [m/s]
W	half-width of a groove [m]
W_t	trapezoidal groove half width [m]
x, y	coordinates [m]
x	equilibrium vapor quality
$\dot{x}, \dot{y}$	coordinates (Fig. 2.3) [m]
Y_L	length of computational domain [m]
Y_B	distance from inlet to meniscus bottom [m]
Y_{mic}	distance from inlet to microfilm control volume [m]
z	axial coordinate [m]

Greek symbols

α	accommodation coefficient
	angle between grooves and longitudinal heat pipe axis [deg.]
β	momentum flux coefficient
γ	half-angle of the corner or of the groove
γ_0	c_p/c_v, ratio of specific heats
δ	liquid film thickness [m]
δ_0	equilibrium (nonevaporating) thickness [m]

Δ_a	absolute error
Δp	$p - p_{v0} + \sigma/R_{m0} + 1$, pressure drop [N/m^2]
Δ_r	relative error
ΔQ	heat flow per unit groove length [W/m]
ΔT	$|T_w - T_v|$, temperature drop [K]
ϵ	emissivity
η	coordinate normal to the solid-liquid interface [m]
θ	meniscus contact angle
θ_f	contact angle obtained from the smooth-surface model
$\theta_{\min}$	minimum wetting contact angle
θ_0	minimum wetting contact angle in Section 2
κ	characteristic angle of top fin
μ	dynamic viscosity [Pa-s]
ν	kinematic viscosity [m^2/s]
ρ	density [kg/m^3]
ϕ	inclination angle from horizontal
σ	liquid surface tension [N/m]
χ	π/N, angle (for circular geometry)
τ	shear stress at the interface [Pa]
ω_1	liquid-wall interface
ω_2	liquid-vapor interface
ω_3	liquid-bottom interface

Subscripts

a	adiabatic
abs	absolute
bot	bottom of a groove
c	condenser
cap	capillary
ch	channel
e	evaporator
eff	effective
ent	enthalpy
ex	external
f	thin film
ft	filtration
ℓ	liquid
ℓv	liquid-vapor interface
loc	local
max	maximum
men	meniscus
mic	microfilm region
o	outer

p	porous
pc	phase change
pen	penetration
rf	reference
s	wall-liquid interface in Section 1
sat	saturation
t	total
tot	total
tr	transition region
v	vapor
w	wall
δ	liquid film free surface

APPLICABLE DOCUMENTS

1. Khrustalev, D., and Faghri, A., "Thermal Analysis of a Micro Heat Pipe," *ASME Journal of Heat Transfer*, Vol. 116, No. 1,1994, pp. 189–198.

2. Khrustalev, D., and Faghri, A., "Heat Transfer During Evaporation on Capillary-Grooved Structures of Heat Pipes," *ASME J. Heat Transfer*, Vol. 117, August, No. 3, p. 740–747, 1995.

3. Khrustalev, D., and Faghri, A., 1995, "Thermal Characteristics of Conventional and Flat Miniature Axially-Grooved Heat Pipes," *ASME Journal of Heat Transfer*, Vol. 117, November, No. 4, pp. 1048-1054.

4. Khrustalev, D. and Faghri, A., "Heat transfer in the inverted Meniscus Type Evaporator at High Heat Fluxes", *Int. J. Heat Mass Transfer*, Vol. 38, No. 16, pp.3091-3101, 1995

5. Khrustalev, D. and Faghri, A., "Estimation of the Maximum Heat Flux in the Inverted Meniscus Type Evaporator of a Flat Miniature Heat Pipe," Int. J. Heat Mass Transfer, No. 9, pp. 1899-1909, 1996.

6. Khrustalev, D., and Faghri, A., "High Flux Evaporative Mini-Channel Heat Sink With Axial Capillary Grooves," *Journal of Enhanced Heat Transfer*, Vol. 3, No. 3, pp. 221-232, 1996.

7. Khrustalev, D., and Faghri, A., 1995, "Boiling Heat Transfer in the Miniature Axially-Grooved Rectangular Channel with Discrete Heat Sources," *Journal of Enhanced Heat Transfer*, in press, to appear in 1997

8. Krustalev, D. and Faghri, A., "Enhanced Flat Axially-Grooved Miniature Heat Pipe," ASME Journal of Heat Transfer, Vol. 118, pp. 261-264, 1996.

9. Krustalev, D. and Faghri, A., "Fluid Flow Effects in Evaporation from Liquid-Vapor Meniscus," ASME Journal of Heat Transfer, Vol. 118, pp. 725-730, 1996.

10. Krustalev, D. and Faghri, A., "Advances in Modeling of Enhanced Miniature Heat Pipes With Capillary Grooves," Journal of Enhanced Heat Transfer, in press, to appear in 1997

11. Khrustalev, D., and Faghri, A., 1997, "Thick-Film Phenomenon During High-Heat-Flux Evaporation from Cylindrical Pores," *ASME Journal of Heat Transfer,*Vol. 119, pp. 272-278, 1997.

12. Hopkins, R., Faghri, A., and Khrustalev, D.,"Flat Miniature Heat Pipes With Micro Grooves," to appear in ASME Journal of Heat Transfer.

13. Hopkins, R., Faghri, A., and Khrustalev, D.,"Critical Heat Fluxes and Pressure Drops in Flat Miniature Heat Sinks With Micro Grooves," to appear in ASME Journal of Heat Transfer.

14. Khrustalev, D., and Faghri, A., "Coupled Liquid and Vapor Flow in Miniature Passages with Microgrooves (FEM)," submitted to ASME Journal of Heat Transfer

FOREWORD

The information in this report was assembled for contract F33615-92-C-2276 with Aero Propulsion and Power Directorate, Wright Laboratory and BMDO/IST as the supporting agencies. The work was carried out at the Department of Mechanical and Materials Engineering at Wright State University and finished at the Department of Mechanical Engineering at the University of Connecticut.

From June 1992-June 1997, all of the tasks were completed as outlined in the Table of Contents. The various tasks dealt with performance characteristics of micro/miniature heat pipes systems. Fourteen journal publications and multiple conference papers were produced from the present work. Dr. John Leland from Wright Laboratory was the technical supervisor for this contract, and the authors are grateful to him for various detailed technical assistance and discussions. We greatly appreciate him for his time and effort in all phases of the contract continuation. Support from Dr. Jerry Beam to initiate this contract is also greatly acknowledged.

Amir Faghri
Dmitry Khrustalev

Chapter 1

INTRODUCTION

This work is focused on development of flat miniature heat pipes capable of withstanding high heat fluxes on the evaporator walls, in excess of 100 W/cm^2. Such heat pipes are needed for cooling of electronic components that usually work at temperatures below 100°C. The highest heat flux on a heat pipe evaporator wall reported in survey of Faghri [1] is 60 W/cm^2. This heat flux is restricted by multiple heat pipe limitations, therefore, profound investigation of these limitations and corresponding heat transfer processes was necessary to develop high-heat-flux miniature heat pipes. This work consists of two major parts: (a) physical and mathematical modeling of fluid flow and heat transfer in miniature heat pipes and (b) experimental testing of high heat flux heat pipes and two-phase heat sinks. Major advances of this work can be grouped as follows.

- A detailed mathematical model is developed which describes heat transfer through thin liquid films in the evaporator and condenser of heat pipes with capillary grooves. The model accounts for the effects of interfacial thermal resistance, disjoining pressure and surface roughness for a given meniscus contact angle. The free surface temperature of the liquid film is determined using the extended Kelvin equation and the expression for interfacial resistance given by the kinetic theory. The numerical results obtained are compared to existing experimental data. The importance of the surface roughness and interfacial thermal resistance in predicting the heat transfer coefficient in the grooved evaporator is demonstrated.

- A mathematical model of the evaporating liquid-vapor meniscus in a capillary slot has been developed. The model includes two-dimensional steady-state momentum conservation and energy equations for both the vapor and liquid phases, and incorporates the existing simplified one-dimensional model of the evaporating microfilm. The numerical results, obtained for water, demonstrate the importance of accounting for the fluid flow in calculating the effective evaporative heat transfer coefficient and the superheat of the vapor over the liquid-vapor meniscus due to the heat transfer from the heated wall. With higher heat fluxes, a recirculation zone appears in the vapor near the heated wall due to extensive evaporation in the thin-film region of the liquid-vapor meniscus.

- A detailed mathematical model of axially-grooved heat pipes (AGHP) is developed in which the fluid circulation is considered along with the heat and mass transfer

1

processes during evaporation and condensation. The predicted results obtained are compared to existing experimental data. Both capillary and boiling limitations are found to be important for the flat miniature copper-water heat pipe, which is capable of withstanding heat fluxes on the order of 40 W/cm^2 applied to the evaporator wall in the vertical position. The influence of the geometry of the grooved surface on the maximum heat transfer capacity of the miniature AGHP is demonstrated.

- To remove high heat fluxes from electronic and optical components, it has been proposed to use flat miniature axially grooved heat pipes enhanced versus those considered by Faghri [1] and Plesch et al. [2] to make them capable of operating with high heat fluxes in the evaporator. This objective can be reached by the proper choice of the grooved surface geometry (Frank [3]) and/or by special enhancements as ivadizing (Grote et al. [4]), which is the deposition of a porous structure on the top of the lands between the grooves. Predictions of the capillary and boiling limitations have been made in the same manner as Khrustalev et al. [5] and Khrustalev and Faghri [6] with some modifications accounting for the presence of the porous layer, as explained in the following sections.

- A one-dimensional mathematical model of the heat transfer during evaporation of the liquid from the liquid-vapor interface located in a porous structure into the dry region between the interface and the solid heated surface is developed for the case when the vapor flows through the narrow dry porous zone along the heated surface towards the vapor channel. The model predicts the location and shape of the liquid-vapor interface, the overall heat transfer coefficient, and the heat fluxes which can be recognized as critical for the evaporator. The numerical results are presented for the case of the miniature evaporator to electronic components cooling.

- A new flat miniature heat pipe configuration for application to cooling electronic components is proposed for high heat fluxes (over 100 W/cm^2) on the evaporator wall. The heat pipe contains the inverted meniscus type evaporator and axial capillary grooves covered with a porous plate for the liquid transport. Numerical results for the capillary limit and maximum heat flux, which has been calculated with respect to the formation of the vapor blanket in the porous structure of the evaporator, are presented for a copper-water miniature heat pipe with the external dimensions 2 × 7 × 120 mm.

- Flat miniature heat pipes (FMHP's) are shown to be very promising in the cooling of electronic component systems. This investigation presents a detailed experimental and theoretical analysis on maximum heat transfer capabilities of two copper-water FMHP's with diagonal trapezoidal micro capillary grooves and one copper-water FMHP with axial rectangular micro capillary grooves. Maximum heat flux on the evaporator wall of the 120 mm long axial grooved heat pipe, with a vapor channel cross-sectional area of approximately (12 mm^2 and rectangular grooves of dimensions 0.20 mm wide by 0.42 mm deep, exceeded 90 W/cm^2 in the horizontal orientation and 150 W/cm^2 in the vertical orientation. Theoretical prediction of the capillary limitation in the horizontal orientation agreed reasonably well with the experimental data.

2

- Four two-phase flat miniature copper-water heat sinks, with hydraulic diameters of under 2.7 mm and various micro grooved enhanced surfaces, have been investigated experimentally for cooling of high-heat-flux electronic devices. Critical heat fluxes (CHF) exceeded 200 W/cm^2 for all four flat miniature heat sinks (FMHS) heated from both wide sides and have been generalized by an empirical correlation. Experimental pressure drop results across the heat sinks, with and without grooves on the inner surface, are shown to be in good agreement with predicted values from a one-dimensional two-phase homogenous model employing an equivalent mass velocity concept.

Chapter 2

MATHEMATICAL MODELING OF FLAT MINIATURE HEAT PIPES

2.1 Evaporation and Condensation on Grooved Surfaces of Heat Pipes

Heat pipes with grooved evaporators and condensers are of great practical interest. For example, it has been proposed recently to cool electronic components using flat miniature axially grooved heat pipes which are capable of withstanding high heat fluxes in the evaporator section (Plesch et al. [2]). In an axially-grooved heat pipe (AGHP), condensate return is accomplished by the flow of liquid in the grooves under the influence of surface tension, and the maximum heat flux in the evaporator is restricted by the fluid transport limit or by the boiling limitation. The value of the evaporative heat transfer coefficient is related to the maximum heat flux by the superheat of the evaporating liquid film, which is critical for the onset of nucleate boiling. Therefore, a detailed mathematical model is developed which includes both the heat transfer through the thin liquid films and heat conduction in the fin between grooves and in the meniscus region film. With this model, the local heat transfer coefficients in the evaporator and condenser sections of low-temperature AGHP's are determined. The present analysis, which incorporates several one-dimensional boundary-value problems, has the following comparatively new features:

- The heat transfer through the liquid films in both the evaporator and condenser is described with respect to the disjoining pressure, interfacial thermal resistance and surface roughness or curvature (Figs. 2.1 and 2.2).

- The free surface temperature of the liquid film is determined using the extended Kelvin equation and the expression for interfacial resistance given by the kinetic theory.

- Heat conduction in the fin between grooves and the liquid meniscus is considered for both the evaporator and condenser sections using a one-dimensional approximation.

Because of these features the proposed model is a significant contribution over the previous investigators' attempts (Kamotani[7,8]; Vasiliev et al.[9]; and Stephan and Busse[11]). Also, the model of ultra-thin film evaporation is employed which is consistent with that given by Carey [12] and Wayner et al. [13]. The present model is developed for rectangular,

triangular and trapezoidal grooves in a circular tube, but flat evaporators and condensers are also described by the presented equations. Heat transfer processes in the heat pipe container and working fluid were considered to be one-dimensional in the radial direction, such that axial heat conduction was neglected. The emphasis has been placed on the formation of the thin liquid films affected by the operational conditions. During the condensation process, liquid in the subcooled thin film flows towards the meniscus region along the s-coordinate, as shown in Fig. 2.1(a). During evaporation, liquid in the superheated thin film flows from the meniscus region in the opposite direction, as presented in Figs. 2.1(b) and 2.2. The numerical results were obtained using an iterative mathematical procedure which involved the following boundary-value problems:

1. Formation of and heat transfer in thin films.
2. Heat transfer in the evaporating film on a rough surface.
3. Heat transfer in the condensate film on the fin top surface.
4. Heat conduction in a metallic fin and liquid meniscus.

These problems are described in detail in the following sections.

2.1.1 Formation of and Heat Transfer in Thin Liquid Films

The thermal resistance of a low-temperature AGHP depends mostly on the thickness of the thin films in the condenser and evaporator sections. Since the heat transfer and fluid dynamics processes in a thin film are similar in both sections, it is possible to describe the formation of the films by the same equations, but taking into account the different directions of the temperature potential. In this section a thin evaporating film on a heat-loaded surface with curvature K_w is considered, as shown in Fig. 2.2(b). The local heat flux through the film due to heat conduction is

$$q = k_\ell \frac{T_w - T_\delta}{\delta} \tag{2.1}$$

where the local thickness of the liquid layer δ and the temperature of the free liquid film surface T_δ are functions of the s-coordinate. For small Reynolds numbers, an assumption of a fully developed laminar liquid flow velocity profile is valid:

$$u_\ell = -\frac{1}{2\mu_\ell} \frac{dp_\ell}{ds} (2\eta\delta - \eta^2) \tag{2.2}$$

where η is the coordinate normal to the solid-liquid interface. The vapor pressure is assumed to be constant along the s-coordinate, and the liquid flow is driven mainly by the surface tension and the adhesion forces.

$$\frac{dp_\ell}{ds} = -\sigma \frac{dK}{ds} + \frac{dp_d}{ds} - K \frac{d\sigma}{dT_\delta} \frac{dT_\delta}{ds}$$

$$+ \frac{d}{ds}(\rho_v^2 v_{v,\delta}^2) \left(\frac{1}{\rho_v} - \frac{1}{\rho_\ell} \right) \tag{2.3}$$

5
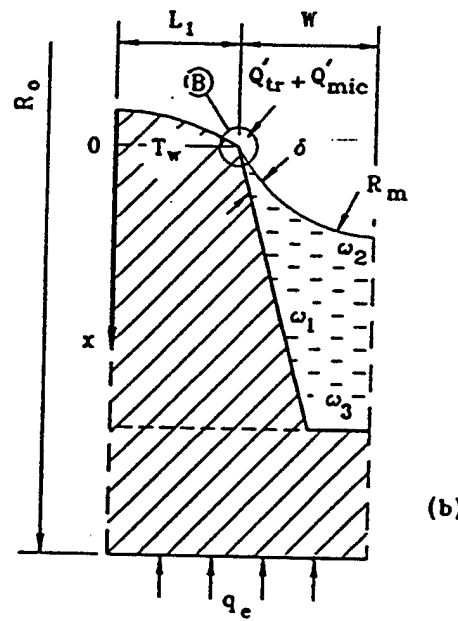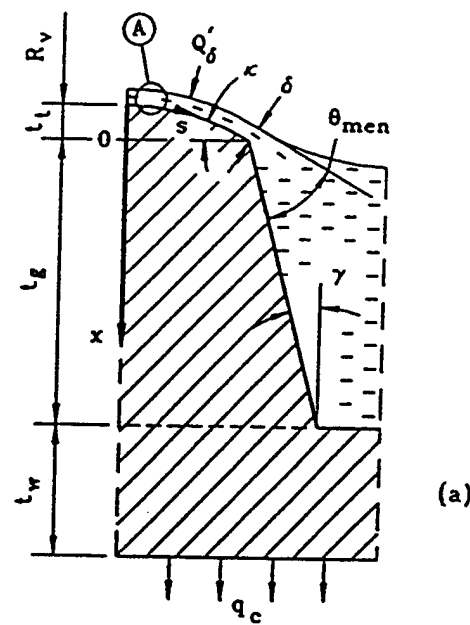
Figure 2.1: Cross sections of the characteristic elements of an axially grooved heat pipe: (a) condenser; (b) evaporator.
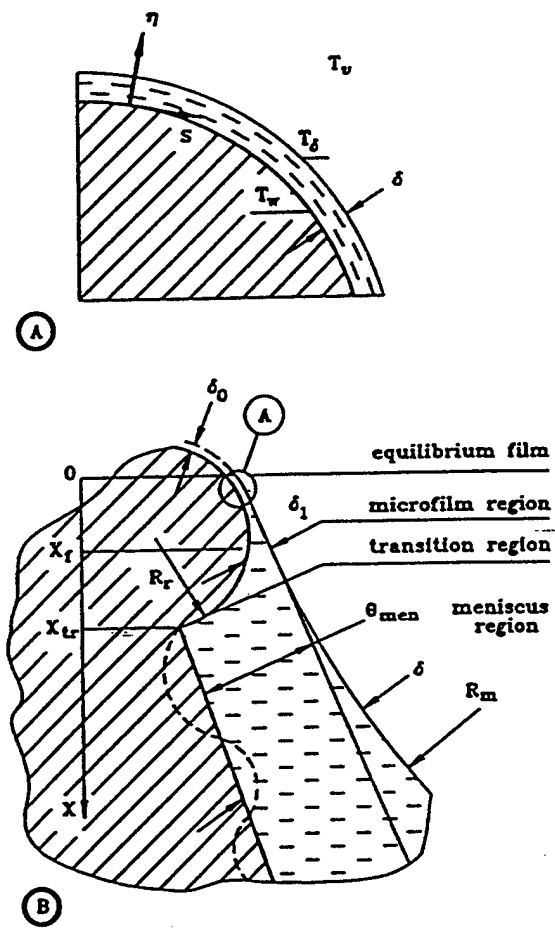
Figure 2.2: Thin evaporating film on a fragment of a rough surface.

K is the local interface curvature, p_d is the disjoining pressure (Derjaguin [14]) and the last term is the kinetic reaction of the evaporating fluid pressure. The impact of the last two terms on the results was found to be negligible in the present analysis, therefore they are omitted in following equations.

The continuity equation for the evaporating liquid layer is

$$\frac{d}{ds} \int_0^\delta u_\ell \, d\eta = \frac{q}{h_{fg}\rho_\ell} \tag{2.4}$$

Substituting equations (2.1)–(2.3) into equation (2.4) gives the following relation for the thickness of the evaporating film, $\delta(s)$:

$$\frac{1}{3\mu_\ell} \frac{d}{ds} \left[\delta^3 \frac{d}{ds}(p_d - \sigma K) \right] = \frac{k_\ell(T_w - T_\delta)}{h_{fg}\rho_\ell\delta} \tag{2.5}$$

The film surface curvature K is expressed in terms of the solid surface curvature K_w and film thickness as

$$K = K_w + \frac{d^2\delta}{ds^2} \left[1 + \left(\frac{d\delta}{ds} \right)^2 \right]^{-3/2} \tag{2.6}$$

Following Potash and Wayner [23], a power-law dependence of p_d on δ is given for non-polar liquids.

$$p_d = -A'\delta^{-B} \tag{2.7}$$

For water, however, the logarithmic dependence is preferable (Holm and Goplen, 16).

It is assumed that the absolute value of the vapor core pressure at any z-location along the groove is related to vapor temperature by the saturation conditions

$$p_v = p_{\text{sat}}(T_v) \tag{2.8}$$

and therefore can be defined for a given T_v using the saturation tables.

The temperature of the interface T_δ is affected by the disjoining and capillary pressures, and also depends on the value of the interfacial resistance, which is defined for the case of a comparatively small heat flux by the following relation.

$$q = -\left(\frac{2\alpha}{2-\alpha}\right) \frac{h_{fg}}{\sqrt{2\pi R_g}} \left[\frac{p_v}{\sqrt{T_v}} - \frac{(p_{\text{sat}})_\delta}{\sqrt{T_\delta}} \right] \tag{2.9}$$

p_v and $(p_{\text{sat}})_\delta$ are the saturation pressures corresponding to T_v in the bulk vapor and at the thin liquid film interface, respectively.

While equation (2.9) is used in the present analysis, it seems useful to mention that for the case of extremely high heat fluxes during intensive evaporation in thin films, Solov'yev and Kovalev [15] have approximated the interfacial heat flux by the following expression:

$$q = 3.2\sqrt{R_g T_v}[(p_{\text{sat}})_\delta - p_v] \tag{2.10}$$

8

Equation (2.10) was derived with the assumption that the accommodation coefficient $\alpha = 1$ from the expressions given by Labuntsov and Krukov [16].

The relation between the vapor pressure over the thin evaporating film, $(p_{\text{sat}})_\delta$, affected by the disjoining pressure, and the saturation pressure corresponding to T_δ, $p_{\text{sat}}(T_\delta)$, is given by the extended Kelvin equation (Carey, [12]):

$$(p_{\text{sat}})_\delta = p_{\text{sat}}(T_\delta) \exp \left[\frac{(p_{\text{sat}})_\delta - p_{\text{sat}}(T_\delta) + p_d - \sigma K}{\rho_\ell R_g T_\delta} \right] \tag{2.11}$$

Equation (2.11) reflects the fact that under the influence of the disjoining and capillary pressures, the liquid free surface saturation pressure $(p_{\text{sat}})_\delta$ is different from the normal saturation pressure $p_{\text{sat}}(T_\delta)$ and varies along the thin film (or s-coordinate), while p_v and T_v are the same for any value of s at a given z-location. This is also due to the fact that T_δ changes along s.

For a thinner evaporating film, the difference between $(p_{\text{sat}})_\delta$ given by equation (2.11) and that for a given T_δ using the saturation curve table is larger. This difference is the reason for the existence of the thin non-evaporating superheated film, which is in the equilibrium state in spite of the fact that $T_\delta > T_v$.

Under steady state conditions the right-hand sides of equations (2.1) and (2.9) can be equated.

$$T_\delta = T_w + \frac{\delta}{k_\ell} \left(\frac{2\alpha}{2 - \alpha} \right) \frac{h_{fg}}{\sqrt{2\pi R_g}} \left[\frac{p_v}{\sqrt{T_v}} - \frac{(p_{\text{sat}})_\delta}{\sqrt{T_\delta}} \right] \tag{2.12}$$

Equations (2.11) and (2.12) determine the interfacial temperature, T_δ, and pressure, $(p_{\text{sat}})_\delta$. T_w has to be provided as an input to the solution procedure, resulting from the solution of the heat conduction problem in the fin between the grooves. The four boundary conditions for equations (2.5) and (2.6) must be developed taking the physical situation into account, as shown in the following sections.

As the liquid film thins, the disjoining pressure, p_d, and the interfacial temperature, T_δ, increase. Under specific conditions, a non-evaporating film thickness is present which gives the equality of the liquid-vapor interface and the solid surface temperatures, $T_\delta = T_w$. This is the thickness of the equilibrium non-evaporating film δ_0, which can be determined from equations (2.11) and (2.12). For a non-evaporating equilibrium film ($q = 0$), it follows from equation (2.12) that

$$(p_{\text{sat}})_\delta = p_v \sqrt{\frac{T_w}{T_v}} \tag{2.13}$$

Substitution of equations (2.7) and (2.13) into equation (2.11) gives

$$\delta_0 = \left\{ \left[p_v \sqrt{T_w/T_v} - p_{\text{sat}}(T_w) \right. \right. \tag{2.14}$$

$$\left. \left. - \rho_\ell R_g T_w \ln \left(\sqrt{T_w/T_v} \frac{p_v}{p_{\text{sat}}(T_w)} \right) - \sigma K \right] \frac{1}{A'} \right\}^{-1/B}$$

For water the following equation for the disjoining pressure was used (Holm and Goplen [17])

$$p_d = \rho_\ell R_g T_\delta \ln \left[a \left(\frac{\delta}{3.3} \right)^b \right] \tag{2.15}$$

where $a = 1.5336$ and $b = 0.0243$. The thickness of the equilibrium film is given for water by

$$\delta_0 = 3.3 \left\{ \frac{1}{a} \exp \left[\frac{p_{\text{sat}}(T_w) - p_v \sqrt{T_w/T_v} + \sigma K}{\rho_\ell R_g T_w} + \ln \left(\frac{p_v}{p_{\text{sat}}(T_w)} \sqrt{T_w/T_v} \right) \right] \right\}^{1/b} \tag{2.16}$$

2.1.2 Heat Transfer in the Thin-Film Region of the Evaporator

This problem has been treated numerically and experimentally by different authors, whose results are mentioned here to understand the basis of the present model. Kamotani [8], Holm and Goplen [17], and Stephan and Busse [11] modeled an evaporating extended meniscus in a capillary groove (Fig. 2.1). In all of the above papers, it is emphasized that most of the heat is transferred through the region where the thickness of the liquid layer is extremely small. The significance of the temperature difference between the saturated vapor core and the interface has been stressed by Solov'yev and Kovalev [15] and Stephan and Busse [11]. In the mathematical models of the above authors, the solid surface was assumed to be smooth. Kamotani [8] noted that this assumption and, generally, inclusion of the heat transfer in the microfilm region in the model could lead to an overestimation of the total heat transfer coefficient. The same concern has been expressed by Vasiliev et al. [9].

In light of these findings, in the present analysis the difference between the saturated vapor temperature and that of the free liquid surface was considered, and the existence of the surface roughness and its influence on evaporative heat transfer was taken into consideration. In general, manufacturing processes always leave some degree of roughness on the metallic surface. Alloys of copper, brass, steel and aluminum invariably have some distinct grain structure, resulting from processing the materials. In addition, corrosion and deposition of some substances on the surface can influence its microrelief. This means the solid surface is totally covered with microroughnesses, where the characteristic size may vary from, for example, $R_r = 10^{-8}$ to 10^{-6} m. Apparently, the thin liquid film formation can be affected by some of these microroughnesses. It can be assumed that at least some part of a single roughness fragment, on which the thin film formation takes place, has a circular cross section and is extended in the z-direction due to manufacturing the axial grooves (Fig. 2.2).

In the present analysis the free liquid surface is divided into four regions (Fig. 2.2). The first region is the equilibrium non-evaporating film. The second (microfilm) region ranges in the interval $\delta_0 \leq \delta \leq \delta_1$, where the increase of the liquid film thickness up to the value δ_1 is described by equations (2.5) and (2.6). In this region, the generalized capillary pressure $p_{\text{cap}} \equiv \sigma K - p_d$ (here p_{cap} was defined so that its value is positive) is changing drastically along the s-coordinate from the initial value up to an almost constant value at point s_1,

10

where the film thickness, δ_1, is large enough to neglect the capillary pressure gradient. It is useful to mention that some investigators have denoted this microfilm region as the "interline region." The third (transition) region, where the liquid-vapor interface curvature is constant, is bounded by $\delta_1 < \delta \leq R_r + \delta_0$, and the local film thickness is determined by the geometry of the solid surface relief and the value of the meniscus radius R_m. In the fourth (meniscus) region, where by definition $\delta > R_r + \delta_0$, the local film thickness can be considered independent of the solid surface microrelief. In the third and fourth regions, the heat transfer is determined by heat conduction in the meniscus liquid film and the metallic fin between the grooves. However, in the second region, the temperature gradient in the solid body can be neglected in comparison to that in liquid due to the extremely small size of this region.

The total heat flow rate per unit groove length in the microfilm region is defined as

$$Q'_{\text{mic}}(s_1) = \int_0^{s_1} \frac{T_w - T_\delta}{\delta/k_\ell} \, ds \equiv \int_0^{s_1} q \, ds \tag{2.17}$$

Equations (2.5)–(2.8), (2.11) and (2.12) must be solved for four variables: δ, δ', p_{cap} and $Q'_{\text{mic}}(s)$ in the interval from $s = 0$ to the point $s = s_1$, where p_{cap} can be considered to be constant. Now, instead of the two second-order equations (2.5) and (2.6), the following four first-order equations should be considered with their respective boundary conditions:

$$\frac{d\delta}{ds} = \delta' \tag{2.18}$$

$$\frac{d\delta'}{ds} = \left(1 + \delta'^2\right)^{3/2} \left(\frac{p_{\text{cap}} - A'\delta^{-B}}{\sigma} + \frac{1}{R_r}\right) \tag{2.19}$$

$$\frac{dp_{\text{cap}}}{ds} = -\frac{3\nu_\ell}{h_{fg}\delta^3} Q'_{\text{mic}}(s) \tag{2.20}$$

$$\frac{dQ'_{\text{mic}}}{ds} = \frac{T_w - T_\delta}{\delta/k_\ell} \tag{2.21}$$

$$\delta|_{s=0} = \delta_0 \tag{2.22}$$

$$\delta'|_{s=0} = 0 \tag{2.23}$$

$$p_{\text{cap}}|_{s=0} = -\frac{\sigma}{R_r + \delta_0} + A'\delta_0^{-B} \tag{2.24}$$

$$Q'_{\text{mic}}|_{s=0} = 0 \tag{2.25}$$

The value of δ_0 is found from equation (2.14), where $K = -1/R_r$.

Though the initial-value problem, equations (2.18)–(2.25) is completely determined, its solution must satisfy one more condition:

$$p_{\text{cap}}|_{s=s_1} = \frac{\sigma}{R_m} \tag{2.26}$$

11

Since the only parameter which is not fixed in this problem is connected with the surface roughness characteristics, the boundary condition (2.26) can be satisfied by the choice of R_r. Physically, it means that the beginning of the evaporating film is shifted along the rough surface depending on the situation so as to satisfy the conservation laws. However, in a smooth surface model ($R_r \to \infty$) the solution will probably not satisfy equation (2.26). As a result of this problem, the values of δ_1 and $Q'_{mic}(s_1)$ can be determined and the transition region can be considered, provided that $\delta_1 < R_r$, where the free liquid surface curvature is constant and its radius R_m is many times larger than R_r. Based on the geometry shown in Fig. 2.2, the following approximation for the liquid film thickness in the transition region $x_f \leq x \leq x_{tr}$ is given:

$$\delta = \delta_0 + R_r - \sqrt{R_r^2 - x^2} - R_m \\ + \left(R_m^2 + x^2 + 2R_m x \sin \theta_f\right)^{1/2} \tag{2.27}$$

Equation (2.27) is valid for the rough surface model (θ_f can be set equal to zero for very small R_r) and also the smooth surface model in the meniscus region ($R_r \to \infty$ and θ_f is given as a result of the microfilm problem solution).

The heat flow rate per unit groove length in the transition region is

$$Q'_{tr} = \int_{x_f}^{x_{tr}} \frac{T_w - T_\delta}{\delta/k_\ell} \, dx \tag{2.28}$$

where x_f and x_{tr} are obtained from equation (2.27) provided $\delta = \delta_1$ and $\delta = R_r + \delta_0$, respectively.

Now the connecting point between the transition and meniscus regions must be considered. At this point, the film thickness, the free surface curvature, and the liquid surface slope angle must coincide from both sides. In the rough surface model, the last condition is always satisfied because the length of the microfilm region is smaller than R_r, and the rough fragment with the film can be "turned" around its center in the needed direction (see Fig. 2.2). In other words, because of the circular geometry of the rough fragment and the constant temperature of the solid surface in the microfilm region, the slope of the film free surface is not fixed in the mathematical model. On the contrary, in the smooth surface model the numerical results give θ_f which is generally not equal to θ_{men} determined by the fluid flow along the groove. Stephan and Busse [11] seem to have answered this contradiction using a rounded fin corner, however, this explanation is not completely satisfactory. Note that in the situation when $\theta_f \approx \theta_{men}$, the smooth surface model can be used along with the rounded fin corner, where the radius is R_{fin}. In this case equation (2.27) can also be used provided R_r is changed to R_{fin}.

It is useful to mention here that the values of R_m and θ_{men} are connected by the geometric relation $\theta_{men} = \arccos(W/R_m) - \gamma$ and should be given as a result of the solution of the problem for the fluid transport along the groove. The fin top temperature T_w should be defined from the consideration of the heat conduction problem in the fin between grooves and in the meniscus liquid film discussed below.

Simplified Model of Heat Transfer in the Evaporating Thin Film

12

The free liquid surface curvature K in the microfilm region varies from the initial value to that in the meniscus region. Its variation is described by equations (2.18)–(2.26) with respect to the p_{cap} and p_d definitions. In spite of a sharp maximum which the K function has in the microfilm region, its variation only slightly affects the total heat transfer coefficient. To check this hypothesis numerically, a simplified version of the heat transfer model of the microfilm region was developed, where it was assumed that the microfilm free surface curvature is equal to that in the meniscus region. Therefore, instead of solving equations (2.18)–(2.26), the microfilm thickness in this region (and also in the transition region) can be given by equation (2.27) for the interval $0 \leq x \leq x_{tr}$. In this case, the heat flow rate per unit groove length in both the microfilm and transition regions is

$$Q'_{\mathrm{mic}} + Q'_{tr} = \int_0^{x_{tr}} \frac{T_w - T_\delta}{\delta / k_\ell} \, dx \tag{2.29}$$

2.1.3 Heat Transfer in the Thin-Film Region of the Condenser

Heat transfer during condensation on a grooved surface has been considered by Kamotani [7] and Babenko et al. [18] for the case of rectangular and trapezoidal fins with rounded corners, respectively, with the assumption that $T_\delta = T_v$. Analyzing their results, the following conclusions are made, which lead to the simplification of equations (2.5) and (2.6):

1. The surface of the liquid film is smooth and the film thickness variation along s-coordinate is weak (see Fig. 2.1):

$$\left(\frac{d\delta}{ds}\right)^2 \ll 1$$

2. The disjoining pressure gradient along the film flow can be neglected in comparison to that of the capillary pressure due to the surface tension force because of the large film thickness.

Taking the above points into consideration, and substituting equation (2.6) into equation (2.5) gives the following differential equation for the film thickness at the top of the fin between grooves:

$$\delta \frac{d}{ds}\left[\delta^3 \left(\frac{d^3\delta}{ds^3} + \frac{dK_w}{ds}\right)\right] = \frac{3\mu_\ell k_\ell}{\sigma h_{fg}\rho_\ell}(T_\delta - T_w) \tag{2.30}$$

The boundary conditions for equation (2.30) at $s = 0$ are

$$\frac{d\delta}{ds} = 0 \; ; \quad \frac{d^3\delta}{ds^3} = 0 \tag{2.31}$$

These conditions imply that the thickness and curvature of the film are symmetric around $s = 0$. For small κ (see Fig. 2.1(a)) at $s = L_2$, the curvature of the film and its surface slope angle are determined by the radius of the meniscus in the groove:

13

$$\frac{d^2\delta}{ds^2} = \frac{1}{R_m} \tag{2.32}$$

$$\frac{d\delta}{ds} = \tan\left(\kappa - \arcsin\frac{W}{R_m} + \arcsin\frac{L_1}{R_v}\right) \tag{2.33}$$

where L_2 is the length of the film, which is equal to L_1 in the case of a flat fin top geometry (Fig. 2.1). The boundary value problem, equations (2.30)–(2.33), is solved approximately by introducing the following polynomial function for the film thickness:

$$\delta(s) = C_0 + C_1(s - L_2) + C_2(s - L_2)^2 + C_3(s - L_2)^3 + C_4(s - L_2)^4 \tag{2.34}$$

From the boundary conditions (2.31)–(2.33) the values of the coefficients are

$$C_1 = \tan\left(\kappa - \arcsin\frac{W}{R_m} + \arcsin\frac{L_1}{R_v}\right), \quad C_2 = \frac{1}{2R_m}$$

$$C_3 = \frac{2C_2L_2 - C_1}{2L_2^2}, \qquad C_4 = \frac{C_3}{4L_2}$$

At the point $s = L_2$, where the thickness of the film is usually at a minimum, equation (2.30) must be satisfied exactly, and the total mass flow rate of the condensate due to the surface tension force must be equal to the total amount of fluid condensed in the region $0 \leq s \leq L_2$. Thus, integrating equation (2.30) we have

$$\frac{\sigma h_{fg}\rho_\ell}{3\mu_\ell}\left[\delta^3\left(\frac{d^3\delta}{ds^3} + \frac{dK_w}{ds}\right)\right]_{(s=L_2)}$$

$$= k_\ell \int_0^{L_2} \frac{T_\delta - T_w}{\delta}\, ds \tag{2.35}$$

Substituting equation (2.34) into equation (2.35) and solving numerically for C_0, the heat flow rate per unit groove length through the thin film region is

$$Q'_\delta = \int_0^{L_2} \frac{k_\ell(T_\delta - T_w)}{C_0 + C_1\dot{s} + C_2\dot{s}^2 + C_3\dot{s}^3 + C_4\dot{s}^4}\, ds \tag{2.36}$$

where $\dot{s} \equiv s - L_2$. The fin top temperature T_w is given from the results of the heat conduction problem in the fin and the meniscus region. Equation (2.35) must also be solved within the following iterative procedure because of the influence of the film surface curvature and the disjoining pressure on T_δ. In the first iteration, T_δ is defined from equations (2.11) and (2.12) assuming that $K = \overline{K}_w$ and $p_d = 0$. In the second and following steps

$$K = \overline{K}_w + \overline{\frac{d^2\delta}{ds^2}}$$

where the last term is calculated using the solution of the previous step for $\delta(s)$ and $p_d = p_d(\overline{\delta})$ (here the bar denotes an average value). While the influence of K on the presented

14

results was negligible in comparison with the effect of the meniscus radius variation, it can be important for extremely thin films of condensate with large free surface curvatures, in which case the problem should be treated numerically in the frames of a more complicated analysis.

Now, the consideration of the meniscus region gives the opportunity to obtain the heat transfer coefficients.

2.1.4 Heat Conduction in the Metallic Fin and Meniscus Region of the Liquid Film

For low-temperature heat pipes, the thermal conductivity of the metallic casing is several hundred times higher than that of the liquid working fluid. Nearly all of the heat is transferred from the metallic fin between grooves to the saturated vapor or vice versa through a thin liquid film in the vicinity of the fin top. The temperature drop in the metallic fin is many times smaller than in the liquid film (Schneider et al.[19]; Stephan and Busse[11]). Therefore, in the present analysis the temperature gradient in the metallic fin in the direction transverse to the x-coordinate is neglected (Fig. 2.1). The heat conduction in the metallic fin and meniscus liquid film is described by the following equation, which was obtained as a result of an energy balance over a differential element (Vasiliev et al. [9]):

$$\frac{d^2 T}{dx^2} + \frac{dT}{dx}\frac{\tan(\gamma + \chi)}{L_{\text{fin}}(x)} + (T_\delta - T)\frac{k_\ell}{k_w \delta(x) L_{\text{fin}}(x)} = 0 \qquad (2.37)$$

The fin thickness variation is due to its wall inclination angle and the circular tube geometry

$$L_{\text{fin}}(x) = L_1 + x\tan(\gamma + \chi) \qquad (2.38)$$

and the liquid film thickness is

$$\delta = \delta_2 - R_m \qquad (2.39)$$

$$+ \left[R_m{}^2 + \frac{x^2}{\cos^2(\gamma + \chi)} + \frac{2R_m x \sin\theta_{\text{men}}}{\cos(\gamma + \chi)} \right]^{1/2}$$

where δ is measured perpendicularly from the liquid-vapor interface. Equations (2.37)–(2.39) are valid for the evaporator and condenser sections. However, the boundary conditions for equation (2.37) in these two sections are different, and the value of δ_2 should be chosen as follows:

$\delta_2 = R_r + \delta_0$ in the rough surface evaporation model,

$\delta_2 = \delta_1$ in the smooth surface evaporation model,

$\delta_2 = \delta|_{s=L_2}$ for the condenser heat transfer model.

The boundary conditions for equation (2.37) in the evaporator are

$$\frac{dT}{dx}\bigg|_{x=0} = \frac{Q'_{\text{mic}} + Q'_{tr}}{k_w L_1} \qquad (2.40)$$

$$\frac{dT}{dx}\bigg|_{x=t_g} = \frac{q_e \pi R_o}{k_w N [L_1 + t_g \tan(\gamma + \chi)]} \quad (2.41)$$

where boundary condition (2.40) is written with the assumption that $x_{tr} \ll t_g$. For the simplified model, equation (2.37) was solved also in the microfilm and transition regions, where δ was given by equation (2.27) and the right-hand side of equation (2.40) was set equal to zero.

The boundary conditions for equation (2.37) in the condenser are

$$\frac{dT}{dx}\bigg|_{x=0} = -\frac{Q_\delta'}{k_w L_1} \quad (2.42)$$

$$\frac{dT}{dx}\bigg|_{x=t_g} = -\frac{q_c \pi R_o}{k_w N [L_1 + t_g \tan(\gamma + \chi)]} \quad (2.43)$$

While the values of Q_{mic}', Q_{tr}' and Q_δ' depend on $T_w \equiv T|_{x=0}$, which is obtained from the solution of equations (2.37)–(2.43), this problem is to be solved in conjunction with those concerning heat transfer in the thin film regions.

The local heat transfer coefficient (for a given z) in the evaporator from the bottom of the groove surface to the vapor is

$$\overline{h}_{e,\text{bot}} = \frac{q_e}{[T|_{x=t_g} - T_v]} \frac{R_o}{R_v + t_t + t_g} \quad (2.44)$$

The local heat transfer coefficient from the external surface of the evaporator to the vapor is

$$\overline{h}_e = \left[\frac{R_o}{k_w} \ln \frac{R_o}{R_v + t_t + t_g} + \frac{1}{\overline{h}_{e,\text{bot}}} \frac{R_o}{R_v + t_t + t_g} \right]^{-1} \quad (2.45)$$

where the thermal resistance of the circular tube wall is taken into account.

For the condenser region, the heat transfer coefficients are defined in a similar manner:

$$\overline{h}_{c,\text{bot}} = -\frac{q_c}{[T|_{(x=t_g)} - T_v]} \frac{R_o}{R_v + t_t + t_g} \quad (2.46)$$

$$\overline{h}_c = \left[\frac{R_o}{k_w} \ln \frac{R_o}{R_v + t_t + t_g} + \frac{1}{\overline{h}_{c,\text{bot}}} \frac{R_o}{R_v + t_t + t_g} \right]^{-1} \quad (2.47)$$

2.1.5 Numerical Treatment

Equations (2.11) and (2.12) were simultaneously solved for T_δ (absolute error $\Delta_a = 0.0001$ K) and $(p_{\text{sat}})_\delta$ ($\Delta_a = 1$ Pa) for every point on s by means of Wegstein's iteration method (Lance [68]). The system of the four first-order ordinary differential equations with four initial conditions and one constitutive condition describing the evaporating microfilm region, equations (2.18)–(2.26), were solved using the fourth-order Runge-Kutta procedure and the shooting method (on parameter R_r). The controlled relative error was less than

16

0.001% for each of the variables. The results obtained for comparatively small temperature drops through the thin film were compared with those from the simplified model. Since the agreement was good, the simplified model was used further in the prediction of the AGHP characteristics. Equation (2.35) was solved for C_0 by means of Muller's iteration method ($\Delta_a = 10^{-11}$ m), and the integration in equation (2.36) was made using Simpson's method. The heat conduction problem, equations (2.37)–(2.43), was also solved by the standard Runge-Kutta method ($\Delta_a = 0.0001$ K and $\Delta_r = 0.001\%$ for the functions T and dT/dx, respectively) along with equations (2.35) and (2.36) within the iterative procedure to find T_w ($\Delta_a = 0.0001$ K).

2.1.6   Results and Discussion

To verify the numerical results obtained, the experimental data provided by Schlitt et al. [20] were used. Therefore, the presented results mostly refer to the AGHP with the following geometry: $L_{\text{tot}} = 0.914$ m, $L_c = 0.152$ m, $0.15 \leq L_e \leq 0.343$ m, $W = 0.305$ mm, t_g = 1.02 mm, $L_1 = 0.215$ mm, $R_v = 4.43$ mm, $R_o = 7.95$ mm, $\gamma = 0$, $N = 27$, $\kappa = 0$, $t_t = 0$. The working fluids were ammonia and ethane, the casing material thermal conductivity was assumed to be $k_w = 170$ W/(m-K), $\alpha = 1$ (if another value is not indicated in the text), dispersion constant $A' = 10^{-21}$ J and $B = 3$.

The data in Figs. 2.3–2.5 were obtained for ammonia with a vapor temperature in the evaporator of $T_v = 250$ K and $\alpha = 1$. The solid surface superheat is $\Delta T = |T_w - T_v|$, and the results obtained using the simplified model for evaporating film are denoted as SIMPL.

Figure 2.3(a) shows the variations of the free liquid surface temperature along the evaporating film for $\Delta T = 0.047$ K, 0.070 K and 0.120 K, which are from the solutions of equations (2.7), (2.11)–(2.13), and (2.18)–(2.26) in the microfilm region. These results are compared to those obtained by the simplified model, where equations (2.7) and (2.11)–(2.13) were solved along with equations (2.27), (2.37) and (2.38) with the boundary conditions

$$ T|_{x=0} = T_w, \qquad \frac{dT}{dx}\Big|_{x=0} = 0 $$

in the microfilm and transition regions for the same values of the roughness characteristic sizes ($R_r = 0.33$ μm, 1.0 μm and $R_r \to \infty$). It should be noted that the temperature drop in the solid body in these regions was negligible in the results of the simplified model in comparison to ΔT, and the equilibrium film thickness was defined within the assumption that its free surface curvature was equal to $1/R_m$. In the simplified model for the case of a smooth surface, the value of the contact angle in the microfilm region was $\theta_f = 7°$, which was given by the numerical solution of equations (2.18)–(2.26).

The corresponding variations of the film thickness δ and generalized capillary pressure p_{cap} are shown in the Figs. 2.3(b) and 2.3(c). The results obtained by the simplified model have been artificially shifted along the s-coordinate in these figures (and also in Fig. 2.4(a)) to make the comparison more understandable. Also, it should be noted that there is some difference between the s-coordinate and the x-coordinate used in the simplified model. The following relation has been used in the present model: $s = R_r \arcsin(x/R_r)$.

In Fig. 2.3(a), the interval of T_δ variation along the evaporating film from the value of T_w
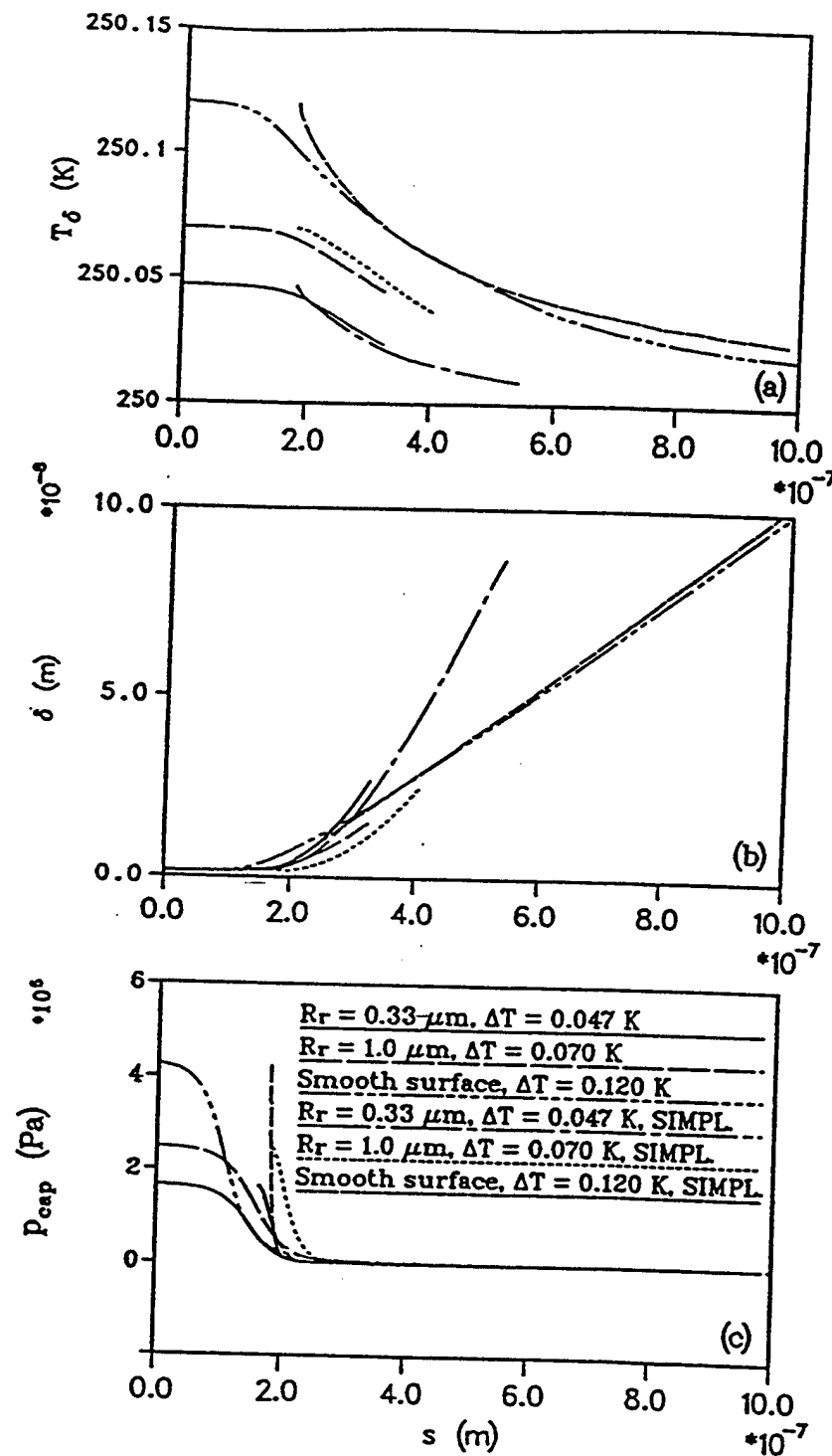
Figure 2.3: Characteristics of the evaporating film along the solid-liquid interface (ammonia, $T_v = 250$ K): (a) free liquid surface temperature; (b)thickness of the film; (c) generalized capillary pressure.

18
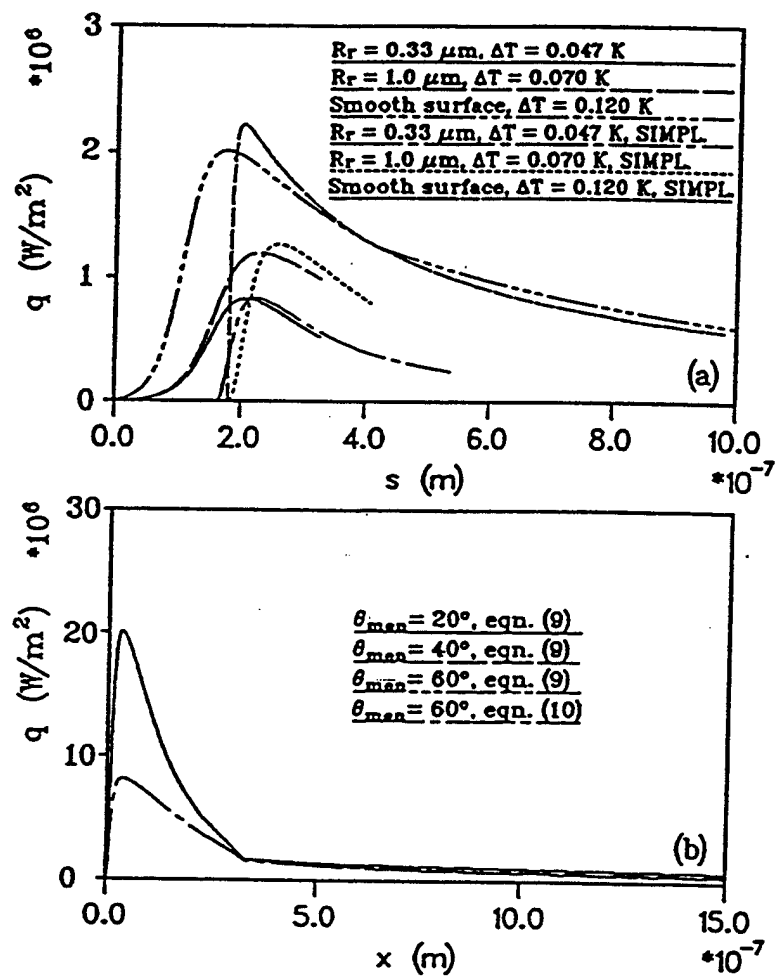
Figure 2.4: Heat flux through the evaporating film (ammonia, $T_v = 250$ K, $\alpha = 1$): (a) along the solid-liquid interface (microfilm region); (b) along the fin axis ($R_r = 0.33$ μm, $\Delta T = 1$ K).
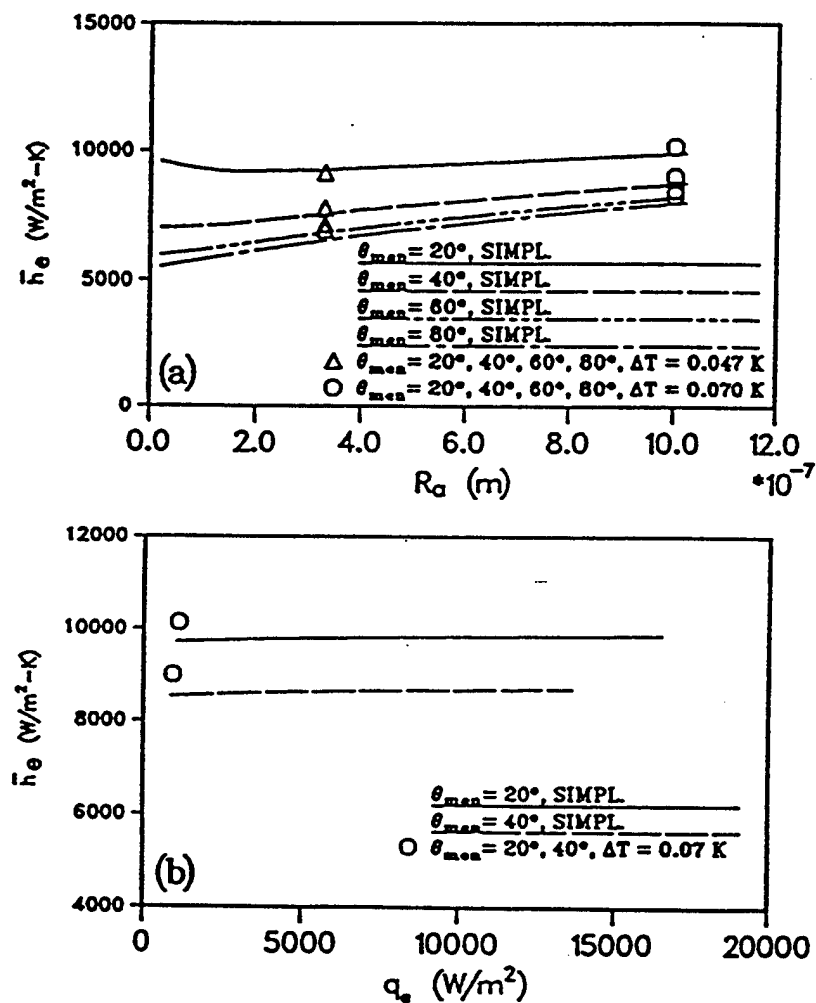
Figure 2.5: Local heat transfer coefficient in the evaporator of the ammonia-Al heat pipe ($T_v = 250$ K): (a) versus roughness size; (b) versus heat flux($R_r = 1$ μm).
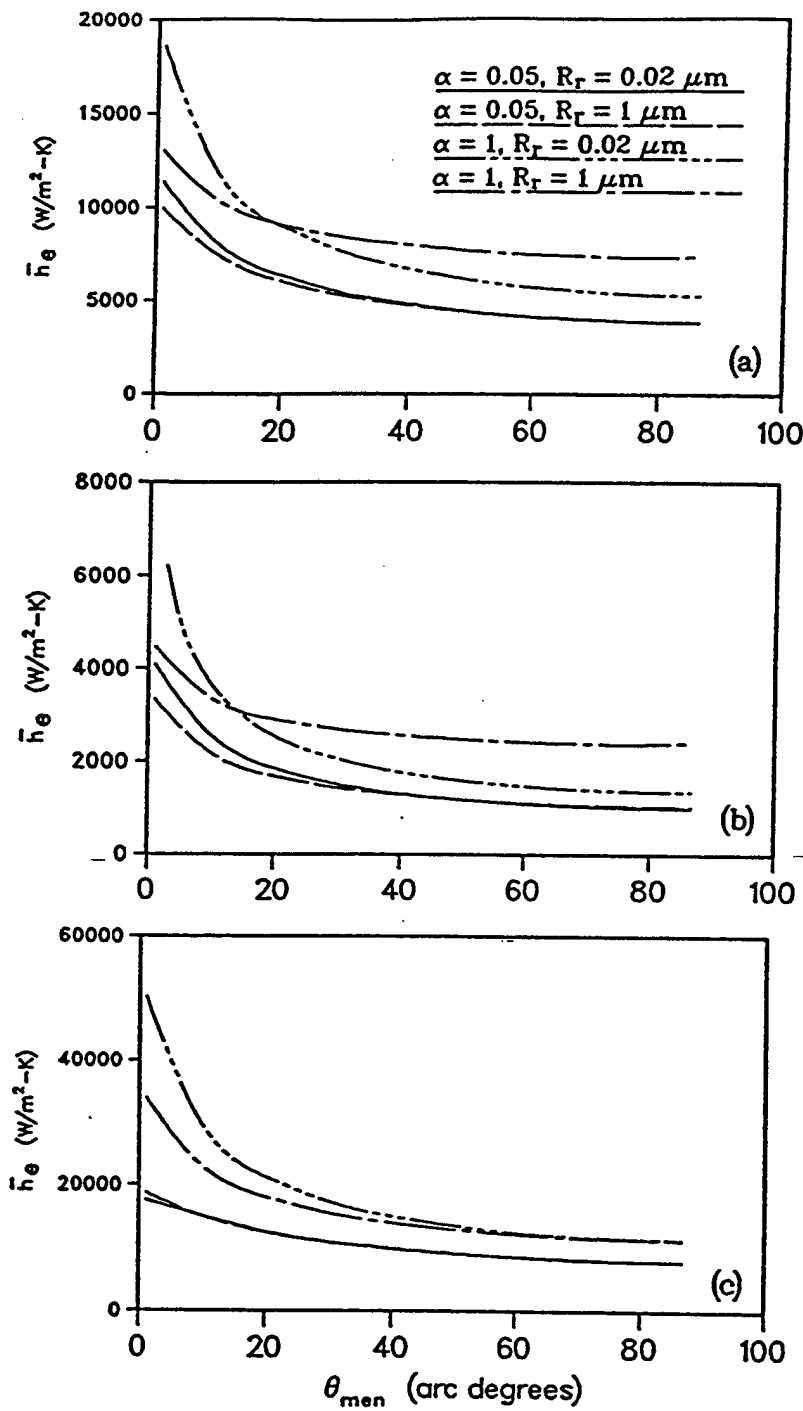
Figure 2.6: Effect of the meniscus contact angle on the local evaporative heat transfer coefficients ($\Delta T = 1$ K): (a) Ammonia-Al heat pipe by Schlitt et al.[20], ($T_v = 250$ K); (b) Ethane-Al heat pipe by Schlitt et al.[20], ($T_v = 200$ K); (c) water-copper evaporator by Ivanovskii et al. [21], ($T_v = 300$ K).

to approximately T_v was more prolonged in comparison to the results by Stephan and Busse [11] and the interfacial thermal resistance was still significant even when the film thickness was larger than 0.1 μm. For a smaller characteristic size R_r, the film thickness increased more sharply along the solid surface (Fig. 2.3(b)), which is in agreement with equation (2.27). It should be mentioned that for the problem, equations (2.18)–(2.26) (unlike for the simplified model) R_r is not a parameter but the result of the numerical solution. The values of the maximum heat flux in the microfilm region were extremely high in comparison to those in the meniscus region (Fig. 2.4).

For $\Delta T = 0.120$ K, the generalized capillary pressure p_{cap} decreased from the initial value to the almost constant by approximately 5000 times (Fig. 2.3(c)). For a larger ΔT, this sharp decrease can cause some difficulties in the numerical treatment while solving equations (2.18)–(2.26); that is why the simplified model is useful. The simplified model has given the variation of p_{cap} along the film which is even more drastic because of the surface tension term is absent in the capillary pressure gradient (Fig. 2.3(c)). However, the decrease of the total heat flow rate in the microfilm region caused by this assumption was comparatively small, which is illustrated by Fig. 2.4(a). The distributions of the heat flux in the microfilm, transition and beginning of meniscus regions for different meniscus contact angles θ_{men} as predicted by the simplified model are presented in Fig. 2.4(b). The total heat flow through the meniscus region was significantly larger in comparison to that through the microfilm region. This means that while estimating the heat transfer coefficient for an evaporator element, shown in Fig. 2.1, the simplified model should provide the accuracy needed. To verify this, the numerical results for the local heat transfer coefficient $\overline{h}_e$ in Fig. 2.5(a) have been obtained. The simplified model underestimated $\overline{h}_e$ by only 5%, which enables its use when it is necessary to avoid the numerical difficulties mentioned above. The local evaporative heat transfer coefficient $\overline{h}_e$ depends upon the meniscus contact angle θ_{men}, especially for small θ_{men}, and is practically independent of the heat flux on the external wall surface of the evaporator and also of ΔT, as shown in Fig. 2.5(b). The characteristic roughness size affected the value of $\overline{h}_e$, decreasing it up to 30% for $\alpha = 1$ in comparison to the value obtained for the smooth solid surface. For large meniscus contact angle the influence of the roughness size on the heat transfer coefficient is at the maximum when R_r is close to the length of the microfilm region. For small values of the accommodation coefficient (for example for $\alpha = 0.05$) the effect of the surface roughness on the heat transfer is insignificant because the heat flux in the microfilm region in this case is comparatively small (Fig. 2.6).

The results of the present model were compared with the experimental data by Schlitt et al. [20] and Ivanovskii et al. [21] for the case of a small heat load applied to the AGHP (or evaporator). For a small heat load ($Q_a \ll Q_{max}$) the values of the meniscus angle in both the evaporator and condenser of the AGHP under consideration are comparatively large: $\theta_{men} \geq 60°$ in the evaporator and $\theta_{men} \geq 80°$ in the condenser. This is valid because in the case without a heat load the grooves of an AGHP in the horizontal position are completely filled with liquid (i.e., the meniscus angle is close to 90°). For $\theta_{men} \geq 60°$ the local evaporative heat transfer coefficients are practically independent on θ_{men}, as shown in Fig. 2.6. The values of the evaporative heat transfer coefficients (based on the outer tube diameter) obtained experimentally by Schlitt et al. [20] and those reported by Ivanovskii et al. [21] were also found to be independent of heat load, which resulted in a valid comparison,

22

Table 2.1: Comparison of the predicted $\bar{h}_e$ with existing experimental data

Investigators	Schlitt et al. [20]	Schlitt et al.[20]	Ivanovskii et al. [21]
Working fluid	Ammonia	Ethane	Water
T_v (K)	250	200	300
Casing material	Aluminum	Aluminum	Copper
Experimental value of $\bar{h}_e$ (W/m²-K)	3920	770	9500
Present prediction, $\bar{h}_e$ (W/m²-K), $\theta = 60°$, $\alpha = 0.05$	4140	1180	8620

Table 2.2: Comparison of the results with simplified models

Authors	Present		Stephan and Busse [11]		Schneider [19]	Shekriladze [24]
Assumption:	$T_\delta > T_v$	$T_\delta > T_v$	$T_{\delta v} > T_v$	$T_{\delta v} = T_v$	$T_\delta = T_v$	$T_\delta = T_v$
Surface:	rough	smooth	smooth	smooth	smooth	smooth
$T_w - T_v$, (K)	1.31	1.31	1.31	1.31	-	-
$\bar{h}_e$,(W/cm²-K)	1.74	2.39	2.3	7.9	6.9	3.9
q_e, (W/cm²)	2.56	3.69	3.0	10.4	-	-
Q'_{mic}/Q'_t, (%)	37	38	45	94	-	-

as given in Table 1.

The agreement of the results for ammonia, ethane and water is good for $\alpha \ll 1$ since it was mentioned by Carey [12] that, for some substances (ethanol, methanol, water, etc.), the accommodation coefficient had been found to have very small values (0.02 to 0.04) in the experiments by Paul [22]. The physical reason for low α values in the microfilm region of the evaporator can be the concentration of the contaminants which usually exist in a heat pipe in this region. For the case of $\alpha = 1$, the prediction gave significant (up to 100%) overestimations of $\bar{h}_e$ even for a rough surface, as can be seen from Fig. 2.6. The experimental data by Ivanovskii et al. [21] correspond to the case of evaporation of water from a copper plate with rectangular grooves for heat fluxes on the wall up to 20 W/cm² ($W = 0.17$ mm, $t_g = 0.8$ mm, $L_1 = 0.25$ mm, $L_e = 100$ mm, $T_v = 300$ K).

A comparison with the numerical data reported by Stephan and Busse [11] has also been made for ammonia with: $T_v = 300$ K, $k_w = 221$ W/(m²-K), $A' = 2 \times 10^{-21}$ J, $\alpha = 1$, $L_1 = 0.5 \times 10^{-5}$ m, $W = 0.5 \times 10^{-3}$ m, $\gamma = 45°$, $t_g = 0.5 \times 10^{-3}$ m, $R_v = 1$ m, $R_o = 1.0015$ m, $\theta_f = \theta_{men} = 19.7°$, $\Delta T = 1.31$ K. The results of the comparison are listed in Table 2, which was prepared by Stephan and Busse [11] except for the data of the present analysis.

$T_{\delta v}$ is the temperature of the vapor side of the interface and Q'_{mic} is the heat flow rate per unit groove length in the region $0 \leq x \leq 1$ μm. The value of the heat transfer coefficient by Stephan and Busse [11] was 23,000 W/(m^2-K), while the result of the present numerical analysis is 17,385 W/(m^2-K) for a rough surface (for $R_r = 0.02$ μm) and 23,900 W/(m^2-K) for a smooth surface, which proves the validity of the present analysis.

The influence of the meniscus contact angle on the local heat transfer coefficient in the condenser (configuration by Schlitt et al. [20]) is demonstrated in Fig. 2.7. The results agree qualitatively with those obtained by Babenko et al. [18]. The increase of the liquid surface curvature causes the strong decrease of the heat transfer coefficient, where a sharp maximum occurs in the vicinity of maximum θ_{men}. In this location, the heat transfer coefficient is also dependent on the temperature drop ΔT. In the numerical experiments the liquid film thickness was comparatively large (Fig. 2.7(a)) and the interfacial thermal resistance was negligible in comparison with that of the film. The values of the heat transfer coefficient in the condenser based on the outer tube diameter for the ammonia ($T_v = 250$ K) and ethane ($T_v = 200$ K) heat pipes reported by Schlitt et al. [20] are 7600 and 3300 W/(m^2-K), respectively. The numerical predictions were of the same order of magnitude as that reported by Schlitt et al. [20].

2.1.7 Conclusions

The results of the numerical simulation of heat transfer during evaporation and condensation on the grooved surfaces of heat pipes are summarized as follows:

1. The validity of the present mathematical model for grooved evaporators has been confirmed, in general, by the comparisons with experimental data by Schlitt et al. [20], Ivanovskii et al. [21] and the numerical results by Stephan and Busse [11]. However, more detailed information concerning the values of the accommodation coefficients and dispersion constants is needed.

2. Accounting for the roughness of the solid surface in the thin evaporating film region resulted in a decrease of the heat transfer coefficient by up to about 30% in comparison to that obtained for a smooth surface for the case when the accommodation coefficient was set equal to unity. For $\alpha \ll 1$ the influence of the surface roughness on the evaporative heat transfer coefficient was insignificant.

3. The simplified model of evaporative heat transfer, where it was assumed that the free film surface curvature in the microfilm region was equal to that in the meniscus region, predicted values of the heat transfer coefficient only up to 5% smaller in comparison to the case where the curvature variation along the film was taken into account (for $\alpha = 1$).

4. The value of the local evaporative heat transfer coefficient (for a fixed θ_{men}) was practically independent of the heat flux on the evaporator external wall.

5. The interfacial resistance significantly influenced the value of the evaporative heat transfer coefficient. Therefore, the more advanced expressions for this resistance during high intensive evaporation are needed.

24

6. The interfacial resistance and the disjoining pressure had negligible effects on the heat transfer in grooved condensers because of the large thickness of the liquid film, while the effect of the meniscus contact angle was significant.

7. Due to the fact that the greatest part of the heat flow through the liquid is transferred in the meniscus region where the liquid film is comparatively small, grooved evaporators are capable of withstanding comparatively high heat fluxes. While the model gives the values of the temperature drop in the liquid during evaporation, it provides an opportunity to predict the onset of the nucleate boiling in grooved evaporators.

In order to make the comparisons with experimental data more profound, the longitudinal variation of the meniscus angle should be taken into account. That means that the fluid circulation in an AGHP should be considered in conjunction with the present analysis.

2.2 Fluid Flow Effects in Evaporation From Liquid-Vapor Meniscus

Heat transfer during evaporation of liquid from the liquid-vapor meniscus attached to the heated solid wall has been considered by many investigators due to its importance in predicting the performance characteristics of various two-phase devices with capillary structures such as heat pipes, evaporators, heat sinks, and separators. Potash and Wayner [23], Schneider and Yovanovich [19], Holm and Goplen [17], and Solov'ev and Kovalev [15] demonstrated the importance of the thin-film region of a liquid-vapor meniscus in the overall heat transfer during evaporation. Heat transfer in evaporating microfilm and the influence of disjoining pressure was considered in various aspects by P. Wayner, Jr., and co-authors. The variation of heat transfer coefficients along the liquid microfilm was modeled by Wayner et al. [13]. Kamotani [24], Stephan and Busse [11], and Stephan [25] emphasized temperature variation at the liquid free surface of the microfilm while modeling evaporative heat transfer on capillary-grooved surfaces. Their results are consistent with section 2.1. The temperature of the saturated vapor over the liquid-vapor interface was assumed constant which resulted in a constant temperature for the meniscus liquid-vapor interface, except in the microfilm region. The vapor was assumed saturated over the interface with constant pressure, p_v, and temperature, $T_v = T_{\text{sat}}(p_v)$. In fact, this assumption was made in all previous models of evaporating menisci in the absence of noncondensible gas. All of the above mentioned works did not consider the flow and heat transfer in the vapor over the interface. Only heat transfer due to conduction in the liquid was considered. However, at high heat fluxes, fluid flow becomes important. The superheat of the vapor exiting the metal capillary structure of a heat pipe evaporator due to the heat transfer between the vapor and the heated structure should also be taken into account in heat pipe numerical simulation.

2.2.1 Objectives of the present analysis

The objective of the present analysis is to investigate the influence of the liquid and vapor flows on the heat transfer in evaporation from the liquid-vapor meniscus and to numerically evaluate the vapor flow patterns in a narrow passage over the curved interface.

25
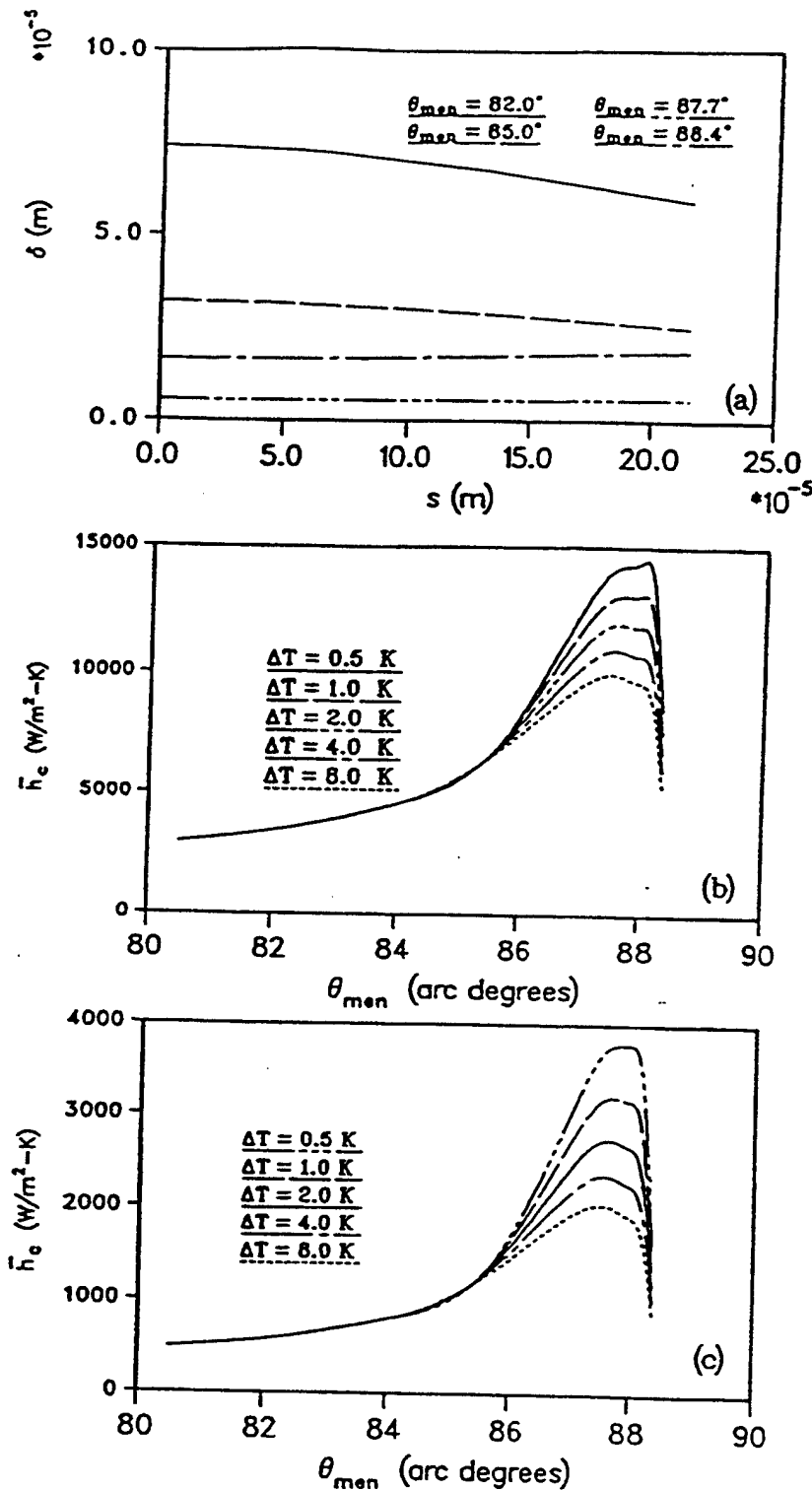
Figure 2.7: Effect of the meniscus contact angle in the Heat pipe condenser on: (a) liquid film thickness variation along the Surface of the fin top (ammonia, $\Delta T = 1$ K. $T_v = 250$ K); (b) local heat transfer coefficient for ammonia ($t_v = 250$ k) (c) local heat transfer coefficient for ethane ($T_v = 200$ K).

Evaporation of liquids from capillary grooves, pores, and slots takes place due to the solid wall superheat. The temperature of the solid-liquid interface, T_w, is higher than that of the vapor-liquid interface. Since the solid wall thermal conductivity is significantly higher than that of liquid in many technical applications, constant wall temperature is assumed in the present analysis. The solid wall in the vicinity of the interline, which is an apparent liquid-vapor-solid boundary, can be dry or covered with non-evaporating liquid film; in both cases, the temperature of the solid wall or of the non-evaporating liquid free surface is T_w. Since the temperature of the vapor over the evaporating meniscus is lower than T_w, the vapor is affected by the superheated wall and/or liquid and becomes superheated itself. This means that the temperature of the vapor some distance from the liquid-vapor interface can be higher than $T_{sat}(p_v)$. Note that for comparatively thick liquid films ($\delta \geq 1 \ \mu m$) the liquid-vapor interface temperature is very close to the vapor temperature. This is due to the fact that the interfacial thermal resistance is small compared to that of the liquid films as shown in section 2.1 (also by Khrustalev and Faghri, [26]). Based on this consideration, the momentum conservation and energy equations for the evaporating liquid and vapor over the liquid-vapor interface are included in the present model of the evaporating extended meniscus.

2.2.2 Mathematical model of evaporating meniscus in a narrow slot

The evaporation of the liquid from the liquid-vapor meniscus interface in a narrow slot considered in the present model is illustrated by Figure 2.8. Gravitational body forces are negligible compared to surface tension forces due to small size of the meniscus. It is assumed that the liquid-vapor interface curvature is constant: $K = 1/R_{men}$. This assumption can be justified by the results of Swanson and Peterson [70] where one-sided formulation of the heat transfer and flow in liquid was used. Actually, the curvature of the liquid-vapor interface of the evaporating non-isothermal meniscus is not exactly constant, especially in the microfilm region. However, the assumption of constant curvature of the interface is sufficient to model the heat transfer and flow in the vapor phase over the evaporating meniscus. In the present model, the evaporating microfilm is the thin-film part of the meniscus where the disjoining pressure is significant and the temperature of the liquid-vapor interface differs from that of the vapor phase over the given point of the interface. This microfilm is considered using the approach of section 2.1, while the fluid flow and heat transfer in the major part of the domain shown in Figure 2.8 is treated by two-dimensional analysis. A special control volume for the microfilm part of the meniscus has been developed to include the characteristics of the microfilm in the two-dimensional analysis.

2.2.3 Governing equations for the 2-D analysis

For an incompressible fluid with constant vapor and liquid viscosities and temperature dependent vapor density, the continuity and momentum equations for both the vapor and liquid are:

$$\frac{\partial u}{\partial x} + \frac{\partial v}{\partial y} = 0 \qquad (2.48)$$

27
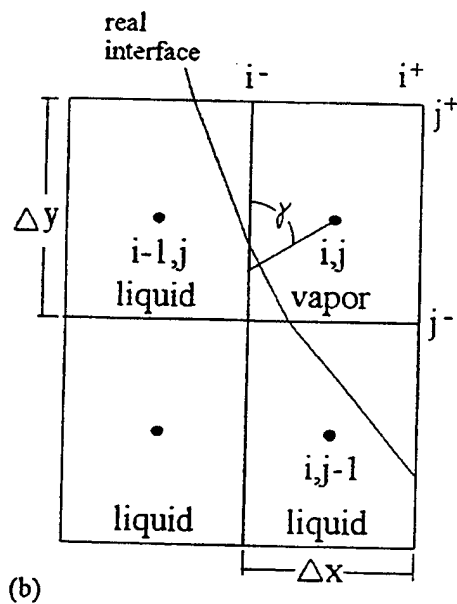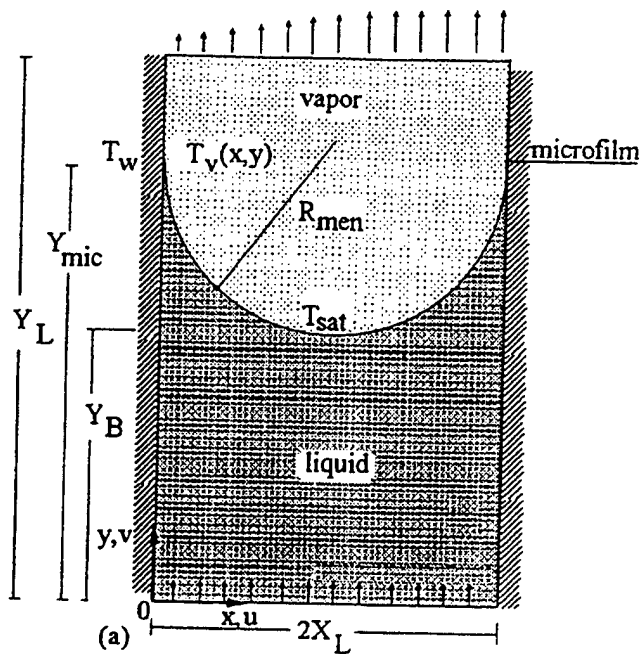
Figure 2.8: Evaporating liquid-vapor meniscus (a) computational domain conventions (b) typical element of the liquid-vapor interface

$$\rho \left(u \frac{\partial u}{\partial x} + v \frac{\partial u}{\partial y} \right) = -\frac{\partial p}{\partial x} + \mu \left(\frac{\partial^2 u}{\partial x^2} + \frac{\partial^2 u}{\partial y^2} \right) \tag{2.49}$$

$$\rho \left(u \frac{\partial v}{\partial x} + v \frac{\partial v}{\partial y} \right) = -\frac{\partial p}{\partial y} + \mu \left(\frac{\partial^2 v}{\partial x^2} + \frac{\partial^2 v}{\partial y^2} \right) \tag{2.50}$$

The energy equation for both the vapor and liquid is

$$\rho c_p \left(u \frac{\partial T}{\partial x} + v \frac{\partial T}{\partial y} \right) = k \left(\frac{\partial^2 T}{\partial x^2} + \frac{\partial^2 T}{\partial y^2} \right) \tag{2.51}$$

2.2.4 Boundary conditions

The wall temperature is assumed constant (except for the control volume enclosing the microfilm).

$$T|_{x=0} = T_w \tag{2.52}$$

The inlet flow temperature is known.

$$T|_{y=0} = T_w \tag{2.53}$$

No-slip conditions at the wall are assumed.

$$u|_{x=0} = v|_{x=0} = 0 \tag{2.54}$$

At the inlet, the parabolic velocity profile is assumed given from the solution of the Stokes equation for viscous flows.

$$u|_{y=0} = 0 \tag{2.55}$$

$$v|_{y=0} = \frac{3\dot{m}_{\ell,in}}{2\rho_\ell} \frac{x}{X_L^3} (2X_L - x) \tag{2.56}$$

At the symmetry line, $x = X_L$, $u = 0$, $dv/dx = 0$, and $dT/dx = 0$.

2.2.5 Consideration of the interface

The heat transported from the liquid to a vapor rectangular control volume at the interface by heat conduction and liquid flow in the neighboring liquid control volumes (from the left and/or from the bottom) is denoted as $\dot{Q}_{\ell,int}$. For the typical vapor control volume with adjacent left and bottom liquid control volumes shown in Fig. 2.8(b), $\dot{Q}_{\ell,int}$ can be expressed as follows.

$$\dot{Q}_{\ell,int} = -k_\ell \left[\frac{\partial T_\ell}{\partial x} \Big|_{(i-)} \Delta y + \frac{\partial T_\ell}{\partial y} \Big|_{(j-)} \Delta x \right]$$

29

$$+ \rho_\ell c_{p,\ell} \left(T_\ell v_\ell|_{(j-)} \Delta x + T_\ell u_\ell|_{(i-)} \Delta y \right) \tag{2.57}$$

The heat transported from the interfacial vapor control volume is denoted as $\dot{Q}_{v,\text{int}}$.

$$\dot{Q}_{v,\text{int}} = -k_v \left[\frac{\partial T_v}{\partial x}|_{(i+)} \Delta y + \frac{\partial T_v}{\partial y}|_{(j+)} \Delta x \right]$$

$$+ \rho_v c_{p,v} \left(T_v v_v|_{(j+)} \Delta x + T_v u_v|_{(i+)} \Delta y \right)$$

$$+ h_{fg} \rho_v \left(u_v|_{(i-)} \Delta y + v_v|_{(j-)} \Delta x \right) \tag{2.58}$$

Note that Eqs. (2.57) and (2.58) are written for a vapor control volume at the interface with respect to the numerical scheme used, similarly to Cao and Faghri [27], and Voller and Prakash [28]. For steady state, $\dot{Q}_{v,\text{int}} = \dot{Q}_{\ell,\text{int}}$. Conservation of mass at the interface takes the form.

$$\rho_v u_v|_{(i-)} = \rho_\ell u_\ell|_{(i-)}, \qquad \rho_v v_v|_{(j-)} = \rho_\ell v_\ell|_{(j-)} \tag{2.59}$$

The vapor velocities at the liquid-vapor faces of the interfacial vapor control volumes due to the phase change are redefined at every step of the numerical procedure by taking into account the inclination of the liquid-vapor interface in a manner consistent with Eqs. (2.57) – (2.58).

$$u'_{v,\text{int}}(i,j) = \frac{\left[\dot{Q}_{\ell,\text{int}} - \dot{Q}_{v,\text{int}} + h_{fg} \rho_v \left(u_v|_{(i-)} \Delta y + v_v|_{(j-)} \Delta x \right) \right]}{h_{fg} \rho_v \Delta y} \frac{\sin \gamma}{\sin \gamma + \cos \gamma} \tag{2.60}$$

$$v'_{v,\text{int}}(i,j) = \frac{\left[\dot{Q}_{\ell,\text{int}} - \dot{Q}_{v,\text{int}} + h_{fg} \rho_v \left(u_v|_{(i-)} \Delta y + v_v|_{(j-)} \Delta x \right) \right]}{h_{fg} \rho_v \Delta x} \frac{\cos \gamma}{\sin \gamma + \cos \gamma} \tag{2.61}$$

The local inclination angle of the interface, γ, is calculated as $\gamma = \arcsin[(X_L - x)/R_{\text{men}}]$. For steady-state situation, the overall inlet and outlet mass flow rates should be equal to the mass flow rate of the evaporating fluid at the liquid-vapor interface.

$$\dot{m}_{\ell,in} = \dot{m}_{v,o} = \sum_{i,j} \rho_v \left[v_{v,\text{int}}(i,j) \Delta y + u_{v,\text{int}}(i,j) \Delta x \right] \tag{2.62}$$

While the conservation of normal and tangential momentum is satisfied for every control volume, including those at the interface, due to the conservative control-volume method used, the pressure jump conditions at the interface due to the surface tension should be addressed. For the case of the isothermal liquid-vapor meniscus with constant interface curvature, the pressure jump across the interface can be approximated by the Young-Laplace equation (Faghri [1]).

$$(p_v - p_\ell)_{\text{int}} = \sigma/R_{\text{men}} \tag{2.63}$$

This pressure jump is not crucial for the present analysis because the pressure drops in the

liquid and vapor in the present problem are infinitesimal compared to $(p_v - p_\ell)_{int}$. Therefore, taking the relative nature of pressure in fluid-flow problems into consideration, the liquid pressure can be simply adjusted by subtracting σ/R_{men} for all grid points in the liquid to satisfy Eq. (2.63).

The effective evaporative heat transfer coefficient characterizing the intensity of the evaporative heat transfer is defined as follows.

$$h_e = \frac{\dot{m}_{\ell,in} h_{fg}}{X_L(T_w - T_{sat})} \tag{2.64}$$

where T_{sat} is the vapor temperature over the liquid-vapor interface. In this study, the vapor temperature at the interface was assumed constant due to saturation conditions and because the curvature of the interface was constant.

The average vapor temperature over the liquid-vapor meniscus for a given y, $\overline{T}_v(y)$, increases along the y-coordinate due to the heat transfer between the wall and the vapor. The intensity of the vapor-wall heat transfer can be depicted by the local Nusselt number calculated based on $\overline{T}_v(y)$ for $Y > Y_{mic}$.

$$\mathrm{Nu}_v(y) = \frac{\partial \overline{T}_v(y)}{\partial y} \frac{\dot{m}_{\ell,\,in} c_{pv}}{[T_w - \overline{T}_v(y)]} \frac{4X_L}{k_v} \tag{2.65}$$

$$\overline{T}_v(y) = \frac{1}{\dot{m}_{\ell,\,in}} \sum_i \rho_v T_v v_{v,i} \Delta x_i \tag{2.66}$$

2.2.6   Consideration of the microfilm

The microfilm is considered using the model in section 2.1, therefore the model of the microfilm is not fully presented in this section. The microfilm region where the temperature of the liquid-vapor interface changes along the interface from T_w at the interline to T_{sat} at the end of the microfilm has been enclosed into a special control volume with the dimensions $\Delta x \times \Delta y$ adjacent to the wall. This is a vapor control volume since the microfilm thickness, δ, is much smaller than Δx. This means that in the two-dimensional analysis the liquid microfilm is represented only by the vapor blowing velocity at the solid wall, $\mathbf{V}_{v,mic}$, and by the temperature of the wall, T_{mic}, (this is the mean temperature of the microfilm free surface) in the special control volume. Note that for the liquid control volume located under the microfilm control volume (see Fig. 2.8) the velocity of the liquid is increased in the numerical procedure by $v_\ell = (\rho_v/\rho_\ell)|\mathbf{V}|_{v,mic}\Delta y/\Delta x$ in order to satisfy conservation of mass given by Eq. (2.62). However, the vapor velocity at the upper liquid-vapor face of this control volume is not changed since the vapor velocity due to evaporation from the microfilm is assigned to the solid-vapor face of the microfilm control volume. The values $\mathbf{V}_{v,mic}$ and T_{mic} are the microfilm characteristics averaged over Δy, that is along its length, which does not exceed Δy.

$$T_{mic} = \int_0^{\Delta y} q_\delta(y) T_\delta(y) dy \bigg/ \int_0^{\Delta y} q_\delta(y) dy \tag{2.67}$$

31

$$|\mathbf{V}|_{v,\text{mic}} = \int_0^{\Delta y} q_\delta(y)dy/(\Delta y h_{fg}\rho_v) \tag{2.68}$$

where q_δ is the heat flux at the interface, which is equal to that due to heat conduction through the liquid film, and defined for the case of a comparatively small heat flux by the following expression (Carey, [12]; Faghri, [1]).

$$q_\delta = -\left(\frac{2\alpha}{2-\alpha}\right)\frac{h_{fg}}{\sqrt{2\pi R_g}}\left[\frac{p_v}{\sqrt{T_v}} - \frac{(p_{\text{sat}})_\delta}{\sqrt{T_\delta}}\right] \tag{2.69}$$

p_v and $(p_{\text{sat}})_\delta$ are the vapor pressures corresponding to the special vapor control volume and at the thin liquid film interface, respectively. The extended Kelvin equation which relates the disjoining pressure, p_d, normal saturation pressure, $p_{\text{sat}}(T_\delta)$, and $(p_{\text{sat}})_\delta$ affected by the disjoining and capillary pressures was also used in the model to find T_δ (section 2.1). In the present model, T_v in Eq. (2.69) is set equal to the saturation temperature.

Note that the interfacial thermal resistance is very important for the microfilm and results in the difference between the interface temperature, T_δ, and that of the vapor over the interface, T_{sat}. For the rest of the meniscus, the interfacial thermal resistance is negligible in comparison to the thermal resistance of the liquid film and $T_\delta \approx T_{\text{sat}}$ which is justified by the calculations made at the end of the microfilm.

2.2.7 Numerical procedure

The problem was solved using Patankar's SIMPLE (Patankar, [29]) algorithm employing the power law discretization scheme and line-by-line TDMA method. The numerical scheme was capable of handling non-uniform properties (Prakash, [30]). The solving procedure consisted of the following consecutive steps:

1. Prescribe the initial temperature field and interfacial velocities $u_{v,\text{int}}$ and $v_{v,\text{int}}$.

2. Solve the continuity and momentum conservation equations (2.48), (2.49), and (2.50).

3. Solve the energy equation (2.51) for the calculated velocity field.

4. With the calculated temperature field, update the interfacial vapor velocities, $u_{v,\text{int}}$ and $v_{v,\text{int}}$, for the control volume liquid-vapor faces at the interface from Eqs. (2.60) and (2.61). Calculate T_{mic} and $|\mathbf{V}_{v,\text{mic}}|$ for the microfilm control volume from Eqs. (2.67) and (2.68), and the model presented in section 2.1 where the microfilm curvature is set to $1/R_{\text{men}}$.

5. Go back to step 2 until a converged solution is obtained.

2.2.8 Computational domain and accuracy of the results

All control volumes in the computational domain were divided in two categories: "liquid" and "vapor", with corresponding thermophysical properties. The following non-equality was used to identify the vapor control volumes.

32

$$x \geq X_L - \left[R_{\text{men}}^2 - (y - Y_{\text{men}} - R_{\text{men}})^2\right] \qquad (2.70)$$

A uniform grid with rectangular control volumes was used with 98 grid points in the x-direction and 270 grid points in the y-direction. This grid size was found sufficient to approximate the curved liquid-vapor interface. The numerical solution was found to be essentially independent of the number of grid points used. For example, the value of the effective heat transfer coefficient, h_e, for the 98×360 grid was only 0.17% higher than that for the 98×270 grid for the same total number of iterations of 12000 (500 iterations for each of the Steps 2 and 3 described above). The convergence of the solution was also verified. The heat transfer coefficients presented in the following figures were calculated with the numerical error of about 0.1% with the 98×270 grid. The overall mass flow rate balances, Eq. (2.62), were satisfied with the accuracy of at least 0.1%.

2.2.9 Results and discussion

Numerical results were obtained for water at the saturation temperature of 373 K for X_L = 50 μm, Y_L = 400 μm, Y_B = 100 μm, and θ_{men} = 15°. The accommodation coefficient, α, was set equal to unity. Typical vapor velocity fields over the evaporating meniscus are shown in Fig.2.9 for comparatively small (a) and large (b) temperature drops ($\Delta T = T_w - T_{\text{sat}}$) between the wall and the saturation temperature. The vapor velocity in the microfilm control volume can be as high as 100 m/s for $\Delta T = 15$ K. Such a high blowing velocity results in a recirculation zone in the vapor near the wall over the interline, as shown in Fig. 2.9(b). Since the velocities in the liquid are much smaller than those in the vapor, they are not shown in Fig. 2.9. For small temperature drops, the vapor flows along the x-coordinate near the heated wall over the interline. However, for larger temperature drops, the vapor flow changes its direction in the mentioned above region due to appearance of the recirculation zone. This effect can be important for micro heat pipes and other applications.

The liquid flow is shown in Fig. 2.10. The liquid-vapor interface in Fig. 2.10 is represented by the velocity vectors at the vapor side of the interface. The liquid flow pattern did not change with temperature drop as can be seen from comparison of Figs. 2.10(a) and 2.10(b). The temperature contours are given in Fig. 2.11 for $\Delta T = 5$ K (a) and $\Delta T = 10$ K (b). For higher ΔT, the shape of the temperature contours changed compared to lower ΔT due to the fluid flow effect on the heat transfer.

The numerical results for the effective heat transfer coefficient, h_e, were compared to those obtained using the model by Khrustalev and Faghri [26] that is presented in section 2.1. In that model, the fluid flow was neglected and the heat conduction problem in the solid wall and meniscus liquid was reduced to 1-D allowing calculation of the overall heat flow rate per unit length of the liquid-vapor meniscus and the effective heat transfer coefficient. In this section, the overall heat flow rate per unit length of the meniscus was also calculated for the purpose of comparison in a similar manner but with a constant wall temperature. For small ΔT the agreement was very good: the simplified model underestimated the heat transfer coefficients by only about 3% as shown in Fig. 2.12. However, for larger temperature drops, the difference between the present (2-D) and the simplified model became 30 % (for $\Delta T = 10$ K) due to the convective heat transfer.

33
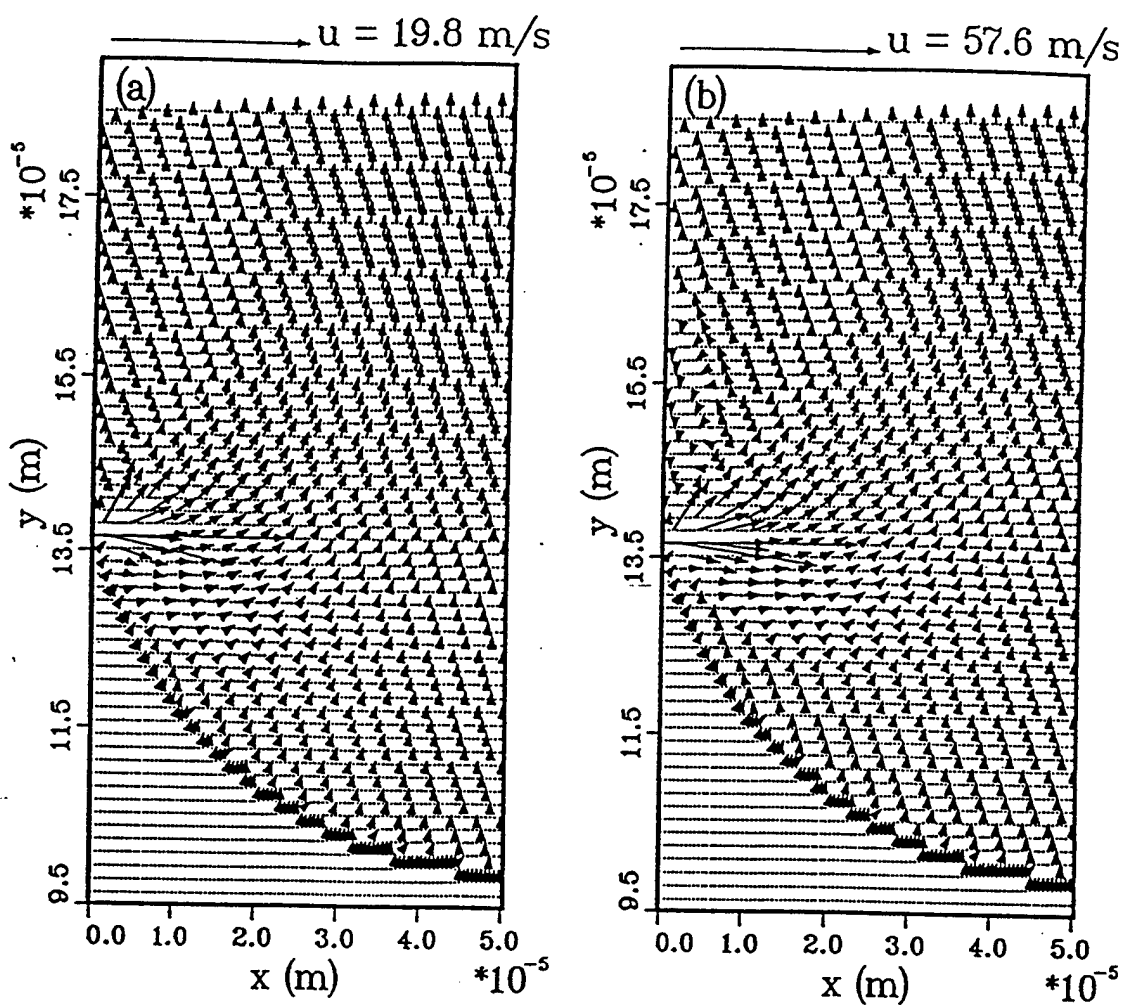
Figure 2.9: Vapor flow over the evaporating meniscus (a) $T_w - T_{sat} = 5$ K (b) $T_w - T_{sat} = 10$ K
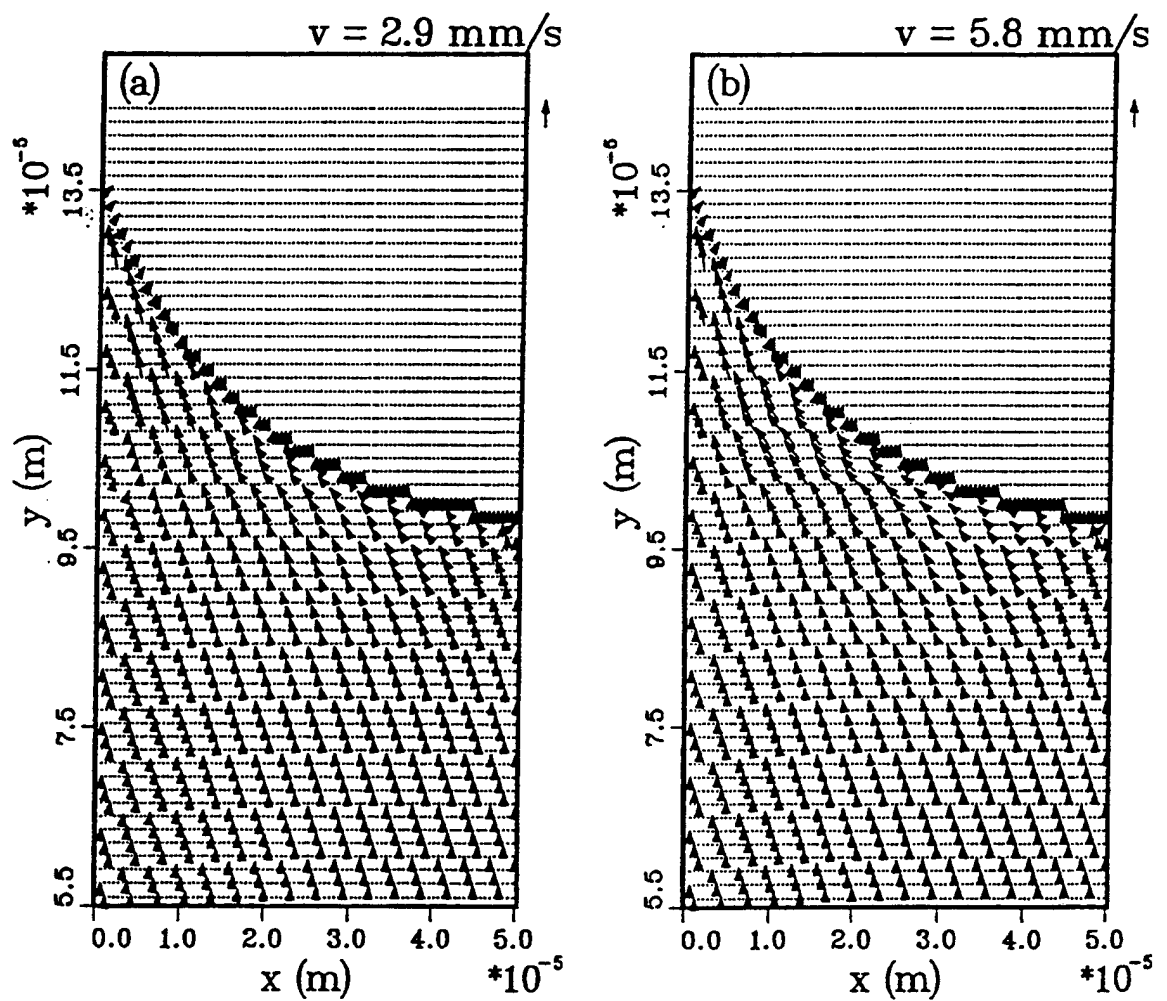
Figure 2.10: Liquid flow in the evaporating meniscus (a) $T_w - T_{sat} = 5$ K (b) $T_w - T_{sat} = 10$ K
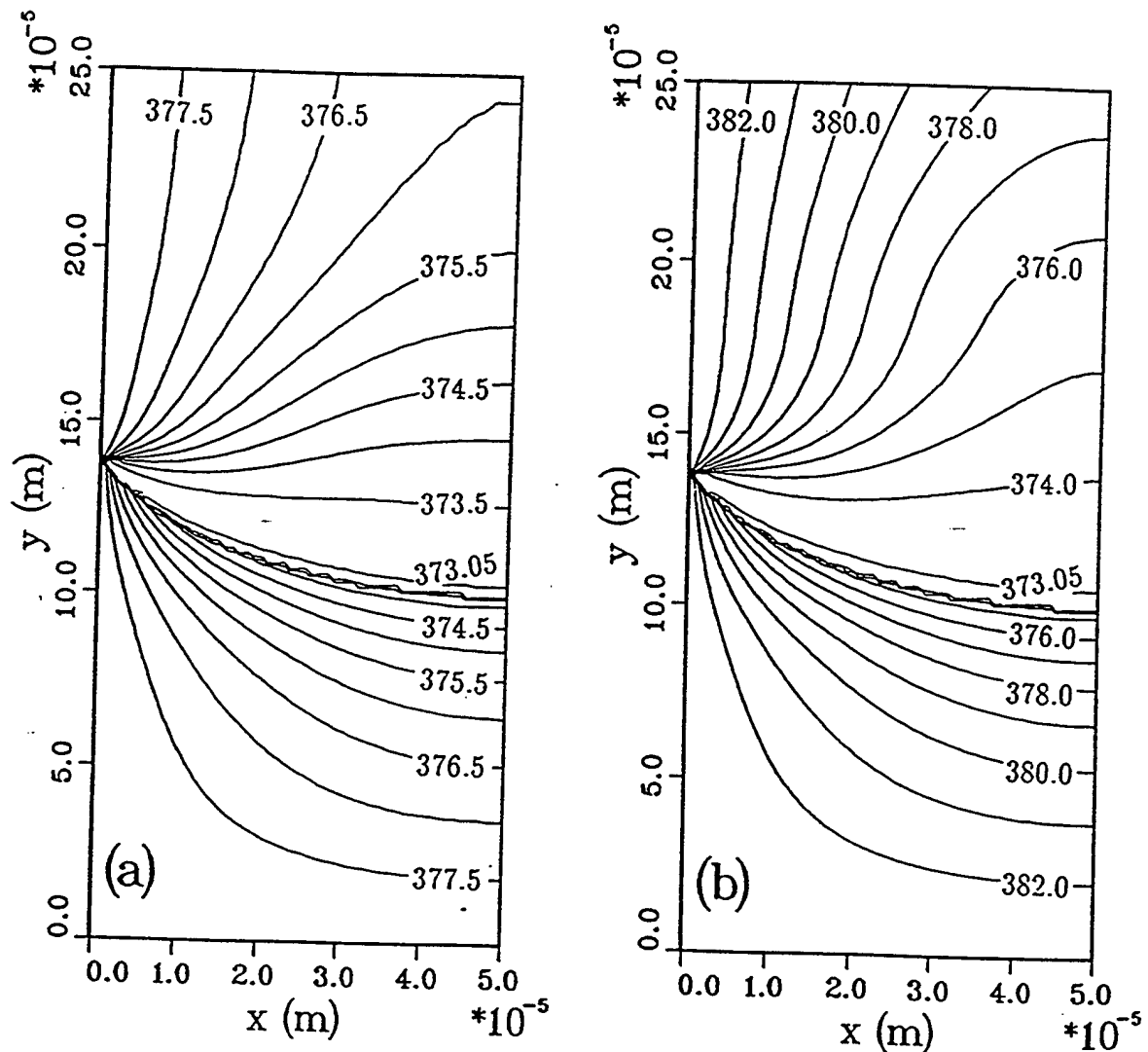
Figure 2.11: Temperature contours in the liquid and vapor (a) $T_w - T_{sat} = 5$ K (b) $T_w - T_{sat}$ = 10 K
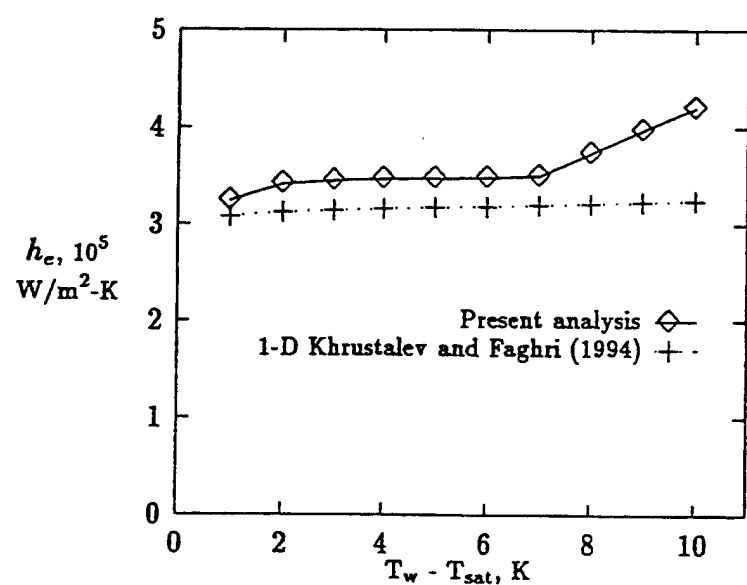
Figure 2.12: Effective heat transfer coefficient versus superheat for water at atmospheric pressure

As the vapor moves in the y-direction, its temperature increases due to heat transfer from the wall. Thus, it can be significantly superheated over the saturation temperature at the slot or pore exit. The local Nusselt numbers are larger some distance away from the microfilm control volume along the y-coordinate than those near the interline or at the outlet of the computational domain, Fig. 2.12. For superheats of 9 K and 10 K, recirculation of vapor near the heated wall decreases the local Nusselt number due to the smaller vapor velocities near the wall in the recirculation zone.

2.2.10 Conclusions

The following conclusions can be made based on the numerical results obtained.

1. For small temperature drops, the agreement between the present 2-D model and the model by Section 2.1 is good. This agreement allows the use of the simplified model for small temperature drops.

2. The fluid flow effect on the heat transfer during evaporation from the liquid-vapor meniscus results in the increase of the effective heat transfer coefficient by up to 30%.

3. For larger temperature drops, a recirculation zone appears in the vapor over the interline which can be important for some applications including evaporation from capillary structures.

4. The vapor exiting a capillary slot or pore can be significantly superheated over the saturation temperature. The heat transfer between the vapor and the heated wall is the most extensive at a distance from the interline of about one slot width along the y-coordinate.

2.3 Fluid Circulation and Performance Limitations of Axially Grooved Heat Pipes

Miniature and conventional heat pipes with axial grooves can be successfully used in electronic components cooling systems (Faghri, [1]). Some experimental data on the performance characteristics of the flat water-copper heat pipe with external dimensions 2 × 7 × 120 mm has been reported by Plesch et al. [2]. The present section deals with the numerical prediction of the thermal characteristics of miniature and conventional axially-grooved heat pipes including the maximum heat flux on the outer evaporator wall. This heat flux is restricted by the fluid transport limit and boiling limitation. The superheat of the evaporating liquid, which is critical for the onset of nucleate boiling, depends on the heat transfer coefficient in the evaporator. Therefore, a detailed mathematical model is developed, including both the heat transfer through liquid films and axial fluid transport phenomena, which provides an opportunity to determine the maximum heat transfer capacity and thermal resistance of low-temperature AGHP's. The present model, which incorporates several one-dimensional boundary-value problems, has the following comparatively new features:

38
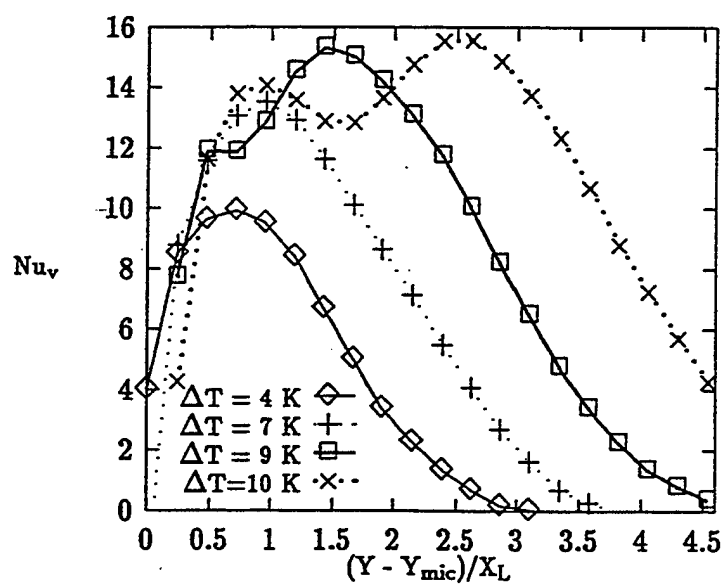
Figure 2.13: Local Nusselt number for the vapor flow along the slot for water at atmospheric pressure

- The heat transfer through the liquid films and the fin between grooves (Fig. 2.13) in both the evaporator and condenser is accounted for in the model, which is described with respect to the disjoining pressure, interfacial thermal resistance and surface roughness or curvature in the same manner as done in section 2.1.

- The effect of shear stresses at the free liquid surface in a groove due to the frictional liquid-vapor interaction on the liquid flow is taken into consideration.

- The boiling limitation and the thermal resistances of the evaporator and condenser are determined by accounting for the longitudinal distribution of the meniscus curvature, which is dependent on heat load and heat pipe inclination angle.

2.3.1   AGHP Mathematical Model

The mathematical model of a low-temperature AGHP is developed in order to optimize the performance of heat pipes and grooved evaporators and condensers for cooling systems. The proposed model is a significant contribution over the previous investigators' attempts (Kamotani, [31]; and Vasiliev et al.,[9]), where the heat transfer during evaporation in the microfilm and boiling limitation were not considered.

The present model is developed for rectangular and triangular (trapezoidal) grooves in circular or flat (rectangular) tubes, but other heat pipes and grooves configurations can also be described using the same general approach. Heat transfer processes in the heat pipe container and working fluid were considered to be one-dimensional in the radial direction, such that axial heat conduction was neglected. It was also assumed that no puddle flow occurred in the AGHP, no part of the condenser was blocked by the liquid working fluid, the liquid was distributed uniformly between the grooves, and the fluid flow along the axis was related to the capillary potential gradient, as described by the main radius of curvature of the liquid in a groove.

The numerical results were obtained using an iterative mathematical procedure which involved the following problems:

1. Heat transfer in the evaporating film on a rough surface.

2. Heat transfer in the condensate film on the fin top surface.

3. Heat conduction in a metallic fin and liquid meniscus.

4. Fluid circulation in the AGHP.

5. Prediction of the onset of the nucleate boiling.

Since the first three problems are presented in detail in section 2.1 and also in the paper by Khrustalev and Faghri [6], their description is omitted here. However, these interconnected problems are included in the mathematical procedure along with the fluid circulation and boiling limitation equations presented in the following sections.

40
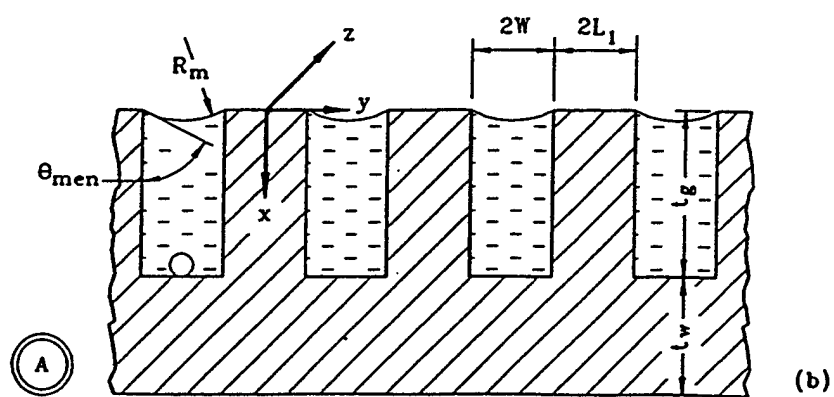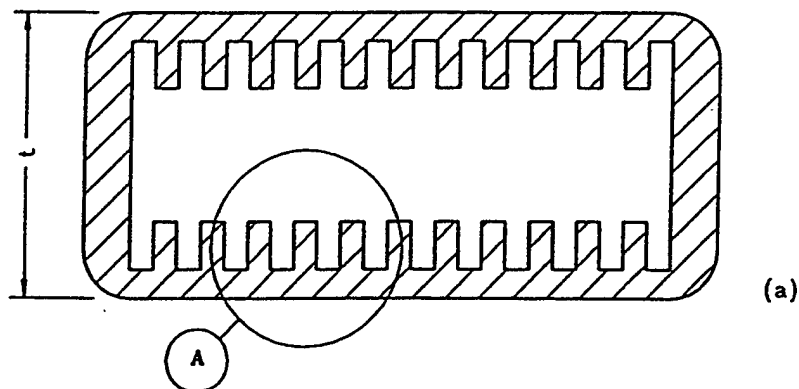
Figure 2.14: Flat miniature axially-grooved heat pipe cross-sections .

2.3.2 Fluid Circulation in an AGHP and the Capillary Limitation

The conservation equations for the steady-state operation of an AGHP are the continuity, momentum and energy equations for the liquid, vapor and wall, and the Laplace-Young equation for the radius of curvature at the liquid-vapor interface. At any axial location, the following mass conservation equation must hold over the cross-section of the AGHP:

$$\overline{w}_v \rho_v A_v = N \overline{w}_\ell \rho_\ell A_\ell \equiv N \dot{m}_\ell \tag{2.71}$$

where $\dot{m}_\ell$ is the mass flow rate through a groove and N is the number of grooves. The average liquid and vapor velocities in the axial direction in equation (2.71) are

$$\overline{w}_\ell = \frac{1}{A_\ell} \int\!\!\int_{A_\ell} w_\ell(x,y) \, dx \, dy, \quad \overline{w}_v = \frac{1}{A_v} \int\!\!\int_{A_v} w_v(x,y) \, dx \, dy \tag{2.72}$$

An AGHP contains a definite amount of a working fluid M_t, which is distributed in accordance to the following relation, provided there is no excess liquid:

$$M_t = N \int_0^{L_t} \rho_\ell A_\ell \, dz + \int_0^{L_t} \rho_v A_v \, dz + M_\delta \tag{2.73}$$

where M_δ is the mass of the liquid film in the condenser section on top of the fins.

The conservation of axial momentum equation for an incompressible vapor flow using the one-dimensional boundary-layer approximation is

$$\frac{d}{dz}(p_v + \rho_v g z \sin\varphi + \rho_v \beta_v \overline{w}_v^2) = -f_v \frac{2\rho_v \overline{w}_v^2}{D_{h,v}} \tag{2.74}$$

where β_v is the momentum flux coefficient, f_v is the friction coefficient, and $D_{h,v}$ is the hydraulic diameter of the vapor channel. These coefficients for a circular vapor channel can be determined using the results of previous investigators for two-dimensional, laminar boundary-layer flow with suction or injection. For the range of radial Reynolds numbers usually seen in miniature AGHP's ($0 \leq \text{Re}_r < 20$) in the evaporator and adiabatic sections, the results given by Bankston and Smith [58] can be approximated as follows

$$(f\,\text{Re})_v = 16 + 0.46\text{Re}_r - 0.017\text{Re}_r^2, \quad \beta_v = 1.33 - 0.005\text{Re}_r$$

In the condenser section (Bowman and Hitchcock, [59]; Jang et al.[60])

$$(f\,\text{Re})_v = 16[1.2337 - 0.2337\exp(-0.0363\text{Re}_r)][\exp(1.2\text{Ma})], \quad \beta_v = 1.33$$

The velocity of the liquid phase is very small in comparison to that of the vapor flow, so the interfacial shear for the vapor is computed by assuming the liquid to be stationary (Longtin et al., [32]). For a flat (rectangular) vapor channel configuration the values of $(f\,\text{Re})_v$ can be defined using the following equation (Shah and Bhatti, [33])

$$(f\,\text{Re})_v = 24(1 - 1.3553C + 1.9467C^2 - 1.7012C^3 + 0.9564C^4 - 0.2537C^5)$$

where $C = [t - 2(t_w + t_g)]/[N(W + L_1)]$ and the Reynolds number is based on the hydraulic

42

diameter.

The axial transport of condensate in an AGHP takes place in the grooves, where most of the liquid resides. The thickness of the liquid film on the fin tops in the condenser section is assumed to be too small to contribute to the axial mass transport. Since the axial Reynolds number for liquid flow in an AGHP is usually less than 10, it can be considered to be viscous and quasi-one-dimensional. Thus, the conservation of momentum equation for the liquid flow in a groove with cross-sectional area A_ℓ is

$$\frac{dp_\ell}{dz} + \rho_\ell g \sin \varphi = f_\ell \frac{2\rho_\ell \overline{w}_\ell^2}{D_{h,\ell}} \tag{2.75}$$

For the liquid flow the inertia effects are negligible in comparison to those due to viscous losses (Khrustalev and Faghri, [6]). The values of f_ℓ can be taken from the numerical solution of the two-dimensional Stokes equation with boundary conditions which take into account shear stress in the liquid at the interface due to liquid-vapor frictional interaction (Vasiliev et al., [9]; Schneider and DeVos, [34]). The expression for the friction factor, given by Schneider and DeVos [34] for rectangular grooves is used in the presented model because of its reliability and accuracy. For the case of a planar free liquid surface geometry

$$(f \, \mathrm{Re})_\ell = (f \, \mathrm{Re})_{\ell 0} \left\{ 1 + \frac{4NW^3}{3\pi D_{h,v}^3} (f \, \mathrm{Re})_v \frac{\nu_v}{\nu_\ell} \left[1 - 1.971 \exp(-\frac{\pi t_g}{2W}) \right] \right\}$$

where $(f \, \mathrm{Re})_{\ell 0}$ corresponds to the case of no liquid-vapor interaction

$$(f \, \mathrm{Re})_{\ell 0} = 8t_g^2 \left[W^2 \left(1 + \frac{t_g}{W} \right)^2 \left(\frac{1}{3} - \frac{64W}{\pi^5 t_g} \tanh \frac{\pi t_g}{2W} \right) \right]^{-1}$$

Accounting for the liquid-vapor interaction seems to be important, especially for a flat miniature AGHP's.

The conservation of energy equation is cast into a form which reflects the change in the axial mass flow rate of liquid due to evaporation and condensation

$$\frac{d}{dz}(\rho_\ell \overline{w}_\ell A_\ell) = \begin{cases} \frac{2\pi R_o}{N h_{fg}} h_{o,e}(T_{o,e} - T_v) \left(1 + \frac{h_{o,e}}{\overline{h}_e} \right)^{-1}, & 0 \leq z \leq L_e \\ 0, \quad \text{(adiabatic section)} & L_e < z < L_e + L_a \\ \frac{2\pi R_o}{N h_{fg}} h_{o,c}(T_{o,c} - T_v) \left(1 + \frac{h_{o,c}}{\overline{h}_c} \right)^{-1}, & L_e + L_a \leq z \leq L_t \end{cases} \tag{2.76}$$

$\overline{h}_e(z)$ and $\overline{h}_c(z)$ are the mean local effective heat transfer coefficients between the external surface of the casing and vapor through the wall and liquid films (Khrustalev and Faghri [6]). $h_{o,e}$ and $h_{o,c}$ are the heat transfer coefficients between the wall and the ambient. The vapor temperature is denoted by T_v. For a given axial heat load function $Q(z)$, equation (2.76) can be rewritten as

43

$$\frac{d}{dz}(\rho_\ell \overline{w}_\ell A_\ell) = \frac{1}{h_{fg} N} \frac{dQ(z)}{dz} \tag{2.77}$$

The interfacial radius of the meniscus curvature is related to the pressure difference between the liquid and vapor by the Laplace-Young equation, which, in differential form, is

$$\frac{dp_\ell}{dz} = \frac{dp_v}{dz} - \frac{d}{dz}\left(\frac{\sigma}{R_m}\right) \tag{2.78}$$

The mean axial liquid and vapor velocities at the evaporator and condenser end caps are

$$\overline{w}_\ell|_{z=0} = \overline{w}_v|_{z=0} = 0 \tag{2.79}$$

$$\overline{w}_\ell|_{z=L_t} = \overline{w}_v|_{z=L_t} = 0 \tag{2.80}$$

which are imposed by the axial heat load function $Q(z)$. The vapor and liquid pressures at the evaporator end cap are

$$p_v|_{z=0} = p_{v0}, \quad p_\ell|_{z=0} = p_{v0} - \frac{\sigma}{R_{m0}} \tag{2.81}$$

The values of p_{v0} and R_{m0} are to be determined using additional conditions. When solving equation (2.76), where $T_v(z)$ is also unknown and depends on p_v, the value of p_{v0} must be chosen such as to satisfy equation (2.80). When $Q(z)$ and T_{v0} are known, $p_{v0} = p_v(T_{v0})$, which can be obtained using the saturation tables. When there is an insufficient liquid fill volume, the radius of curvature of the meniscus at the evaporator end cap, R_{m0}, is found using equation (2.73), since the value of R_{m0} influences the axial distribution of liquid. In general, the radius of curvature of the meniscus is bounded by $R_{m,min} \le R_{m0} \le R_v$. Since in the presented numerical experiments the situation of a sufficient liquid charge was considered, the following conditions for R_{m0} definition were used

$$\min\left\{\frac{1}{R_m(z)}\right\} = \frac{1}{R_v}; \quad \min\left\{\frac{1}{R_m(z)}\right\} = 0 \tag{2.82}$$

for circular and flat heat pipes, respectively. Equation (2.82) implies that for a given $Q(z)$, the value of R_{m0} which provides the equality of R_m to the vapor channel radius (for the circular tube case) at a single location on z along the AGHP should be chosen, while equations (2.74)–(2.81) are satisfied along the entire length of the AGHP. Note that this point is not always situated at the condenser end cap.

The solution of equations (2.74)–(2.81) gives the longitudinal distribution of the meniscus radius $R_m(z)$ and hence the meniscus contact angle $\theta_{men}(z)$, which are related for contact angles of $\theta_{men} \ge \theta_{men,min}$ by

$$\theta_{men}(z) = \arccos\left[\frac{W}{R_m(z)}\right] - \gamma \tag{2.83}$$

For rectangular grooves $R_{m,min}$ is defined by equation (2.83) provided $\theta_{men} = \theta_{men,min}$, where $\theta_{men,min}$ is the minimum wetting contact angle, which is fixed for a specific working-

fluid/container combination (Stepanov et al. [69]). This value of $R_{m,\min}$ along with equation (2.82) determines the maximum heat transfer through an AGHP (capillary limit) at which equations (2.74)–(2.81) and the boundary conditions are still satisfied. For triangular (trapezoidal) grooves in the situation $\theta_{\text{men}} = \theta_{\text{men,min}}$, equation (2.83) gives the relation between the meniscus radius and the width of the liquid cross section.

When the longitudinal vapor pressure distribution, $p_v(z)$, and the temperature at the evaporator end cap (for the case of an unknown heat load function), T_{v0}, are found, the corresponding temperature distribution along the vapor flow, $T_v(z)$, can be calculated using the Clausius-Clapeyron equation.

2.3.3 Boiling Limitation and Heat Transfer Coefficients

Nucleation within the wick is undesirable for wicked heat pipe operation because the bubbles can obstruct the liquid circulation and hence cause hot spots on the evaporator walls. An estimation of the vapor bubble departure diameter during nucleate boiling of water was made using the correlations obtained by Jensen and Memmel [35]. The bubble departure diameter was much larger than the groove width of the considered water-copper heat pipes, which means that the normal operation of an AGHP in the situation when nucleate boiling occurs in the evaporator is not realistic except for some special cases. Thus, for heat pipe performance optimization, it is necessary to predict the value of the heat flux which initiates vapor bubble formation in the working liquid. This task can be subdivided into two independent parts:

1. Estimation of the superheat of the liquid in the wick $(T_{\text{bot},\ell} - T_v)$ which causes generation of vapor bubbles at the wall-wick interface. Here $T_{\text{bot},\ell}$ corresponds to the plane $x = t_g$ (Fig. 2.13(b)).

2. Computation of the heat transfer coefficient in the evaporator, $\bar{h}_e$, for the situation when no boiling occurs, which relates the values of the heat flux, q_e, and temperature drop across the wick, $(T_{\text{bot},\ell} - T_v)$.

Critical liquid superheat. A review on heterogeneous nucleation and bubble growth in liquids has been given by Carey [12]. Since the inner surface of heat pipes are invariably covered with machine-formed pits, cavities and scratches, vaporization usually begins on these irregularities. The process of bubble formation depends upon the solid surface microrelief, wetting contact angles and liquid properties. While theoretical prediction of the superheat which causes boiling is extremely difficult, some empirical correlations should be involved in the analysis. Note that the vapor bubble embryo diameter is much smaller than the groove width, therefore, some of the correlations obtained for planar surfaces can be used in the present analysis.

Lorenz et al. [36] reported experimental data for boiling of four different liquids on a copper surface with a #240 (sandpaper) finish. In these experiments, the number of active sites per square centimeter (n^{prime}), which increased rapidly with superheat, were determined by visual counting at different superheat values. Experimental results by Lorenz et al. [36] can be approximated by the following equation

$$n^{p}rime = C_1 - C_2 [\frac{h_{fg}(T_{\text{bot},\ell} - T_v)\rho_v}{2\sigma T_v} + \frac{1}{2R_m}]^{-1} \qquad (2.84)$$

where for water $C_1 = 77$, $C_2 = 19 \times 10^6$ and $1 \leq n^{p}rime \leq 6$, and for R-113, methanol and benzene $C_1 = 39.6$, $C_2 = 19.6 \times 10^6$ and $0.5 \leq n^{p}rime \leq 10$. Note that in the analysis by Lorenz et al. [36] $T_{\text{sat}}(p_\ell)$ was used instead of T_v and $1/R_m$ was equal to zero. The following relation between $T_{\text{sat}}(p_\ell)$ and T_v was used in the derivation of equation (2.84) (Carey, [12])

$$T_v - T_{\text{sat}}(p_\ell) = \frac{T_v \sigma}{h_{fg} \rho_v R_m}$$

with the assumptions that $\rho_v \ll \rho_\ell$ and $\sigma / \rho_\ell R_m \ll 1$. For a known superheat $(T_{\text{bot},\ell} - T_v)$, equation (2.84) indicates whether boiling occurs at a given point along the evaporator length, which is characterized by the local radius of curvature of the meniscus, R_m. The values of the heat flux on the external surface of the wall and the superheat are related as follows

$$q_e = \overline{h}_{e,\text{bot}}(T_{\text{bot},\ell} - T_v) \left(\frac{R_v + t_t + t_g}{R_o}\right) \qquad (2.85)$$

where $\overline{h}_{e,\text{bot}}$ is the local effective heat transfer coefficient between the saturated vapor and the bottom of a groove, which is generally dependent on the value of R_m at this location.

Heat transfer coefficients. The coefficients of heat transfer during evaporation and condensation on the grooved surface were calculated using the mathematical model developed by Khrustalev and Faghri [6]. It is essential to mention that in the model by Khrustalev and Faghri [6] the thin film formation on the fin surface for both evaporation and condensation was described by the following equation:

$$\frac{1}{3\mu_\ell} \frac{d}{ds} \left[\delta^3 \frac{d}{ds}(p_d - \sigma K)\right] = \frac{k_\ell(T_w - T_\delta)}{h_{fg}\rho_\ell \delta} \qquad (2.86)$$

where s is the coordinate along the solid-liquid interface where the temperature is T_w, and δ is the local film thickness. The temperature of the liquid-vapor interface T_δ is affected by the disjoining and capillary pressures, and also depends on the value of the interfacial resistance, which is defined for the case of a comparatively small heat flux by the following relation for the heat flux at the interface (Carey, [12]).

$$q = - \left(\frac{2\alpha}{2 - \alpha}\right) \frac{h_{fg}}{\sqrt{2\pi R_g}} \left[\frac{p_v}{\sqrt{T_v}} - \frac{(p_{\text{sat}})_\delta}{\sqrt{T_\delta}}\right] \qquad (2.87)$$

p_v and $(p_{\text{sat}})_\delta$ are the saturation pressures corresponding to T_v in the bulk vapor and at the thin liquid film interface, respectively. The extended Kelvin equation which relates p_d, $p_{\text{sat}}(T_\delta)$ (normal saturation pressure corresponding to T_δ), and $(p_{\text{sat}})_\delta$ was also used in the model. The following equations for the disjoining pressure were used in the present model for non-polar liquids and for water, respectively:

$$p_d = -A'\delta^{-B} \qquad (2.88)$$

46

$$p_d = \rho_\ell R_g T_\delta \ln \left[a \left(\frac{\delta}{3.3} \right)^b \right] \tag{2.89}$$

where $a = 1.534$ and $b = 0.0243$. Solution of the heat conduction equation in the fin and liquid in conjunction with the equations for the thin film formation for a given q_e gives the temperature of the fin bottom as $T|_{x=t_g} = T_{\text{bot},\ell}$. The local heat transfer coefficient from the bottom of the groove to the vapor is defined as

$$\bar{h}_{e,\text{bot}} = \frac{q_e}{[T|_{x=t_g} - T_v]} \left(\frac{R_o}{R_v + t_t + t_g} \right) \tag{2.90}$$

The local heat transfer coefficient from the external surface of the heat pipe to the vapor is

$$\bar{h}_e = \left[\frac{R_o}{k_w} \ln \left(\frac{R_o}{R_v + t_t + t_g} \right) + \frac{1}{\bar{h}_{e,\text{bot}}} \left(\frac{R_o}{R_v + t_t + t_g} \right) \right]^{-1} \tag{2.91}$$

where the thermal resistance of a circular tube wall is taken into account. It was found in the results by Khrustalev and Faghri [6] that for $\alpha = 1$ the values of $\bar{h}_e$ for the rough solid surface were up to 30% less than for the smooth solid surface. However, for the case of small α (for example, $\alpha = 0.05$) the influence of the roughness on the evaporative heat transfer coefficient was insignificant. The characteristic roughness size R_r in the referred results varied from 0.02 to 1 μm. Obviously, equations (2.85), (2.90) and (2.91) are valid also for a planar evaporator in which $R_o \to \infty$, $R_v \to \infty$ and $R_o = R_v + t_t + t_g + t_w$.

In the present analysis the values of $\bar{h}_{e,\text{bot}}$ were calculated for every point along the axial direction in the evaporator of the modeled AGHP's for a given total heat load Q_a, and equation (2.84) was used with the corresponding R_m to predict the onset of nucleate boiling ($n^{prime} \geq 1$). The mean temperature drop in the evaporator was calculated using the following expression:

$$T_{w,o} - T_v = \frac{1}{2\pi R_o L_e} \int_0^{L_e} \frac{dQ}{dz} \frac{1}{\bar{h}_e} \, dz \tag{2.92}$$

For the condenser section similar expressions were used (Khrustalev and Faghri [6]).

2.3.4 Numerical Treatment

For the fluid circulation in the AGHP (equations (2.74)–(2.83)), the four main variables dependent on z to be found are
$K = R_m^{-1}$: curvature of the free surface of the meniscus,
$\dot{m} = \overline{w}_\ell \rho_\ell A_\ell$: mass flow rate of liquid in one groove,
p_ℓ: liquid pressure,
p_v: vapor pressure.
The system of four ordinary differential equations, equations (2.74), (2.75), (2.77) and (2.78), was solved with the respective boundary conditions using the fourth-order Runge-Kutta procedure and the shooting method (on parameter R_{m0}). For each of the four functions the

47

relative error was less than 0.0001%. While the AGHP for the case of a given axial heat load function $Q(z)$ was modeled, the structure of the numerical AGHP simulation was as follows:

1. The fluid circulation along the AGHP was solved with the known function $Q(z)$ and T_{v0}, which gave $R_m(z)$, $\theta_{\text{men}}(z)$ and $T_v(z)$.

2. For every point on z, the heat transfer in the evaporator and condenser thin film regions along with the heat conduction in the fin were solved and the functions $\overline{h}_e(z)$, $\overline{h}_{e,\text{bot}}(z)$, $\overline{h}_c(z)$ and $T_{w,o}(z)$ were determined.

3. The number of active sites $n^p rime$ was calculated for every point on z in the evaporator with the corresponding R_m to determine whether boiling occurred.

4. The values of the temperature drops in the evaporator and condenser were found.

5. Steps 1–4 were repeated several times for larger values of Q_a until the capillary or boiling limitation was indicated (with the relative error less than 1%).

2.3.5 Results and Discussion

To verify the numerical results obtained, the experimental data provided by Schlitt et al. [20] were first used. Therefore, part of the presented results refers to the AGHP with the following geometry: $L_t = 0.914$ m, $L_c = 0.152$ m, $0.15 \leq L_e \leq 0.343$ m, $W = 0.305$ mm, $t_g = 1.02$ mm, $L_1 = 0.215$ mm, $R_v = 4.43$ mm, $R_o = 7.95$ mm, $\gamma = 0$, $N = 27$, $t_t = 0$. The working fluids were ammonia and ethane, the casing material thermal conductivity was assumed to be $k_w = 170$ W/(m-K), and dispersion constant $A' = 10^{-21}$ J. The axial heat distribution was specified as

$$
Q = \begin{cases}
Q_a z/L_e, & 0 \leq z \leq L_e \\
Q_a, & L_e < z < L_e + L_a \\
Q_a \left(1 + \dfrac{L_e + L_a - z}{L_c}\right), & L_e + L_a \leq z \leq L_t
\end{cases}
\tag{2.93}
$$

and equation (2.77), instead of equation (2.76), was used in the numerical procedure. The longitudinal distribution of the meniscus contact angle, which is influenced by the inclination angle and the fluid pressure variation (Δp), is shown in Fig. 2.14(a) for ammonia ($L_e = 0.343$ m, $T_v = 250$ K). For positive values of the inclination angle φ (when the condenser end is elevated) the points of minimum and maximum liquid surface curvature (the so-called "dry" and "wet" points) were shifted from the ends of the heat pipe towards the adiabatic section. As a result, the meniscus contact angle distributions in the heat loaded sections were even more uniform than those in the horizontal case. Note that the meniscus angles in the condenser differ very slightly from the maximum value, and their values in the evaporator can be almost the same as that in the condenser for positive φ. The corresponding longitudinal distributions of the local heat transfer coefficients in the evaporator and condenser and also wall and vapor temperature variations are shown in Figs. 2.14(b) and 2.14(c). The local heat transfer coefficient in the middle of the condenser was about two times larger than at the entrance or end cap, which resulted in the external wall temperature variation shown in Fig. 2.14(c). In the evaporator section, the variation of the local heat transfer coefficient

48

was weaker (for heat loads which are not close to the maximum), so the wall temperature profile was very smooth. The temperature drop along the vapor flow was less than 0.01 K.

The comparison of the computational results with the experimental data on heat transfer for the AGHP's evaporators by Schlitt et al. [20] and for the planar water-copper evaporator by Ivanovskii et al. [21] is presented in Fig. 2.15 for ammonia ($L_e = 0.343$ m, $T_v = 250$ K), ethane ($L_e = 0.15$ m, $T_v = 200$ K) and water ($W = 0.17$ mm, $t_g = 0.8$ mm, $L_1 = 0.25$ mm, $L_e = 100$ mm, $T_v = 300$ K; the heated surface was of about 40 cm^2). The agreement of the results is good for $\alpha \ll 1$ since it was noted by Carey [12] that, for some substances (ethanol, methanol, water, etc.), the accommodation coefficient had been found to have very small values (0.02 to 0.04) in the experiments of Paul [22]. The physical reason for low values of α in the microfilm region of the evaporator can be the concentration of the contaminants which usually exist in a heat pipe in this region. While the experimental data for the temperature drops for ethane were still higher than those predicted, more precise values of the accommodation coefficient and dispersion constants are needed. For the copper-water evaporator the predicted boiling limit heat flux was 37 W/cm^2, and no boiling was reported by Ivanovskii et al. [21], even though the liquid superheat exceeded 20 K at $q_e = 20$ W/cm^2 in the experiments. For a larger number of grooves per unit width such as in the AGHP by Plesch et al. [2], the heat transfer coefficient should be higher because of the increase in the thin film region over the same area. The characteristic values of the evaporative heat transfer coefficients for the evaporator by Ivanovskii et al. [21] were 10,000 W/(m^2-K), while for the miniature AGHP by Plesch et al. [2] the predicted values of $\overline{h}_e$ were larger than 40,000 W/(m^2-K). Thus, the boiling limitation should take place at larger heat fluxes for narrower grooves.

The agreement between the predicted temperature drop in the condenser and the experimental results by Schlitt et al. [20] can be seen from Fig. 2.16 for the ammonia ($T_v = 250$ K) and ethane ($T_v = 200$ K) heat pipes. As the heat load increased, the thermal resistance of the condenser increased and the evaporator thermal resistance decreased (see Figs. 2.15 and 2.16) due to the changes in the meniscus contact angle longitudinal distribution.

The numerically obtained values for the maximum heat transfer capacity of the AGHP's have been also compared with the experimental data by Schlitt et al. [20] for ammonia (Fig. 2.17(a), $L_e = 0.3$ m, $T_v = 203$ K) and ethane (Fig. 2.17(b), $L_e = 0.15$ m, $T_v = 200$ K) within the assumption that $\theta_{men,min} = 0$. Some disagreement of the results for comparatively large inclination angles (elevation) when the evaporator end is elevated can be explained by the complicated meniscus shape at the evaporator end, which is not described by the present model. However, for smaller tilt angles the agreement is satisfactory.

The second heat pipe configuration considered here is the AGHP investigated experimentally by Plesch et al. [2]. The cross-sections are shown in Fig. 2.1 and the AGHP's geometrical characteristics are: $W = 0.06$ mm, $L_1 = 0.02$ mm, $t_g = 0.24$ mm, $t = 2$ mm, $t_w = 0.22$ mm, $L_e = 20$ mm, $L_a = 80$ mm, $L_c = 20$ mm, $N = 80$. The casing material was copper and the working fluid was pure water. Therefore, the minimum contact angle was set to $\theta_{men,min} = 33°$ (Stepanov et al., [69]). The heaters were situated at both sides of the evaporator with an overall heated surface of 2.56 cm^2. The numerical results for the maximum heat flow, Q_{max}, transferred by the flat miniature AGHP are shown in Fig. 2.17(c), where it can be seen that Q_{max} increased with the operating temperature. However,
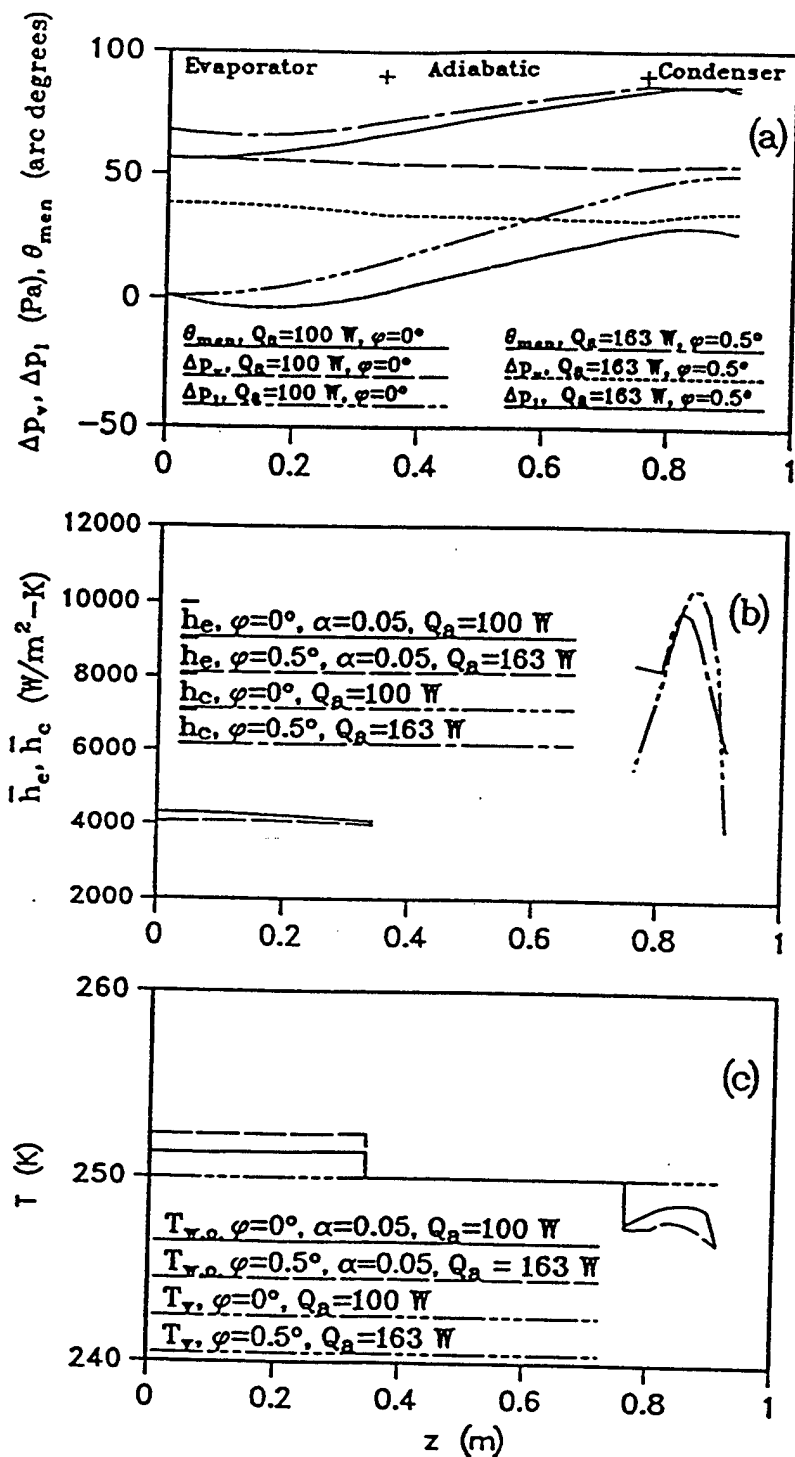
Figure 2.15: Performance characteristics of the ammonia-Al heat pipe (T_v =250 K): (a) Meniscus contact angle and fluid pressure; (b) Local heat transfer coefficients; (c) Wall and vapor temperatures.
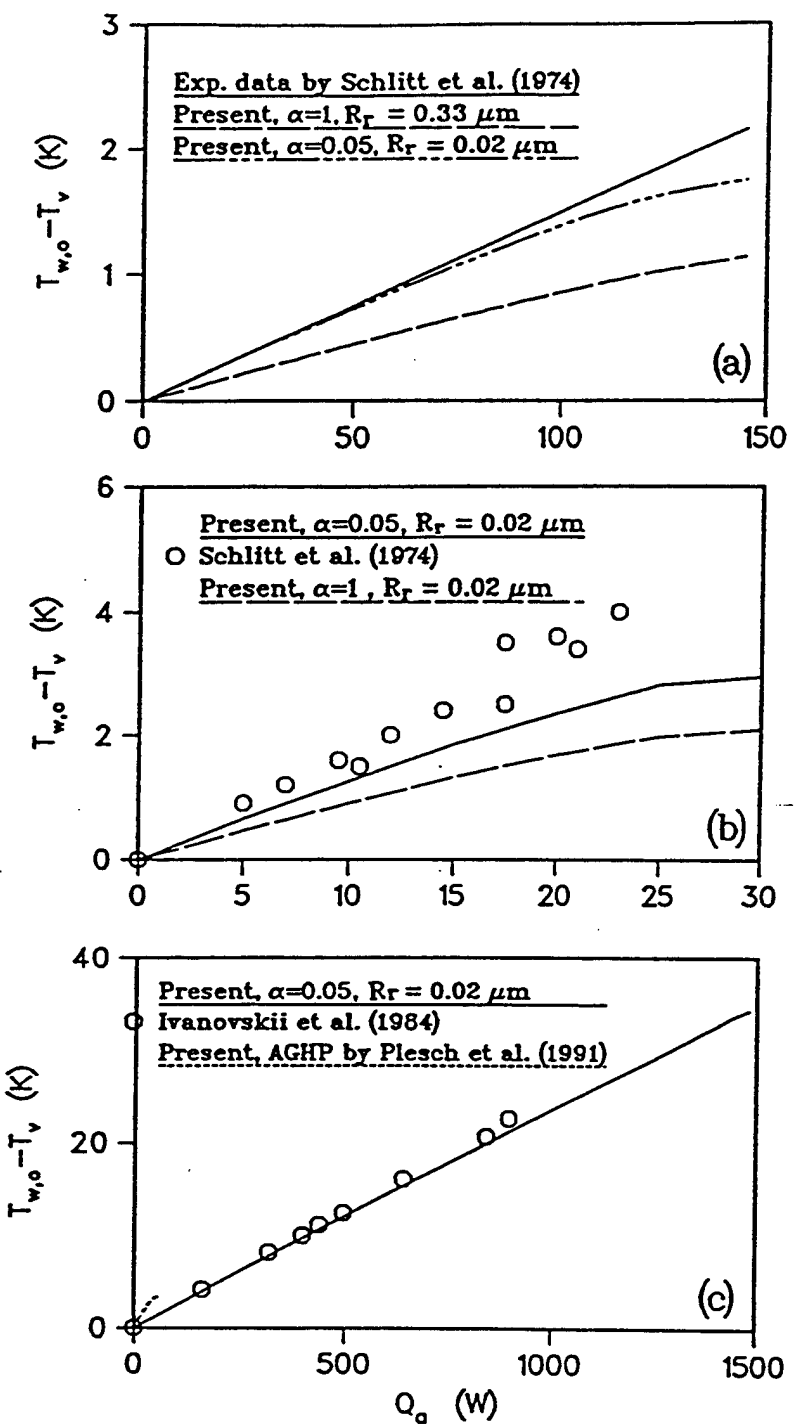
Figure 2.16: Temperature drop in the evaporator versus heat load: (a) Ammonia-Al heat pipe $(T_v = 250$ K); (b) Ethane-Al heat pipe $(T_v = 200$ K); (c) Water-Copper planar evaporator $(T_v = 300$ K) and flat miniature AGHP $(T_v = 378$ K).
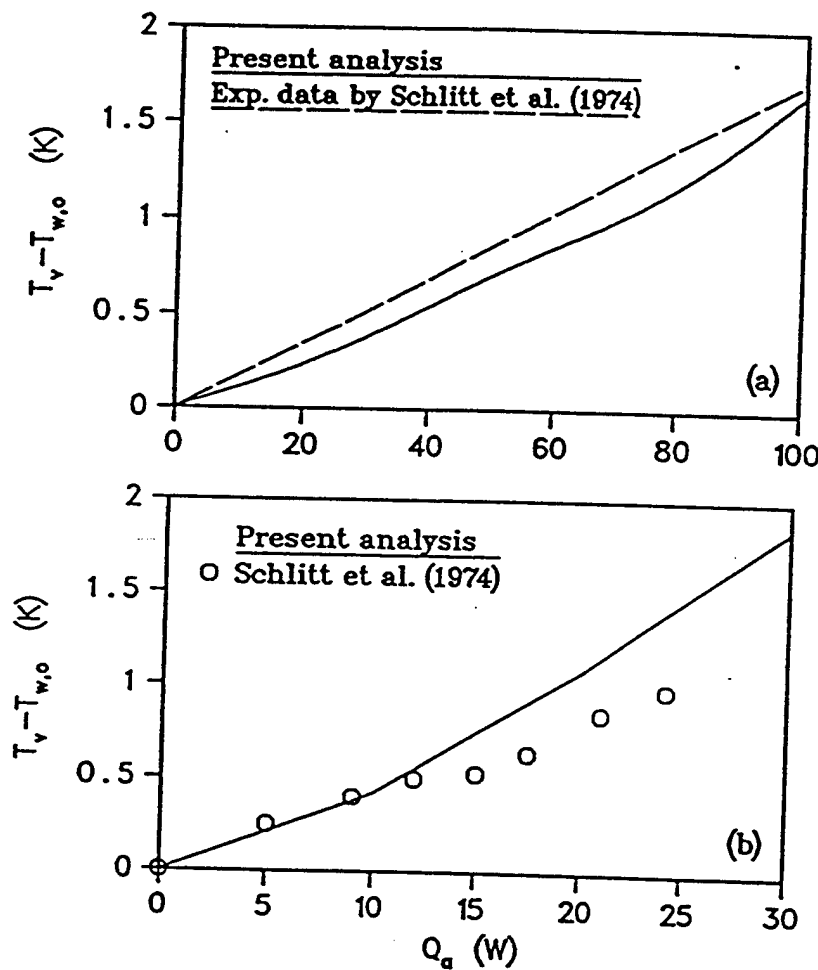
Figure 2.17: Temperature drop in the condenser versus heat load: (a) Ammonia-Al heat pipe ($T_v = 250$ K); (b) Ethane-Al heat pipe ($T_v = 200$ K) .
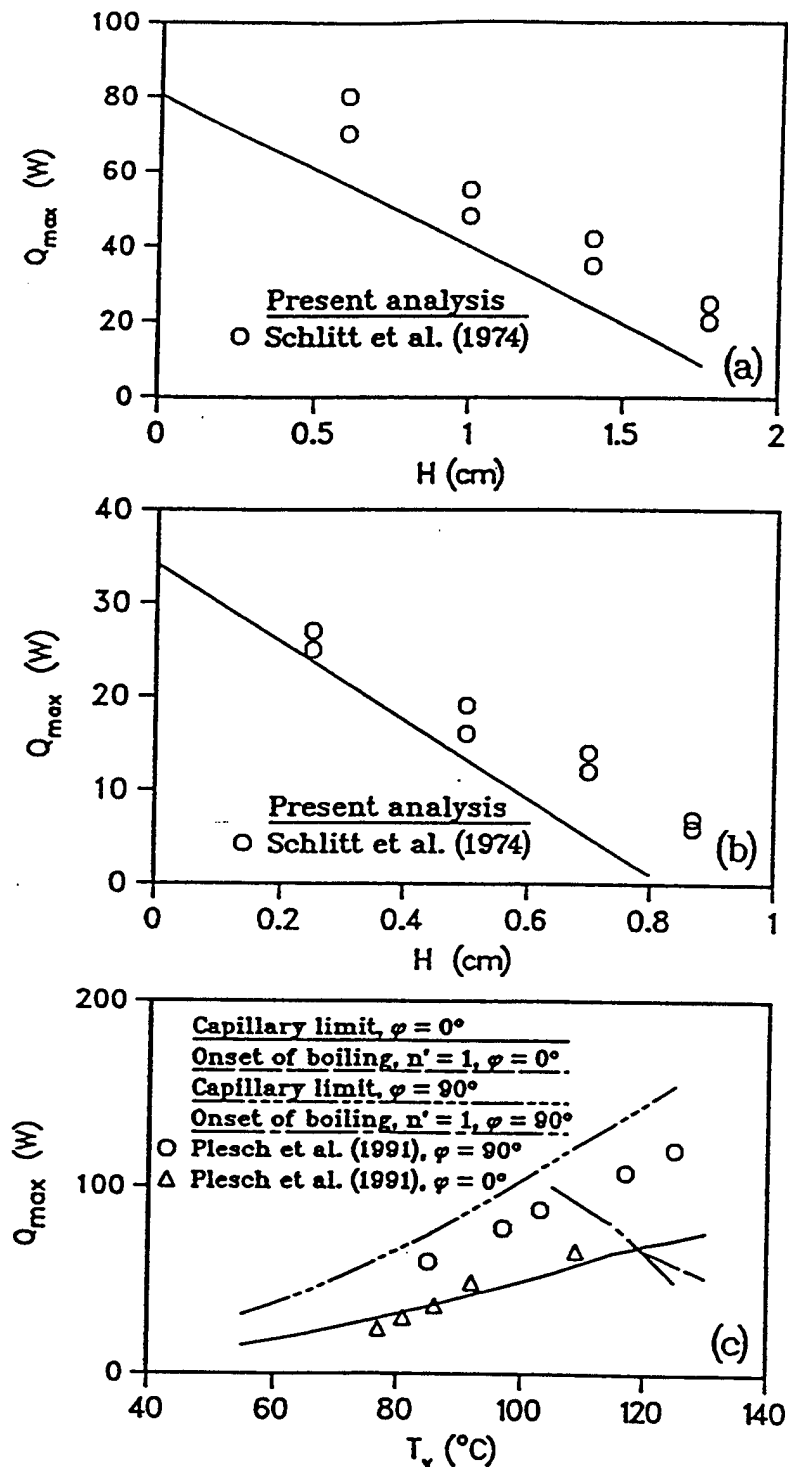
Figure 2.18: Maximum heat transfer of the AGHP's: (a) Ammonia-Al heat pipe ($T_v = 203$ K); (b) Ethane-Al heat pipe ($T_v = 200$ K); (c) Water-Copper flat miniature heat pipe .

for $T_v > 100°C$, it was restricted by the boiling limitation. To validate the numerical results, a comparison with two of the most representative series of the experimental data by Plesch et al. [2] was made, as shown in Fig. 2.17(c). It should be noted that the experimental results by Plesch et al. [2] were given (and plotted in Fig. 2.17(c)) versus the evaporator surface temperature, and it was not mentioned directly if the data for the measured heat flow rate were at a maximum. The numerical predictions of the capillary limit for both the horizontal ($\varphi = 0$) and vertical ($\varphi = 90°$) orientations follow the experimental data. The temperature drop along the vapor flow was less than 0.4 K in the numerical experiments while the temperature drop in the evaporator reached several degrees (Fig. 2.15(c)). The influence of the grooved surface geometry on the maximum heat transfer through the flat AGHP with the external dimensions $2 \times 7 \times 120$ mm is shown in Figs. 2.18 and 2.21 for the vertical and horizontal orientations, respectively. While the values of W and t_g were changed, the fin half-width and the wall thickness were kept constant at $L_1 = 0.02$ mm and $t_w = 0.22$ mm. The number of grooves N was different for different W, while the external dimensions were the same. Also, the vapor channel height was dependent on t_g because of the same reason. For the vertical orientation at $T_v = 55°C$, the capillary limit restricted the maximum heat flux in the evaporator, which had a maximum value of about 15 W/cm^2 for $W = 0.03$ to 0.04 mm (Fig. 2.18(a)). For $T_v = 105°C$ both the capillary and boiling limits occurred as shown in Fig. 2.18(b), and the optimal groove half width was about 0.05 mm with an absolute maximum heat flux of 40 W/cm^2. In the horizontal orientation the maximum heat fluxes were 8 W/cm^2 (for $W = 0.03$ mm, $T_v = 55°C$) and 25 W/cm^2 (for $W = 0.04$ mm, $T_v = 105°C$) as shown in Fig. 2.18.

It is anticipated that in order to reach higher heat fluxes, more advanced heat pipe configurations should be used.

2.3.6 Conclusions

The numerical results of the mathematical model describing the fluid flow and heat transfer in the conventional and miniature axially-grooved heat pipes are summarized as follows:

1. The validity of the present mathematical model for axially-grooved heat pipes has been confirmed, in general, by comparisons with existing experimental data. However, more detailed information concerning the values of the accommodation coefficients and dispersion constants is needed.

2. An increase of the heat load decreased the evaporator thermal resistance and increased the condenser thermal resistance due to changes in the longitudinal meniscus angle distribution along the AGHP in the horizontal position.

3. The maximum heat flux in the evaporator of the flat miniature copper-water AGHP was restricted by both the capillary and boiling limitations in the interval of the operating temperature from $T_v = 90$ to $120°C$.

4. Due to the fact that the greatest part of the heat flow through the liquid is transferred in the region where the liquid film thickness is comparatively small,
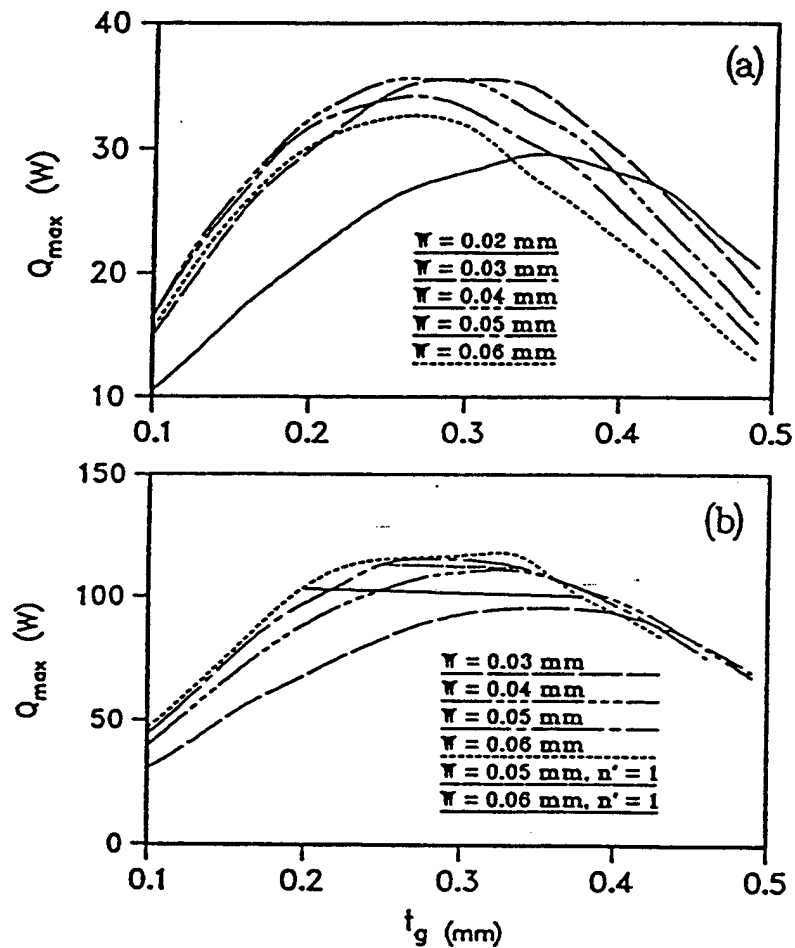
Figure 2.19: Maximum heat transfer of the flat miniature heat pipe versus groove depth (vertical orientation): (a) $T_v = 55°$; (b) $T_v = 105°$.
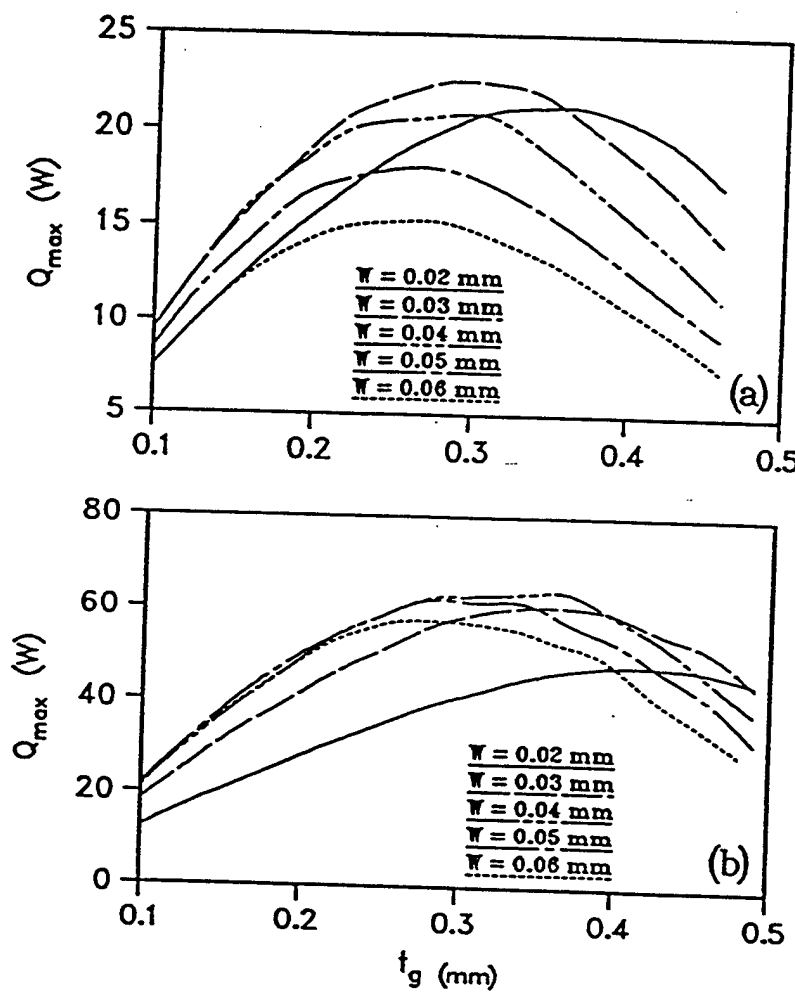
Figure 2.20: Maximum heat transfer of the flat miniature heat pipe versus groove depth (horizontal orientation): (a) $T_v = 55°$; (b) $T_v = 105°$.

grooved evaporators are capable of withstanding high heat fluxes. The optimized copper-water flat AGHP with external dimensions $2 \times 7 \times 120$ mm could operate at maximum heat fluxes in the evaporator of 25 and 40 W/cm^2 for the horizontal and vertical orientations, respectively, provided that the operating temperature was high enough ($T_v = 90$ to 120°C).

2.4 Enhanced Grooved Heat Pipes

To remove high heat fluxes from electronic and optical components, it has been proposed to use flat miniature axially grooved heat pipes (Plesch et al., [2]; Faghri, [1]). In an axially-grooved heat pipe (AGHP), the maximum heat flux in the evaporator is restricted by the longitudinal fluid transport limitation (or capillary limit) and by the boiling limitation. These limitations should be taken into account during the design and optimization of an AGHP with the aim to make it capable of operating with high heat fluxes in the evaporator. This objective can be reached by the proper choice of the grooved surface geometry (Frank, [3]) and/or by special enhancements as ivadizing (Grote et al., [4]), which is the deposition of a porous structure on the top of the lands between the grooves. The main purpose of this analysis is to predict the maximum heat transfer capability of the proposed flat miniature copper-water heat pipe with the grooved-ivadized structure. Predictions of the capillary and boiling limitations have been made in the same manner as shown in Section 2.3 and also in Khrustalev and Faghri [5] with some modifications accounting for the presence of the porous layer, as explained in the following sections.

2.4.1 Heat Pipe Configurations

The prototype heat pipe considered here is the AGHP investigated experimentally by Plesch et al. [2]. The cross-sections of the heat pipe are shown in Figs. 2.21(a) and (b) and its characteristic dimensions are represented in Table 2.3. The casing material was copper and the working fluid was pure water. The heaters were situated at both sides of the evaporator with the overall heated surface 2.56 cm^2.

In order to consider the enhanced AGHP, some experimental results of Grote et al. [4] and Khrustalev et al. [37] should be mentioned first. In the experiment by Grote et al. [4], an aluminum plate was machined with rectangular grooves ($W = 0.0635$ mm, $t_g = 0.64$ mm, $L_1 = 0.06465$ mm) and then enhanced by an inexpensive process called ivadizing. During ivadizing, aluminum was vapor deposited onto the surface, forming a slightly porous coating on the top of the lands between the grooves ($t_p = 0.15$ mm, $W_p = 0.02$ mm, Fig. 2.21(b)).

Table 2.3: Characteristic dimensions of the prototype AGHP

W	t_g	L_1	t	t_w	L_e	L_a	L_c	N
0.06 mm	0.24 mm	0.02 mm	2 mm	0.22 mm	20 mm	80 mm	20 mm	80
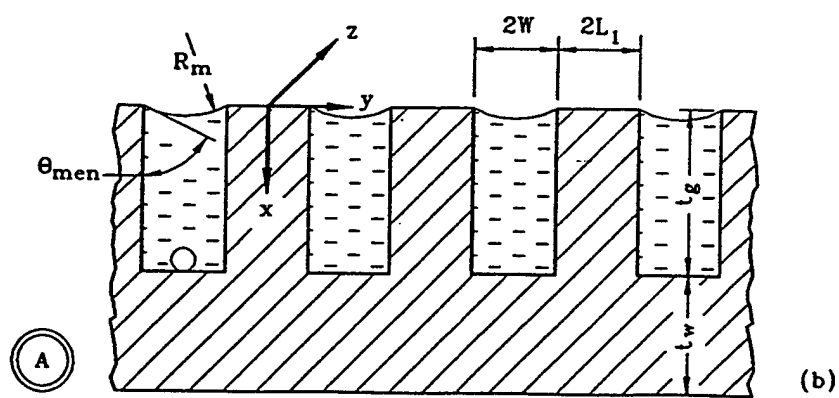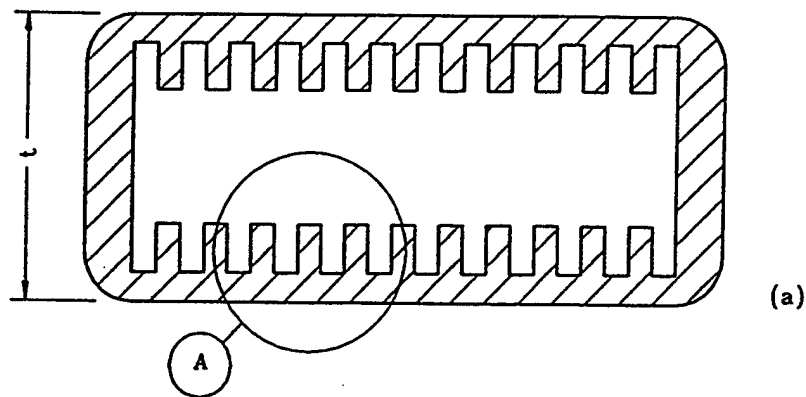
Figure 2.21: Flat miniature axially-grooved heat pipe cross sections

Tests of this enhanced plate with R-11 showed an improvement in the evaporative heat transfer coefficient by a factor of four compared to the surface with plain grooves. A copper heat pipe with a similar combined porous structure was tested by Khrustalev et al. [37]. The porous copper coating was deposited on the inner surface of a tube with longitudinal rectangular grooves ($W = 0.37$ mm, $t_g = 0.46$ mm, $L_1 = 0.43$ mm), serving as a cathode in the process of cathodic deposition from solution. A significant increase (about three to four times for acetone) in the evaporative heat transfer coefficient was registered due to the presence of the porous coating . In both papers, it was mentioned that the enhanced surfaces had a larger capillary pumping ability than that with plain grooves. Since the increase of the evaporative heat transfer coefficient means a decrease in the liquid superheat in the evaporator, which is crucial for the onset of nucleate boiling, the described enhanced surfaces are very promising for high heat flux heat pipes. Therefore, the enhanced heat pipe with the same characteristics as the prototype by Plesch et al. [2] is considered in this study, except that a porous coating was added on the land area between the grooves with $t_p = 0.15$ mm and $W_p = 0.02$ mm (Fig. 2.21(b). The maximum heat flow rates restricted by capillary and boiling limitations were predicted for both heat pipes and compared.

2.4.2 Boiling Limitation in Enhanced AGHP's

Nucleation within the wick is undesirable for operation of heat pipes with wicks because the bubbles can obstruct the liquid circulation and cause hot spots on the evaporator walls, and/or oscillatory heat pipe performance (Faghri, [1]). Thus, for heat pipe design optimization, it is necessary to predict the value of the heat flux which initiates vapor bubble formation in the working liquid. This task can be subdivided into two parts:

1. Estimation of the critical superheat of the liquid in the wick, $(T_{b,\ell} - T_v)$, which causes generation of vapor bubbles at the wall-wick interface.

2. Computation of the heat transfer coefficient in the evaporator, $\bar{h}_{e,b}$, for the situation when no boiling occurs in the liquid, which relates the values of the heat flux, q_e, and the temperature drop across the wick, $(T_{b,\ell} - T_v)$.

Critical liquid superheat. The process of bubble formation depends upon the solid surface microrelief, wetting contact angles and liquid properties. Since theoretical prediction of the superheat which causes boiling is difficult, empirical correlations should be involved in the analysis.

Lorenz et al. [36], obtained experimental data for boiling of four different liquids on a copper surface with a #240 (sandpaper) finish. In the mentioned experiment, the number of active bubble formation sites per square centimeter (n'), which increased rapidly with superheat, were determined by visual counting at different superheat values. Experimental results by Lorenz et al. [36] can be approximated by the following equation

$$n' = C_1 - C_2[\frac{h_{fg}(T_{b,\ell} - T_v)\rho_v}{2\sigma T_v} + \frac{1}{R_m}]^{-1} \tag{2.94}$$

where for water $C_1 = 77$, $C_2 = 19\times10^6$; and $1 \leq n' \leq 6$, and for R-113, methanol and benzene $C_1 = 39.6$, $C_2 = 19.6\times10^6$ and $0.5 \leq n' \leq 10$. Note that the vapor bubble embryo diameter is much smaller than the groove width, therefore, this correlation obtained for

59

planar surfaces can be used in the present analysis to predict the incipience of boiling. For a known superheat, $(T_{b,\ell} - T_v)$, equation (2.94) indicates whether boiling occurs $(n' \geq 0)$ at a given point along the evaporator length, which is characterized by the local radius of curvature of the meniscus, R_m. The values of the heat flux and superheat are related as follows

$$q_e = \overline{h}_{e,b}(T_{b,\ell} - T_v) \tag{2.95}$$

where $\overline{h}_{e,b}$ is the local effective heat transfer coefficient between the bottom of a groove and the saturated vapor, which is generally dependent on the value of R_m at this location.

Heat transfer coefficient. The effective evaporative coefficient of heat transfer for the heat pipe with plain grooves was calculated in the same manner as Khrustalev and Faghri [5]. The heat transfer during evaporation was considered by accounting for the effects of heat conduction through thin liquid films and the metallic fin, interfacial thermal resistance, disjoining pressure and surface roughness. The values of $\overline{h}_{e,b}$ were calculated for every point along the axial direction in the evaporator of the modeled AGHP's for a given heat load Q_a, and equation (2.94) was used with the corresponding R_m to predict the onset of nucleate boiling $(n' = 1)$.

The heat transfer coefficient of the enhanced AGHP, $\overline{h}_{e,b}$, was estimated as follows. The three main thermal resistances which have the most important influence on the heat transfer in the evaporator of the enhanced AGHP (Fig. 2.21(b)) are those associated with the heat conduction in the fin between grooves, heat conduction in the porous layer, and evaporation from the porous surface wetted with liquid $(1/h_p)$. This can be expressed by the following equation.

$$\overline{h}_{e,b} = \left[\frac{t_g}{k_w} \frac{W + L_1}{L_1} + \frac{t_p}{k_p} \frac{W + L_1}{L_1 + 0.5(W - W_p)} + \frac{W + L_1}{(W - W_p + L_1)h_p} \right]^{-1} \tag{2.96}$$

Heat transfer during the evaporation of water from a porous surface was considered in the same manner as Solov'ev and Kovalev (1984). The predicted values of h_p were extremely high, especially for small pore sizes, R_p. For example, for $R_p = 20$ μm, $T_v = 100°$C, and $\theta_0 = 33°$ (Stepanov et al., [69]) h_p exceeded 500,000 W/(m^2-K). Thus, the heat transfer coefficient $h_{e,b}$ was estimated by equation (2.96), where the impact of the last term was small in comparison with those of the two other terms.

2.4.3 Capillary Limitation and Fluid Circulation

The mathematical model of the fluid circulation in AGHP's is given in detail in section 2.3. Some distinguishing features of the model related with the considered enhanced AGHP should be mentioned here. The expression for the friction factor for liquid flow along capillary grooves affected by the vapor flow, originally obtained by Schneider and DeVos [34] for rectangular grooves, was used for the prototype AGHP because of its reliability and accuracy. Accounting for the liquid-vapor interaction is important for the prototype AGHP because the liquid-vapor interface is a significant part of the perimeter of the liquid cross-section. However, for the enhanced AGHP, for the case when $W_p \ll W$, the liquid-vapor interface is

a comparatively small portion of the perimeter. Therefore, the friction factor for the liquid flow along the capillary channel of the enhanced AGHP was defined using the following equation (Shah and Bhatti, [33])

$$(f\,\mathrm{Re}) = 24(1 - 1.3553C + 1.9467C^2 - 1.7012C^3 + 0.9564C^4 - 0.2537C^5) \qquad (2.97)$$

where $C = 2W/(t_g + t_p)$ and the Reynolds number is based on the hydraulic diameter which is defined accounting for the geometry of the porous layer.

The conditions for the capillary limit in the prototype AGHP used in the present analysis imply that the curvature of the meniscus is at a minimum at a single point in the condenser, and at a maximum at a single point in the evaporator with the maximum heat load.

$$\min\{K_{\mathrm{men}}(z)\} = 0 \qquad (2.98)$$

$$\max\{K_{\mathrm{men}}(z)\} = \frac{\cos(\theta_0)}{W} \qquad (2.99)$$

where K_{men} is the curvature of the meniscus. For the enhanced AGHP, equation (2.99) was changed to reflect the different width of the groove outlet due to the porous structure.

$$\max\{K_{\mathrm{men}}(z)\} = \frac{\cos(\theta_0)}{W_p} \qquad (2.100)$$

For heat loads which were less than the maximum, only condition equation (2.98) was applied, which determined the value of the main meniscus radius at the evaporator end cap, R_{m0}. For the copper-water heat pipes modeled, θ_0 was set equal to 33° (Stepanov et al., [69]).

2.4.4 Results and Discussion

The numerical results for the maximum heat flow rate, Q_{max}, transferred by the AGHP's modeled are shown in Fig. 2.22 Q_{max} increased with the operating temperature (vapor temperature at the evaporator end cap). However, for $T_v > 100°C$, it was restricted by the boiling limitation. To validate the numerical results, obtained with an uncertainty of about ±0.2%, a comparison with the two best series of the experimental data by Plesch et al. [2] was made, as shown in Fig. 2.22(a). It should be noted that the experimental results by Plesch et al. [2] were given versus the evaporator surface temperature, and it was not directly stated if the data for the measured heat rate were at a maximum. The numerical predictions of the capillary limit for both the horizontal ($\varphi = 0$) and vertical ($\varphi = 90°$) orientations follow the experimental data. Note that a heat pipe can also work in the vertical orientation as a two-phase thermosyphon with boiling liquid in the evaporator.

For the enhanced AGHP, the maximum capillary potential, which is related to W_p (see Fig. 2.21), was much larger than that for the prototype AGHP because W_p was significantly smaller than W. The resulting maximum heat flow rate was also higher, and this heat pipe could effectively operate in the vertical orientation with elevated evaporator ($\varphi = -90°$, see Fig. 2.22(b)). In the enhanced AGHP, evaporation takes place on the surface of the porous

61
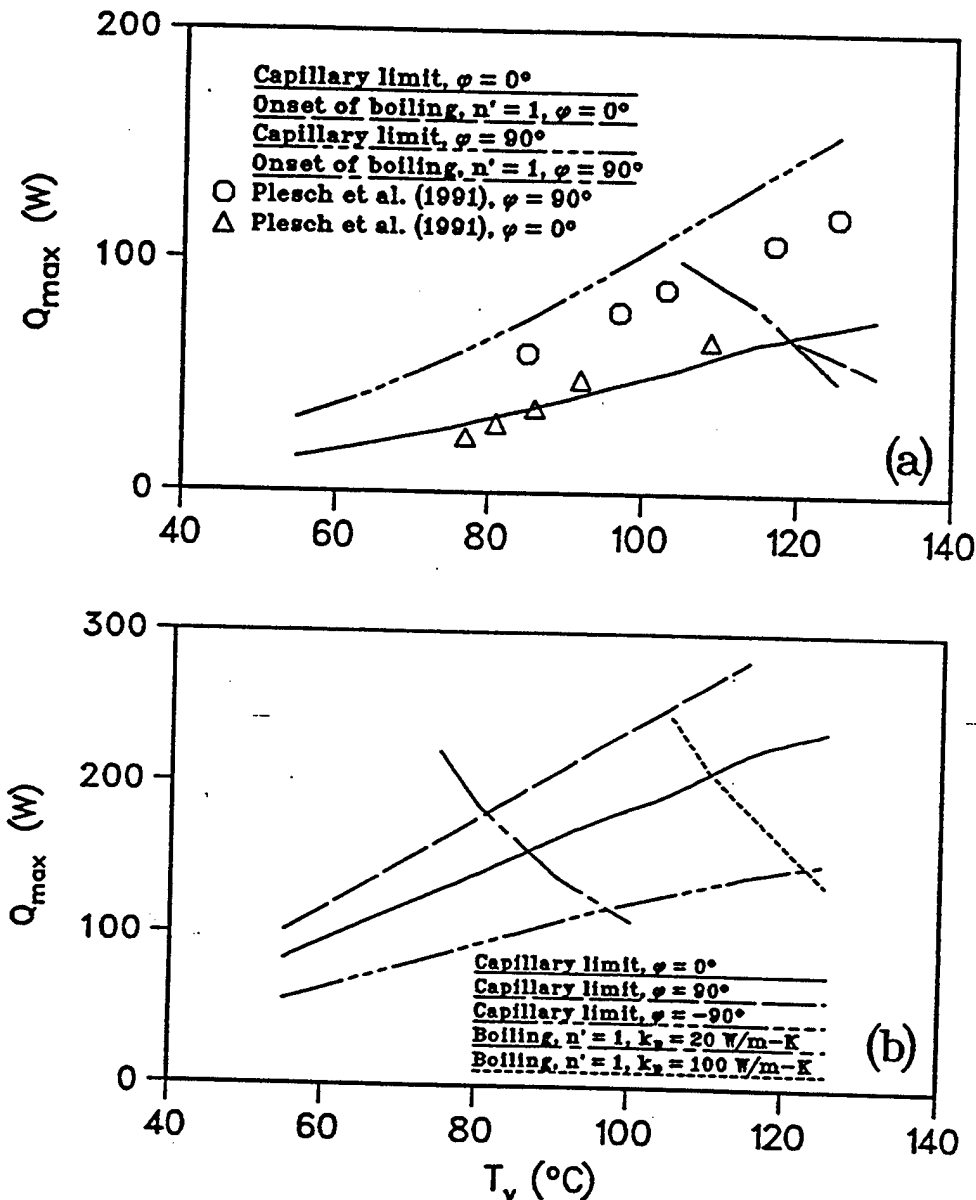
Figure 2.22: Maximum heat transfer of the copper-water heat pipes versus operating temperature: (a) Configuration by Plesch et al. [2]; (b) Configuration by Plesch et al. [2] plus porous coating.

layer where the total area of the thin film region is many times larger than that of the grooved evaporator without a porous coating. Therefore, the heat transfer coefficient and hence the maximum heat flux restricted by the boiling limit should be much larger for the enhanced AGHP provided that the thermal conductivity of the porous layer is not very low. The prediction of the maximum heat transfer of the AGHP with a porous coating is shown in Fig. 2.22(b) where the porous layer thermal conductivity, k_p, was set equal to 20 and 100 W/(m-K). At $T_v = 110°C$, the AGHP with porous coating could operate at a heat flux of 80 W/cm^2 in the horizontal position. It is anticipated that in order to reach higher heat fluxes, more advanced heat pipe configurations should be developed.

2.4.5 Conclusions

The results of the numerical prediction of the enhanced flat miniature axially-grooved copper-water heat pipe are summarized as follows:

1. The copper-water flat AGHP with external dimensions the same that by Plesch et al. [2] and with a porous coating on the lands between grooves ($k_p = 100$ W/(m-K)) could operate at a maximum heat flux in the evaporator of 80 W/cm^2 in the horizontal orientation at $T_v = 110°C$ and about 100 W/cm^2 in the vertical orientation with elevated condenser end at $T_v = 105°C$.

2. The AGHP with a porous coating, unlike an ordinary AGHP, could effectively perform in the vertical orientation when its evaporator end was elevated.

Therefore, the enhanced AGHP with a porous coating has been found superior over the prototype AGHP with plain axial grooves. Such a heat pipe could be successfully used in thermal control systems for high heat flux electronic equipment.

2.5 Miniature Inverted-Meniscus Evaporator

Evaporators which are capable of withstanding high heat fluxes, for example larger than 100 W/cm^2, are of great interest for electronic components cooling systems. The most promising evaporator design is the so-called "inverted meniscus" type which has been considered by Raiff and Wayner [38], Feldman and Noreen [39], and Solov'ev and Kovalev [40]. These authors carried out some experimental and analytical investigations of the performance characteristics of the inverted meniscus type evaporators. However, some critical mechanisms related with the formation of the vapor blanket in the porous structure along the heated solid surface were not simulated numerically. In order to predict the critical heat flux and effective heat transfer coefficients in the evaporator, the following mathematical model has been developed. The model includes the following interconnected problems which are treated simultaneously in the frames of the numerical analysis.

- Heat transfer during evaporation from a pore.

- Heat transfer and vapor flow in the dry region of a porous structure with the stable side boundary the location of which depends on the operational conditions.

63

- Heat conduction in a solid fin (or wall) with a non-uniform heat sink on side surfaces.

These interconnected problems are considered in detail in the following sections.

2.5.1 Physical Model of the Inverted Meniscus Evaporator

Schematics of the two configurations of the characteristic elements of the inverted meniscus evaporators are shown in Fig. 2.23. In the first configuration (Fig. 2.23(a,b)), the heated triangular fin is inserted in the porous plate and sintered with it in order to provide good thermal contact. In the second configuration (Fig. 2.23(c)), the heated wall is flat. With a small heat flux, evaporation of the liquid, which saturates the porous element, can take place exclusively from the surface of the porous body into the vapor channel as shown in Fig. 2.23(a). However, with extremely high heat fluxes, which are significantly more interesting for the industrial applications, the existence of the stable vapor blanket inside the uniform porous structure along the heated solid surface was anticipated (Raiff and Wayner [38]; Solov'ev and Kovalev [3]; Wulz and Embacher [41]) as shown in Fig. 2.23(b,c). Note, that one more operational regime can possibly exist, which is unstable and referred to by Ku [42], where the vapor bubbles form at heating surface and migrate until vented into vapor channel. In the present model only the case of the stable vapor blanket is considered. In this case evaporation takes place into the dry region of the porous structure at the liquid-vapor interface the location of which shifts depending on the operational conditions. The heat is conducted to this interface from the heated surface through the dry region of the porous element, and the vapor flows mainly along the solid surface through this region towards the vapor channel. The vapor flow is provided by the capillary pressure gradient due to the difference in the curvature of the menisci along the liquid-vapor interface. While the vapor flow takes place in a comparatively narrow porous passage, the liquid with the same total mass flow rate (steady state) is filtered perpendicularly through the entire porous element to the liquid-vapor interface, and the pressure gradient in liquid along this interface is negligible in comparison to that in vapor. This assumption can be justified in the case when the maximum pressure drop in liquid over the wetted region of the characteristic element in consideration is negligible compared to the pressure drop in vapor in the dry region, and it allows to describe the heat transfer in the vapor blanket in a one-dimensional approximation as shown below. The validity of the discussed assumption can be checked after the numerical results for the pressure drop in the vapor blanket have been obtained as explained in the section concerning the numerical results.

The thickness of the vapor blanket, δ_v, increases with the heat flux which can lead to the increase of the thermal resistance of the element. In the situation when $\delta_v|_{x=0}$ is of the same order of magnitude as the minimum thickness of the porous element (see Fig. 2.23(b)), the vapor can penetrate into the liquid channels which can obstruct the liquid supply of the evaporator and result in the dry out. The value of the heat flux at which the dry out takes place can be considered as critical.

The operating parameters of the evaporator depend upon the heat and mass circulation in the entire system (for example in a heat pipe) with the evaporator in consideration. In the present model the physical situation for the characteristic element is determined by the three parameters: the pressure in the liquid near the interface, $p_{\ell\delta}$, the temperature of the solid

64
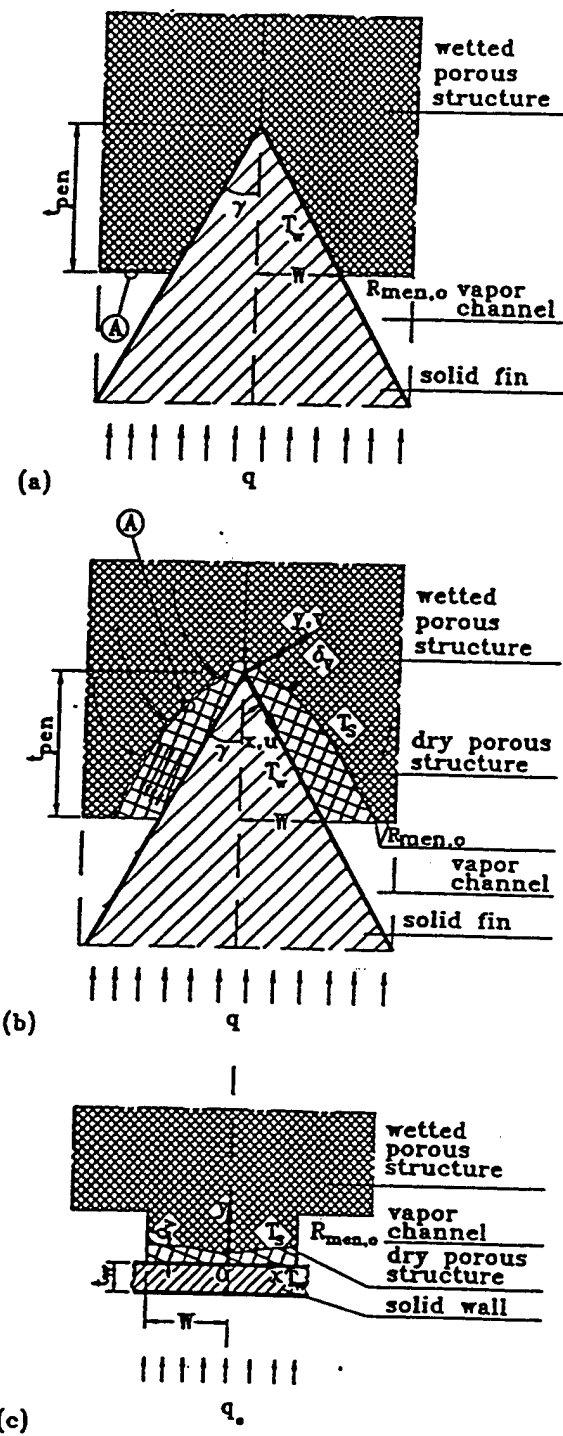
Figure 2.23: Schematics of the modeled elements of the inverted meniscus evaporators: (a) With the triangular fin for low heat fluxes; (b) With the triangular fin for high heat fluxes; (c) With the flat heated wall for high heat fluxes..

surface, T_0, at $x = 0$, and the liquid-vapor meniscus radius at the end of the vapor blanket ($x = L_{v\delta}$), $R_{men,o}$. Note that the superheat of the fin exists at the following condition:

$$T_0 > T_{sat}(p_{\ell\delta} + 2\sigma/R_{men,min}) \qquad (2.101)$$

where the subscript "sat" denotes the normal saturation temperature corresponding to a pressure $(p_{\ell\delta} + 2\sigma/R_{men,min})$, and $R_{men,min} = R_p/\cos\theta_{men,min}$. Inequality (2.101) characterizes the value of the solid/liquid superheat. $R_{men,o}$ is related with the fluid circulation in the entire device. For the case of the evaporator with the forced liquid supply it can be set $R_{men,o} \gg R_{men,min}$ because in this case the pressure drop in liquid is not due to the capillary pressure. For the case of the heat pipe, $R_{men,o}$ can be defined from the pressure balance for the whole heat pipe at the steady state

$$2\sigma/R_{men,o} = \Delta p_v + \Delta p_\ell + \Delta p_{p,\ell} \qquad (2.102)$$

(provided that $R_{men,max} \to \infty$) where Δp_v is the pressure drop due to the vapor flow along the heat pipe, Δp_ℓ is the pressure drop due to liquid flow along the liquid channels of the heat pipe, and $\Delta p_{p,\ell}$ is the pressure drop due to the liquid filtration through the porous plate in the evaporator section (and in the condenser section if it also contains the porous plate). That means that the capillary pressure drop presented in the left hand side of equation (2.102) supports the fluid circulation in the heat pipe while the capillary pressure drop $2\sigma(1/R_{men,min} - 1/R_{men,o})$ provides the vapor flow in the vapor blanket. Since these two pressure drops can be of the same order of magnitude, the existence of the vapor blanket in the inverted meniscus evaporator is important for the analysis of the heat pipe with evaporator of this type. At high heat fluxes the liquid-vapor interface doesn't touch the solid superheated wall, $\delta_v|_{x=0} > 0$, and the liquid meniscus radius is supposed to reach its minimum, $R_{men,min}$, at least at one point along this interface. Note that analytical investigation by Solov'ev and Kovalev [40] was restricted by the case $\delta_v|_{x=0} = 0$. The vapor blanket thickness, δ_v, depends on the values of the mentioned parameters ($p_{\ell\delta}$, T_0, and $R_{men,o}$), and can significantly affect the local effective evaporative heat transfer coefficient, h_{eff}. It can be anticipated that in the heat pipe with the considered evaporator an increase in the heat input causes a decrease of $R_{men,o}$ and the corresponding growth of the thickness of the dry zone. Therefore, the thermal resistance of the evaporator should increase with the heat flow rate in the heat pipe. This trend has been observed in the experiments by Solov'ev and Kovalev [40]. Note that the steady-state situation is modeled when no boiling of the liquid occurs at the liquid-vapor interface, and the phase change due to evaporation of the liquid at this interface takes place.

2.5.2 Heat Transfer During Evaporation from a Pore

Evaporation of the liquid occurs from the surface of the liquid menisci situated at the liquid-vapor interface. Schematic of the cylindrical pore and liquid meniscus is shown in Fig. 2.24. The description of the heat transfer during evaporation from a pore is given here with the two following main assumptions:

66
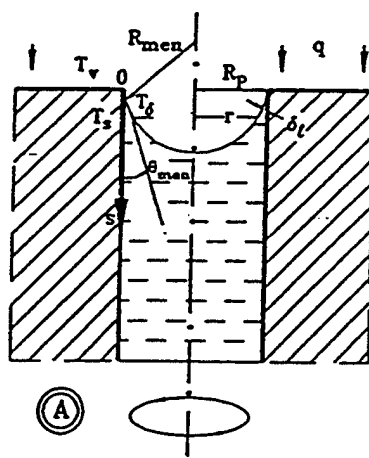
Figure 2.24: Schematic of the evaporation from a cylindrical pore..

- The temperature of the solid-liquid interface T_s can be considered constant along the s coordinate for small s:

- The curvature of the axisymmetrical liquid-vapor surface of the meniscus is defined by the main radius of curvature $K = 2/R_{\text{men}}$ and hence is independent of s.

The validity of the second assumption has been proved numerically in section 2.1, where it was shown that this assumption could give an error less than 5% when calculating the overall heat transfer coefficient during evaporation from a capillary groove. Since heat transfer during evaporation from thin films in a pore is similar to that in a capillary grove, this assumption can be justified for the present analysis.

The local heat flux through the liquid film due to heat conduction is

$$q_\ell(s) = k_\ell \frac{T_s - T_\delta}{\delta_\ell} \tag{2.103}$$

where the local thickness of the liquid layer δ_ℓ and the temperature of the free liquid film surface T_δ are functions of the s-coordinate. T_δ is affected by the disjoining and capillary pressures, and also depends on the value of the interfacial resistance, which is defined for the case of a comparatively small heat flux at the interface, q_δ, by the following relation given by the kinetic theory (Carey [12]):

$$q_\delta = - \left(\frac{2\alpha}{2 - \alpha} \right) \frac{h_{fg}}{\sqrt{2\pi R_g}} \left[\frac{p_{v\delta}}{\sqrt{T_v}} - \frac{(p_{\text{sat}})_\delta}{\sqrt{T_\delta}} \right] \tag{2.104}$$

where $p_{v\delta}$ and $(p_{\text{sat}})_\delta$ are the saturation pressures corresponding to T_v and at the thin liquid film interface, respectively.

The relation between the saturation vapor pressure over the thin evaporating film, $(p_{\text{sat}})_\delta$, affected by the disjoining pressure, and the normal saturation pressure corresponding to T_δ, $p_{\text{sat}}(T_\delta)$, is given by the extended Kelvin equation (Carey [12]):

$$(p_{\text{sat}})_\delta = p_{\text{sat}}(T_\delta) \exp \left[\frac{(p_{\text{sat}})_\delta - p_{\text{sat}}(T_\delta) + p_d - \sigma K}{\rho_\ell R_g T_\delta} \right] \tag{2.105}$$

Equation (2.105) reflects the fact that under the influence of the disjoining and capillary pressure, the liquid free surface saturation pressure $(p_{\text{sat}})_\delta$ is different from normal saturation pressure $p_{\text{sat}}(T_\delta)$ and varies along the thin film (or s-coordinate), while $p_{v\delta}$ and T_v are the same for any value of s. This is also due to the fact that T_δ changes along s. While the evaporating film thins approaching the point $s = 0$, the difference between $(p_{\text{sat}})_\delta$ given by Eq. (2.105) and the pressure obtained for a given T_δ using the saturation table becomes larger. This difference is the reason for the existence of the thin non-evaporating superheated film, which is in equilibrium state in spite of the fact that $T_\delta > T_v$.

Under steady state conditions, $q_\ell = q_\delta$, and it follows from Eqs. (2.103) and (2.104):

$$T_\delta = T_s + \frac{\delta_\ell}{k_\ell} \left(\frac{2\alpha}{2 - \alpha} \right) \frac{h_{fg}}{\sqrt{2\pi R_g}} \left[\frac{p_{v\delta}}{\sqrt{T_v}} - \frac{(p_{\text{sat}})_\delta}{\sqrt{T_\delta}} \right] \tag{2.106}$$

Equations (2.105) and (2.106) determine the interfacial temperature, T_δ, and pressure, $(p_{sat})_\delta$, for a given vapor pressure, $p_{v\delta}(x)$, temperature of the solid-liquid interface, T_s, and the liquid film thickness, $\delta_\ell(s)$.

As the liquid film thins, the disjoining pressure, p_d, and the interfacial temperature, T_δ, increase. Under specific conditions, a non-evaporating film thickness is present which gives the equality of the interfacial and solid surface temperatures, $T_\delta = T_s$. This is the thickness of the equilibrium non-evaporating film δ_0. For water the following equation for the disjoining pressure was used in the present analysis (Holm and Goplen [17]):

$$p_d = \rho_\ell R_g T_\delta \ln \left[a \left(\frac{\delta_\ell}{3.3} \right)^b \right] \tag{2.107}$$

where $a = 1.5336$ and $b = 0.0243$. From Eqs. (2.105), (2.106) and (2.107), the following expression for the thickness of the equilibrium film is given :

$$\delta_0 = 3.3 \left\{ \frac{1}{a} \exp \left[\frac{p_{sat}(T_s) - p_{v\delta}\sqrt{T_s/T_v} + \sigma K}{\rho_\ell R_g T_s} + \ln \left(\frac{p_{v\delta}}{p_{sat}(T_s)} \sqrt{\frac{T_s}{T_v}} \right) \right] \right\}^{1/b} \tag{2.108}$$

The total heat flow through a single pore is defined as

$$Q_p = \int_0^{R_p} \frac{T_s - T_\delta}{\delta_\ell/k_\ell} 2\pi r \, ds \equiv \int_0^{R_p} \frac{T_s - T_\delta}{\delta_\ell/k_\ell} 2\pi R_{men} \sin \left[\arctan \frac{R_p}{s + \sqrt{R_{men}^2 - R_p^2}} \right] ds \tag{2.109}$$

The surface of the pore wall is totally covered with microroughnesses, where the characteristic size varies from, for example, $R_r = 10^{-8}$ to 10^{-6} m. Apparently, the thin liquid film formation can be affected by some of these microroughnesses. The following approximation for the liquid film thickness was given in section 2.1: for $\delta_0 \leq \delta_\ell \leq \delta_0 + R_r$ and $R_r \gg \delta_0$

$$\delta_\ell = \delta_0 + R_r - \sqrt{R_r^2 - s^2} - R_{men} + \sqrt{R_{men}^2 + s^2 + 2R_{men}s \sin \theta_f} \tag{2.110}$$

where for surface with microroughness $\theta_f = 0$, and the liquid film thickness in the interval $\delta_\ell \geq \delta_0 + R_r$ is

$$\delta_\ell = R_r + \delta_0 - R_{men} + \sqrt{R_{men}^2 + s^2 + 2R_{men}s \sin \theta_{men}} \tag{2.111}$$

For the smooth surface model, θ_f is the angle between the solid-liquid and liquid-vapor interfaces at the point on s where the disjoining pressure and dK/ds become zero. Note that for small values of the accommodation coefficient (for example $\alpha = 0.05$) the value of R_r has not affected the total heat flow rate through the liquid film (Khrustalev and Faghri [26]).

The interfacial radius of curvature is related to the pressure difference between the liquid and vapor by the extended Laplace-Young equation:

69

$$p_{v\delta} - p_{\ell\delta} = \frac{2\sigma}{R_{\text{men}}} + \frac{\rho_v^2 v_{v\delta}^2}{\varphi^2}\left(\frac{1}{\rho_\ell} - \frac{1}{\rho_v}\right) \tag{2.112}$$

where $v_{v\delta}$ is the vapor mean blowing velocity specified for a given meniscus, and φ is the porosity which is needed in this equation because the evaporation takes place into the dry region of the porous structure. Temperature of the saturated vapor near the interface, T_v, is related to its pressure by the saturation conditions:

$$T_v = T_{\text{sat}}(p_{v\delta}) \tag{2.113}$$

Then the heat transfer coefficient during evaporation from the porous surface is defined as

$$h_{e,p} = \frac{\varphi_s Q_p}{\pi R_p^2(T_s - T_v)} \tag{2.114}$$

where $\varphi_s \equiv A_p/A_t$ is the surface porosity which is the ratio of the surface of the pores to the total surface of the porous structure for a given cross-section (it is assumed that $\varphi_s = \varphi$).

2.5.3 Heat Conduction in the Solid Fin or Wall

Since it can be anticipated that the temperature drops in metallic fin or wall are much smaller than those across the dry zone of the porous structure because $k_w \gg k_{\text{eff}}$, the heat conduction in the solid fin or wall is considered using a one-dimensional approach. For the case of the flat wall (Fig. 2.23(c)) it means that dT_w/dy is not included into consideration. The heat conduction in the triangular metallic fin is described by the following equation (Fig. 2.23(b)), which was obtained as a result of energy balance on a differential element consideration:

$$\frac{d^2 T_w}{dx^2} + \frac{dT_w}{dx}\frac{1}{x} + (T_s - T_w)\frac{k_{\text{eff}}\cos\gamma}{x\delta_v(x)k_w\sin\gamma} = 0 \tag{2.115}$$

where T_s is the local temperature of the porous structure at the liquid-vapor interface location. Similarly, the heat conduction equation for the wall in Fig. 2.23(c) is

$$\frac{d^2 T_w}{dx^2} + (T_s - T_w)\frac{k_{\text{eff}}}{t_w\delta_v(x)k_w} + \frac{q_o}{t_w k_w} = 0 \tag{2.116}$$

The boundary conditions for Eqs. (2.115) and (2.116) are

$$T_w|_{x=0} = T_0 \tag{2.117}$$

$$\frac{dT_w}{dx}\Big|_{x=0} = 0 \tag{2.118}$$

For the second configuration q_o is the uniform heat flux at the outer surface of the heated part of the flat wall. The value of q_o and the functions $\delta_v(x)$ and $T_s(x)$ should be given by the results of the vapor flow and heat transfer in the dry region solution considered below.

70

2.5.4 Vapor Flow and Heat Transfer in the Dry Region of the Porous Structure

The local heat flux due to heat conduction across the dry region of the porous structure from the solid surface to the liquid-vapor interface where evaporation takes place is

$$q_{\text{loc}}(x) = k_{\text{eff}} \frac{T_w(x) - T_s(x)}{\delta_v(x)} \tag{2.119}$$

Equation (2.119) is valid for the case $k_v \ll k_{\text{eff}}$ and $c_{p,v}(T_w - T_s) \ll h_{fg}$. Hence, the mean velocity of the vapor flow for a given x along the solid surface is (the mass and energy conservation balances)

$$\bar{u}_v(x) = \frac{1}{\delta_v(x) h_{fg} \rho_v} \int_0^x q_{\text{loc}}(x) \, dx \equiv \frac{k_{\text{eff}}}{\delta_v(x) h_{fg} \rho_v} \int_0^x \frac{T_w(x) - T_s(x)}{\delta_v(x)} \, dx \tag{2.120}$$

where $\bar{u}_v(x)$ is the mean vapor velocity along the x-coordinate. The modified Darcy's equations for the vapor flow in both directions through a porous structure where the value of 0.55 is used for a dimensionless form-drag constant, Nield and Bejan [10], are

$$\frac{\partial p_v}{\partial x} = -\frac{\mu_v}{K} u_v(x) - \frac{0.55}{\sqrt{K}} \rho_v u_v^2(x) \tag{2.121}$$

$$\frac{\partial p_v}{\partial y} = \frac{\mu_v}{K} v_v(y) + \frac{0.55}{\sqrt{K}} \rho_v v_v^2(y) \tag{2.122}$$

Where u_v and v_v are the area-averaged vapor velocities. The corresponding continuity equation is

$$\frac{\partial u_v}{\partial x} + \frac{\partial v_v}{\partial y} = 0 \tag{2.123}$$

It should be noted that the Darcy's equation is semi-empirical and describes the flow with the uniform velocity profile, therefore, it is assumed in the present analysis that u_v does not depend on y. Taking the definitions of the mean vapor pressure and axial velocity for a given x, $\bar{p}_v$ and $\bar{u}_v$, into consideration (see the Nomenclature) and integrating Eq. (2.121) over y, the following equation can be obtained for the gradient of the mean vapor pressure along the x-coordinate

$$\frac{d\bar{p}_v}{dx} = -\frac{\mu_v}{K} \bar{u}_v(x) - \frac{0.55}{\sqrt{K}} \rho_v \bar{u}_v^2(x) \tag{2.124}$$

Since the situation when $\delta_v \ll L_{vb}$ is considered, the vapor pressure drop across the vapor blanket is much smaller than that along the x-coordinate. At the solid fin (or wall) surface $v_v|_{y=0} = 0$, and at the liquid-vapor interface $v_v|_{y=\delta_v} = v_{v\delta} \epsilon$ where $\epsilon = \cos[\arctan(d\delta_v/dx)]$ is the cosine of the angle between the y coordinate and the normal to the liquid-vapor interface and $v_{v\delta}$ is the blowing velocity (normal to the liquid-vapor interface):

$$v_{v\delta} = k_{\text{eff}} \frac{T_w - T_s}{\delta_v h_{fg} \rho_v} \tag{2.125}$$

Equation (2.125) implies that the total amount of energy transferred from the heated solid surface to the liquid-vapor interface by the heat conduction across the dry porous zone, is spent on vaporization of the liquid. Since the axial velocity profile is nearly uniform, it follows from Eq. (2.123) that $v_v = v_{v\delta}\epsilon y/\delta_v$. Integrating Eq. (2.122) twice over y for a given x and implementing the definition of $\overline{p}_v$, the difference between the vapor pressure near the liquid-vapor interface, $p_{v\delta}$, and the mean vapor pressure of the vapor flow, $\overline{p}_v$, for a given x can be estimated as follows

$$p_{v\delta} - \overline{p}_v = \delta_v \left(\frac{v_{v\delta}\epsilon\mu_v}{3K} + \frac{0.55}{4\sqrt{K}}\rho_v v_{v\delta}^2\epsilon^2 \right) \tag{2.126}$$

Combining Eqs. (2.120) and (2.124), finally we have for the vapor filtration flow pressure gradient along the x-coordinate:

$$\frac{d\overline{p}_v}{dx} = -\frac{\nu_v k_{\text{eff}}}{\delta_v h_{fg} K} \int_0^x \frac{T_w - T_s}{\delta_v}\, dx - \frac{0.55}{\rho_v\sqrt{K}} \left[\frac{k_{\text{eff}}}{\delta_v h_{fg}} \int_0^x \frac{T_w - T_s}{\delta_v}\, dx \right]^2 \tag{2.127}$$

The boundary condition for the Eq. (2.127) follows from Eqs. (2.112), (2.125), and (2.126)

$$\overline{p}_v|_{x=0} = p_{\ell\delta} + \frac{2\sigma}{R_{\text{men}}|_{x=0}} + \frac{\rho_v^2 v_{v\delta}^2|_{x=0}}{\varphi^2} \left(\frac{1}{\rho_\ell} - \frac{1}{\rho_v} \right) - \frac{k_{\text{eff}}\mu_v\epsilon(T_w - T_s)|_{x=0}}{3K h_{fg}\rho_v} - \frac{0.55\rho_v}{4\sqrt{K}}(\epsilon^2 v_{v\delta}^2\delta_v)|_{x=0} \tag{2.128}$$

Now, the equation for T_s should be derived. The local heat flux at the liquid-vapor interface due to the evaporation of the liquid is:

$$q_{\text{loc}}(x) = [T_s(x) - T_v(x)]h_{e,p}(x) \tag{2.129}$$

Combining Eqs. (2.119) and (2.129) because of the steady state situation in the consideration, the expression for the local temperature of the porous structure at the liquid-vapor interface location is:

$$T_s(x) = \frac{T_w(x) + h_{e,p}(x)T_v(x)\delta_v(x)/k_{\text{eff}}}{1 + h_{e,p}(x)\delta_v(x)/k_{\text{eff}}} \tag{2.130}$$

Substituting Eqs. (2.125) and (2.126) into Eq. (2.112) and differentiating it, the following equation for the radius of the meniscus curvature can be obtained

$$\frac{d}{dx}\left(\frac{2\sigma}{R_{\text{men}}} \right) = \frac{d\overline{p}_v}{dx} - \frac{2\rho_v v_{v\delta}}{\varphi^2}\left(\frac{1}{\rho_\ell} - \frac{1}{\rho_v} \right)\frac{k_{\text{eff}}}{h_{fg}\delta_v^2}\left[\left(\frac{dT_w}{dx} - \frac{dT_s}{dx} \right)\delta_v - (T_w - T_s)\frac{d\delta_v}{dx} \right] +$$

$$\frac{k_{\text{eff}}\mu_v}{3K h_{fg}\rho_v}\left[\epsilon\left(\frac{dT_w}{dx} - \frac{dT_s}{dx} \right) + (T_w - T_s)\frac{d\epsilon}{dx} \right] + \frac{0.55\rho_v}{4\sqrt{K}}\left(\frac{k_{\text{eff}}}{h_{fg}\rho_v\delta_v} \right)^2 \times$$

$$\left\{ \epsilon^2\left[2(T_w - T_s)\left(\frac{dT_w}{dx} - \frac{dT_s}{dx} \right)\delta_v - (T_w - T_s)^2\frac{d\delta_v}{dx} \right] + 2\epsilon\delta_v(T_w - T_s)^2\frac{d\epsilon}{dx} \right\} \tag{2.131}$$

with the boundary condition

$$R_{\text{men}}|_{x=0} = C_0 \tag{2.132}$$

where C_0 should be chosen from the constitutive condition for the minimum value of the meniscus radius along the liquid-vapor interface

$$\min\{R_{\text{men}}(x)\} = R_p / \cos\theta_{\text{men,min}} \tag{2.133}$$

Now, the condition of the liquid-vapor interface mechanical equilibrium should be considered which is necessary in order to find its location or $\delta_v(x)$. In the analysis by Solov'ev and Kovalev [40] it was assumed that $\delta_v(x) = \text{const} \cdot x^{0.33}$ which is not quite satisfactory because of some reasons. For example, for the hypothetical situation when starting from a definite point along the x-coordinate, x_1, there is no evaporation from the liquid-vapor interface, it should be $\delta_v|_{x>x_1} = \text{const}$, which condition is not satisfied by the discussed expression. Wulz and Embacher [41] have modeled the vapor flow in the uniform zone of the dry porous structure. The thickness of the vapor zone was determined as 0.1 mm at $q_{\text{max}} = 17500 \text{ W/m}^2$ by comparing the calculated temperature difference between the fin top and the phase boundary with the value determined by experiment, using the simpler vapor zone model. Chung and Catton [43] have considered the problem of steam injection into a slow water flow through porous media, where the interface location was also unknown. They have found "...that the interface can be idealized as a stream line as far as the momentum equations are concerned." In the present model the concept of a streamline is used indirectly as explained below. For the asymptotic case, K $\rightarrow \infty$, $\mu_v \rightarrow 0$, integrating Euler's equation along a streamline gives

$$p_v + \frac{\rho_v u_v^2}{2} + \frac{\rho_v v_v^2}{2} = p_v|_{x=0} \tag{2.134}$$

where the terms containing u_v^2 and v_v^2 correspond to the inertia effects due to acceleration of fluid. In the present analysis the vapor flow through a porous medium is described by Darcy's momentum equation. However, it is assumed that since the velocity profile of the vapor flow along the x-coordinate, u_v, is nearly uniform, Eq. (2.134) can be used for the description of the inertia effects at the liquid-vapor interface concerning acceleration of the vapor. It can be anticipated that the liquid-vapor interface can be stable provided it has the shape which eliminates the influence of the inertia effects due to acceleration of the vapor flow on the vapor pressure near this interface. While the steady-state situation is analyzed, the liquid pressure along the interface is constant, and the pressure losses in the vapor flow in both directions due to friction and solid obstacles are compensated by the capillary pressure, the vapor pressure gradient along the stable interface due to these inertia effects should be equal to zero. Since the velocity profile of the vapor flow along the x-coordinate is nearly uniform, it follows from Eq. (2.134)

$$\frac{\rho_v \bar{u}_v^2}{2} + \frac{\rho_v v_{v\delta}^2 \epsilon^2}{2} = \text{const} \tag{2.135}$$

Note that Eq. (2.135) is not used for the fluid flow in the porous medium but describes the

inertia effects at the adjustable liquid-vapor interface while the momentum equations for the vapor flow in the porous medium are concerned. Equation (2.135) is necessary in order to find the equilibrium location of the liquid-vapor boundary. Substituting Eqs. (2.120) and (2.125) into Eq. (2.135) and differentiating it after some rearrangements gives the equation for the vapor blanket thickness, δ_v:

$$\frac{d^2\delta_v}{dx^2}\left\{\delta_v(T_w-T_s)^2\epsilon\sin\left(\arctan\frac{d\delta_v}{dx}\right)\left[1+\left(\frac{d\delta_v}{dx}\right)^2\right]^{-1}\right\} =$$

$$(T_w-T_s)\left[\int_0^x\frac{T_w-T_s}{\delta_v}dx+\delta_v\epsilon^2\left(\frac{dT_w}{dx}-\frac{dT_s}{dx}\right)\right] -$$

$$\frac{d\delta_v}{dx}\left[\left(\int_0^x\frac{T_w-T_s}{\delta_v}dx\right)^2+\epsilon^2(T_w-T_s)^2\right] \tag{2.136}$$

where all of the terms containing $(T_w - T_s)$ can be calculated in the numerical procedure using the functions $T_w(x)$ and $T_s(x)$ determined at the previous iteration. The second-order differential equation (2.136) should be solved with the two boundary conditions for the variables δ_v and $d\delta_v/dx$. The first boundary condition is

$$\delta_v|_{x=0} = C_1 \tag{2.137}$$

C_1 should be chosen from the constitutive condition that it is the value of $\delta_v|_{x=0}$ which provides the satisfaction of the following boundary condition

$$R_{\mathrm{men}}|_{x=L_{vb}} = R_{\mathrm{men},o} \tag{2.138}$$

The second boundary condition is due to the symmetry of the considered element (Fig. 2.22). Since at the point $x = 0$ $dT_w/dx = 0$, $dT_s/dx = 0$, and $dv_{v\delta}/dx = 0$ because of the physical reasons, it follows from Eq. (2.125)

$$\frac{d\delta_v}{dx}|_{x=0} = 0 \tag{2.139}$$

Thus we have six main variables (or unknown functions $f_i(x)$): $p_{v\delta}, \bar{p}_v, R_{\mathrm{men}}, T_s, v_{v\delta}$ and δ_v which should be found from the six equations: (2.112), (2.125), (2.127), (2.130), (2.131) and (2.136). These six equations should be solved along with those presented in the previous sections for variables $h_{e,p}(x)$ and $T_w(x)$. Note that the value q_o which is needed for Eq. (2.116) now can be found as:

$$q_o = \frac{1}{W}\int_0^{L_{vb}} k_{\mathrm{eff}}\frac{T_w(x)-T_s(x)}{\delta_v(x)}\,dx \tag{2.140}$$

For the first configuration, q_o is the heat flux in the solid fin corresponding to the porous structure/vapor channel plane. The heat flux on the outer surface of the evaporator (and the corresponding effective heat transfer coefficient) can be recalculated taking the geometry of the evaporator into consideration. Although the vapor leaving the dry zone of the porous structure is superheated, it is convenient to relate the local effective heat transfer coefficient

to the vapor saturation temperature because $c_{p,v}(T_w - T_s) \ll h_{fg}$. Thus the local effective heat transfer coefficient corresponding to the point $x = L_{vb}$ (outlet of the vapor flow) is defined as:

$$h_{\text{eff}} = \frac{1}{W(T_w - T_v)_o} \int_0^{L_{vb}} k_{\text{eff}} \frac{T_w(x) - T_s(x)}{\delta_v(x)} \, dx \tag{2.141}$$

2.5.5 Numerical Treatment

The numerical procedure was organized as a sequence of the following steps:

1. The initial approximation for the functions $\delta_v(x)$, $h_{e,p}$, $T_w(x)$ and $R_{\text{men}}(x)$ was chosen: $\delta_v(x) = C_1 + C_2 x$, $T_w(x) = T_0$, $R_{\text{men}}(x) = R_{\text{men,min}}(C_0 + C_3 x / t_{\text{pen}})$, and $h_{e,p} = C_4$;

2. The function $p_{v\delta}(x)$ (actually $p_{v\delta}(x) - p_{\ell\delta}$) was calculated from Eq. (2.112) with $v_{v\delta} = C_5$;

3. The function $T_v(x)$ was calculated from the saturation table;

4. The function $T_s(x)$ was calculated from Eq. (2.130);

5. The function $v_{v\delta}(x)$ was calculated from Eq. (2.125);

6. Equations (2.127), (2.131) and (2.136) with the boundary conditions (2.128), (2.132), (2.137), and (2.139) were solved using the Runge-Kutta procedure and new functions $\bar{p}'_v(x)$, $1/R'_{\text{men}}(x)$, and $\delta'_v(x)$ were found;

7. Equation (2.115) (or Eq. (2.116) for the second configuration) with the boundary conditions (2.117) and (2.118) was solved for the variables T_w and dT_w/dx using the Runge-Kutta procedure and new function $T'_w(x)$ was obtained;

8. New functions $p'_{v\delta}$ and $T'_v(x)$ were calculated from Eq. (2.112) and the saturation table;

9. Equations (2.105)–(2.113) were solved for every point on x and new function $h'_{e,p}(x)$ was found;

10. The values of q_o (Eq. (2.140)) and h_{eff} (Eq. (2.141)) were calculated;

11. Every previous function, f_i, was replaced by the new one using new function, f'_i, according to the following formula:

$$f_i(x) + \Delta_i [f_i(x)' - f_i(x)] \ \rightarrow f_i(x)$$

where Δ_i belong to the interval from zero to unity; and steps 4–10 were repeated many times until the convergence of the solution has been reached (about 90 to 150 iterations were required to gain the converged solution for every of the functions: $\max\{|f'_i - f_i|/f_i\} \leq 0.001$);

12. The smaller value of C'_1 was set and the steps 1-11 were repeated several times with different C_1 until the boundary condition $R_{\text{men}}|_{x=L_{vb}} = R_{\text{men},o}$ has been satisfied.

The results were obtained with constant thermophysical properties corresponding to the saturation temperature $T_{\text{sat}}(p_{\ell\delta}) = 100°\text{C}$.

2.5.6 Results and Discussion

In order to verify the assumption that the liquid pressure along the liquid-vapor interface, $p_{\ell\delta}$, can be considered constant, the following estimation for the pressure drop in the wetted porous structure was made for all of the numerical results with the calculated values of q_o.

$$\Delta p_{\text{pen},\ell} = \frac{t_{\text{pen}}\mu_\ell}{K}\frac{q_o}{h_{fg}\rho_\ell} \tag{2.142}$$

and $\Delta p_{\text{pen},\ell}$ were compared with the calculated pressure drops in the vapor blanket along the fin surface, $\Delta p_{\text{pen},v} = \bar{p}_v|_{x=0} - \bar{p}_v|_{x=L_{vb}}$. For the presented numerical results the values of the $(\Delta p_{\text{pen},\ell}/\Delta p_{\text{pen},v})$ were less than 0.5% which proves the validity of the accepted assumption. This also means that solving the corresponding two-dimensional problem for the liquid pressure in the wetted porous structure (Cao and Faghri [44]) simultaneously with the problem solved in the present model would not cause significant changes in the presented numerical results. In that case the pressure in liquid along the liquid-vapor interface would be a comparatively weak function of x, $p_{\ell\delta}(x)$, which would result in only a slightly different menisci radii distribution along the x-coordinate, $R_{\text{men}}(x)$, because the vapor pressure distribution in the dry zone of the porous structure, $\bar{p}_v(x)$, is the predominant function for the considered situation.

The numerical results were obtained for the first configuration (Fig. 2.22(b)) for the case of the miniature evaporator: $\gamma = 30°$, $t_{\text{pen}} = 0.2$ mm, $R_p = 20$ μm, $R_r = 0.02$ μm, $\theta_{\text{men,min}} = 33°$ (Stepanov et al. [69]), $\alpha = 0.05$ (Paul [22]), $k_{\text{eff}} = 10$ W/(m-K), $k_w = 438$ W/(m-K), $\varphi = 0.5$, $\varphi_s = 0.5$, $K = 0.5 \times 10^{-12}$ m^2, $p_{\ell\delta} = 1.013 \times 10^5$ Pa, and the working fluid was water.

Since the longitudinal circulation of the fluid in the heat pipe which determines the value of $R_{\text{men},o}$ was not considered in the present analysis, the numerical results were obtained for several fixed values of $R_{\text{men},o}$.

The maximum values of Reynolds numbers for the vapor flow in the dry zone, $\text{Re}_v = \bar{u}_v\sqrt{K}/\nu_v$, in the numerical experiments were up to 250, which means that the quadratic term in the modified Darcy's equation was predominant. Moreover, the vapor flow in the pores at high heat fluxes could be turbulent. Note that for the turbulent regime the macroscopic Eqs. (2.121), (2.122), and (2.124) are still applicable (Nield and Bejan [10]).

The data in Fig. 2.25 shows that the heat transfer coefficient during evaporation from the porous surface, $h_{e,p}$, significantly depended on the curvature of the liquid meniscus (Fig. 2.25(a)) and, hence, changed along the liquid vapor interface (Fig.2.25(b)) because the curvature of the liquid menisci changed along this interface. For smaller pore sizes the values of $h_{e,p}$ are larger because of the larger relative surface occupied by the thin films.

The thickness of the dry zone increased along the x-coordinate as shown in Fig. 2.26(a), and the value of $C_1 \equiv \delta_v|_{x=0}$ increased as $R_{\text{men},o}$ decreased for a given superheat value, $T_0 - T_v|_{x=0}$. For the larger values of $\delta_v|_{x=0}$ variation of the vapor blanket thickness along the x-coordinate becomes weaker. The liquid menisci radii changed along the liquid-vapor

76
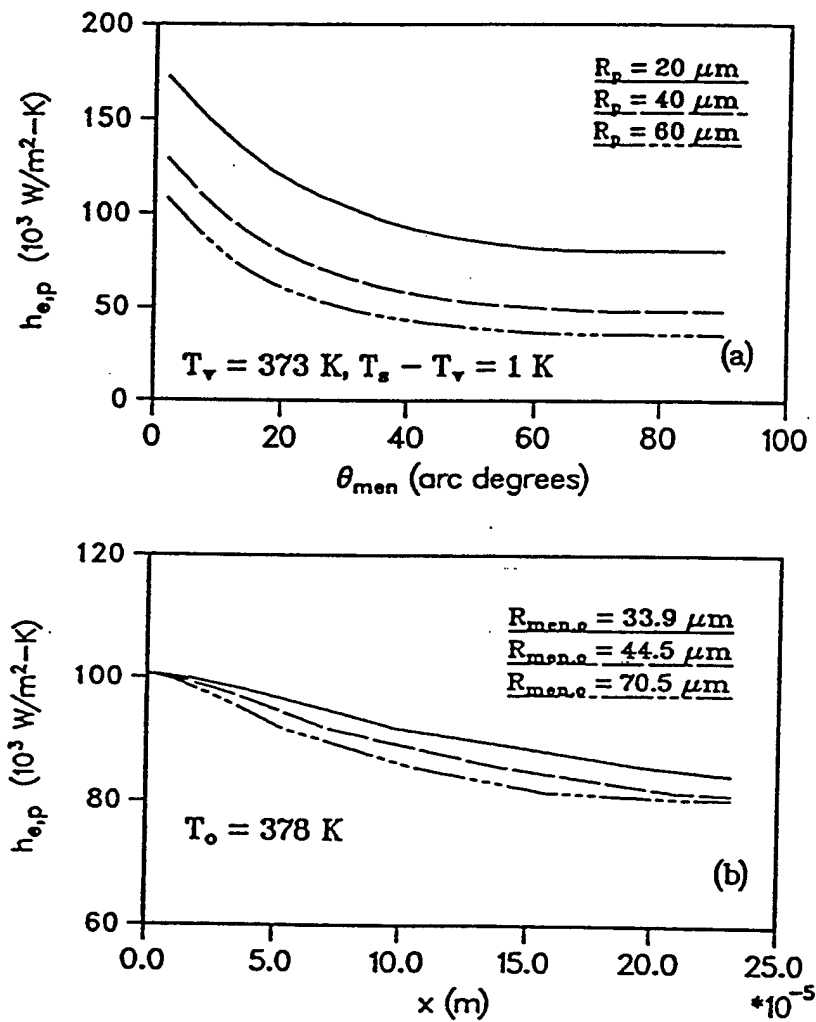
Figure 2.25: Heat transfer coefficient during evaporation from the porous surface: (a) Versus liquid meniscus contact angle (for a single pore); (b) Along the heated fin surface.

77

interface so that the capillary pressure gradient provided the vapor flow in both directions in the dry zone, Fig. 2.26(b). The average vapor pressure drop along the x-coordinate reached several thousand Pascals, Fig. 2.26(c). The minimum physically reasonable average pressure in the vapor blanket, $\bar{p}_v \rightarrow p_{\ell\delta}$, can occur in the situation when the liquid-vapor meniscus radius is still greater than zero. The temperature drops at the solid heated surface were significantly smaller than those corresponding to the porous skeleton at the liquid-vapor interface, Fig. 2.27(a). The local heat fluxes across the dry zone had their maximums at the point $x = 0$, Fig.2.27(c).

The data presented in Fig. 2.28 were obtained for the case $R_{men,o} > 8R_{men,min}$ which corresponds to the evaporator with the forced liquid supply. The thickness of the dry zone at the point $x = 0$, C_1, and the superheat of the solid surface at the point $x = L_{vb}$, which is the outlet of the vapor flow, $(T_w - T_v)_o$, increased progressively with the heat flux, q_o, while the effective heat transfer coefficient, h_{eff}, decreased as shown in Fig. 2.28. In the situation when the minimum thickness of the porous element could be 100 μm, at the heat flux of $q_o = 200$ W/cm^2 while $C_1 = 100\mu$m, the dry out of the evaporator could occur due to the penetration of the vapor into the liquid channels. If the temperature drop on the evaporator was restricted by 20 K because of the technical reasons, the maximum corresponding heat flux could be no more than $q_o = 200$ W/cm^2. For the case of the heat pipe with a heat load corresponding to the heat fluxes in consideration, the value of $R_{men,o}$ would be significantly smaller than $8R_{men,min}$ which could result in the larger thickness of the dry zone for the same q_o. The increase of the permeability of the porous structure resulted in the decrease of the thickness of the vapor blanket for the same operational conditions and, hence, could provide higher critical heat fluxes.

For extremely high heat fluxes, q_{loc}, when the temperature drop $(T_s - T_v)$ is large, boiling of the liquid at the liquid-vapor interface can occur which can cause instabilities at the liquid-vapor interface. However, boiling of the liquid does not necessarily result in the dry out of the evaporator of this type. Since $q_o > q_{loc}$ due to $L_{vb} > W$, the triangular geometry of the solid fin helps to postpone boiling and, therefore, can be advantageous compared to the case of the flat wall in the second configuration shown in Fig. 2.23(c). In other words, the triangular geometry of the fin provides higher value of the heat flux on the outer surface of the evaporator which corresponds to the beginning of the boiling of the liquid at the liquid-vapor interface.

2.5.7 Conclusions

1. The numerical results proved the possibility of the existence of the stable dry zone (vapor blanket) in the porous structure along the heated solid surface for a definite interval of the heat fluxes.

2. The pressure drop in the vapor blanket along the fin surface with the turbulent vapor flow in the pores was many times larger than the estimated pressure drop in liquid over the porous element which enabled us to assume the liquid pressure to be constant along the liquid-vapor boundary.

3. Two critical mechanisms were observed in the inverted meniscus evaporator both being related with the increase of the vapor blanket in the porous plate for increas-
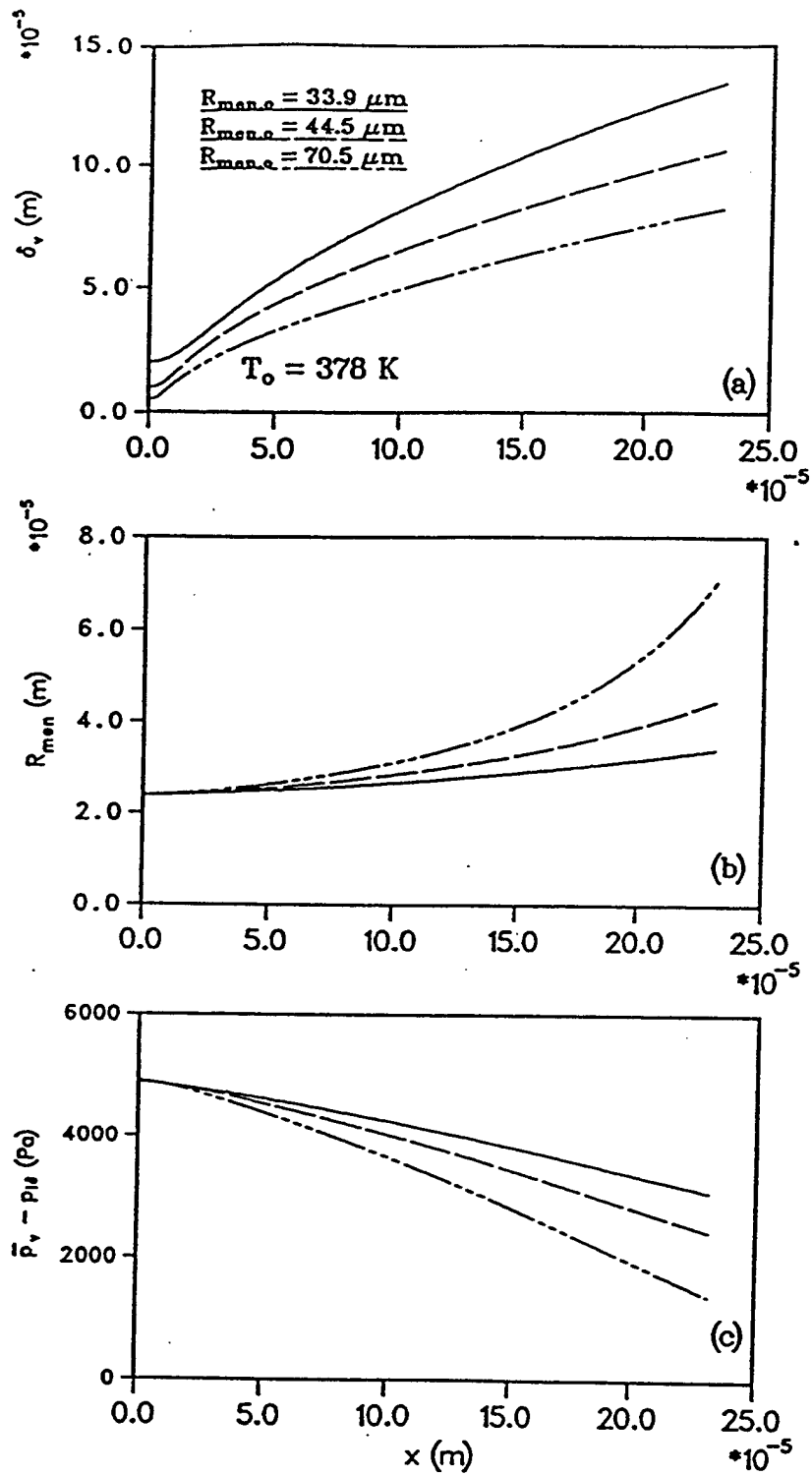
Figure 2.26: Performance characteristics of the modeled evaporator element along the heated fin surface: (a) Vapor blanket thickness; (b) Liquid menisci radii; (c) Mean vapor-liquid pressure drop..

79
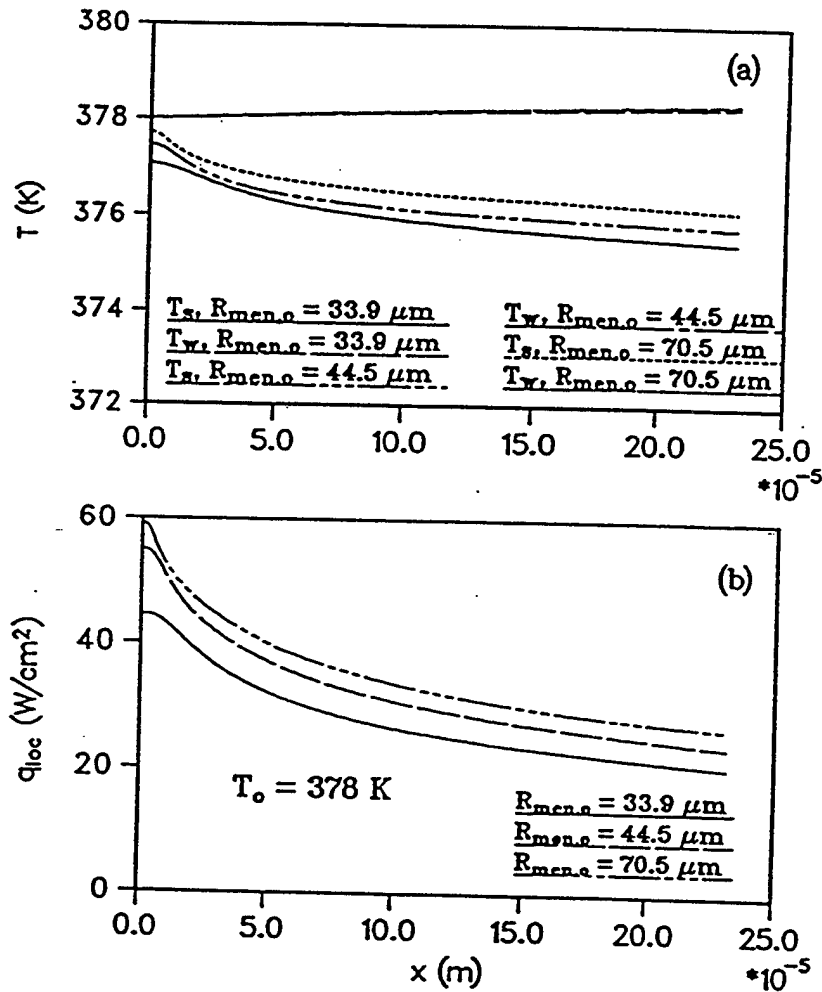
Figure 2.27: Performance characteristics of the modeled evaporator element along the heated fin surface: (a) Temperatures of the fin surface and of the porous structure at the liquid-vapor interface; (b) Local heat flux across the vapor blanket.
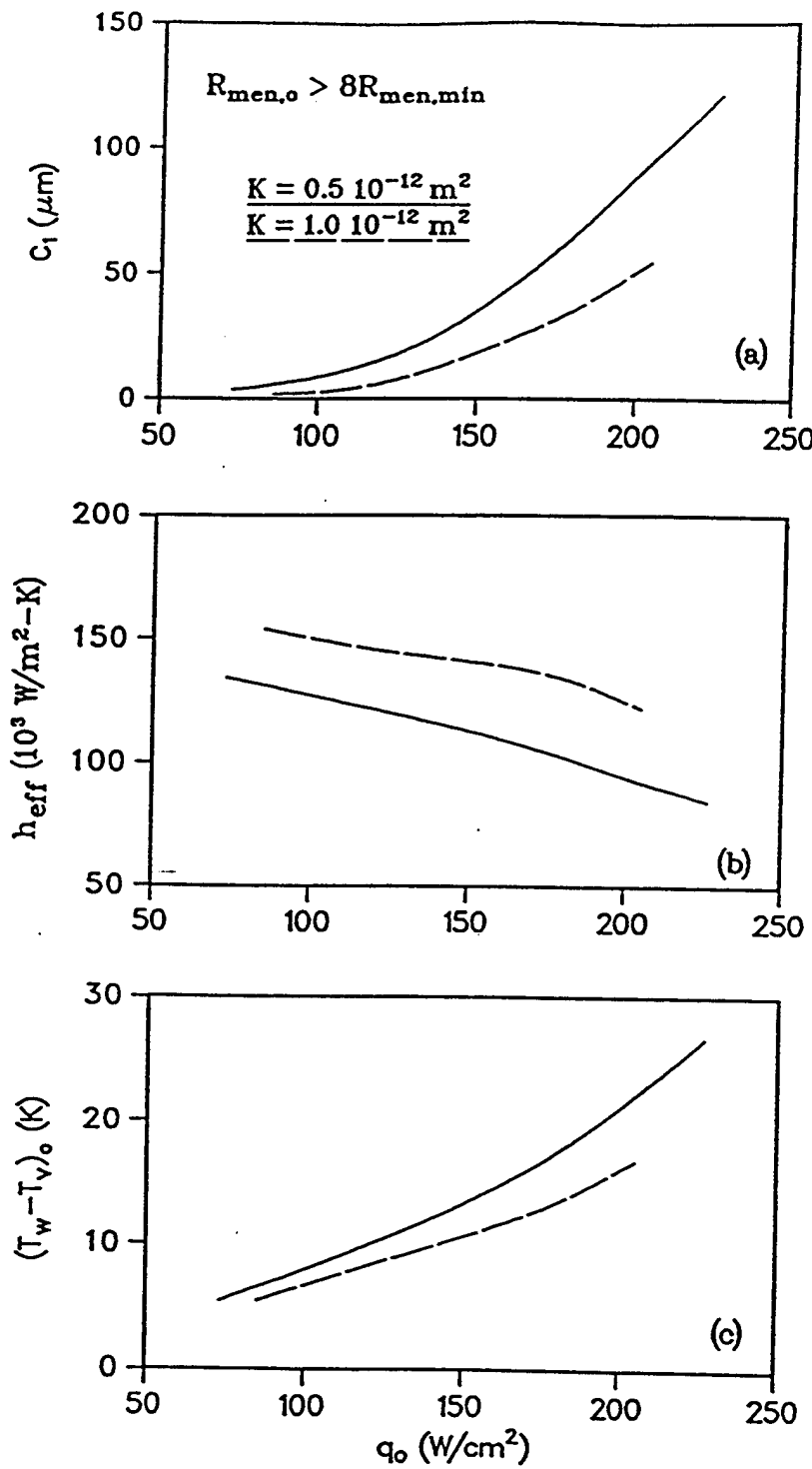
Figure 2.28: Influence of the heat flux on the performance characteristics of the modeled element; (a) Vapor blanket thickness at $x = 0$; (b) Effective heat transfer coefficient; (c) The superheat of the fin surface.

ing heat fluxes. The first mechanism was the growth of the evaporator thermal resistance for increasing heat fluxes which could lead to an unacceptable thermal resistance of the evaporator in the case when the thermal conductivity of the porous structure was low. The second mechanism was the dry out of the evaporator which could take place for a definite heat flux q_{max} in the situation when the vapor blanket thickness at the fin top was equal to the minimum thickness of the porous plate. Thus, for the case of a heat pipe, the dry out of the inverted meniscus type evaporator can occur before the traditional capillary limit or the conditions for the beginning of the boiling are reached.

2.6 Miniature Grooved Heat Pipe with Inverted-Meniscus Evaporator

Flat miniature heat pipes with a porous plate and axial grooves for the liquid flow are proposed for the case when only one wall of the evaporator is heated (Fig. 2.29). The so-called "inverted meniscus scheme" (Raiff and Wayner [38], Feldman and Noreen [39], Solov'ev and Kovalev [40], Wulz and Embacher [41], and Khrustalev and Faghri [6]) is used in the evaporator in order to avoid boiling of the liquid in the liquid channels. This circumstance and also high capillary potential of the porous plate can enable operation of the heat pipe with extremely high heat fluxes, provided that the main constructive parameters are optimized and all of the technological problems have been resolved. For example, the effective pore radius of the copper porous plate, R_p, should be rather small (Freggens [61]), and the porous plate should be sintered with both grooved surfaces under pressure in order to decrease the contact thermal resistance. Because of a significant pressure drop during the vapor flow through miniature channels, the evaporator length should not be large. By the same reason, in both the adiabatic and condenser sections, the fins between vapor channels are deleted in order to provide more space for the vapor flow, as shown in Figs. 2.29 and 2.30. The goal of this analysis is to estimate the maximum heat flux which can be achieved on the heat pipe evaporator wall before the dry out of the evaporator occurs.

2.6.1 Operation of the Heat Pipe

Since the heat pipe configuration illustrated in Figs. 2.29 and 2.30 contains some distinguishing features in comparison with ordinary heat pipes, some explanations concerning the fluid circulation in it are useful for a better understanding of the numerical results. The axial liquid flow takes place along the liquid channels and through the porous plate which is pressed from both sides by the grooved walls of the heat pipe, as shown in Figs. 2.29 and 2.30. While heat is added on the evaporator wall, the liquid contained in the wetted porous structure evaporates from the surfaces of the liquid-vapor menisci in the vicinity of the solid fin penetrating the porous plate, Fig. 2.30(a). The vapor moves through the triangular-shaped channels (in the y-direction) towards the rectangular vapor channels and then along the heat pipe axis (z-coordinate) as can be seen from Fig. 2.29 where the coordinate system is shown. Since the heat pipe can be cooled from both sides in the condenser section , the condensation of the vapor on the walls of the vapor channel (Fig. 2.30(b)) takes place on the surfaces of the both porous plate and the heat pipe wall. The condensate forming on the surface of the porous plate is filtered through it mainly into the liquid channels because
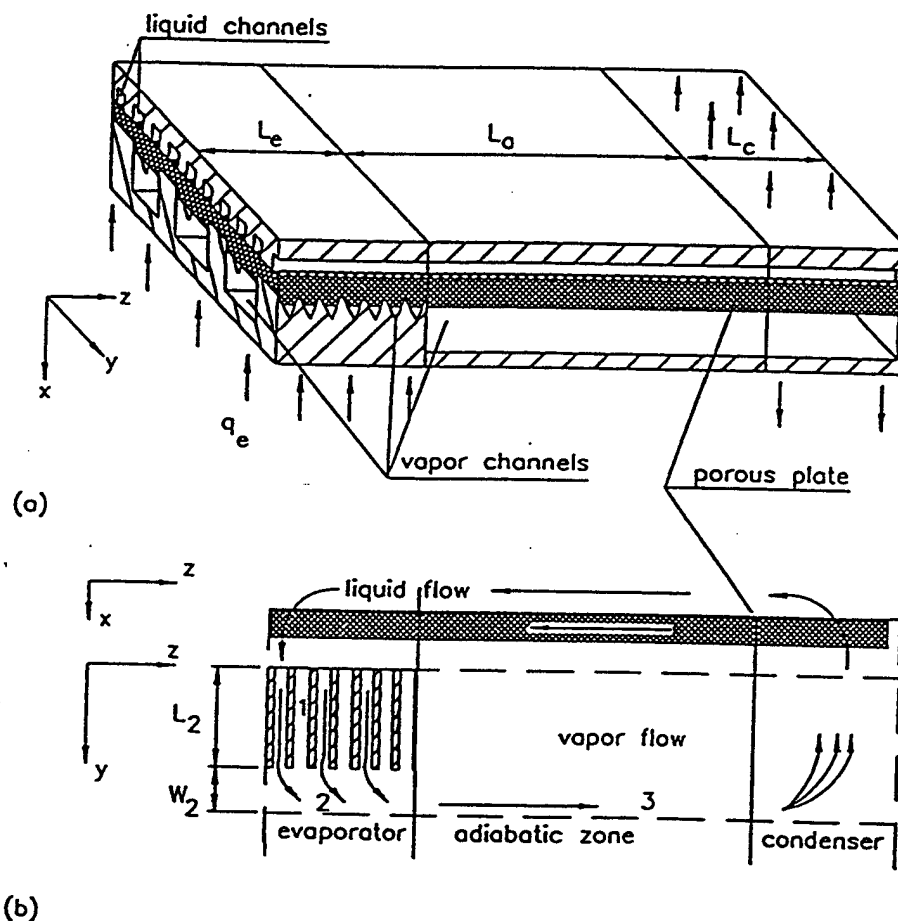
Figure 2.29: Flat miniature heat pipe with the inverted meniscus evaporator: (a) Schematic of the heat pipe; (b) Schematic of the fluid circulation in a characteristic element..

83

the pressure in the vapor channel is higher than that in the liquid channels. The condensate forming on the inner surface of the heat pipe wall flows under the influence of the surface tension in a thin film along the y-coordinate towards the corners of the vapor channel, where the bulk liquid resides, and along the z-coordinate (due to the vapor-liquid frictional interaction) toward the condenser end, which is partially blocked with the liquid. The blocking liquid is also filtered through the porous plate under the influence of the pressure drop between the vapor and the liquid channels. The fluid circulation is initiated by the capillary pressure, and the maximum heat transfer capacity of the heat pipe with small heat fluxes on the evaporator wall is usually restricted by the traditional capillary limit (Faghri [1]).

With extremely high heat fluxes, a vapor blanket appears inside the uniform porous structure in the evaporator along the heated solid surface (Raiff and Wayner [38], Solov'yev and Kovalev [40], Wulz and Embacher [41], Khrustalev and Faghri [6]), as shown in Figs. 2.30(a) and 2.31(b). In this case, evaporation takes place into the dry region of the porous structure at the liquid-vapor interface, the location of which shifts depending on the operational conditions. The heat is conducted to this interface from the heated surface through the dry region of the porous element, and the vapor flows mainly along the solid surface through this dry porous region towards the triangular vapor channel. The vapor flow is provided by the capillary pressure gradient due to the difference in the curvature of the menisci along the liquid-vapor interface inside the porous structure. Therefore, with high heat fluxes, part of the capillary pressure is spent on the compensation of the pressure drop in the vapor flow through the dry porous region. Hence, the maximum heat flux for this configuration should be calculated with respect to the formation of this vapor blanket and can be less than that estimated from the traditional capillary limit. This statement is explained and illustrated with the numerical results in the following sections.

2.6.2 Capillary Limit for the Case of Small Heat Fluxes

Because of the complicated configuration of the heat pipe in the consideration (Figs. 2.29 and 2.30), the capillary limit is estimated using the traditional simplified one-dimensional integral approach (Faghri [1]). According to this approach, a balance between the pressure drops in the fluid along the circulation path (Fig. 2.29(b)) takes place in a heat pipe. For the considered heat pipe this results in the following equation

$$\Delta p_{v,1} + \Delta p_{v,2} + \Delta p_{v,3} + \Delta p_\ell + \Delta p_{ft,e} + \Delta p_{ft,c} + \Delta p_g = \Delta p_{cap,max} \qquad (2.143)$$

All of the terms in equation (2.143) are considered below in detail. For the vapor flow along a heat pipe, it can be assumed that the inertia effects are mutually compensated in the evaporator and condenser sections where acceleration and deceleration of the vapor occur (Dunn and Reay [45]). For the liquid flow the inertia effects are negligible in comparison to those due to viscous losses (Khrustalev and Faghri [6]). The local hydraulic resistances for the vapor flow are also negligible. To estimate the pressure drops due to friction in the channels with fluid flow, the following traditional equation is used

$$\Delta p_{v,i} = 2 L_{eff,i} \frac{\rho_v \overline{w}_{v,i}^2 f_{v,i}}{D_{h,v,i}} \qquad (2.144)$$
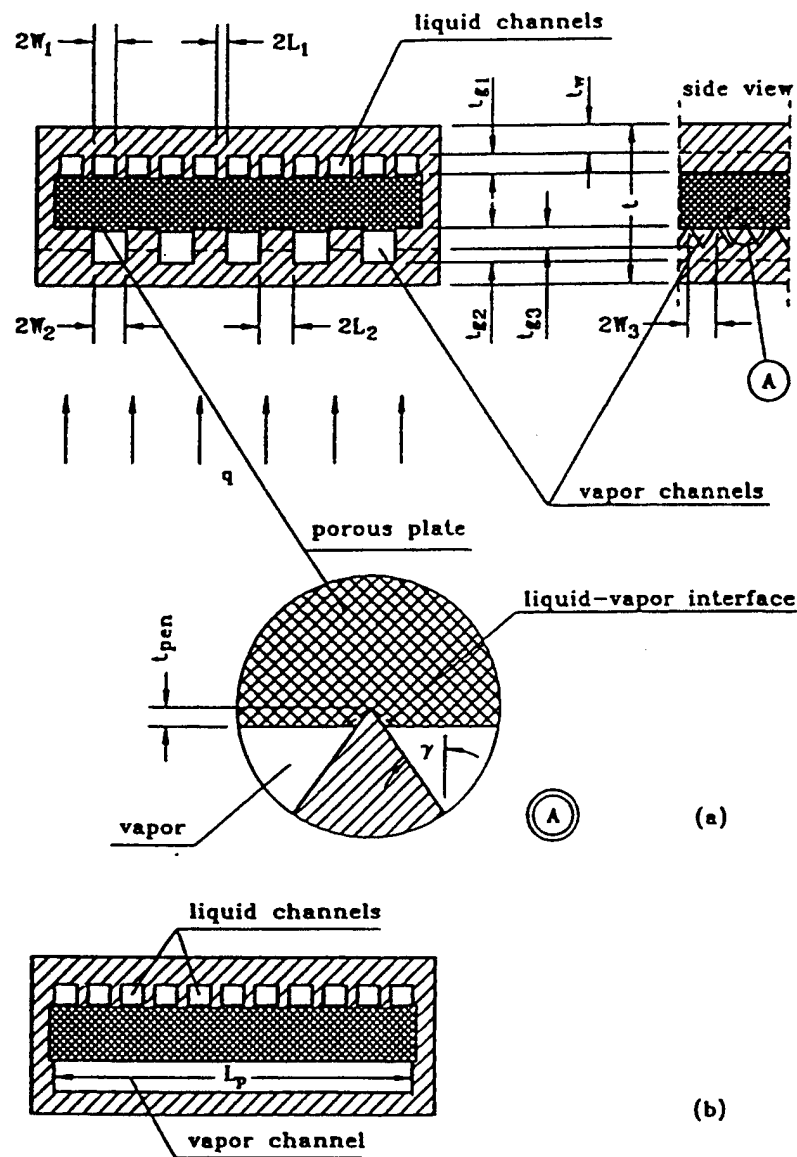
Figure 2.30: Cross sections of the miniature heat pipe: (a) Evaporator; (b) Adiabatic and condenser zones.
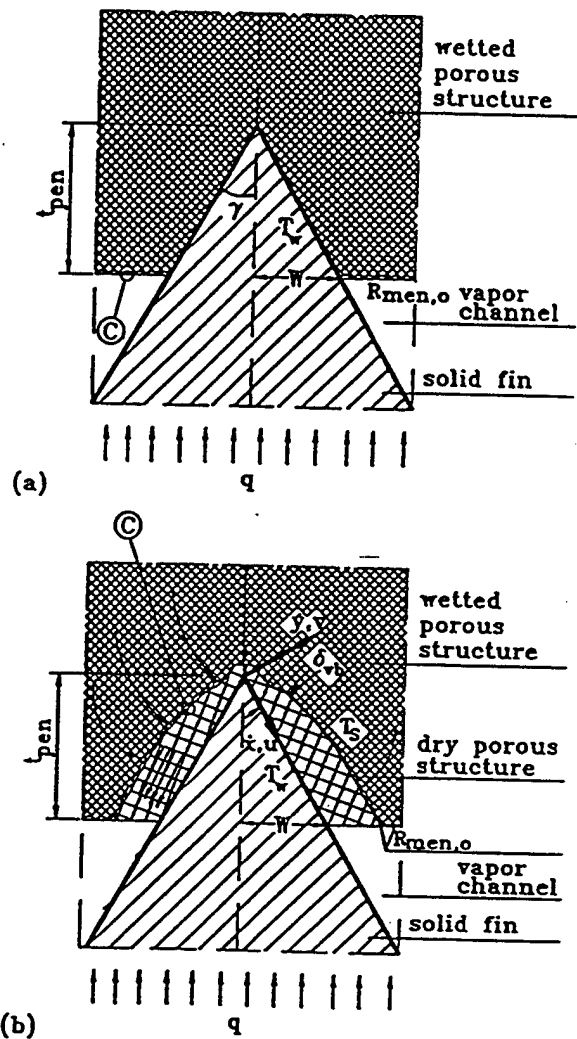
Figure 2.31: Schematic of the modeled element of the inverted meniscus type evaporator with the triangular fin: (a) With low heat fluxes; (b) With high heat fluxes.

86

where

$$f_{v,i} = \frac{(f\mathrm{Re})_{v,i}}{\mathrm{Re}_{v,i}} = \frac{(f\mathrm{Re})_{v,i}\nu_v}{\overline{w}_{v,i}D_{h,v,i}} \qquad (2.145)$$

$$\overline{w}_{v,i} = \frac{Q_i}{h_{fg}\rho_v A_{v,i}} \qquad (2.146)$$

The subscript "i" is needed because there are three types of vapor channels in the heat pipe, as shown in Fig. 2.29: triangular, rectangular (in the evaporator), and flat (in the adiabatic and condenser sections). For these channels $i = 1, 2$ and 3, respectively. $Q_i = Q/N_i$ is the total heat input corresponding to one particular channel with the cross-sectional area $A_{v,i}$. The number of the i-type channels is denoted as N_i, and the total heat load of the heat pipe is Q. Substituting equations (2.145) and (2.146) into equation (2.144), gives

$$\Delta p_{v,i} = 2\frac{(f\mathrm{Re})_{v,i}\mu_v}{\rho_v h_{fg}}Q\frac{L_{\mathrm{eff},i}}{N_i D_{h,v,i}^2 A_{v,i}} \qquad (2.147)$$

The difference between $\Delta p_{v,i}$ is due to the number and geometry of the channels: N_i, $D_{h,v,i}$, $A_{v,i}$, $L_{\mathrm{eff},i}$ and $(f\mathrm{Re})_{v,i}$. These parameters are specified below for the three types of the vapor channels and also for the liquid channels.

$\Delta p_{v,1}$ in equation (2.143) is the pressure drop in the short triangular channels in the evaporator along the y-coordinate which is transverse to the axial z-coordinate.

$$L_{\mathrm{eff},1} = L_2/2, \qquad W_3 = t_{g3}/\tan\gamma, \qquad A_{v,1} = (W_3 - t_{\mathrm{pen}}\tan\gamma)(t_{g3} - t_{\mathrm{pen}}),$$

$$D_{h,v,1} = \frac{4(W_3 - t_{\mathrm{pen}}\tan\gamma)(t_{g3} - t_{\mathrm{pen}})}{2(W_3 - t_{\mathrm{pen}}\tan\gamma) + 2(t_{g3} - t_{\mathrm{pen}})/\cos\gamma}, \qquad N_{v,1} = L_e L_p/[2W_3(W_2 + L_2)],$$

and $(f\mathrm{Re})_{v,1} = 13.33$ for $\gamma = 30°$ (Shah and Bhatti [33]).

$\Delta p_{v,2}$ is the pressure drop in the rectangular channels in the evaporator where the vapor flows along the z-coordinate (Fig. 2.30).

$$L_{\mathrm{eff},2} = L_e/2, \qquad A_{v,2} = 2W_2(t_{g2} - t_{\mathrm{pen}}),$$

$$D_{h,v,2} = \frac{4W_2(t_{g2} - t_{\mathrm{pen}})}{2W_2 + (t_{g2} - t_{\mathrm{pen}})}, \qquad N_{v,2} = 0.5L_p/(W_2 + L_2)$$

For rectangular and flat configurations of a vapor channel, the values of $(f\mathrm{Re})_{v,i}$ can be defined using the following equation (Shah and Bhatti [33]):

$$(f\mathrm{Re})_{v,i} = 24(1 - 1.3553C_i + 1.9467C_i^2 - 1.7012C_i^3 + 0.9564C_i^4 - 0.2537C_i^5) \qquad (2.148)$$

where $C_2 = 0.5(t_{g2} - t_{\mathrm{pen}})/W_2$ and the Reynolds number is based on the hydraulic diameter.

$\Delta p_{v,3}$ is the pressure drop in the flat vapor channel in the adiabatic and condenser sections where the vapor flows along the z-coordinate (Figs. 2.30 and 2.31).

$$L_{\text{eff},3} = L_a + L_c/2, \qquad A_{v,3} = L_p(t_{g2} - t_{\text{pen}}),$$

$$D_{h,v,3} = \frac{2L_p(t_{g2} - t_{\text{pen}})}{L_p + (t_{g2} - t_{\text{pen}})}, \qquad N_{v,3} = 1,$$

and $(f\text{Re})_{v,3}$ is also defined from equation (2.148) where $C_3 = (t_{g2} - t_{\text{pen}})/L_p$.

For turbulent flow in a channel when

$$\text{Re}_{v,i} = \frac{QD_{h,v,i}}{N_{v,i}h_{fg}\rho_v A_{v,i}\nu_v} > 2300 \qquad (2.149)$$

the following expression is used for $(f\text{Re})_{v,i}$:

$$(f\text{Re})_{v,i} = 0.079\text{Re}_{v,i}^{0.75} \qquad (2.150)$$

The pressure drop during the co-current flow of the liquid in the liquid channels and porous plate, Δp_ℓ, can be estimated as shown below. For the liquid flow in a channel

$$\frac{dp_\ell}{dz} = \frac{2(f\text{Re})_\ell \mu_\ell \overline{w}_{\ell,ch}}{D_{h,\ell}^2} \qquad (2.151)$$

For these channels

$$L_{\text{eff},\ell} = L_a + (L_e + L_c)/2, \qquad A_\ell = 2W_1 t_{g1},$$

$$D_{h,\ell} = \frac{4W_1 t_{g1}}{2W_1 + t_{g1}}, \qquad N_\ell = 0.5L_p/(W_1 + L_1),$$

and $(f\text{Re})_\ell$ is defined from equation (2.148) where $C_\ell = 2W_1/t_{g1}$. For the liquid flow in the porous plate

$$\frac{dp_\ell}{dz} = \frac{\mu_\ell \overline{w}_{\ell,p}}{K} \qquad (2.152)$$

For any point on z in the adiabatic section the liquid pressure gradients along the z-coordinate in the porous plate and in the liquid channel (equations (2.151) and (2.152)) are equal, and they can be assumed to be approximately equal along the entire effective heat pipe length. In a steady-state situation, conservation of mass across any cross section of the heat pipe requires:

$$\frac{Q}{N_\ell h_{fg}} = \rho_\ell[2\overline{w}_{\ell,ch}W_1 t_{g1} + 2\overline{w}_{\ell,p}t_p(W_1 + L_1)] \qquad (2.153)$$

From equations (2.152) and (2.153) it follows that

$$\overline{w}_{\ell,ch} = \frac{Q}{2N_\ell h_{fg}\rho_\ell W_1 t_{g1}} - \frac{dp_\ell}{dz}\frac{Kt_p(W_1 + L_1)}{\mu_\ell W_1 t_{g1}} \tag{2.154}$$

Then, substituting equation (2.154) into equation (2.151), the liquid pressure gradient during the co-current liquid flow in the channels and porous plate is

$$\frac{dp_\ell}{dz} = \left[1 + \frac{2(f\mathrm{Re})_\ell Kt_p(W_1 + L_1)}{D_{h,\ell}^2 W_1 t_{g1}}\right]^{-1} \frac{Q(f\mathrm{Re})_\ell \mu_\ell}{N_\ell h_{fg}\rho_\ell W_1 t_{g1} D_{h,\ell}^2} \tag{2.155}$$

and the pressure drop in the liquid, with respect to equation (2.155), is

$$\Delta p_\ell = \frac{dp_\ell}{dz}L_{\mathrm{eff},\ell} = \frac{dp_\ell}{dz}\left(L_a + \frac{L_e + L_c}{2}\right) \tag{2.156}$$

Δp_{ft} is the transverse pressure drop due to the filtration of the liquid through the porous plate in the evaporator and condenser sections. Using Darcy's law for this pressure drop we have:

$$\Delta p_{ft,e} = \frac{\mu_\ell Q t_p}{K h_{fg}\rho_\ell L_p L_e}\frac{W_1 + L_1}{W_1} \tag{2.157}$$

$$\Delta p_{ft,c} = \frac{\mu_\ell Q t_p}{K h_{fg}\rho_\ell L_p L_c}\frac{W_1 + L_1}{W_1} \tag{2.158}$$

For the case of operation against the gravity field with an inclination angle ϕ, the so-called "dry" and "wet" points are usually situated at the end caps of the heat pipe (Faghri [1]). Therefore,

$$\Delta p_g = \rho_\ell g(L_e + L_c + L_a)\sin\phi \tag{2.159}$$

The capillary limit, Q_{cap}, is calculated from equations (2.143)–(2.159) and the following condition, which is correct for the case when $R_{\mathrm{men,max}} \to \infty$

$$\Delta p_{\mathrm{cap,max}} = \frac{2\sigma\cos\theta_{\mathrm{men,min}}}{R_p} \tag{2.160}$$

2.6.3 Maximum Heat Transfer Capacity for the Case of High Heat Fluxes

The distinguishing feature of the heat pipe in the consideration is its capability to withstand high heat fluxes on the evaporator wall. For the case of extremely high heat fluxes, a dry zone (vapor blanket) appears in the porous structure along the heated solid surface (Fig. 2.31(b)). The vapor flow in the vapor blanket towards the vapor channel takes place with a corresponding pressure drop, Δp_{vb}. The thickness of the vapor blanket, $\delta_{vb}(\dot{x})$, can be calculated using the methodology by Khrustalev and Faghri [6]. The capillary pressure drop $2\sigma/R_{\mathrm{men,o}}$, supports the fluid circulation in the heat pipe, described in the following section, while the capillary pressure drop

$$\Delta p_{vb} = 2\sigma(\cos\theta_{\mathrm{men,min}}/R_p - 1/R_{\mathrm{men,o}}) \tag{2.161}$$

89

is expended to compensate for the pressure drop in the vapor flow through the dry porous region. $R_{\text{men},o}$ is the radius of the liquid-vapor meniscus at the outlet of the vapor blanket into the vapor channel or, in other words, the driving meniscus radius at the surface of the porous plate in the evaporator. Since this pressure drop, Δp_{vb}, should be also compensated by the capillary pressure, for the case of high heat fluxes in the evaporator, the pressure balance equation (2.143) should be rewritten as follows

$$\Delta p_{v,1} + \Delta p_{v,2} + \Delta p_{v,3} + \Delta p_\ell + \Delta p_{ft,e} + \Delta p_{ft,c} + \Delta p_g = \frac{2\sigma}{R_{\text{men},o}} \qquad (2.162)$$

It should be also noted that in the considered heat pipe, dry out can take place in the evaporator due to the penetration of the vapor into the liquid channels through the porous plate and the consequent obstruction of the fluid circulation. It can happen when the thickness of the vapor blanket at the top of the fin, δ, is approximately equal to the minimum thickness of the porous plate, $t_p - t_{\text{pen}}$. Therefore, in order to determine the effective maximum heat transfer capacity of the heat pipe, Q_{max}, equation (2.162) should be solved for $R_{\text{men},o}$ with different Q simultaneously with the procedure developed by Khrustalev and Faghri [6] to find δ at the top of the solid heated fin. In the steady-state situation, these two problems (axial fluid circulation and formation of the vapor blanket) have to be solved with the same driving meniscus radius, $R_{\text{men},o}$, and with the condition

$$q_{ex} = \frac{Q}{L_e L_p} \qquad (2.163)$$

The largest Q at which these two problems can be solved simultaneously is the effective maximum heat transfer capacity of the heat pipe, Q_{max}. The value of Q_{max} for the given operational conditions (which is less than Q_{cap}) can be restricted by either of the two following conditions:

$$\delta = t_p - t_{\text{pen}} \qquad (2.164)$$

$$\bar{p}_{vb} - p_{\ell\delta} \to 0 \qquad (2.165)$$

The first condition, equation (2.164), corresponds to the penetration of the vapor into the liquid channels. The second condition, equation (2.165), describes the limiting case when the available capillary potential at the end of the vapor blanket is spent entirely on the vapor flow across the vapor blanket, and therefore, the larger heat fluxes cannot be obtained with the same or larger vapor blanket thickness at the fin top, δ. Thus, for the case of the thick porous plate ($t_p - t_{\text{pen}} \gg t_{\text{pen}}$), Q_{max} is also less than Q_{cap} because, although in this case the thickness of the vapor blanket can be comparatively large, the pressure drop across it can also be comparatively large.

Thus the model includes the following interconnected problems which are treated simultaneously in the frames of the numerical analysis.

- Heat transfer during evaporation from a pore.

- Heat transfer and vapor flow in the dry region of a porous structure with a side boundary, the location of which depends on the operational conditions.

- Heat conduction in a solid fin with a non-uniform heat sink on the side surfaces.

Although the vapor leaving the dry zone of the porous structure is superheated, it is convenient to relate the local effective heat transfer coefficient to the vapor saturation temperature because $c_{p,v}(T_w - T_s) \ll h_{fg}$. Thus the local effective heat transfer coefficient corresponding to the point $\dot{x} = L_{vb}$ (outlet of the vapor flow) is defined as:

$$h_{\text{eff,pen}} = \frac{1}{W(T_w - T_v)_o} \int_0^{L_{vb}} k_{\text{eff}} \frac{T_w(\dot{x}) - T_s(\dot{x})}{\delta_{vb}(\dot{x})} \, d\dot{x} \qquad (2.166)$$

In the numerical results of Khrustalev and Faghri [6], the pressure drop in the vapor blanket along the fin surface with turbulent vapor flow in the pores was many times larger than the estimated pressure drop in the liquid over the porous element. That enabled the assumption of the constant liquid pressure along the liquid-vapor boundary.

2.6.4 Numerical Treatment, Results, and Discussion

The numerical results were obtained for the case of the miniature heat pipe, the characteristic dimensions of which are listed in Table 2.3. The working fluid was water, $\theta_{\text{men,min}} = 33°$ (Stepanov et al. [69]), $\alpha = 0.05$ (Paul [22]), $k_{\text{eff}} = 10$ W/(m-K), $k_w = 379$ W/(m-K), $\varphi = 0.35$. The calculations were made with constant thermophysical properties corresponding to the operating temperature, T_v. The superheat of the vapor in the dry zone of the porous structure was neglected. Therefore, the maximum heat transfer capacity of the heat pipe was underestimated because the vapor enthalpy heat transfer, $Q_{v,\text{ent}}$, was not taken into account. The relative error for $q_{ex,\text{max}}$ because of this assumption can be estimated as follows

$$\frac{Q_{v,\text{ent}}}{Q} \approx \frac{c_{p,v}}{h_{fg}} \frac{(T_0 - T_v)}{2} \approx \frac{c_{p,v}}{2h_{fg}} \frac{q_{ex}}{h_{\text{eff},ex}} \qquad (2.167)$$

where T_0 is the temperature of the fin top. This error does not exceed 9% for the presented results.

In order to find the effective maximum heat transfer capacity of the heat pipe, Q_{max}, a graphical method was used as explained below. In the first step, the dependence of the driving meniscus radius on heat load, $R_{\text{men,o}}(Q)$, resulting from equation (2.162) was obtained and plotted for a given operating temperature, T_v. In the second step, another dependence $R_{\text{men,o}}(Q)$, resulting from the solution of the vapor blanket formation for a given thickness of the vapor blanket at the fin top, δ, was obtained and plotted in the same figure. The intersection of these two curves gives the values of Q and $R_{\text{men,o}}(Q)$ which correspond to the steady state with the chosen δ. Repeating this process with different values of δ, the function $\delta(Q)$ was obtained, and the maximum heat transfer capacity, Q_{max}, for the steady state was defined with respect to the conditions (2.164) and (2.165). In Figures 2.32 – 2.34 the values of the maximum heat transfer capacity, Q_{max}, found by this method for different operating temperatures, T_v, are indicated by the ring and square symbols for horizontal and vertical

91

(the evaporator end of the heat pipe is elevated) orientations, respectively. The bullets in these figures correspond to the situations when $\delta = t_p - t_{\text{pen}}$ and $\overline{p}_{vb} - p_{\ell,\delta} \rightarrow 0$ simultaneously, which determines the absolute maximum heat transfer capacity in the evaporator, $Q_{\text{max,abs}}$, which can be reached in some cases as discussed further. For $T_v = 120°C$, $Q_{\text{max}} = Q_{\text{max,abs}} = 116.4$ W for the horizontal orientation and $Q_{\text{max}} = 93$ W for the vertical orientation, as shown in Fig. 2.31(a). For lower operating temperatures the maximum heat transfer capacity is smaller; for example, for $T_v = 90°C$ at the steady state $Q_{\text{max}} = 26$ W for the horizontal orientation, $Q_{\text{max}} = 36$ W for the vertical orientation, and $Q_{\text{max,abs}} = 45$ W, as shown in Fig. 2.32(b). While for the heat input of 45 W at $T_v = 90°C$, a steady state does not exist (within the frames of the considered model), there is no restriction of the heat transfer because of the axial fluid circulation for the heat load lower than 45 W. Therefore, an unstable regime of the heat pipe operation can occur with heat loads from 26 to 45 W for the horizontal orientation and from 36 to 45 for the vertical orientation at $T_v = 90°C$. Physical models of unstable regimes are not obvious yet. Ku [42] referred to the regime when the vapor bubbles (instead of the vapor blanket) form at the heating surface and migrate until vented into vapor channel. Other models of the unstable regimes are also possible. Comparison of Figs. 2.32(b) and 2.32(c) shows that for a decreased permeability of the porous structure Q_{max} is smaller. It can be also seen from Figs. 2.32 and 2.33 that with the growth of the operating temperature Q_{max} increases.

Analyzing Fig. 2.32(a), one can come to the conclusion that the thickness of the vapor blanket at the fin top, δ, increases with the heat load, which should result in the decrease of the effective heat transfer coefficients and lead to larger temperature drops in the evaporator. These trends are presented in Fig. 2.32 for the horizontal orientation. Two characteristic temperature drops are shown in Fig. 2.32(a), both being related to the operating temperature, T_v. The first is measured from the temperature of the external surface of the heat pipe wall, T_{ex}, and the second is the superheat of the solid particles of the porous structure at the liquid-vapor boundary of the vapor blanket over the operating temperature, $T_s - T_v$, at the outlet of the vapor blanket into the vapor channel ($\dot{x} = t_{\text{pen}}/\cos\gamma$). The last temperature drop does not increase with the heat flux on the external surface of the evaporator, q_{ex}, because for larger heat fluxes the radii of the menisci along the vapor blanket are smaller, which results in the increase of the local heat transfer coefficients during the evaporation from the pores. That is why $T_s - T_v < 20°C$ even for the enormously high heat fluxes of 200 W/cm^2, which means that the evaporative regime is predominant at the boundary of the vapor blanket. However, a mixed regime of vaporization at this boundary when both the evaporation and formation of the small vapor bubbles occur can be imagined without changing the entire physical model. The total temperature drop, $T_{ex} - T_v$, consists of several components: those in the metallic wall and fin, across the vapor blanket, and that corresponding to the evaporation from the liquid vapor interface, which can be expressed by the following equation:

$$\frac{T_{ex} - T_v}{q_{ex}} = \frac{t_w}{k_w} + \frac{W_2 + L_2}{L_2}\left[\frac{t_{g2} - t_{g3}}{k_w} + \frac{2L_2}{L_2 + t_{\text{pen}}\tan\gamma}\frac{t_{g3} - t_{\text{pen}}}{k_w} + \frac{1}{h_{\text{eff,pen}}}\frac{W_3}{t_{\text{pen}}\tan\gamma}\right]$$

(2.168)
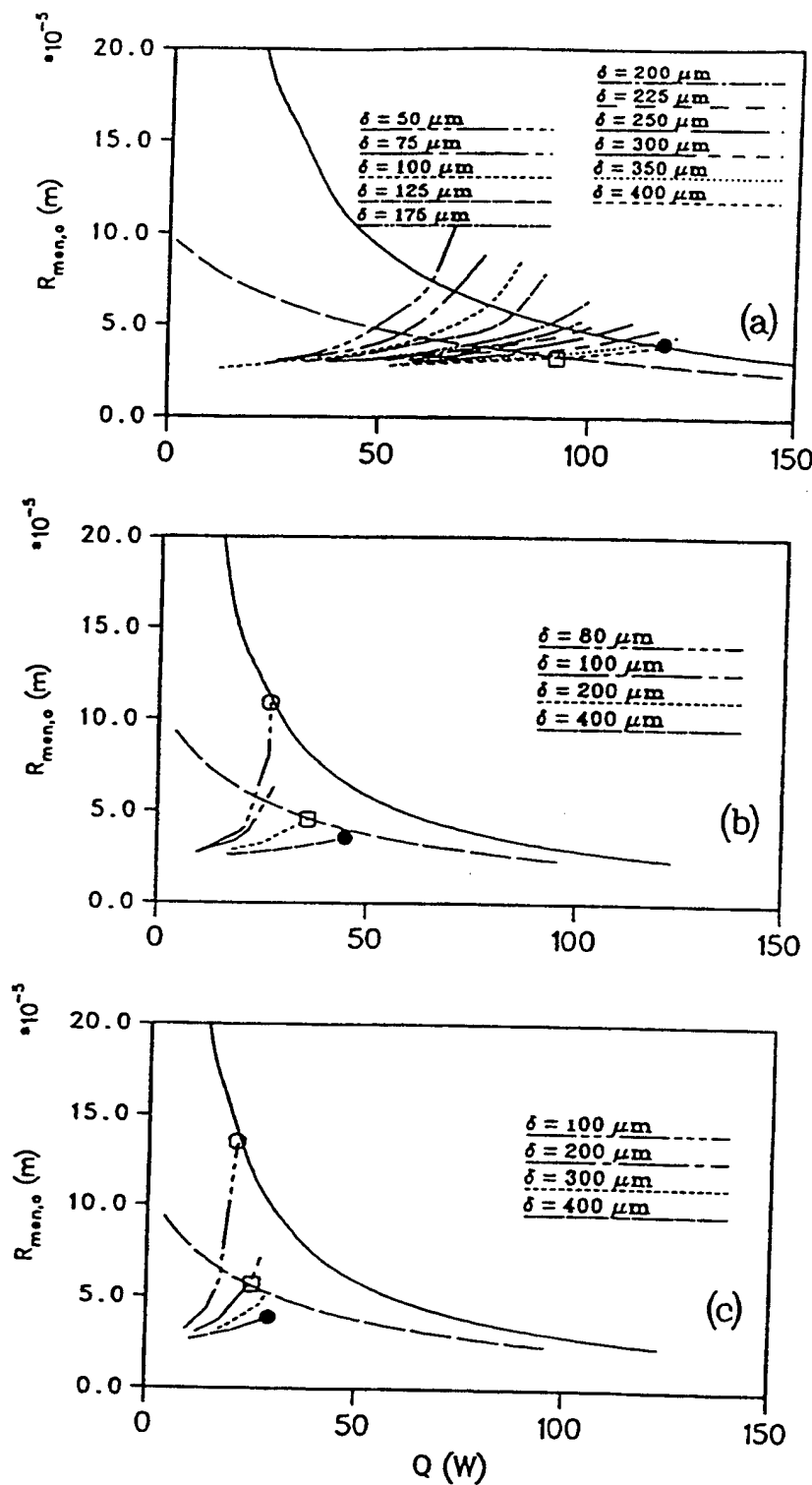
Figure 2.32: Variation of the driving meniscus radius and thickness of the vapor blanket at the fin top with heat input: (a) $T_v = 120°C$, $K = 1.0 \times 10^{-12}$ m^2; (b) $T_v = 90°C$, $K = 1.0 \times 10^{-12}$ m^2; (c) $T_v = 90°C$, $K = 0.5 \times 10^{-12}$ m^2.

93
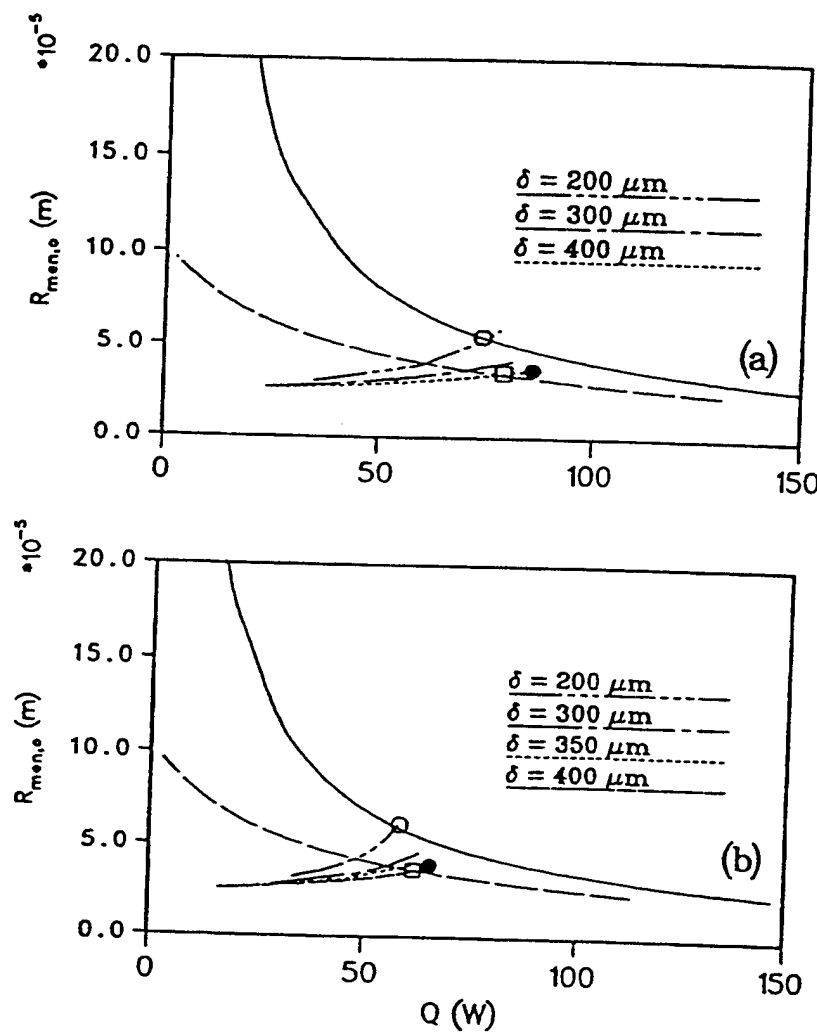
Figure 2.33: Variation of the driving meniscus radius and thickness of the vapor blanket at the fin top with heat input ($K = 1.0 \times 10^{-12}$ m^2): (a) $T_v = 110°C$; (b) $T_v = 100°C$.
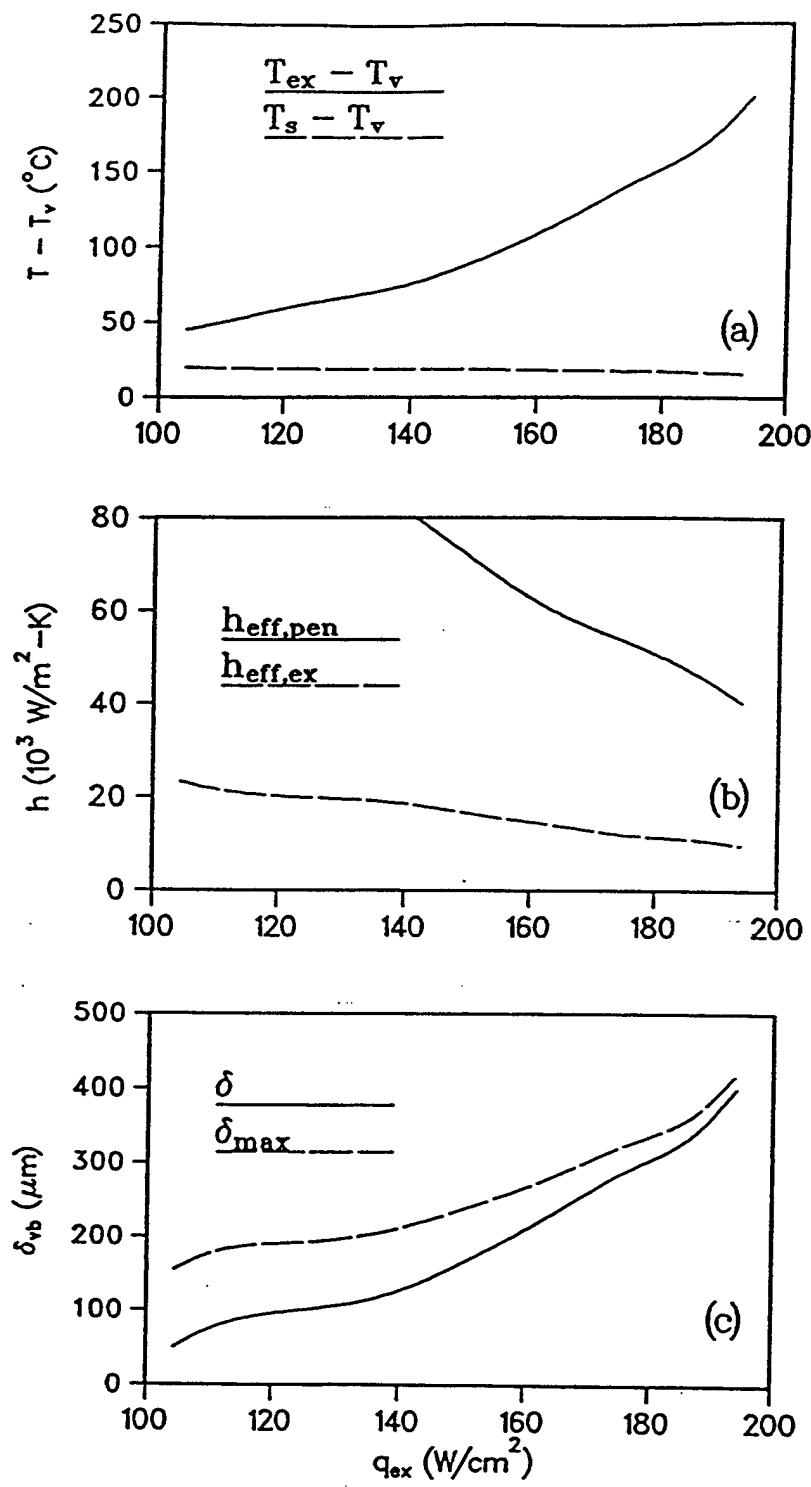
Figure 2.34: Performance characteristics of the heat pipe evaporator ($T_v = 120°C$, $K = 1.0 \times 10^{-12}$ m², horizontal orientation): (a) Temperature drops; (b) Heat transfer coefficients; (c) Vapor blanket thickness.

While the temperature drops in the metallic walls of the heat pipe are comparatively small, it can be seen in Fig. 2.34(a) that the main component of the total temperature drop is that across the dry porous structure zone due to the heat conduction from the fin surface to the liquid-vapor interface. The total temperature drop increases progressively with the heat flux and reaches almost 200°C when q_{ex} approaches 200 W/cm². This happens because the thickness of the vapor blanket, δ_{vb}, increases and the effective heat transfer coefficients, $h_{eff,pen}$ and $h_{eff,ex}$, decrease with the heat flux as shown in Figs. 2.34(b) and 33(c). Therefore, the thermal conductivity of the porous structure plays an important role in the heat transfer in the evaporator. $h_{eff,pen}$ is the effective heat transfer coefficient concerning only the part of the fin penetrating the porous structure (equation (2.166)), and $h_{eff,ex}$ is the total effective heat transfer coefficient defined as follows.

$$h_{\text{eff,ex}} = \frac{q_{ex}}{T_{ex} - T_v} \qquad (2.169)$$

Two curves in Fig. 2.34(c) correspond to the minimum and maximum thicknesses of the vapor blanket at the fin top and at the vapor blanket outlet into the vapor channel, respectively. It follows from this figure that when the vapor blanket is comparatively thick, it is almost uniform along the heated surface.

From Figs.2.32 and 2.33, the dependencies of the maximum heat flux, which can be reached on the evaporator wall, on the operating temperature result for the cases of horizontal and vertical orientations, Fig. 2.35. The maximum heat fluxes, predicted by the model accounting for the vapor blanket formation in the porous structure, are much smaller than those obtained from the traditional capillary limit calculations. The zone situated between the two lower curves in Fig. 2.35(a) supposedly corresponds to the unstable regime of the heat pipe operation. However, for the temperatures higher than 120°C only the stable regime takes place for all values of the heat flux which can be as high as 200 W/cm². For operating temperatures lower than 100°C the maximum heat flux does not exceed 100 W/cm². Figure 2.35(b) indicates that the heat pipe can successfully operate against the gravity field.

2.6.5   Conclusions

The results of the numerical modeling of the miniature copper-water heat pipe with the inverted meniscus type evaporator are summarized as follows:

1. At high heat fluxes part of the available capillary potential is expended on the compensation of the pressure drop in the vapor flow through the dry region of the porous structure in the evaporator. As a result of this, the dry out of the inverted meniscus type evaporator of the heat pipe occurs with the maximum heat flux on the evaporator wall which is about two times smaller than that corresponding to the traditionally calculated capillary limit.

2. The proposed heat pipe configuration with the external dimensions 2 × 7 × 120 mm is capable of withstanding high heat fluxes on the evaporator wall which can be about 200 W/cm² for the horizontal orientation and 150 W/cm² for the vertical orientation at the operating temperature of 120°C.
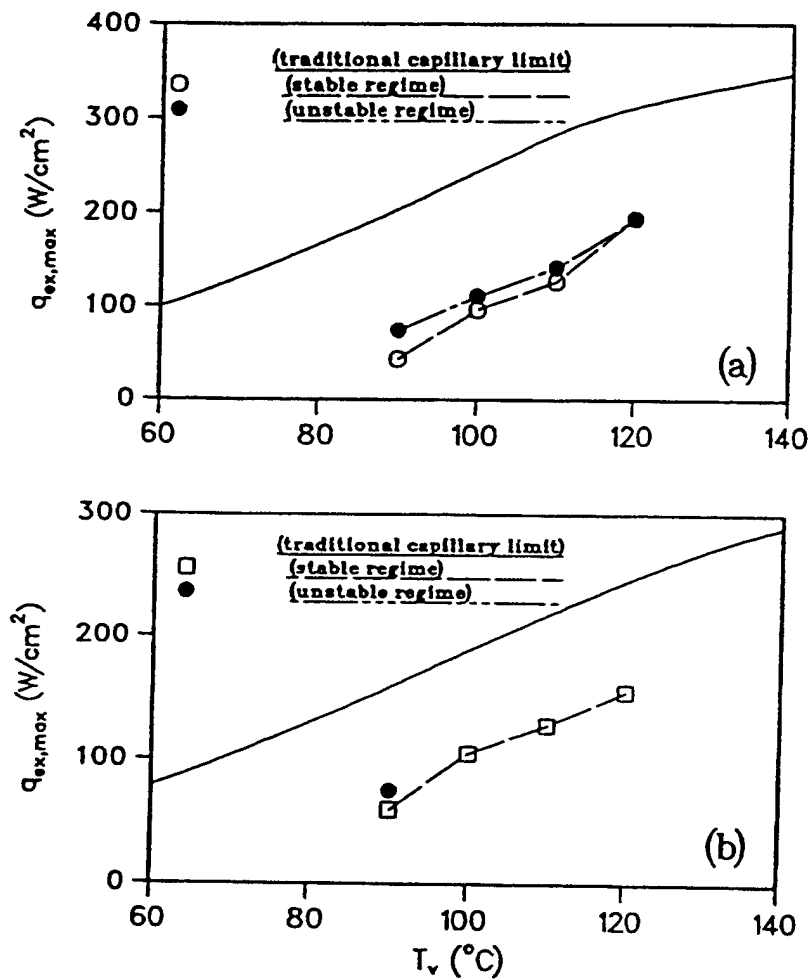
Figure 2.35: Dependence of the maximum heat flux in the heat pipe evaporator on the operating temperature ($K = 1.0 \times 10^{-12}$ m^2): (a) Horizontal orientation; (b) Vertical orientation.

97

3. The unstable operating regime can possibly occur in the heat pipe with heat fluxes on the evaporator wall which are close to the maximum, especially for the operating temperatures lower than 100°C.

4. The effective evaporative heat transfer coefficient decreases with the heat flux on the evaporator external wall because of the growth of the vapor blanket thickness inside the porous structure.

5. With high heat fluxes, the temperature drop of the heat pipe evaporator can be critical for the heat pipe applications. The main component of the temperature drop in the evaporator is that across the vapor blanket due to the heat conduction from the heated solid surface to the liquid-vapor interface. Therefore, it is reasonable to choose the porous structure with high thermal conductivity, permeability, and capillary potential.

Chapter 3

EXPERIMENTAL TESTING OF FLAT MINIATURE HEAT PIPES

3.1 Axially Grooved Heat Pipes

Flat miniature heat pipes are an emerging technology in the cooling of high heat flux electronic devices such as computer chips and thyristors. Jacobs and Hartnett [62] predicted that chip heat fluxes in mainframe computers will exceed 100 W/cm^2 by the year 2000. Cao et al. [46] noted that heat fluxes generated by metal oxide semiconductor controlled thyristors are already in the range of 100 W/cm^2 to 300 W/cm^2. North and Avedisian [47] also investigated heat pipes for cooling high flux/power semiconductors or chips. Many other miniature heat pipe applications exist such as cooling of very thin leading edges of turbine stator vanes and bio-engineering reactors used in the separation of biological material. Industrial applications of FMHP's are restricted due to several heat pipe performance limitations (Cao and Faghri, [44]; Faghri,[1]). Most critical of these is the capillary limitation which is the limit of the pumping ability of the capillary structure to provide enough liquid return to the evaporator and is characterized by an increase in the maximum heat flow rate with operating temperature. Boiling limitation can also occur for high-heat-flux applications in which boiling of the working fluid in the wick may form a vapor blanket on the evaporator inner surface and prevent it from being rewetted with returning liquid flow. Boiling limitation usually occurs at elevated operating temperatures and is characterized by a decrease in maximum heat flow rate with an increase in operating temperature (as discussed in section 2.3 and also Khrustalev and Faghri, [65]). Consideration of the heat flux restrictions should be made based on FMHP experimental data and corresponding theoretical predictions.

Plesch et al. [2] performed a limited investigation of copper-water heat pipes with overall dimensions of 7mm × 2mm × 120 mm with a series of 80 axial rectangular capillary grooves (0.12 mm wide and 0.24 mm deep) machined on the inner surface. Power was uniformly applied to both wide evaporator walls over a surface area of 2 cm^2 and removed at the condenser by a constant temperature (42°C) coolant flow. A maximum heat flux was found of 35 W/cm^2 in the horizontal orientation and 60 W/cm^2 in the vertical orientation where the condenser was above the evaporator.

Cao et al. [46] tested a 82 mm long copper-water miniature heat pipe with overall

dimensions similar to the Plesch et al [2] heat pipe. The capillary structure consisted of a series of axial rectangular grooves (0.1 mm wide by 0.25 mm deep) along the entire inner perimeter of the heat pipe and the vapor passage cross sectional area was approximately 4 mm². Maximum heat flux obtained was restricted by the capillary limit and reached 18.3 W/cm² with a positive inclination angle of 20°.

Section 2.3 and also Khrustalev and Faghri [65] developed a one-dimensional model describing the fluid flow and heat and mass transfer in a miniature axial rectangular grooved heat pipe to predict the maximum heat transfer restricted by both capillary limitation and incipience of nucleate boiling. Their model showed reasonably good agreement with limited experimental data of Plesch et al. [2], however, the existing experimental data were not sufficient for a more profound understanding of FMHP performance limitations. Therefore, it was the objective of this investigation to extensively manufacture, experimentally investigate and theoretically model a variety of flat miniature heat pipes. In particular the experimental investigation mainly sought out the maximum heat flow rates and heat fluxes that could be applied uniformly to the evaporator wall for a range of operating temperatures, orientations and heating configurations. A predictive model was developed to predict the capillary limitation of all investigated flat miniature heat pipes while a closed form solution of the predictive model was also included for the limiting case of axial rectangular grooved flat miniature heat pipes.

3.1.1 Experimental Investigation

Steady-state performance characteristics of three individual copper-water FMHP's have been experimentally investigated for horizontal and vertical orientations using similar experimental techniques and assumptions discussed in Faghri [1]. The detailed experimental investigation determined the maximum heat flow rates and heat fluxes that can be applied to the evaporator wall for a range of operating temperatures and heating configurations.

Geometrical parameters of the three experimental copper-water FMHP's are given in Figure 3.1 for their respective cross sections. Other relevant specifications of all the flat miniature heat pipes such as section lengths and working fluid amounts are given in Table 3.1. The capillary structures of two of the flat miniature heat pipes (FMHP's #1 and #2) are micro trapezoidal capillary grooves that were at a slight angle to the longitudinal axis of the heat pipe (see Table 3.1) while FMHP#3 contained rectangular axial grooves.

Copper-water FMHP's #1 and #2, where the cross-sectional geometry is shown by Figures 3.1(a) and 3.1(b) respectively, were manufactured with trapezoidal micro capillary grooves at a slight angle to the heat pipes longitudinal axis. The capillary groove structure of FMHP's #1 and #2 were manufactured by a rolling method and charged with working fluid by a conventional boiling off method. FMHP#1 and FMHP#2 were respectively manufactured by the Furukawa Electric Company and Fujikura Ltd. with quoted liquid fill amounts of 0.20 ml and 20% of interior volume. All other relevant geometric parameters of FMHP#1 and FMHP#2 are provided in Table 3.1.

Copper-water FMHP#3 was manufactured at The University of Connecticut with an axial and rectangular micro capillary groove structure (0.2 mm wide by 0.42 mm deep). Manufacturing of FMHP#3 began with the capillary grooves being machined by a high

100

Table 3.1: Flat miniature heat pipe experimental configurations

	FMHP#1	FMHP#2	FMHP#3
Groove Depth (mm)	0.24	0.20	0.42
Groove Top Width (mm)	0.20	0.45	0.20
Groove Bottom Width (mm)	0.15	0.30	0.20
Fin Top Width (mm)	0.16	0.20	0.10
Total Number of Grooves	52	50	62
Angle Between Grooves and Heat Pipe Axis	4	18	0
Liquid Fill	0.20 ml	20% of volume	0.84 ml
Evaporator Length (mm)	15.6	9.6	15.6
Adiabatic Length (mm)	70.0	56.0	70.0
Condenser Length (mm)	34.4	34.4	34.4
Evaporator Thermocouple Locations (mm)	(3 TC's) 1, 7.8, 14.6	(2 TC's) 2.0, 10	(3 TC's) 4.5, 7.3, 10.1
Adiabatic Thermocouple Locations (mm)	(2 TC's) 36.6, 64.6	(2 TC's) 29.0, 48.0	(2 TC's) 37.9, 61.2
Condenser Thermocouple Locations (mm)	(3 TC's) 86.6, 102.13, 119.0	(2 TC's) 67.0, 99.0	(3 TC's) 84.6, 101.8, 119.0
Thermocouple Mounting Method	Clamped to heated side or soldered to thin side	clamped to heated side	Embedded at corner

(a) FMHP#1, β = 4°

(b) FMHP#2, β = 18°
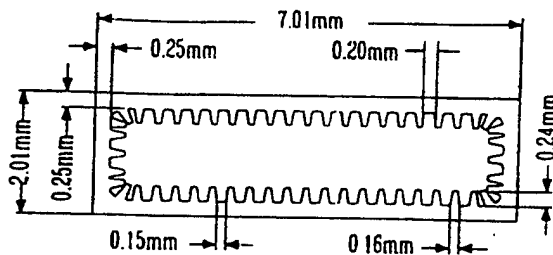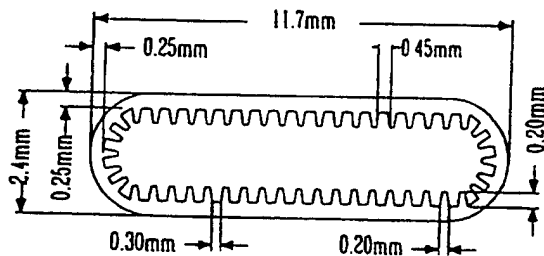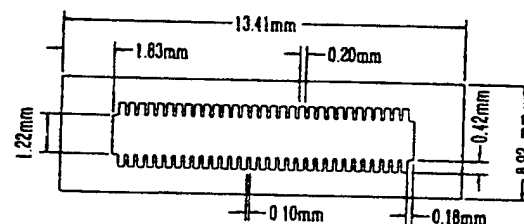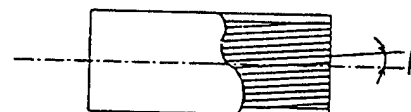
(c) FMHP#3, β = 0°

(d) top view

Figure 3.1: Schematic cross sections of experimental FMHP's: (a) FMHP#1, (b) FMHP#2, (c) FMHP#3, (d) angle between groove axis and heat pipe centerline.

102

speed dicing saw employing a circular carbon steel blade with high diamond content. The heat pipe body was manufactured in two symmetric halves by this procedure and joined together by a low temperature silver solder. Outer rectangular dimensions of FMHP#3 were relatively large at 8.92 mm x 13.41 mm with a length of 120.65 mm and a wall thickness of 1.83 to 3.43 mm. FMHP#3 was charged with 0.84 ml of water (not including liquid in the filling tubes) which was determined by the weighting method after the investigation was completed. It should be noted that the total volume of the axial grooves was approximately 0.63 ml and therefore some surplus liquid existed in the heat pipe. Slight overfill of FMHP#3 was unavoidable since introduction of a determined exact amount is difficult on these small scales. Sufficient fill criteria for FMHP#3 was therefore defined as the fill ratio that produced a sufficiently small temperature drop in the condenser during normal heat pipe operation which signified that the condenser was not blocked with excess liquid.

3.1.2 Experimental setup

A simple but effective experimental setup was employed for the investigation of flat miniature heat pipes as shown for the case of FMHP#1 in Figure 3.2. Slight physical modifications were made for the investigation of the other two heat pipes and are shown in Table 3.1 which provides a detailed list of the physical attributes of the individual miniature heat pipes. The heat pipe testing apparatus was mounted to a rigid flat stainless steel base plate that contained threaded legs set in each corner which allowed for precise horizontal adjustment of the rigid base plate and flat miniature heat pipes. Nine precisely machined teflon blocks (0.05mm) encased the FMHP's which were configured and designed to provide three functions that included a level base support, insulation for the heat pipe and, in some special cases, a clamping device for the thermocouple-heat pipe contact. A shallow groove was machined along the length of the bottom blocks in order to hold and align the miniature heat pipes in a flat orientation parallel to the rigid baseplate. Six Type "T" copper-constantan (36 gage) thermocouples were soldered to the narrow side surface of FMHP#1 while two thermocouples were also clamped to the wide wall in the adiabatic section as shown in Figure 3.2. Heat was applied to the evaporator by two thick film resistors placed on either wide side of the heat pipe. Each resistor had an effective heating area of 0.7 cm^2 and was held in place at the evaporator by a simple teflon clamp. Contact resistance at the resistor-wall interface was reduced by applying an Omegatherm 101 high thermal conductive paste. The resistors were wired in parallel (when both resistors were powered) and powered by a 0-140 volt variable ac transformer. A pair of Keithley 197A multimeters were used to determine and record the power supplied to the resistors. The first multimeter was used to measure voltage across the resistors and had an accuracy of 0.006% of true voltage while the second measured the ac current and had an accuracy of 0.8% of true ac current. Actual power input to the heat pipe was adjusted by subtracting experimentally determined heat losses to the environment. This power adjustment was carried out by applying a series of small heat loads to the evaporator of the heat pipe, with cold plates removed and condenser insulated, and determining the average steady state adiabatic temperature. Heat losses to the environment of a functional heat pipe were then closely approximated (less than 1%) by subtracting the small heat load applied from the

experimental maximum heat load results for the corresponding operating temperature. Heat was removed by copper cold plates clamped by teflon elements to both wide sides of the heat pipes condenser section as shown in Figure 3.2 through the cold plates from a Lauda RM-20S constant temperature refrigerator/circulator which was adjusted for every evaporator power setting in order to maintain a constant temperature in the adiabatic section of the heat pipe. Thermocouples were connected to a Fluke 2285B datalogger and were calibrated against the Lauda RM-20S constant temperature liquid bath to an accuracy of 0.3°C. FMHP#2 differed from FMHP#1 in that it was outfitted with six Type "T" thermocouples clamped to the outer wide surface instead of soldered to the thin side walls. This technique was considered valid after repeatability data were taken with FMHP#1 with thermocouples soldered or clamped. The temperatures recorded along FMHP#1 were very similar (0.2°C) for both methods and therefore confidence was gained that the correct temperatures were obtained using either technique. FMHP#3 was fitted with eight thermocouples: three thermocouples were placed in the evaporator, two in the adiabatic and three in the condenser section. These thermocouples were mounted differently to take advantage of the thick walls by embedding the thermocouples in the copper at one corner of the outer rectangular body. Evaporator temperature, for all three FMHP's, was taken to be the temperature monitored by the first thermocouple at the evaporator end as shown in Figure 3.2. The flat miniature heat pipe operating temperature was taken to be the average temperature of the thermocouple readings in the adiabatic zone. Additional thermocouples in the evaporator and condenser sections were used to complete the observation of the temperature distribution along the heat pipe axis.

3.1.3 Experimental Procedure

Experimental investigation of the flat miniature heat pipes was accomplished to find the maximum heat load that could be applied to the evaporator section at operating temperatures of $60°$, $70°$, $80°$, $90°$ and $95°C$. The maximum heat load was found for the cases where the heat load was applied to both wide sides or to a single wide side in both the horizontal (wide or thin) and vertical orientations. In the process the temperature distribution of the heat pipe along the longitudinal axis was observed and recorded. All experimental data were obtained with a systematic and consistent methodology that is as follows. First, the flat miniature heat pipe was positioned in the proper orientation and a small heat load was applied to the evaporator section by use of the thick film resistors. Secondly, the heat pipe operating temperature, defined as the average adiabatic temperature, was obtained and maintained by adjusting the liquid coolant flow temperature to the copper cold plates. Once the operating temperature was obtained, the system was allowed to reach steady state over 15-20 minutes. After steady state was reached, temperature readings at all thermocouples were recorded and power to the evaporator was increased by a small increment. This cycle was repeated until dryout of the heat pipe evaporator was observed which was characterized by a sudden and steady rise of the evaporator temperature. To verify that the experimental results were reliable, a significant portion of all experimental points for the heat pipes maximum heat transport capabilities were repeated with negligible difference.
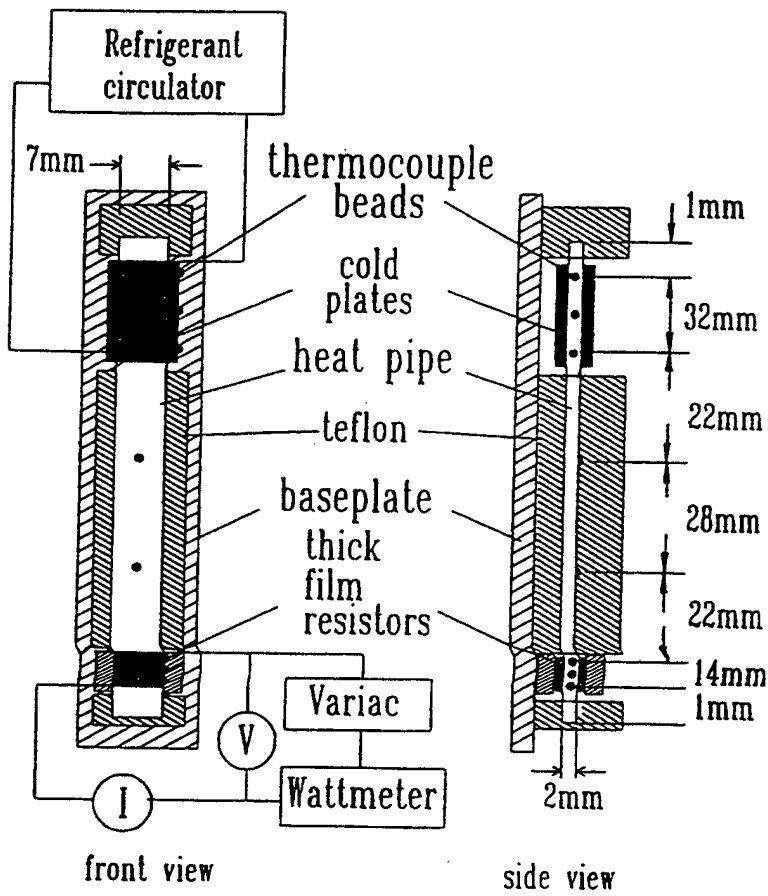
Figure 3.2: Schematic of flat miniature heat pipe test apparatus (shown here for FMHP#1).

3.1.4 Capillary Limit Analysis

A one-dimensional model describing the fluid flow in a miniature grooved heat pipe has been used to predict the maximum heat transfer restricted by capillary limitation. The present model of fluid circulation in a flat miniature heat pipe differs from the axial rectangular grooved heat pipe model of section 2.3 and Khrustalev and Faghri [65] by the following main features:

1. The recession of the liquid-vapor meniscus interface to the groove bottom along the liquid flow in a trapezoidal groove is described by the model.

2. The effective groove length for the liquid flow depends on the angle between the groove structure and the heat pipe axis.

3. A closed form solution has been included for the limiting case of axial rectangular grooves

Accordingly, the following improvements distinguish this model from that of section 2.3 and Khrustalev and Faghri [65]. The first improvement over Khrustalev and Faghri [65] is that the liquid momentum conservation equation is modified to account for the longer return path of angled grooves compared to axial grooves by introducing $\cos\alpha$ as follows.

$$\frac{d}{dz}\left(p_l + \rho g z \sin\phi\right) = \frac{f_l}{\cos\alpha}\frac{2\rho_l \bar{w}_l^2}{D_{h,l}} \tag{3.1}$$

It is assumed in Eq. 3.1 that all axial mass transport of the liquid occurs in the grooves and is a quasi one- dimensional viscous flow. The $\cos\alpha$ term was also introduced in the expression for liquid friction factor-Reynolds number product since there was an angle between the directions of the liquid and vapor flows

$$(fR_e)_l = (fR_e)_{l,o}\left\{1 + \cos\alpha\frac{4NW^3}{3\pi D_{h,v}}(fR_e)_v\frac{v_v}{v_l}\left[1 - 1.971\exp\left(-\frac{\pi t_g}{2W}\right)\right]\right\} \tag{3.2}$$

where t_g and W are the equivalent rectangular groove depth and half-width of the trapezoidal grooves, as shown in Figure 3.3, and $(fR_e)_{lo}$ corresponds to the case of no liquid-vapor interaction (as in section 2.3 and also Schneider and DeVos, [34], and Khrustalev and Faghri, [65]). Other governing equations used in this capillary limitation analysis of flat miniature heat pipes are the mass conservation, conservation of vapor momentum, mass and energy balance and the Laplace-Young equation which describes the interfacial radius of the meniscus curvature related to the liquid-vapor pressure difference. These governing equations are respectively listed as Eqs. 3.3 through 3.6 and are discussed in detail along with boundary conditions and numerical procedure in section 2.3 as well as Khrustalev and Faghri [65] and Hopkins [48].

$$\bar{w}_v \rho_v A_v = N\bar{w}_l \rho_v A_l \equiv N\dot{m}_l \tag{3.3}$$

$$\frac{d}{dz}\left(p_v + \rho_v g z \sin\phi + \rho_v \beta_v \bar{w}_v^2\right) = -f_v\frac{2\rho_v \bar{w}_v^2}{D_{h,v}} \tag{3.4}$$
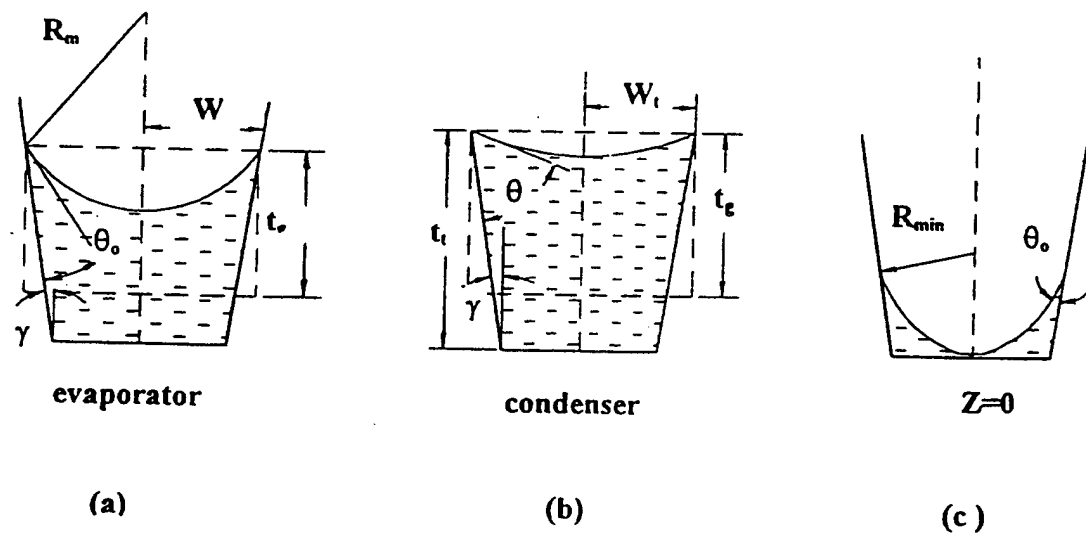
Figure 3.3: Schematic depicting the geometric configuration used in the capillary limitation analysis (a) liquid-vapor meniscus in Region I, (b) liquid-vapor meniscus in Region II, (c) liquid-vapor meniscus at evaporator end cap.

107

$$\frac{d}{dz}\left(\rho_l \bar{w}_l A_l\right) = \frac{1}{h_{fg}N}\frac{dQ\left(z\right)}{dz} \tag{3.5}$$

$$\frac{dp_l}{dz} = \frac{dp_v}{dz} - \frac{d}{dz}\left(\frac{\sigma}{R_m}\right) \tag{3.6}$$

The solution of Eqs. 3.1 through 3.6, along with others presented in section 2.3 and Khrustalev and Faghri [65] and Hopkins [48], provides the longitudinal distribution of the meniscus radius $R_m(z)$ and hence the meniscus contact angle $\theta_{men}\left(z\right)$, which are related for contact angles of $\theta_{men} \geq \theta_o$ (θ_o is the minimum contact angle for the working fluid-solid wall interface) by

$$\theta_{\text{men}}\left(z\right) = \arccos\left[\frac{W}{R_m\left(z\right)}\right] - \gamma \tag{3.7}$$

where θ_{men} is the half angle of the groove as shown in Figure 3.3. The second major improvement over the model of section 2.3 and Khrustalev and Faghri [65] for rectangular grooves, is that there are two intervals of the liquid-vapor meniscus variation along the heat pipe axis with trapezoidal grooves which are shown in Figures 3.3(a) and 3.3(b). Along the first interval, beginning at the evaporator end cap, the meniscus contact angle is constant and at the minimum, $\theta_{\text{men}} = \theta_0$, while the meniscus radius varies. In this interval, the meniscus is not attached to the top of the fins and is instead recessed into the groove structure along the z axis. Along the second interval, usually situated in the condenser zone and the majority of the adiabatic region, the meniscus contact angle, θ_{men}, is larger than θ_o and varies along the z axis. Along this interval, the meniscus is attached to the fin top as the condensation process proceeds. For both intervals, the equivalent height of the liquid cross section varies along the liquid flow.

The minimum radius of the liquid-vapor meniscus, shown in Figure 3.3(c) as $R_{m,\text{min}}$, that can occur along the heat pipe axis (usually at the evaporator end cap) is obtained from the condition that the liquid-vapor interface touches the groove bottom which is geometrically determined as follows

$$R_{m,\text{min}} = \frac{W_t t_t \tan\gamma}{\cos\left(\gamma + \theta_o\right) - \tan\gamma\left[1 - \sin\left(\gamma - \theta\right)\right]} \tag{3.8}$$

$R_{m,\text{min}}$, along with other conditions and geometric expressions of the liquid and vapor channels cross-sectional areas and hydraulic diameters which are fully presented in Hopkins [48]

3.1.5 Closed form solution for the case of axial ($\alpha=0$) rectangular grooves

For axial rectangular grooves, the system of four ordinary differential equations can be reduced to a single algebraic formula to predict the maximum heat transport capacity, Q_{max}. This reduction can be made based on the following additional simplifying assumptions:

1. There is no first interval in the capillary groove structure. In other words, the meniscus is attached to the top of the fin structure along the full heat pipe axis.

108

2. The liquid cross-sectional area can be considered constant along the grooves in all expressions.

3. Inertial forces are neglected in the vapor momentum.

4. The length of the fluid circulation path with varying mass flow rate can be substituted by the effective length, L_{eff}, with a constant mass flowrate.

$$L_{\text{eff}} = \frac{1}{Q_a} \int_o^{L_t} Q(z)\, dz \qquad (3.9)$$

For uniform heat fluxes in the evaporator and condenser sections the effective length is given as the following

$$L_{\text{eff}} = \frac{L_e}{2} + L_a + \frac{L_c}{2} \qquad (3.10)$$

Introducing the liquid and vapor conservation of momentum equations (Eqs. 3.1 and 3.4) and the energy and mass balance equation (Eq. 3.5) into the Laplace-Young expression (Eq.3.6) and integrating along the effective length, L_{eff}, the following expression for maximum heat transfer in axial rectangular grooved heat pipes can be found

$$Q_{\max} = h_{fg} \left[\frac{\sigma \cos \theta_o}{W L_{eff}} + (\rho_l - \rho_v) g \sin \gamma \right] \times \left[(fR_e)_v \frac{2\mu_v}{D_{h,v}^2 \rho_v A_v} + (fR_e)_l \frac{2\mu_l}{D_{h,l}^2 \rho_l N A_l} \right] \qquad (3.11)$$

This closed-form solution is very convenient in the estimation of the maximum heat transport capabilities of axial rectangular grooved flat miniature heat pipes.

3.1.6 Results

Figure 3.4 shows the experimentally determined temperatures in the adiabatic section and at the evaporator and condenser end caps of FMHP#3 in horizontal and vertical orientations. The temperature distribution trends of FMHP#1 and FMHP#2 are very similar to FMHP#3 and are not shown here. However, the thermal resistance values discussed below and shown in Figure 3.5 allows for easy computation of the approximate temperature drop from evaporator to condenser end cap. It is noted that the temperatures were averaged over thirty readings taken over five minutes to avoid possible errors due to minor temperature fluctuations in the experiment. The temperature distributions shown in Figure 3.4 show that the evaporator thermal resistance of FMHP#3 was higher in the vertical orientation while in the horizontal orientation the thermal resistance was higher in the condenser. The higher evaporator thermal resistance in the vertical orientation can be explained by flooding of the evaporator with excess liquid due to gravity. At the heat load of 100 W, FMHP#3 had the total temperature drop from end to end of only 25°C in the horizontal wide orientation.

The effective end cap to end cap thermal resistance of the three FMHP's are shown in Figure 3.5 for various orientations where the heat load is applied to both sides. Effective end cap to end cap thermal resistance, R, is defined here as the overall end cap to end cap temperature drop divided by the total applied heat load, Q_a

109
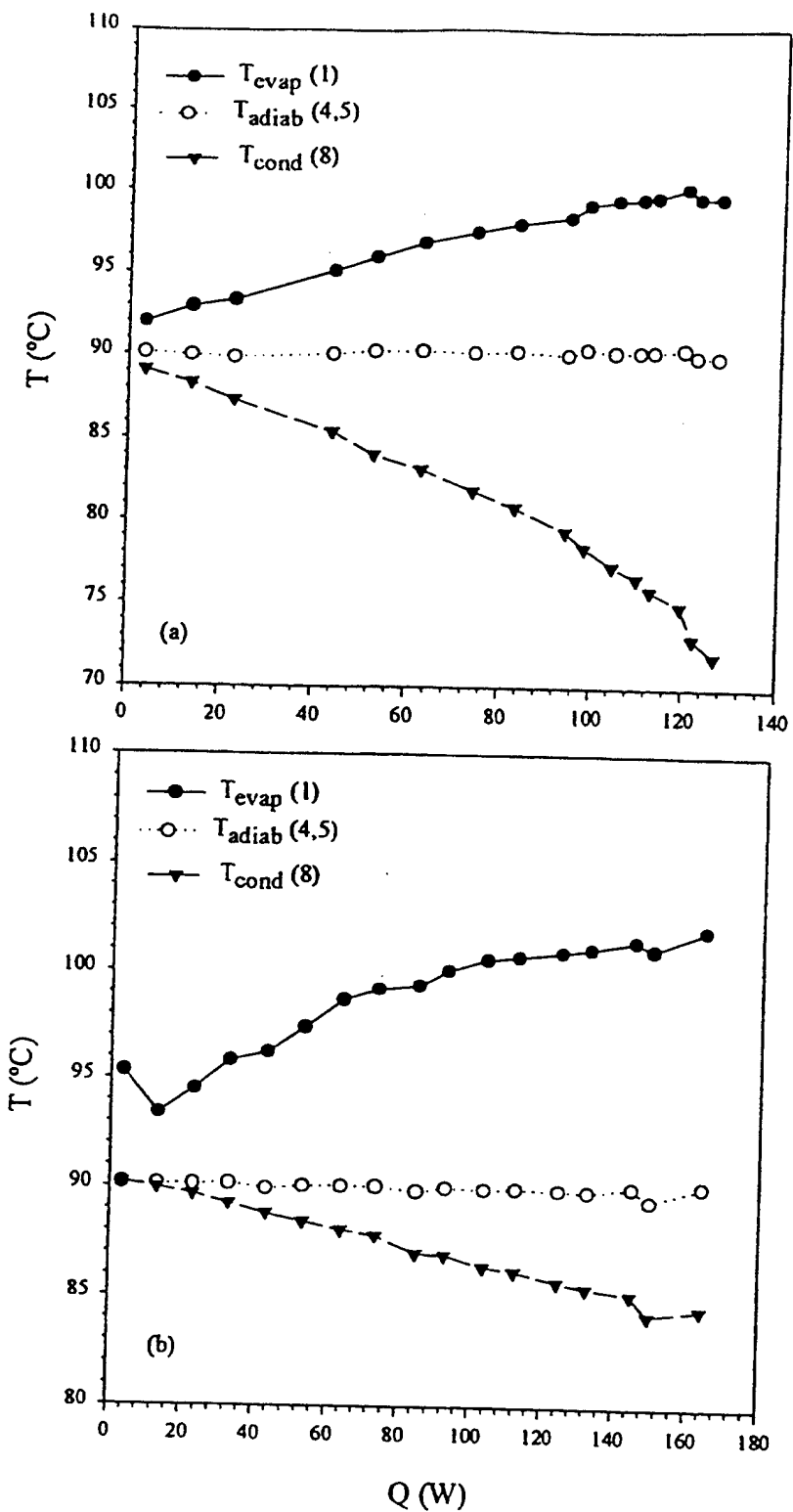
Figure 3.4: Temperature distribution along the outer surface of FMHP#3 versus total heat load applied from both sides in (a) horizontal wide at $T_v=90C$; (b) vertical at $T_v=90C$.
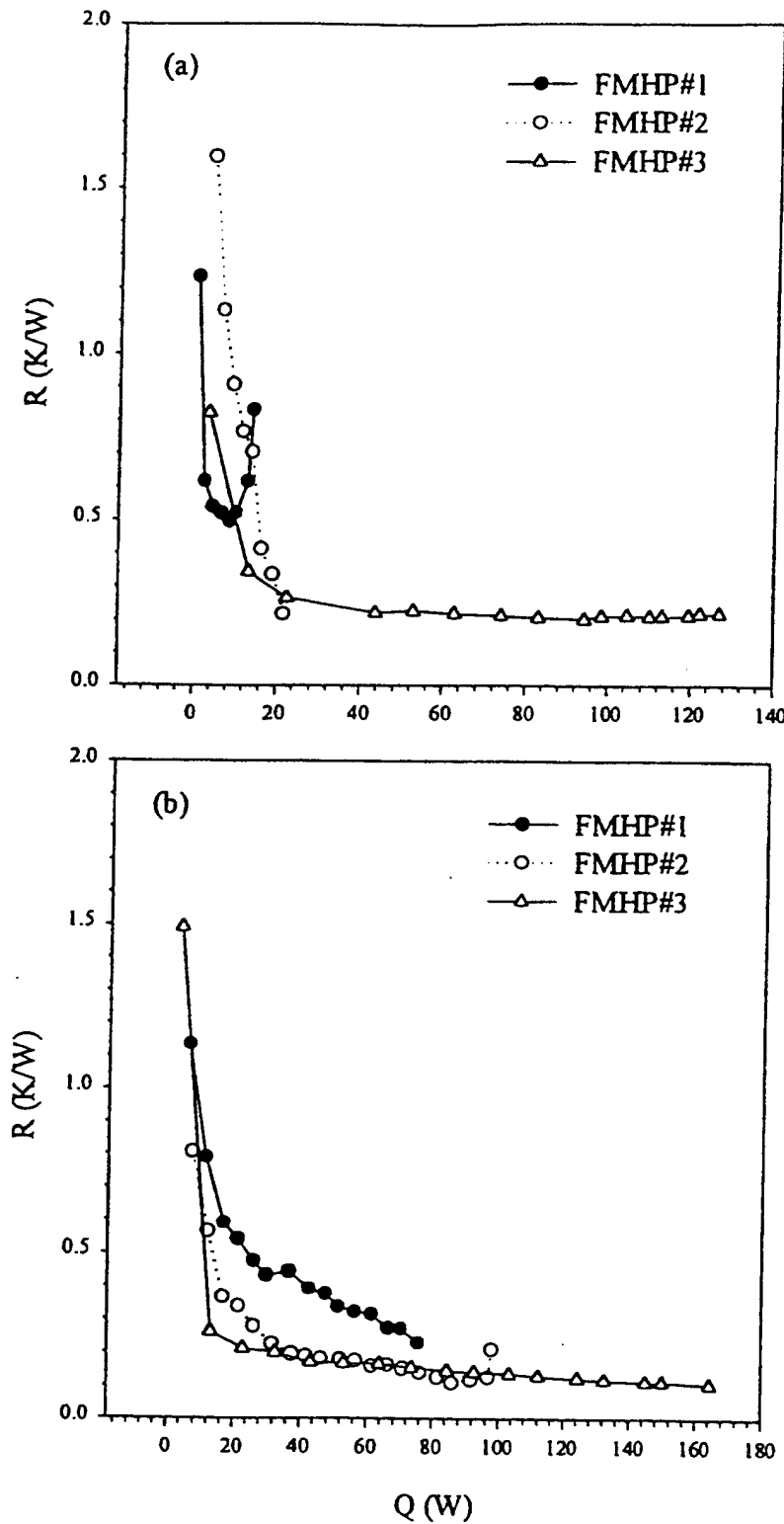
Figure 3.5: Effective thermal resistance of the flat miniature heat pipes at operating temperature of $T_v = 90°C$ in the (a) horizontal wide orientation and (b) vertical orientation. The heat load is applied to both sides.

$$R = (T_e - T_c)/Q_a \qquad (3.12)$$

A common characteristic of all thermal resistances presented here is that the thermal resistance of the FMHP's is high at low heat loads as a relatively thick liquid film resides in the evaporator. However, this thermal resistance decreases rapidly to its minimum value as the applied uniform heat load is increased. Overall, FMHP#1 was found to have an approximate minimal thermal resistance of 0.5 K/W while FMHP#2 operated with a minimal thermal resistance of 0.3 K/W. FMHP#3 was found to have the minimal thermal resistance of 0.2 K/W for all investigated heat pipes. It should be noted that the thermal resistance is a function of the heated and cooled surface areas in the evaporator and condenser sections respectively and was found to be independent of the heat pipe operating temperature.

Figures 3.6 through 3.9 present the experimental maximum heat flow rate and maximum heat flux of all flat miniature heat pipes in the range of operating temperature of $T_v = 60°C$ to 95°C. $Q_{\max}$ was defined to occur when the evaporator temperature, and hence the end cap to end cap thermal resistance, began to rise unboundedly All heat flow rates presented have an uncertainty of less than 1 W which included equipment and experimental errors with a 95% confidence level. Figures 3.6 and 3.7 present the maximum heat flow rate and maximum heat flux of FMHP's #1 and #2.

Figure 3.6(a) presents the results of FMHP#1 when the heat load was applied uniformly to both wide sides of the heat pipe. The dashed lines with symbols indicate the experimental data for the horizontal wide (where the heat pipe was positioned with the heat load applied from the bottom and top of the evaporator), horizontal thin (where the heat pipe was positioned with the heat load applied to wide vertical sides) and vertical orientation where the condenser was above the evaporator. FMHP#1 showed a maximum heat flux of 11.5 W/cm^2 in the horizontal wide orientation and 18.8 W/cm^2 in the horizontal thin orientation at $T_v = 95°C$. A maximum heat flux of 63.0 W/cm^2 at $T_v = 95°C$ was obtained in the vertical orientation for FMHP#1 with both wide sides subjected to the heat load. The solid and dashed lines without symbols in Figure 3.6(a) show the theoretical prediction results obtained by these efforts for minimum meniscus contact angles of 33 and zero degrees, respectively. While the difference between these two cases is small for trapezoidal grooves, it is significant for rectangular grooves as will be demonstrated for FMHP #3. Figure 3.7 presents the maximum heat load and heat flux results for FMHP#1 when the heat load was applied to a single wide side. The maximum heat flux obtained in this orientation was approximately 37.0 W/cm^2 in the horizontal orientation and 113.2 W/cm^2 in the vertical orientation. No significant difference was observed in the maximum heat flux between the two horizontal orientations for the single side case unlike for the situation when the heat load was applied to both sides. The 60% increase in maximum heat flux for FMHP #1 obtained in the two horizontal orientations when the heat load was applied to both sides may have been caused by a overfill of working fluid. In the horizontal thin orientation, excess liquid may have pooled at the evaporator end cap on the inner thin surface where no heat load was applied providing more liquid for the evaporative heat transfer process through capillary forces through the angled grooves that wrapped around the full inner perimeter of the heat pipe. This would not occur as easily in the horizontal wide orientation since the excess liquid would pool on an inner surface directly subjected to the heat load. For the single heated side case, the

112
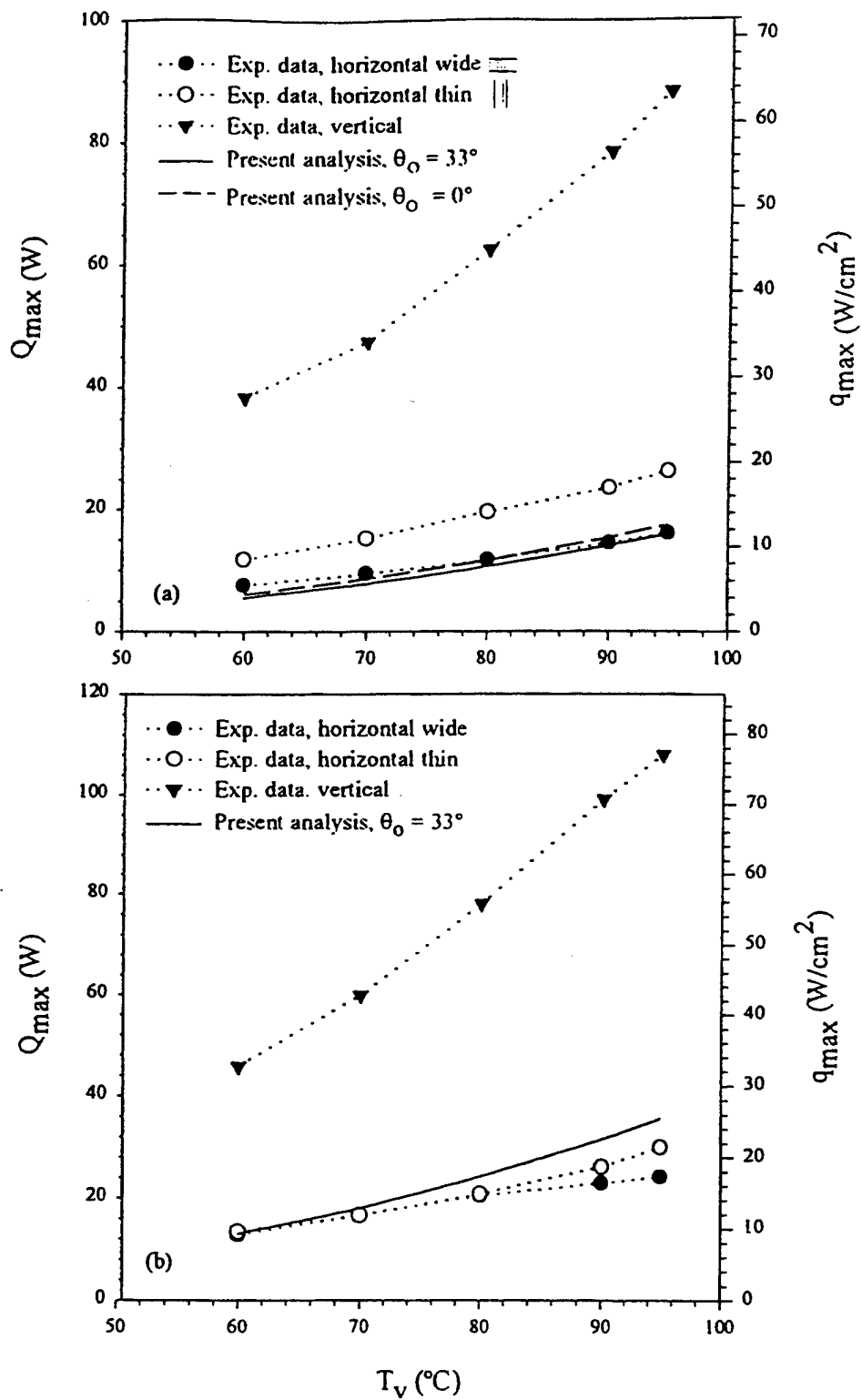
Figure 3.6: Maximum heat transfer of (a) FMHP#1 and (b) FMHP#2 heated from both sides in various orientations.
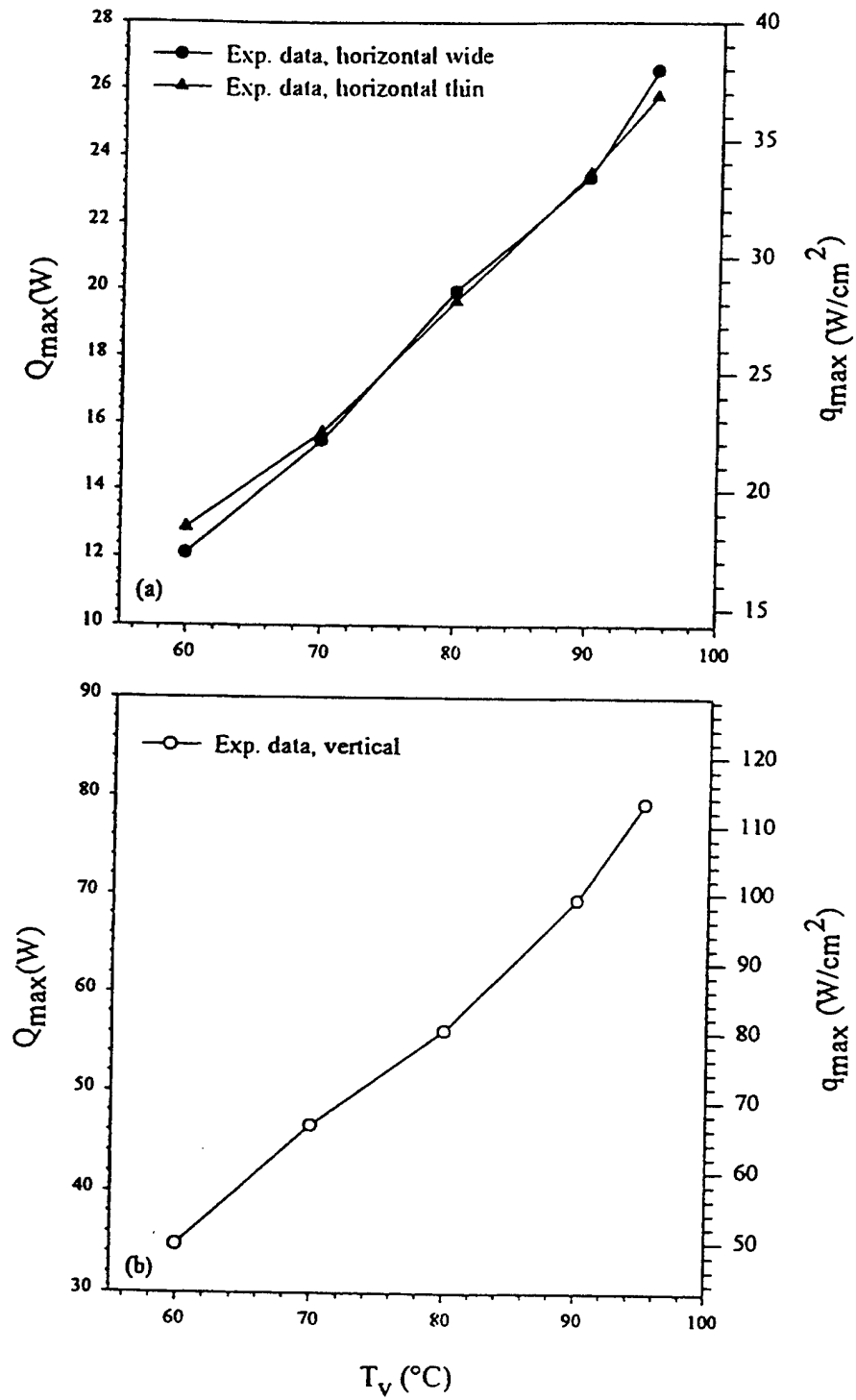
Figure 3.7: Maximum heat transfer of FMHP#1 heated from one side in (a) horizontal and (b) vertical orientations.
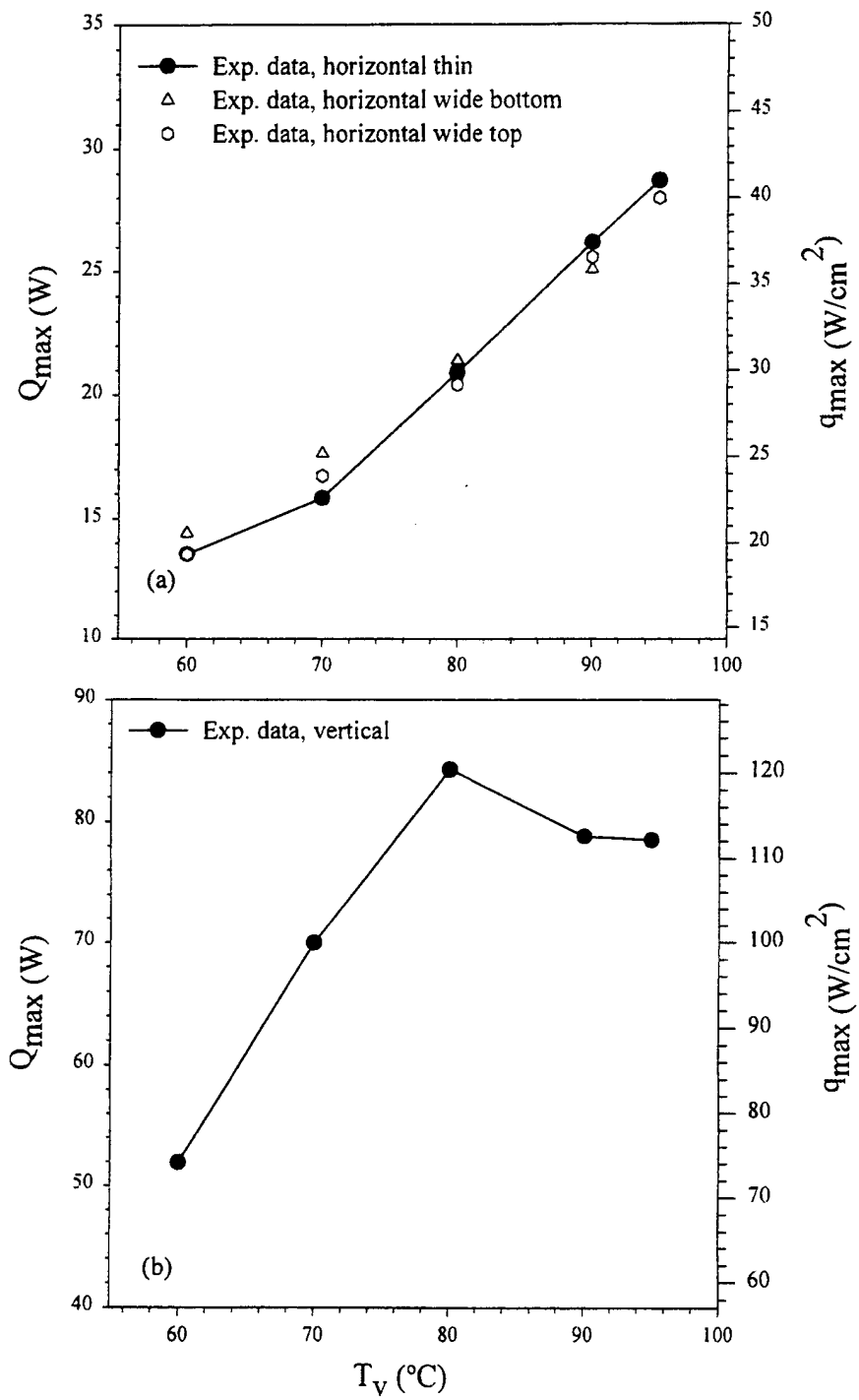
Figure 3.8: Maximum heat transfer of FMHP#2 heated from one side in (a) horizontal and (b) vertical orientations.
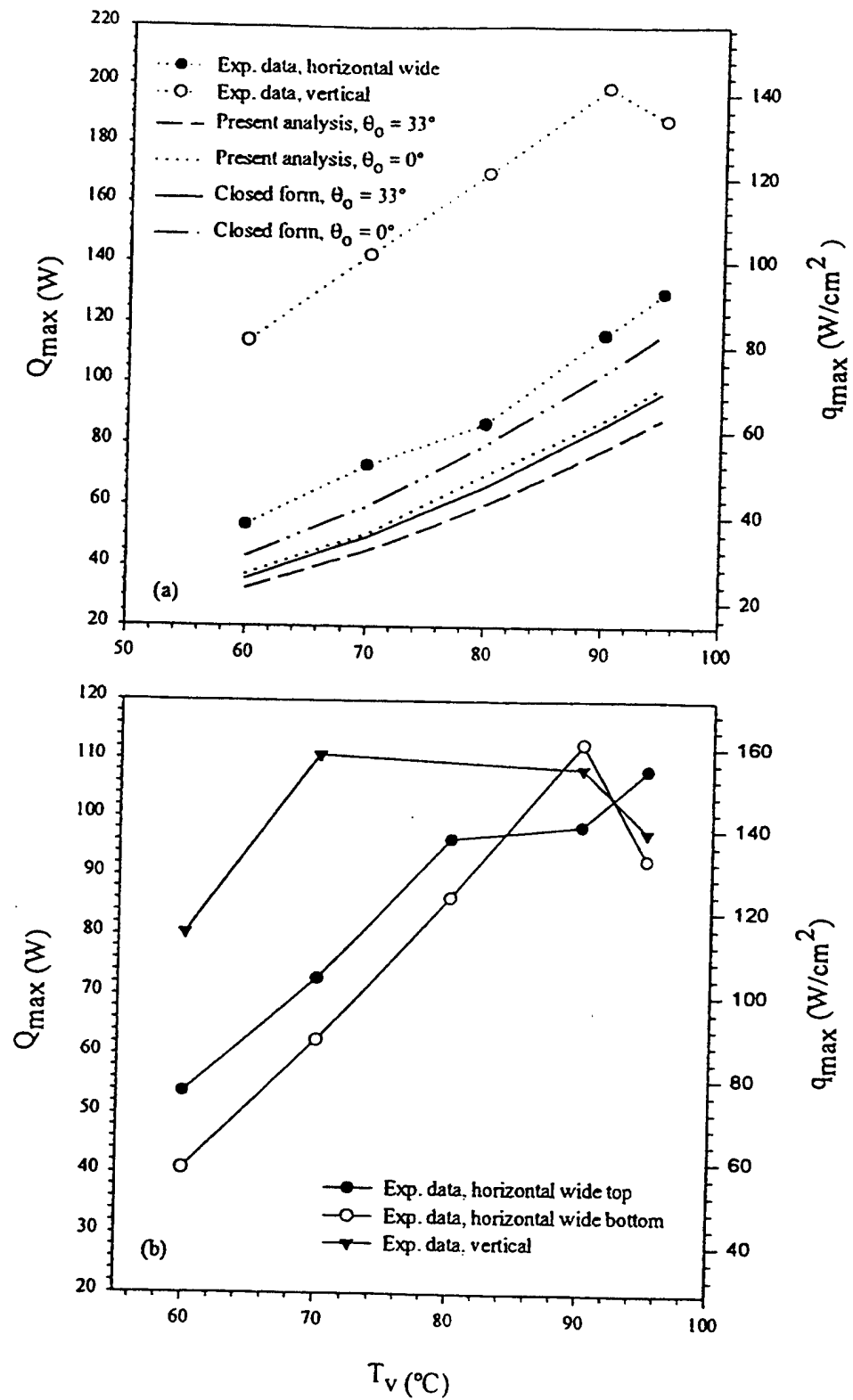
Figure 3.9: Maximum heat transfer of FMHP#3 heated in vertical and horizontal orientations from (a) both sides and (b) one side.

116

excess liquid pooling mechanism cannot be effective because of the higher heat fluxes which would initiate film boiling in the pool. Figures 3.6(a) and 3.7 both show a consistent increase in maximum heat flux with increase in operating temperature. Therefore, for FMHP#1, it was determined that capillary limitation was the controlling heat transfer mechanism in all orientations.

Figure 3.6(b) presents the experimental maximum heat flow rate and maximum heat flux of FMHP#2 with a heat load applied uniformly to both wide sides where the dashed lines with symbols signify the experimental results. The maximum heat flux found for this heating configuration was 17.3 W/cm^2 in the horizontal wide orientation and 21.5 W/cm^2 in the horizontal thin orientation at an operating temperature of $T_v = 95°C$. Once again, a slight increase in the maximum heat flux (20%) occurs between the two horizontal orientations possibly due to a slight working fluid overfill of the heat pipe. FMHP#2 in the vertical orientation had a maximum heat flux at $T_v = 95°C$ of 77.2 W/cm^2 when both wide sides were heated. Performance of FMHP#2 was restricted by the capillary limit in all orientations when heat was applied to both wide sides since the maximum heat flux consistently increased with operating temperature. The predicted values of maximum heat flux in the horizontal orientation found from the capillary limitation analysis are presented as the solid line in Figure 3.6(b). Figure 3.8(a) presents the maximum heat flux obtained for FMHP#2 when heated from a single wide side in the vertical orientation while Figure 3.8(b) presents maximum heat load and heat flux results for various horizontal orientations when the heat load was applied to a single wide side. In the vertical orientation the maximum heat flux occurs at an operating temperature of $T_v = 80°C$ and is 120.4 W/cm^2 while at higher operating temperatures, the maximum heat flux falls to approximately 112.0 W/cm^2. This signifies for the lower operating temperatures, up to and including $T_v = 80$, that the controlling heat transfer mechanism is the capillary limit. However, at higher operating temperatures and respective higher heat fluxes, the boiling limitation becomes the controlling heat transfer mechanism. The maximum heat flux in various horizontal orientations with the heat load applied to a single side is restricted by the capillary limit and is approximately 40.5 W/cm^2 at an operating temperature of $T_v = 95°C$.

Figure 3.9(a) presents the experimental maximum heat flow rate and heat flux of FMHP#3 in various orientations over the operating temperature range of $T_v = 60°C$ to 95°C when the heat load is applied to both wide sides. Maximum heat flux obtained for FMHP#3 in the horizontal orientation with an uniform heat load applied to both sides was found to be 92.13 W/cm^2. In the vertical orientation, the maximum heat flux occurred at an operating temperature of $T_v = 90°C$ and was 141.8 W/cm^2 and then decreased for an operating temperature of $T_v = 95°C$. Therefore, it was determined that the capillary limitation was the controlling mechanism for FMHP#3 in the horizontal orientation with a heat load applied to both sides and in the vertical orientation up to the operating temperature of $T_v = 90°C$. FMHP#3 was then restricted by the boiling limit in the vertical orientation for operating temperatures above $T_v = 90°C$ when the heat load was applied to both wide sides. Theoretical prediction results for the maximum heat flux in the horizontal orientation are also presented by the dotted and dashed lines based on different minimum meniscus contact angles of zero and 33 degrees. The theoretical values under predicted the experimental results by as much as 35% and is believed to be caused by a significant overfill of working

fluid which would increase the experimental results in the gravity field due to liquid pooling effects. The predictive results indicate that a decrease in the minimum contact angle increases the maximum heat flow rate. Contact angles below the minimal values for a given working fluid - wall combination are possible due to surface microroughness. Khrustalev and Faghri [49] noted that thick liquid films can appear attached to the liquid-vapor meniscus at high heat fluxes. This phenomenon results in the interface curvature equal to that of zero contact angle. For zero contact angle, the agreement between the dotted theoretical curve and experimental results is better. The question of contact angle effects on maximum heat flux should be further investigated for high-heat-flux miniature heat pipes. The other two theoretical curves in Figure 3.9(a) are for the closed form solutions of zero and 33 degree contact angle which over predict the capillary limitation analysis by approximately 10% due to the four assumptions discussed above.

Figure 3.9(b) presents the maximum heat flux obtained with FMHP#3 when the heat load is applied to a single side. In the vertical orientation, a maximum heat flux of approximately 155.0 W/cm^2 was obtained at an operating temperature of $T_v = 70°C$ and 90°C. Therefore, it is determined that the boiling limit is the critical heat transfer mechanism for all operating temperatures above $T_v = 70°C$ in the vertical orientation. A maximum heat flux of approximately 160 W/cm^2 was obtained for FMHP#3 in the horizontal orientation with the heat load applied to a single wide side for an operating temperature of T = 90°C. The maximum heat flux then drops off significantly to approximately 130 W/cm^2 at the operating temperature of $T_v = 95$ signifying that the boiling limitation restricts heat pipe performance above $T_v = 90°C$. FMHP#3 in the horizontal wide orientation with the heat load applied to the top of the FMHP provided a maximum heat flux of 154.6 W/cm^2 at the operating temperature of $T_v = 95°C$. It should be noted here that the concept of boiling limit traditionally used in heat pipes can have different meanings for gravity-assisted heat pipes (Figure 3.9(a)) and for those operating in zero-gravity environment. For the zero gravity case, incipience of nucleate boiling can be considered a limitation. A gravity-assisted heat pipe can perform with vapor bubbles forming in the evaporator provided that they can exit the capillary structure. In this case, transition to film boiling is a more likely limitation. This film boiling limitation is assumed to be the most important one for the results shown in Figure 3.9(b) for higher operating temperatures.

3.1.7 Conclusions

Three flat miniature heat pipes were experimentally investigated and theoretically modeled for maximum heat flow rates and heat flux for a range of operating temperatures. The temperature distribution along the heat pipes longitudinal axis and the corresponding thermal resistance were also observed.

FMHP#3 produced the highest obtainable heat flow rate and flux in all orientations in the gravity field. It is concluded from this that flat miniature heat pipes with deep and narrow axial capillary grooves and thicker walls are much more promising than flat miniature heat pipes with shallower trapezoidal grooves and thin walls. The majority of the experimental data showed that the controlling mechanism of the maximum uniform heat flux at the evaporator was the capillary limitation. However, especially in the vertical orientation,

the maximum heat load applied to FMHP#2 and #3 was restricted by the boiling limitation at higher operating temperatures.

A theoretical prediction of the maximum heat transfer was also carried out to compare to the experimental data. Results were good for FMHP#1 and #2 and were reasonable for FMHP#3. However, both experimental results and theoretical predictions undeniably signify that flat miniature heat pipes with a micro capillary groove structure demonstrate excellent performance characteristics and are very promising in the cooling of miniature electronic components with high heat fluxes.

3.2 Critical Heat Fluxes in Forced Convection Evaporators

Two-phase forced convection cooling of high-heat-flux/high-power electronic devices is one of the most powerful means of thermal management. This method becomes especially important due to the continuous miniaturization and increase in power dissipation per unit surface area of modern electronic devices that have already reached 300 W/cm^2 (Jacobs and Hartnett [62], Cao et al. [46] 1994; Bowers and Mudawar, [50]; Ravigururajan et al., [51]; Takahashi and Isiikawa, [52], Khrustalev and Faghri, [66]; Hopkins, [48].

Peng and Wang [53] investigated a stainless steel-water flat heat sink with a series of small rectangular channels. They reported that nucleate boiling in the microchannels occurred with smaller wall surface superheats than those usually observed in larger diameter channels. Ravigururajan et al. [51] investigated a 20 mm long copper-R124 heat sink with 54 channels with dimensions of 0.27 mm wide and 1.0 mm deep. In this experimental investigation, the wall superheat exceeded 80°C with the heat flux under 70 W/cm^2. Bowers and Mudawar [50] experimentally investigated the critical heat flux and pressure drop in 10 mm long smooth walled mini and micro copper-R113 channels with diameters of 2.54 mm and 510 mm respectively. Bowers and Mudawar [50] investigated these heat sinks with low flowrates and with the heat load applied to a single side. Their investigation obtained critical heat flux values in excess of 200 W/cm^2 and low pressure drops ($\Delta P < 0.32$ bar) while the inlet subcooling effects were found negligible. They concluded that mini-channels were favorable to micro-channels in that comparable heat fluxes were achieved with much lower pressure drops, 0.01 bar, and that the manufacturing of mini-channels was much simpler. For both channels, a uniform wall superheat of 100°C occurred at higher heat fluxes indicating that large thermal resistances resulted for these smooth walled heat sinks.

Khrustalev and Faghri [67] tested an axially grooved copper-water flat miniature heat sink with external dimensions of 2.6 × 7.7 × 40 mm in the horizontal orientation with a uniform heat load applied to both sides. Effective heat transfer coefficients were found to be up to 1 x 10^5 W/m·K while observed temperature distributions were comparatively uniform to within 12°C and the average wall superheat was about 2°C. They also observed that the critical heat flux decreased with heated length.

Takahashi and Isiikawa [52] developed a heat sink consisting of several flat channels with cross sections of 2 × 0.5 mm^2, 4 ×0.5 mm^2 and 16×0.5 mm^2. In their results, the maximum heat flux was found to be up to 300 W/cm^2 for a four channel copper-water heat sink. A theoretical analysis for CHF prediction was included which considered hydrodynamic instability on the liquid-vapor interface.

119

Yang and Webb [54] experimentally investigated and modeled the pressure drop for two-phase flow across plain rectangular and enhanced shallow micro-finned tubes (0.40 mm wide and 0.20 mm deep) with hydraulic diameters of 2.64 and 1.56 mm respectively. They found that a predictive method of determining the frictional pressure drop employing Akers et al. [55] equivalent mass velocity concept provided a good prediction of the experimental data to within 20%.

It appears that more profound understanding of critical mechanisms inducing CHF in micro/miniature passages is needed to design enhanced heat sinks and heat pipes for ultra high heat fluxes approaching 1000 W/cm^2. To gain such understanding, wider and more systematic data bases for critical heat fluxes and pressure drops should be first obtained. Therefore, it is the objective of the present investigation to obtain a detailed experimental data base for performance characteristics of four flat miniature heat sinks with enhanced and smooth inner surfaces and to generalize the experimental results for critical heat fluxes and pressure drops by an empirical correlation and a one-dimensional two-phase homogenous model, respectively.

In this effort, the flat miniature heat sinks enhanced inner surfaces will range from smooth to shallow and wide trapezoidal micro grooves to deep and narrow rectangular grooves. This experimental investigation seeks out the critical heat flux that can be applied uniformly to the two wide evaporator walls for a range of outlet saturation temperature, heated lengths and total mass flow rates. Also observed during this investigation is the longitudinal wall temperature distribution and effective heat transfer coefficient.

3.2.1 Experimental Methodology

Flowloop operation

Figure 3.10 presents a schematic of the experimental flowloop with all relevant components. Water is introduced to the flowloop and maintained in the pressure reservoir tank. The pressure reservoir has two functions which include maintaining a constant test section outlet saturation temperature by adjusting the pressure reservoir tank temperature and to provide a large reservoir where the working fluid is collected and deareated periodically. The temperature and hence the pressure of the tank is controlled by a 2,000 W hotplate for gross adjustments and an internal copper cooling coil for fine adjustment. Water coolant was pumped through this coil from a Lauda RM-20S constant temperature bath/circulator. A reflux condenser, used periodically in the deaeration of the working fluid, is immediately located above the pressure reservoir tank. The deaeration of the working fluid was periodically carried out in order to remove any trapped or generated non-condensable gas from the flowloop. The working fluid was circulated through the flowloop by a Tuthill 0.5 l/min seal-less, hi-torque, magnetically coupled driven gear liquid pump. Throughout experimentation, valves (3), (4) and (5) were constantly monitored and adjusted to maintain a constant flow to the test section while the majority of the liquid was bypassed through valve (3) to the pressure/reservoir tank. After passing through the flowmeter, the working fluid flowed through the preheater which was used to bring the temperature of the working fluid to the desired subcooled temperature. In all experiments performed for this investigation the working fluid was introduced to the test section at a five degree subcooled temperature. The pressure drop

120

across the test section was measured by a Sensotec wet-wet differential pressure transducer that had a performance range of 0.0 kPa to 68.9 kPa with an announced accuracy of 0.15% of the full scale value.

Test modules

Investigated heat sinks, which are described below, were mounted in the flowloop with the use of specially formed copper adapters soft soldered to the miniature heat sinks. Figure 3.11 schematically shows the rigid bracket used to mount the heat sink in the flowloop. Heat sinks were installed with the wide surfaces vertically oriented to guarantee that both heated surfaces were uniformly wetted. Four discrete pairs of thick film resistor heating elements were placed along the longitudinal axis of the heat sink on the wider vertical surfaces. Individual resistor pairs, with an effective heating area of 1.4 W/cm^2 were placed in a straight row, separated by 1 mm, and were positioned symmetrically around the midpoint of the heat sink length. Each pair of thick film resistors was individually powered by four 0-120 volt variable ac transformer and the supplied power was measured by four individual digital wattmeters. The thick film resistor pairs were clamped securely to the heat sink surface by individual teflon clamps with asbestos and fiberfrax insulated backing. The rigid asbestos backing provided for a uniform pressure on the backside of the thick film resistors while the soft fiberfrax insulation was included to absorb any expansion of the heat sink during operation to prevent damage. A layer of Omegatherm 101 high thermal conductive paste was applied at the thick film resistor/heat sink contact area to reduce thermal resistance. For the thin walled heat sinks (FMHS#1 and FMHS#2) the thick film resistors were first soft soldered to copper blocks 1 cm thick in order to help distribute the heat uniformly across the heat sink surface. The copper blocks were precisely machined to have the same length of the resistors (1.26 cm) and width of the heat sink wall. For the thick heat sinks (FMHS#3 and FMHS#4), this was not necessary since the heat load was assumed to be uniform at the interior surface due to the thick walls.

Twelve Type "T" copper-constantan (36 gage) thermocouples were soldered along the longitudinal centerline on the upper thin horizontal wall to measure the longitudinal temperature distribution. For each resistor pair, one thermocouple was centered while two others were placed 0.5 mm from the ends of the resistor pairs as shown in Figure 3.2. Thermocouple data was measured and recorded by a Fluke 2625A Hydra Data Logger data acquisition. All thermocouples were calibrated to within 0.3 C against a Lauda RM-20S constant temperature bath.

Heat sinks investigated

Four individual copper-water flat miniature heat sinks, as shown in Figure 3.12, were investigated in this effort and relevant geometrical parameters are listed in Table 3.2. Two of the flat miniature heat sinks (FMHS#1 and #2) contained micro trapezoidal capillary grooves that were at a slight angle to the longitudinal axis of the heat sink and were respectively manufactured by The Furukawa Electric Company and Fujikura Ltd. The capillary groove structure of FMHS #1 and #2 was manufactured by a rolling method. The capillary groove structure of FMHS#3 consisted of axial rectangular micro capillary grooves produced by a high speed dicing saw employing a high diamond content carbon blade at the University of Connecticut. A smooth walled flat miniature heat sink, FMHS#4, with the same interior cross-sectional area as FMHS#3 was also produced at the University of Connecticut in order

121
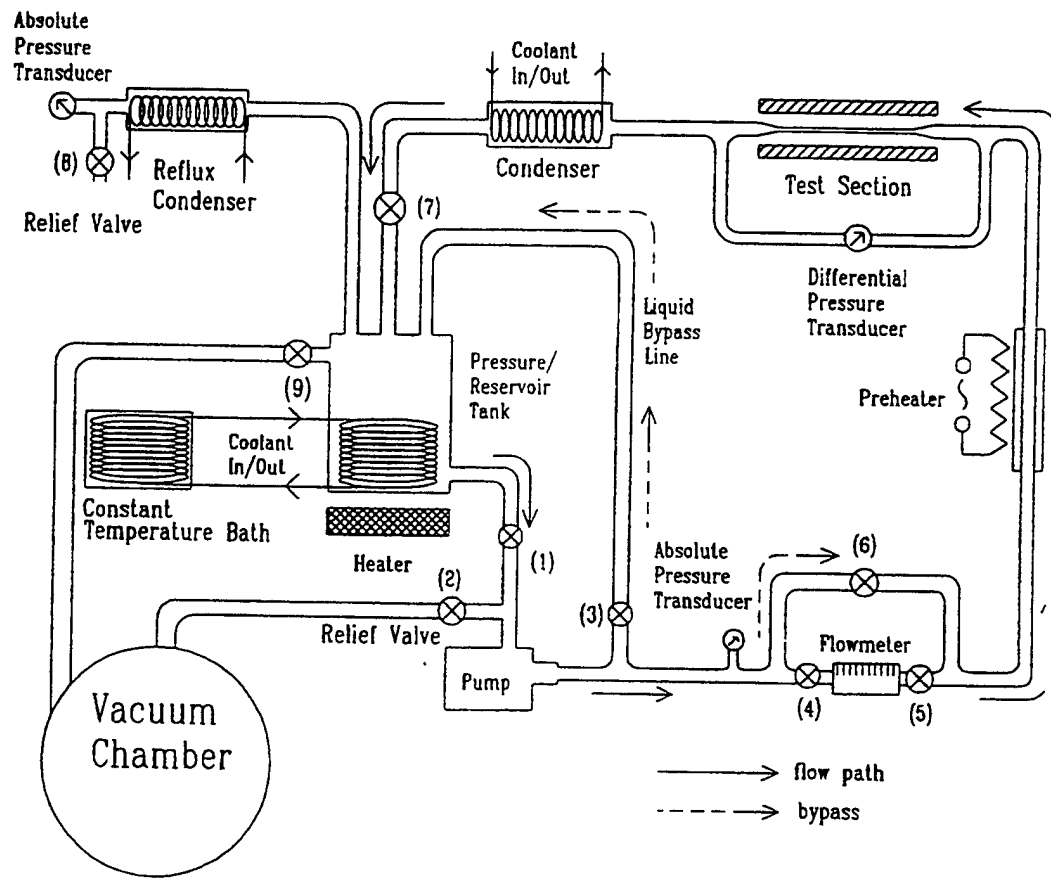
Figure 3.10: Schematic of the experimental flowloop for testing of the flat miniature heat sinks.
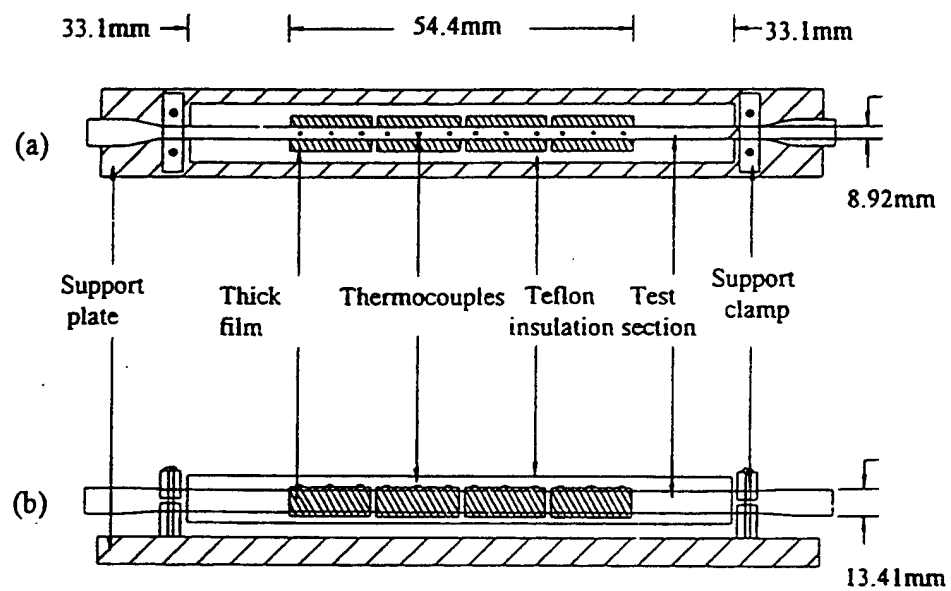
Figure 3.11: Schematic of the flat miniature heat sink test apparatus (a) top view (b) front view (shown here for FMH3#3 and #4).

Table 3.2: Geometrical parameters of investigated flat miniature heat sinks

Parameter	FMHS#1	FMHS#2	FMHS#3	FMHS#4
External Width	7.01	11.7	13.41	13.41
External Thickness	2.01	2.4	8.92	8.92
Vapor Channel Width	6.03	10.8	9.75	9.75
Vapor Channel Thickness	1.03	1.5	1.22	1.52
Number of Grooves	52	50	62	-
Groove Depth	0.24	0.20	0.42	-
Groove Top Width	0.20	0.45	0.20	-
Groove Bottom Width	0.15	0.30	0.20	-
Fin Top Width	0.16	0.20	0.10	-
Groove Angle to Heat Sink Axis	4°	18°	0°	-
Hydraulic Diameter	0.87	2.07	1.02	2.63

to investigate the advantages/disadvantages of enhancing the interior surface.

Experimental Procedure

Four parameters were constantly monitored and adjusted during the experimental investigation of the flat miniature heat sinks critical heat flux. These parameters included: the test section outlet saturation temperature/pressure (40°C/7.39 kPa to 80°C/47.39 kPa), test section inlet subcooled temperature ($T_{sub,i}$= 5°C), the total liquid mass flowrate (0.25 and 0.50 g/s) and the power applied to the individual resistor pairs. Also, the heated length ranged from 1 pair of resistors (13.6 mm) to 4 pairs (54.4 mm). Pressure drop across the miniature heat sink and wall temperatures were also monitored and recorded. The following is a description of the operation of the experimental flowloop for the testing of flat miniature heat sinks. After safe start-up of the liquid flow, the flowloop was brought to the desired operating inlet subcooled temperature and outlet saturation pressure and temperature. Inlet subcooling was necessary in order to avoid vapor bubbles at the heat sink inlet and was

124
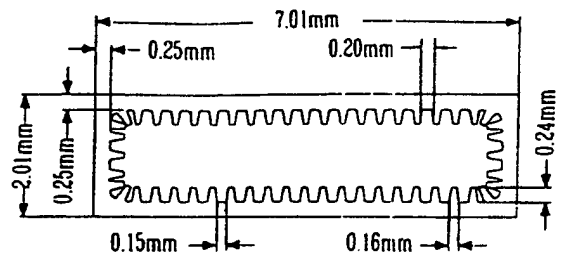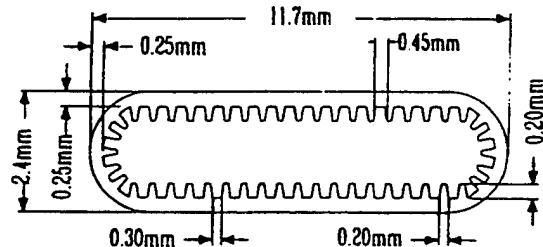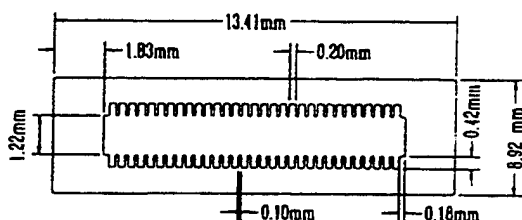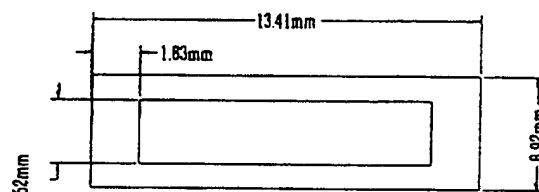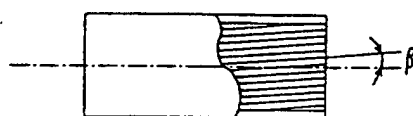
Figure 3.12: Schematic of interior capillary groove structure and angle to flat miniature heat sink axis for: (a) FMHS#1 (b) FMHS#2 (c) FMHS#3 (d) FMHS#4 (smooth interior) (e) angle between groove axis and heat pipe centerline.

maintained by adjusting the preheater voltage supply. After all experimental parameters were obtained, an initial heat load, Q, of approximately 20 W/pair was applied.

All experimental results were obtained with a systematic and consistent methodology that is as follows. After all parameters reached steady state, the system was allowed to remain at steady state for fifteen minutes. Thirty sets of data were recorded over five minutes and than the applied heat load was increased by 10 Watts/pair (5 Watts/pair as CHF was approached) for five minutes as an intermediate step with no data recorded. This intermediate step was included in the experimental procedure as a check to help insure that the heat load had sufficient time to uniformly heat the test section surface and also to indicate whether CHF was being approached. Applied heat load was then increased again by an increment of 10 Watts/pair (5 Watts/pair as CHF was approached) and the system was allowed to reach and maintain steady state for fifteen minutes before thirty sets of data were recorded as above. This iteration was repeated until CHF was obtained which was characterized by a sudden and sustained increase of the test section temperature at one or more thermocouple locations for longer heated lengths as the outlet equilibrium vapor quality approached unity or by a sudden cracking of a single resistor for shorter heated lengths caused by local dryout. Critical heat flux results obtained were described by an empirical correlation and the pressure drops measured were compared to predictions of an one-dimensional model considered below.

3.2.2 Axial Pressure Drop Analysis for Flat Miniature Heat Sinks

Yang and Webb [54] investigated the pressure drop in extruded miniature aluminum-R12 heat sinks with and without micro-fins. An equivalent mass velocity was incorporated into their model which was first introduced by Akers et al. [55] that took into account the large difference in mass velocity between the vapor and liquid. Their experimental and theoretical investigation showed that the pressure drop was dominated by vapor shear. The present model, given below, is similar to that used by Collier & Thome, [70] and Bowers and Mudawar [50] which takes into account the contributions of acceleration and friction in the two-phase flow. However, an equivalent mass velocity will be incorporated into the present model as Yang and Webb [54] included in their two-phase friction pressure drop analysis.

Three individual lengths comprise the total length of the investigated miniature heat sink: (1) the single phase friction inlet length, L_s, (2) the two phase boiling length, L_b, comprising the contributions of acceleration and friction and (3) the two-phase friction outlet length, L_o. The pressure drop expression therefore takes the following general form

$$\Delta p = \Delta p_s + \Delta p_b + \Delta p_o \qquad (3.13)$$

The boiling length pressure drop, Δp_b, includes terms which account for the frictional pressure loss, $\Delta p_{b,f}$ and the acceleration pressure loss, $\Delta p_{b,a}$. These pressure gradients are found by performing a detailed one-dimensional momentum balance on the heat sink. Assuming that the cross-sectional area of the flow channel is uniform and that the two-phase flow is steady, these terms are found to be as follows (Collier & Thome, [70])

$$-\left(\frac{dp}{dz}\right)_{b,f} = \frac{2f_{TP}G_{eq}^2}{\bar{\rho}D_h} \qquad (3.14)$$

126

$$-\left(\frac{dp}{dz}\right)_{b,a} = G_{eq}^2 \frac{d\left(1/\bar{\rho}\right)}{dz} \tag{3.15}$$

where the two-phase friction factor, f_{TP}, can be found from the Blausius correlation

$$f_{TP} = 0.079 \left(\frac{G_{eq}^2 D_h}{\bar{\mu}}\right)^{-\frac{1}{4}} \tag{3.16}$$

and the mean dynamic viscosity,$\bar{\mu}$, and the mean density,$\bar{\rho}$, are respectively defined as

$$\bar{\mu} = 1/\frac{x_L}{\mu_v} + \frac{(1+x_L)}{\mu_l} \tag{3.17}$$

$$\frac{1}{\bar{\rho}} = \frac{x_L}{\bar{\rho}_v} + \frac{(1-x_L)}{\bar{\rho}_l} \tag{3.18}$$

and where Eqs. 3.17 and 3.18 are based on the equilibrium vapor quality at the boiling length outlet, x_L, and is defined as

$$x_L = \frac{Q_{total}}{h_{fg}\,\dot{m}} \tag{3.19}$$

and $\dot{m} \equiv GA$ is the total liquid mass flowrate at the flat miniature heat sink inlet. Also, the hydraulic diameter, D_h, of the flat miniature heat sink is defined in this analysis as

$$D_h = \frac{4A}{P} \tag{3.20}$$

where A is the cross sectional area of the miniature channel and P is the wetted perimeter of the flat miniature heat sink including the perimeter of the inner grooves.

An equivalent mass velocity of the two-phase flow first proposed by Akers et al. [55] is used in this analysis and is defined as

$$G_{eq} = G\left[(1-x_L) + x_L\left(\frac{\rho_l}{\rho_v}\right)^{\frac{1}{2}}\right] \tag{3.21}$$

This weighted expression is a function of the known inlet single phase mass velocity, G, and the outlet equilibrium vapor quality,x_L. Substituting Eqs. 3.16 - 3.21 into Eqs. 3.14 and 3.15 and integrating over the channels boiling length, the following simple algebraic expressions are found for the portions of the pressure drop contributed by friction and acceleration

$$\Delta p_{b,f} = \frac{2f_{TP}G_{eq}^2 L_b}{\rho_l D_h}\left[1 + \frac{x_L}{2}\frac{\rho_l}{\rho_l - \rho_v}\right] \tag{3.22}$$

$$\Delta p_{b,a} = \frac{G_{eq}^2}{\rho_l}\frac{\rho_l}{\rho_l - \rho_v}x_L \tag{3.23}$$

Eqs. 3.22 and 3.23 were found assuming linear variation of the equilibrium vapor quality along the z axis. Single phase pressure drop, Δ_{ps}, over the heat sinks unheated entrance length, L_s, is found by a simple force balance over the cross sectional area at the inlet and outlet of the single phase region and is given by

$$\Delta p_s = \frac{2 f_s G^2 L_s}{\rho_l D_h} \tag{3.24}$$

where f_s is the single phase friction factor and is given as follows for a flat rectangular channel (Shah and Bhatti, [33])

$$f_s = \frac{24}{Re_{l,D_h}} \left[1 - 1.3553C + 1.9467C^2 - 1.7012C^3 + 0.9564C^4 - 0.2537C^5 \right] \tag{3.25}$$

where $C = t_{hor}/t_{ver}$ and the liquid Reynolds number is based on the hydraulic diameter.

Finally, the frictional pressure drop over the unheated outlet length, L_o, of the two-phase heat sink is found in a similar manner as Eq. 3.22 by integrating Eq. 3.14 over the outlet length.

$$\Delta p_o = \frac{2 f_{TP} G_{eq}^2 L_o}{\rho_l D_h} \left[1 + x_L \frac{\rho_l}{\rho_l - \rho_v} \right] \tag{3.26}$$

3.2.3 Results and Discussion

Pressure drop

Overall pressure drops predicted by the present model agree reasonably well with experimental results as shown in Fig. 3.13 where only a small part of all data is presented. Experimental pressure drop results of FMHP's #1, #3 and #4 agree well with the model, however, valid experimental data for FMHS#2 were not available. Experimental results shown are the mean values of thirty readings over five minutes of steady state and have an uncertainty of 0.225 kPa which accounted for experimental and equipment error with 95% confidence.

The inlet single phase liquid region accounted for less than 1% of the total pressure drop for all cases and is insignificant in this discussion. Outlet two-phase flow in the flat miniature heat sink contributes as much as 70% of the total pressure drop as predicted by the model and shown by experimental results, however, only the contributions of the acceleration and friction terms on the pressure drop across the boiling length are important in this investigation and will be discussed here. Pressure drops across the short lengths of tubing, with relatively large cross-sectional flow areas, that connect the miniature heat sink to the differential pressure transducer ports are less than 0.5% of the overall pressure drop and are negligible.

For a boiling length of 13.6 mm in a grooved FMHS, the percentage of the pressure drop due to friction increases, from 35% to 45%, as the outlet saturation temperature increases from $T_{sat,o} = 40$ to 80°C. This increase is directly due to the increased equivalent mass velocity as the temperature is increased. For a longer boiling length, L_b=54.4 mm, the percentage
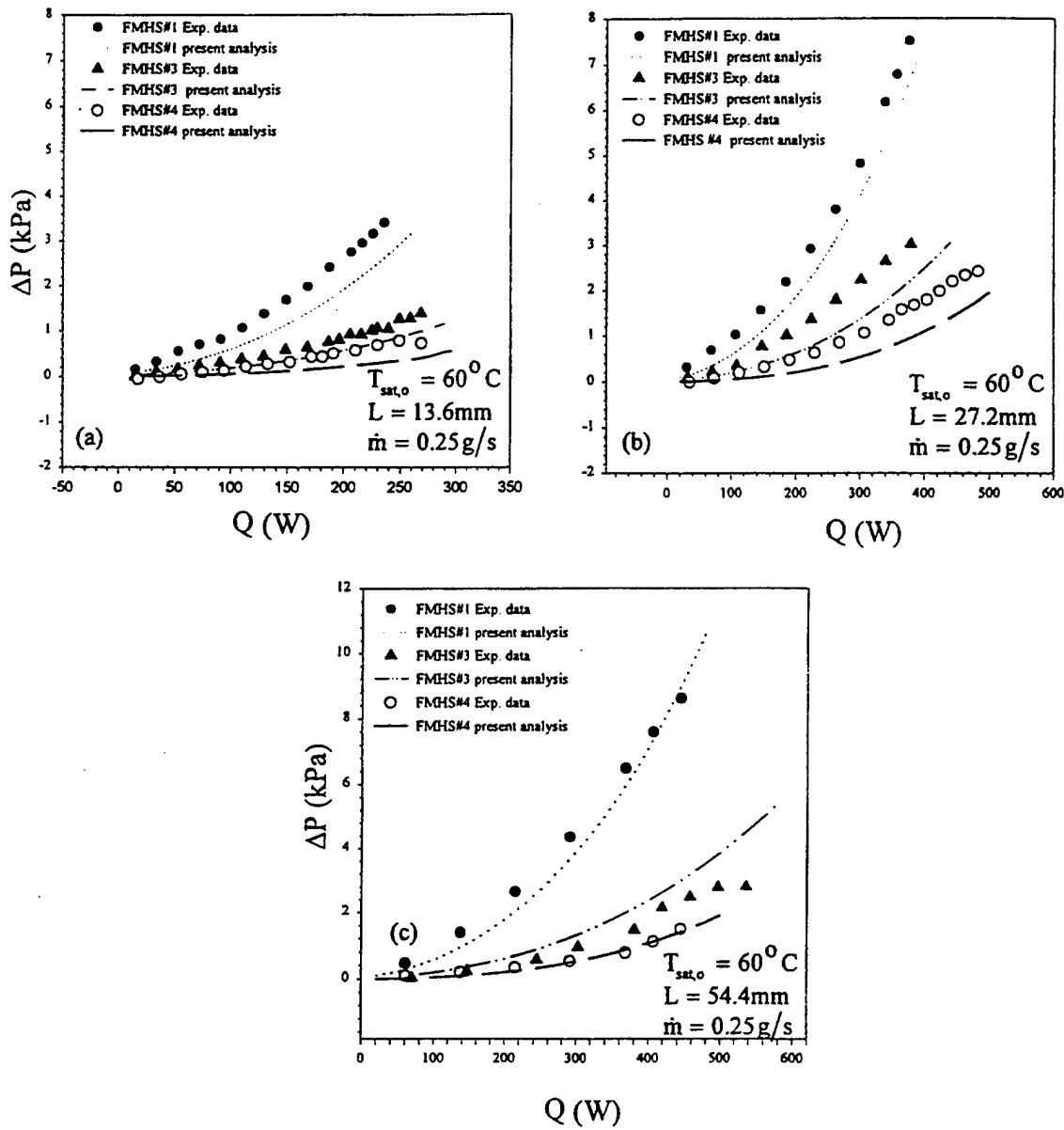
Figure 3.13: Experimentally determined and predicted pressure drop versus total heat load at $T_{sat,o} = 60C$ and total mass flowrate of 0.25 g/s to the heated lengths of: (a) 13.6 mm [pair #1 for FMHS#1, pair #2 for FMHS#3 and FMHS#4]; (b) 27.2 mm [pairs #1 & #2 for all heat sinks]; (c) 54.4 mm [pairs #1 to #4 for all heat sinks].

of the pressure drop due to friction for the same outlet saturation temperature range is predicted to be 44% to 62%. This increase in the contribution of friction to the pressure drop over the boiling length for longer heated lengths is expected due to the increased heated surface length.

Finally, when the outlet saturation temperature ($T_{sat,o}$=60°C), heated length (L_b=54.4) and mass flow rate ($\dot{m}$=0.25 g/s) are held constant, the contribution of friction to the pressure drop over the boiling length decreases from 35% to 12% when comparing the grooved FMHS#3 to the smooth walled FMHS#4 This phenomenon is expected due to the significantly larger hydraulic diameter of the smooth walled heat sink in comparison to the smooth walled heat sink. It is interesting to note that the contribution of the acceleration term to the boiling length pressure drop in the smooth walled heat sink is approximately 88% which is very comparable to the 90% that Bowers and Mudawar [50] obtained for smooth walled circular channels. Therefore, it is stated that the acceleration term is dominant for smooth wall channels while for enhanced groove surfaces the frictional term prevails.

Critical heat fluxes

Figure 3.14 presents a portion of the experimentally determined critical heat fluxes, q_{CHF}, and outlet vapor quality values at critical heat flux, x_L, of FMHS#1 and FMHS#3 while all other experimental results are presented in Table 3.3. CHF's are shown in Figure 3.14 for outlet saturation temperatures of $T_{sat,o} = 40$°C, 60°C and 80°C and mass flow rates of $\dot{m}$=0.25 g/s and 0.5 g/s as a function of total heated length. All heat fluxes presented have an uncertainty of approximately 2.5 W/cm² which include experimental and equipment error with 95% confidence.

Outlet vapor qualities at critical heat flux are approximated by Eq. 3.19 and were shown to increase with an increase in heated length and decreases with an increase in outlet saturation temperature and total mass flowrate. Figure 3.14(a) shows the effect of total mass flowrate on the critical heat flux of FMHS#1 with an outlet saturation temperature of $T_{sat,o} = 60$°C. It is seen that the critical heat flux increases with an increase in total mass flowrate and also appears that the increase in mass flowrate has more of an effect with longer total heated lengths. At the longer heated length of $L = 54.4$ mm, an increase in total mass flowrate from $\dot{m}$=0.25 g/s to 0.50 g/s provides an increase in the critical heat flux from 82.14 W/cm² to 116.1 W/cm² or approximately 29%. However, at the shortest heated length of $L = 13.6$ mm, the increase in critical heat flux is only approximately 11% from 171.6 W/cm² to 193.5 W/cm².

Figure 3.14(b) presents critical heat flux results obtained for FMHS#3 as a function of heated length and outlet saturation temperatures of $T_{sat,o} = 40$°C, 60°C, and 80°C at a total mass flowrate of $\dot{m}$=0.25 g/s. Experimental results for FMHS#3 follow the same general trends as FMHS#1 in that the critical heat flux increases with a decrease in outlet saturation temperature and total heated length. Maximum critical heat flux found for FMHS#3 with a total mass flowrate of $\dot{m}$=0.25 g/s was 209.7 W/cm² for an outlet saturation temperature of $T_{sat,o} = 40$C and a total heated length of $L = 13.6$ mm.

Influence of mass flowrate on the critical heat flux of the flat miniature heat sinks seems to suggest that two critical heat flux mechanisms exist dependent on heated length and total mass flowrate. As the heated length becomes longer, for the lower mass flowrate of

Table 3.3: Critical heat flux (W/cm^2) and outlet vapor quality at critical heat flux (in parentheses) of various investigated flat miniature heat sinks (N/A - not available)

| Operating Conditions	Heated Length	FMHS#1	FMHS#2	FMHS#3	FMHS#4
	L=13.6 mm	197.1 (0.46)	170.4 (0.40)	209.7 (0.49)	N/A
$\dot{m}$= 0.25 g/s	L=27.2 mm	164.6 (0.77)	124.4 (0.58)	N/A	N/A
$T_{sat} = 40°C$	L=40.8 mm	N/A	N/A	138.2 (0.97)	N/A
	L=54.4 mm	N/A	96.8 (0.90)	102.7 (0.96)	N/A
	L=13.6 mm	171.6 (0.41)	178.3 (0.42)	195.3 (0.46)	185.8 (0.46)
$\dot{m}$= 0.25 g/s	L=27.2 mm	137.8 (0.65)	11.2 (0.53)	156.3 (0.74)	171.5 (0.81)
$T_{sat} = 60°C$	L=40.8 mm	102.4 (0.73)	96.2 (0.69)	138.81 (0.97)	138.0 (0.98)
	L=54.4 mm	82.14 (0.79)	94.6 (0.90)	105.2 (1.00)	93.5 (0.89)
	L=13.6 mm	156.1 (0.38)	185.7 (0.45)	176.2 (0.43)	N/A
$\dot{m}$= 0.25 g/s	L=27.2 mm	117.0 (0.57)	110.3 (0.54)	145.3 (0.71)	N/A
$T_{sat} = 80°C$	L=40.8 mm	N/A	N/A	125.8 (0.92)	N/A
	L=54.4 mm	N/A	87.5 (0.85)	91.1 (0.88)	N/A
	L=13.6 mm	193.5 (0.23)	221.4 (0.26)	206.1 (0.25)	195.7 (0.23)
$\dot{m}$= 0.50 g/s	L=27.2 mm	166.2 (0.40)	N/A	187.7 (0.45)	168.7 (0.40)
$T_{sat} = 60°C$	L=40.8 mm	146.2 (0.52)	N/A	N/A	165.6(0.59)
	L=54.4 mm	116.1 (0.55)	138.4 (0.66)	154.2 (0.73)	137.2 (0.65)
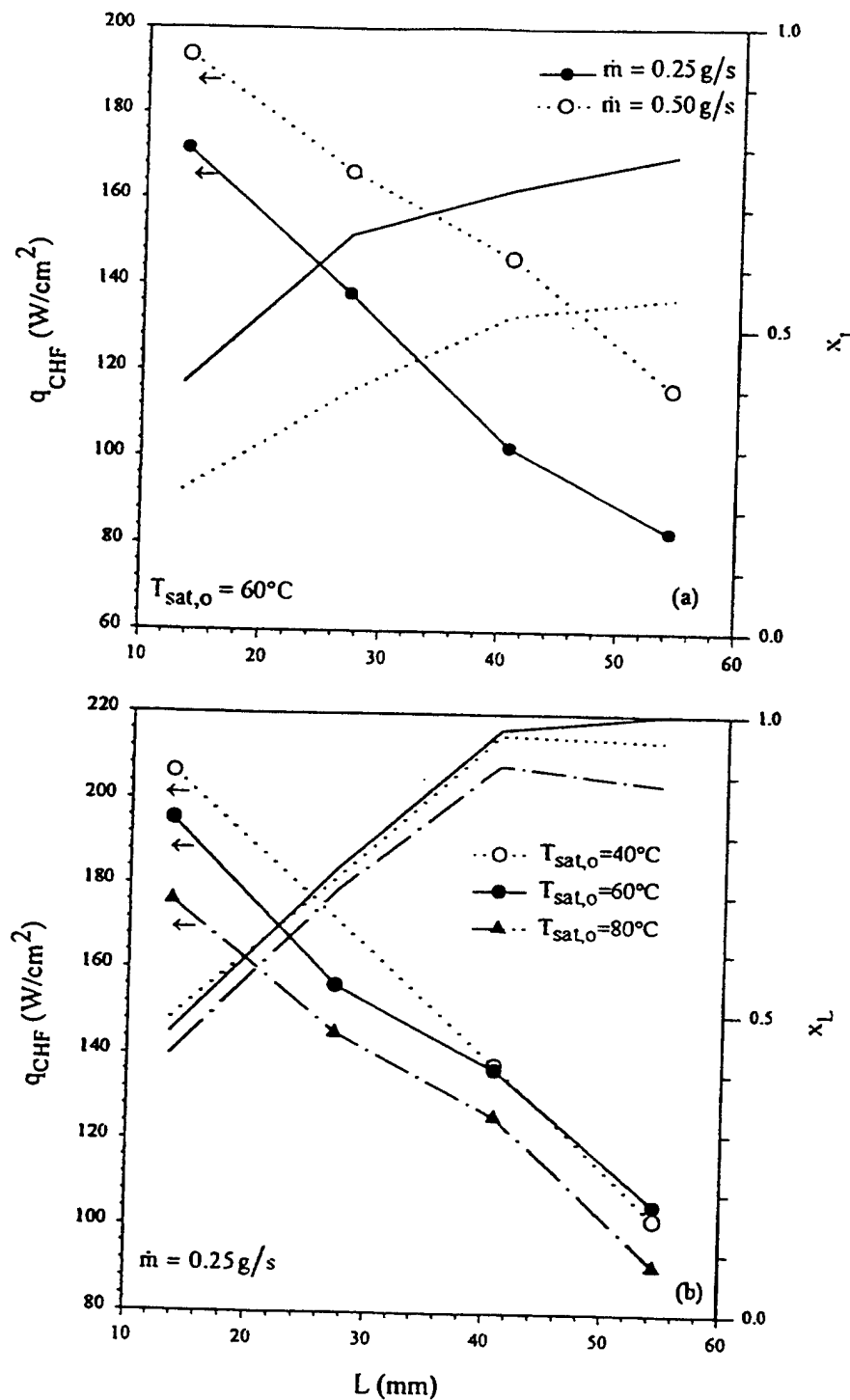
Figure 3.14: Experimentally determined critical heat flux (lines with symbols) and outlet vapor quality (lines without symbols) versus heated length for (a) FMHS#1 and (b) FMHS#3.

$\dot{m}$=0.25 g/s, it appears that q_{CHF} is restricted by the outlet vapor quality approaching unity. However, as the total mass flowrate is increased to $\dot{m}$=0.50 g/s, the outlet vapor quality at critical heat flux dramatically decreases, and therefore, local vapor blanketing is assumed to be the critical heat flux mechanism at higher mass flow rates.

3.2.4 Critical Heat Flux Empirical Correlation

An empirical correlation of the critical heat flux results for all investigated flat miniature heat sinks is developed based on saturated fluid properties and hydrodynamic conditions of the two-phase vapor-liquid flow in a manner consistent with Katto [56]. The empirical correlation is helpful in the design of flat miniature heat sinks with and without micro capillary grooves at the inner surface. All experimental critical heat flux data obtained in this investigation were correlated using a group of dimensionless parameters similar to those chosen by Katto [56]. The final form of the present investigations correlation took the following form

$$\frac{q_{pred}}{Gh_{fg}} = a \left(\frac{L}{D_h}\right)^b \left(\frac{\rho_l}{\rho_v}\right)^c \left(\frac{G^2 D_h}{\sigma \rho_l}\right)^d \tag{3.27}$$

where the coefficients were found to be $a = 0.006154$, $b = -0.29988$, $c = -0.03483$, and $d = -0.3371$. Subcooling of the incoming water was 5C for all cases. It is noticed that the diameter, D, of Kattos' [56] correlation was replaced by the hydraulic diameter, $Dh = 4A/P$, of the investigated flat miniature heat sinks taking into account the enhanced surface. The area used for the calculation of the hydraulic diameter was the total area of the vapor channel and grooves while the perimeter included the groove structure. Coefficients were found by the use of the Marquardt-Levenberg nonlinear regression algorithm. In this correlation and Figure 3.15, q is calculated using the total heated surface area of the flat miniature heat sink outer wall. This is in contrast to Figure 3.15 where it was calculated using the surface area of the heating element. This was done in order to allow direct comparison between the four individual flat miniature heat sinks.

From Figure 3.15, it is seen that the correlation predicts the critical heat flux with good accuracy. The majority of the predicted points are within 20% of the experimental results. FMHS#2, however, is slightly over predicted for most points. This small over prediction is explained by the contact resistance at the heating element - wall surface interface. FMHS#2 was pressed flat from a circular shape which resulted in a slight curvature at the wall surface. This curvature prevented uniform contact between the heating element and outer wall unlike the other FMHS's which had a uniform flat surface.

From Figure 3.16 compares the critical heat flux of the grooved FMHS#3 and the smooth walled FMHS#4 with same interior cross-sectional area. Results are presented as a function of total heated length for an outlet saturation temperature of $T_{sat,o} = 60C$. Fig. 3.16(a) presents results for a mass flowrate of $\dot{m}$=0.25 g/s and Fig.3.16(b) presents results for a total mass flowrate of $\dot{m}$=0.50 g/s. The results show that enhancing the heated surface has a surprising minimal effect on the critical heat flux. Fig. 3.16(a) shows no discernible difference at all and in fact the results appear to overlap one another for FMHS#3 and FMHS#4. With

133
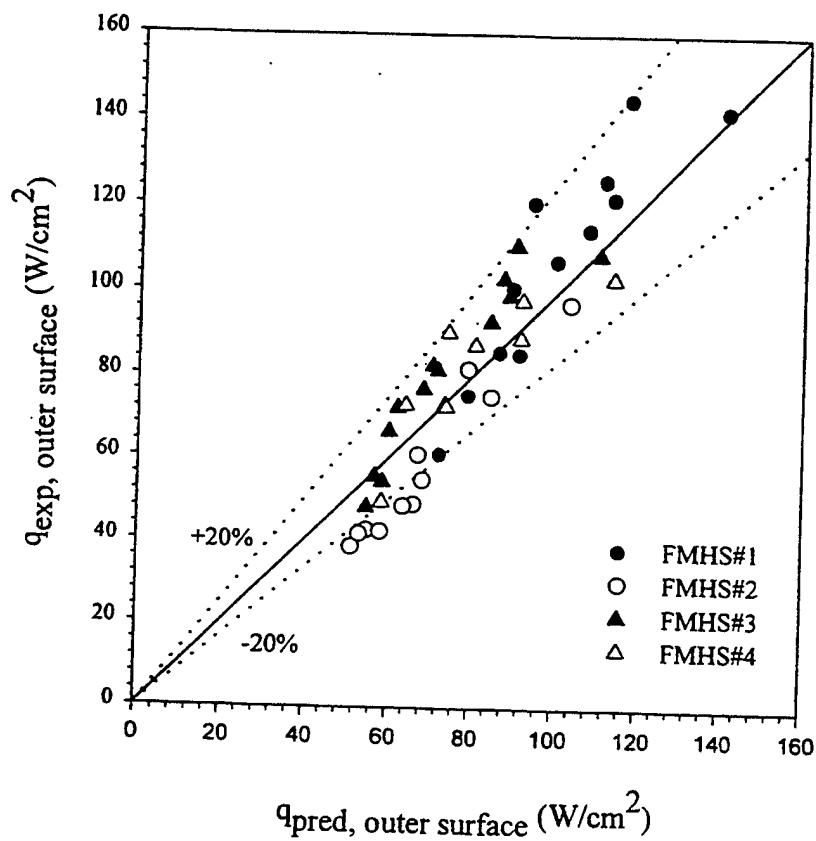
Figure 3.15: Experimental CHF of the four heat sinks versus predicted using the empirical correlation.

an increase in total mass flowrate, Fig. 3.16(b) seems to show that enhancement of the inner surface could effect the critical heat flux, however, the difference is still minimal. For completeness sake, it is reported that for the longest heated length of $L = 54.4$ mm, the critical heat flux increased 11% from 137.2 W/cm^2 for the smooth walled FMHS#4 to 154.2 W/cm^2 for axial grooved FMHS#3. For the shortest heated length of $L = 13.6$ mm, the increase is 5% from 195.7 W/cm^2 to 206.1 W/cm^2. The small effect of surface enhancement on the CHF at high heat fluxes was also observed by Schroeder-Richter [57]. CHF at high mass flow rates can be directly related to ultra-thin liquid film behavior as explained by the adsorption model used by Reyes and Wayner [58] which developed a correlation for the critical wall-vapor superheat.

Figure 3.17 presents experimental temperature distribution results of FMHS#3 and #4, with a constant heated length ($L = 54.4$ mm) and mass flowrate ($\dot{m}$=0.25 g/s), as a function of axial location and moderate total heated loads for various outlet saturation temperatures. All temperature distribution results are approximated to have an error of 1.1°C with 95% confidence. Trends observed are that the wall-vapor superheat increases with applied total heat load and decreases with an increase in outlet saturation temperature. It was also observed that the wall-vapor temperature difference was slightly lower for the grooved FMHS#3 than for the smoothed walled FMHS#4.

Experimental results on the effective heat transfer coefficients for an individual resistor pair were found by calculating the local heat transfer coefficient, $h = q/(T_w - T_{sat})$, for each thermocouple along the resistor pair. The three calculated heat transfer coefficients were then averaged to obtain the effective average heat transfer coefficient for an individual resistor pair. Experimental results showed a general trend of increasing heat transfer coefficients with outlet saturation temperature. Effective heat transfer coefficients found for FMHS #1 through #3 had an order of magnitude approaching 105 W/m^{2}K for $T_{sat,o}$ = 80C. It was also found that the heat transfer coefficient decreased with an increase in heated length.

3.2.5 Conclusions

Based on the experimental results obtained , the following conclusions are made.

1. All four flat miniature heat sinks achieved very similar trends for critical heat flux for equivalent test parameters. The highest critical heat fluxes were in the area of 200 W/cm^2 on each of the two sides of miniature heat sinks. It was found that critical heat flux increased with a decrease in heated length and increase of mass flowrate.

2. No significant difference in the critical heat flux was observed between the axial grooved FMHS#3 and the smooth walled FMHS#4 for any test parameter except for a slight difference at the higher mass flowrate. Therefore, it can be assumed that for higher mass flow rates, CHF is directly related to the ultra thin liquid film phenomena.

3. The two-phase homogenous pressure drop model with an equivalent mass flowrate concept was shown to accurately predict all experimental pressure drops within 25%. However, most experimental pressure drop values were within 15% of the predicted values. It was also found that the pressure drop over the smooth walled heat sink was dominated by the acceleration component while all grooved heat sinks were dominated by friction terms.

4. The largest observed wall-vapor temperature drop was found to be approximately
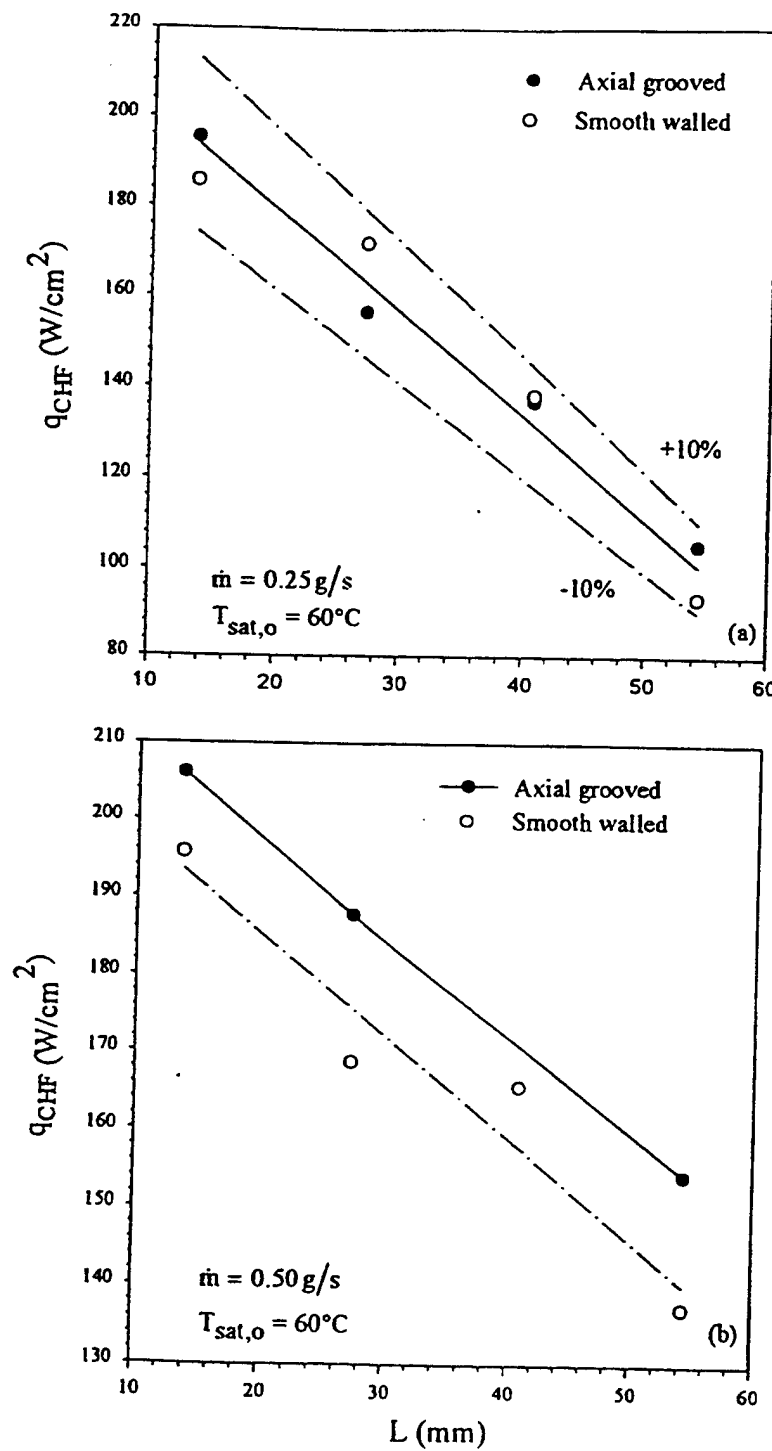
Figure 3.16: Comparison of the experimental critical heat flux of the grooved FMHS#3 and the smooth walled FMHS#4 for different mass flowrates (a) = 0.25 g/s and (b) = 0.50 g/s.

136
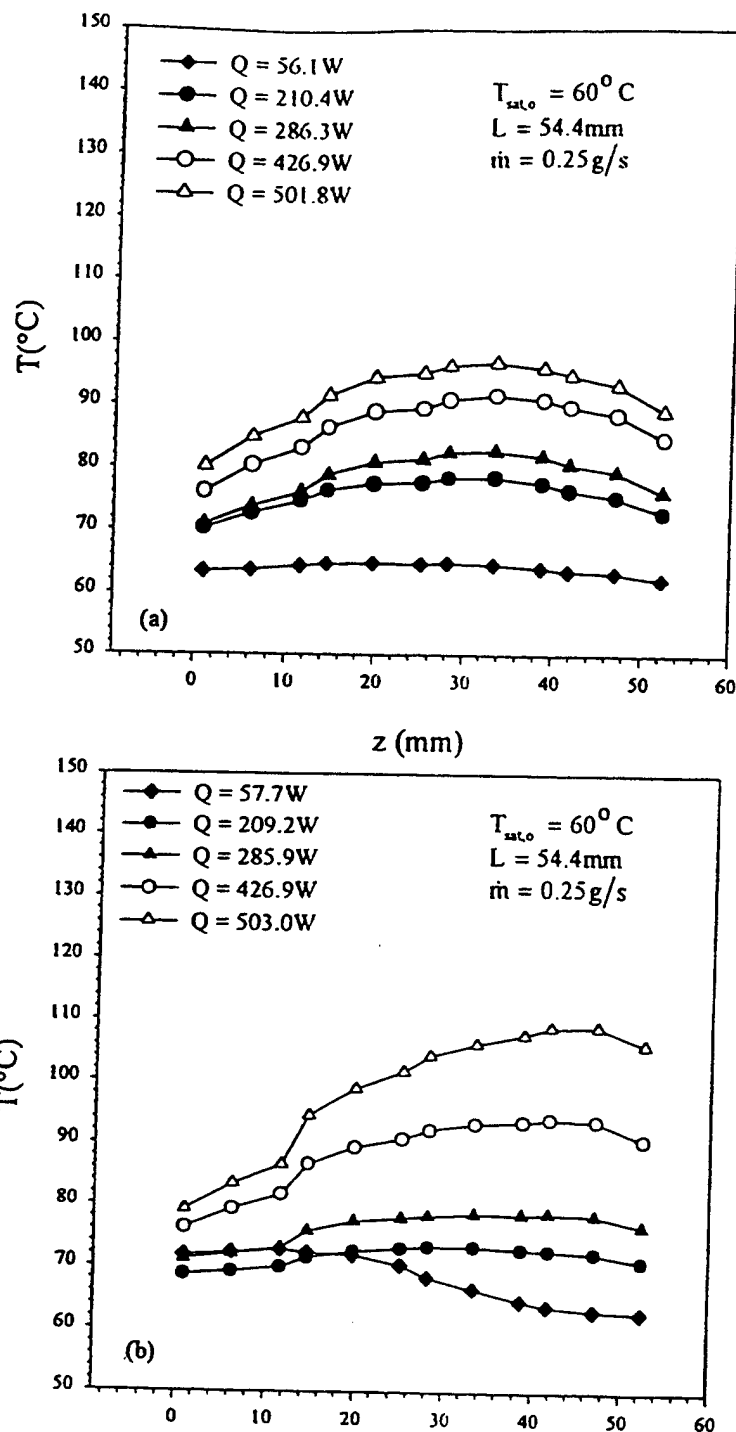
Figure 3.17: Comparison of the experimental temperature drop along the heat sink length for (a) the grooved FMHS#3 and (b) the smooth walled FMHS#4 20.

137

35°C for a high applied heat flux. However, for moderate applied heat fluxes, the maximum temperature drop for all heat sinks was within 20°C. It was also found that the axially grooved FMHS#3 achieved slightly lower overall temperature drops than the smooth walled FMHS#4.

5. Heat transfer coefficients for all four FMHS's were found to increase with an increased outlet saturation temperature and decreased heated length. Heat transfer coefficient values approached and surpassed an order of magnitude of 105 W/m²K for shorter heated lengths.

6. An empirical correlation was developed that generalized experimental CHF's for the four heat sinks with an accuracy of 20%.

Chapter 4

CONCLUSIONS AND RECOMMENDATIONS

A profound understanding of grooved miniature heat pipe operation was gained in the course of this work and high heat flux miniature heat pipes have been developed. In addition to concluding remarks following each chapter section in this report, major achievements of this work are reiterated below.

1. Maximum heat flux results for a miniature heat pipe with deep rectangular micro grooves greatly surpassed all available literature results. The maximum heat flux at the evaporator wall was found to be 145 W/cm^2 in the vertical orientation and 95 W/cm^2 in the horizontal when the heat load was applied to both wide sides. When the heat load was applied to a single wide evaporator side, the maximum heat flux increased to 160 W/cm^2 in the vertical and horizontal orientations. These extremely high heat fluxes were achieved due to design of the grooved capillary structure that was chosen based on the detailed analytical and numerical simulation of miniature heat pipes. Deep and narrow rectangular grooves provided high capillary potential for circulation of working liquid and low thermal resistances in the evaporator and condenser. The fact that heat fluxes obtained for a single heated side are much higher than for two heated sides is partially due to having similar heat flow rate for both cases and more pronounced circumferential heat conduction in the single sided mode.

2. It was shown that the manufacturing of axial rectangular micro groove structures could be accomplished with the use of a high speed automated dicing saw employing high diamond content carbon blades and/or electro discharge machining (EDM). The deep axial rectangular micro grooves with narrow fins between them were manufactured by dicing saw.

3. An effective filling procedure was developed and carried out for the described miniature heat pipe where the appropriate fill ratio was determined by a sufficiently low temperature drop across the condenser during normal miniature heat pipe operating conditions. Thus, the amount of working fluid was chosen based on a minimum heat pipe thermal resistance.

4. Evaporative heat transfer from ultra-thin films, affected by the disjoining pressure, micro grooves and micro pores has been modeled. Numerical results predicted that miniature heat pipes with microgrooves, unlike conventional heat pipes, can withstand high heat fluxes on the evaporator wall. This prediction has been confirmed experimentally.

139

5. Modeling of the inverted-meniscus type evaporator, which can be employed for extremely high heat fluxes, has been accomplished. It revealed that vapor blankets restricted the heat transfer capability of loop heat pipes and miniature heat pipes with an inverted-meniscus evaporator and some principles were suggested to improve the heat pipe performance characteristics.

6. Modeling of a miniature heat pipe containing a grooved structure covered with a porous layer demonstrated that such heat pipes would be superior over those with plain grooves. These grooved heat pipes with a porous layer outperform plain grooved heat pipes in that they operate better in various orientations and obtain higher heat fluxes.

7. In most cases, the capillary limitation was found to restrict the maximum heat flux, however, the boiling limitation (associated with formation of the vapor blanket on the capillary structure in the evaporator) was found to be important in the vertical orientation at higher operating temperatures. This conclusion has been made based on the consideration of the experimental results for maximum heat fluxes versus theoretical prediction of the capillary limitation and also by comparison with critical heat fluxes obtained from the grooved heat sinks with forced convection.

8. Further R&D efforts should be made to develop final miniature heat pipe-based products for various commercial applications. Therefore, the objective of the continued effort is to advance scientific understanding, develop, design, test and prepare a series of heat pipe-based heat sinks for various electronic cooling applications.

Chapter 5

REFERENCES

1. Faghri, A., 1995, Heat Pipe Science and Technology, Taylor and Francis.

2. Plesch, D., Bier, W., Seidel, D., and Schubert, K., 1991, "Miniature Heat Pipes for Heat Removal from Microelectronic Circuits." In *Micromechanical Sensors, Actuators, and Systems* (Edited by D.Cho, R.Warrington, Jr., et al.), DCS-Vol. 32, 303–313, ASME, New York.

3. Frank, S., 1967, "Optimization of a Grooved Heat Pipe," *Proc. Intersociety Energy Conversion Conf.*, pp. 833–845.

4. Grote, M.G., Stark, J.A., and Tefft, E.C., III, 1986, "Enhanced Evaporative Surface for Two-Phase Mounting Plates," *Proc. 16th ICES Conf.*, Paper No. 860979, pp. 617–624.

5. Khrustalev, D., Faghri, A., and J. Leland, 1994a, "Thermal Analysis of Axially-Grooved Heat Pipes," Proceedings of the *Second Biennial ASME European Joint Conference on Engineering Systems, Design, and Analysis*, London, England, PD-Vol. 64-1, pp. 39-54.

6. Khrustalev, D., and Faghri, A., 1994b, "Thermal Analysis of a Micro Heat Pipe," *ASME Journal of Heat Transfer*, Vol. 116, No. 1, pp. 189–198.

7. Kamotani, Y., 1976b, "Analysis of Axially Grooved Heat Pipe Condensers," AIAA Paper No. 76-147.

8. Kamotani, Y., 1978, "Evaporator Film Coefficients of Grooved Heat Pipes," *Proc. 3rd Int. Heat Pipe Conf.*, Palo Alto, pp. 128–130.

9. Vasiliev, L.L., Grakovich, L.P. and Khrustalev, D.K., 1981, "Low-Temperature Axially Grooved Heat Pipes," *Proc. 4th Int. Heat Pipe Conf.*, London, pp. 337-348.

10. Nield, D.A. and Bejan, A.,(1992)*Convection in Porous Media*, p.9, Springer-Verlag New York Inc.

11. Stephan, P.C., and Busse, C.A., 1992, "Analysis of the Heat Transfer Coefficient of Grooved Heat Pipe Evaporator Walls," *Int. J. Heat Mass Transfer,* Vol. 35, No. 2, pp. 383–391.

12. Carey, V.P., 1992, *Liquid-Vapor Phase-Change Phenomena: An Introduction to the Thermophysics of Vaporization and Condensation Processes in Heat Transfer Equipment,* Hemisphere, New York.

13. Wayner, P.C., Jr., Kao, Y.K. and LaCroix, L.V., 1976, "The Interline Heat-Transfer Coefficient of an Evaporating Wetting Film," *Int. J. Heat Mass Transfer,* Vol. 19, pp. 487–492.

14. Derjaguin, B.V., 1955, "Definition of the Concept of and Magnitude of the Disjoining Pressure and its Role in the Statics and Kinetics of Thin Layers of Liquid," *Kolloidny Zhurnal,* Vol. 17, pp. 191–197.

15. Solov'yev, S.L., and Kovalev, S.A., 1984, "Mechanism of Evaporation of a Liquid from a Porous Surface," *Proc. 5th Int. Heat Pipe Conf.,* Tsukuba, Japan, Preprints Vol. II, pp. 77–82.

16. Labuntsov, D.A., and Krukov, A.P., 1977, "Intensive Evaporation Processes," *Thermoenergetics,* No. 4, pp. 8–11.

17. Holm, F.W., and Goplen, S.P., 1979, "Heat Transfer in the Meniscus Thin-Film Transition Region," *ASME J. Heat Transfer,* Vol. 101, No. 3, pp. 543–547.

18. Babenko, V.A., Levitan, L.L. and Khrustalev, D.K., 1981, "Heat Transfer in Condensation on a Grooved Surface," *J. Engineering Physics and Thermophysics,* Vol. 40, No. 6, pp. 615–619.

19. Schneider, G.E., Yovanovich, M.M. and Wehrle, V.A., 1976, "Thermal Analysis of Trapezoidal grooved Heat Pipe Evaporator Walls," AIAA Paper 76-481.

20. Schlitt, K.R., Kirkpatrick, J.P. and Brennan, P.J., 1974, "Parametric Performance of Extruded Axial Grooved Heat Pipes from 100 K to 300 K," *Proc. AIAA/ASME Thermophysics and Heat Transfer Conf.,* AIAA Paper 74-724.

21. Ivanovskii, M.N., Privezentsev, V.V., Il'in, Yu.A., and Sidorenko, E.M., 1984, "Experimental Investigation of Heat Transfer with Evaporation of the Agent from a Corrugated Capillary Structure," *J. Engineering Physics and Thermophysics,* Vol. 46, No. 4, 377–381.

22. Paul, B., 1962, "Compilation of Evaporation Coefficients," *ARS J.,* Vol. 32, pp. 1321–1328.

23. Potash, Jr., M., and Wayner, Jr., P.C., 1972, "Evaporation from a Two-Dimensional Extended Meniscus," *Int. J. Heat Mass Transfer,* Vol. 15, pp. 1851–1863.

24. Shekriladze, I.G. and Rusishvili, D.G., 1987, "Evaporation and Condensation on Grooved Capillary Surfaces," *Proc. 6th Int. Heat Pipe Conf.*, Grenoble, pp. 173–176.

25. Stephan, P., 1992, *Wärmedurchgang bei Verdampfung aus Kapillarrillen in Wärmerohren*, Fortschr.-Ber. VDI Reihe 19 Nr. 59. Düsseldorf: VDI-Verlag.

26. Khrustalev, D., and Faghri, A., 1995, "Heat Transfer During Evaporation on Capillary-Grooved Structures of Heat Pipes," *ASME J. Heat Transfer*, Vol. 117, August, No. 3, p. 740–747.

27. Cao, Y., and Faghri, A., 1990, "Transient Two-Dimensional Compressible Analysis for High-Temperature Heat Pipes with Pulsed Heat Input," *Numerical Heat Transfer*, Part A, Vol. 18, pp. 483–502.

28. Voller, V.R., Brent, A.D., and Prakash, C., 1989, "The Modeling of Heat, Mass and Solute Transport in Solidification Systems," *Int. J. Heat Mass Transfer*, Vol. 32, No. 9, pp. 1719–1731.

29. Patankar, S.V., 1980, "Numerical Heat Transfer and Fluid Flow," McGraw-Hill, New York.

30. Prakash, C., 1994, "Numerical Heat Transfer and Fluid Flow," Postgraduate Course, Wright State University, Dayton, OH.

31. Kamotani, Y., 1976a, "Thermal Analysis of Axially Grooved Heat Pipes," *Proc. 2nd Int. Heat Pipe Conf.*, Bologna, Italy, pp. 83–91.

32. Longtin, J.P., Badran, B., and Gerner, F.M., 1992, "A One-Dimensional Model of a Micro Heat Pipe During Steady-State Operation," *Proc. 8th Int. Heat Pipe Conf.*, Beijing, China, Preprints, pp. C-5-1 to C-5-7.

33. Shah, R.K., and Bhatti, M.S., 1987, "Laminar Convective Heat Transfer in Ducts," in *Handbook of Single Phase Convective Heat Transfer*, edited by Kakac et al., Wiley, New York.

34. Schneider, G.E., and DeVos, R., 1980, "Nondimensional Analysis for the Heat Transport Capability of Axially-Grooved Heat Pipes Including Liquid/Vapor Interaction," AIAA Paper No. 80–0214.

35. Jensen, M.K., and Memmel, G.J., 1986, "Evaluation of Bubble Departure Diameter Correlations," *Proc. 8th Int. Heat Transfer Conf.*, Vol. 2, pp. 1907–1912.

36. Lorenz, J.J., Mikic, B.B., and Rohsenow, W.M., 1974, "The Effect of Surface Conditions on Boiling Characteristics," *Proc. 8th Int. Heat Transfer Conf.*, Vol. 4, p. 35.

37. Khrustalev, D.K., Grakovich, L.P., Denisevich S.V., Yanitski, B. and Sheleg, V.K., 1987, "Heat Pipe With a Combined Capillary-Porous Structure," *J. Engineering Physics and Thermophysics*, Vol. 52, No. 4, pp. 587–592.

38. Raiff , R.J. and Wayner, P.C., Jr.,(1973), Evaporation from a Porous Flow Control Element on a Porous Heat Source, *Int. J. Heat Mass Transfer*, **16**, 1919–1929 (1973).

39. Feldman, K.T. and Noreen, D.L.,(1980), Design of Heat Pipe Cooled Laser Mirrors with an Inverted Meniscus Evaporator Wick, AIAA paper , No. 148 (1980).

40. Solov'yev, S.L. and Kovalev, S.A.,(1987), Heat Transfer and Hydrodynamics in the Inverted Meniscus Evaporator of a Heat Pipe, *Proceedings of the Sixth International Heat Pipe Conference,* Grenoble, France, Vol. I, pp. 116–120 (1987).

41. Wulz, H., and Embacher, E.,(1990), Capillary pumped Loops for Space Applications Experimental and Theoretical Studies on the Performance of Capillary Evaporator Designs, *Proceedings of the AIAA/ASME Fifth Joint Thermophysics and Heat Transfer Conference,* Seattle, WA, Paper AIAA 90-1739 (1990).

42. Ku, J., Overview of Capillary Pumped Loop Technology,(1993), *Proceedings of the Twenty Ninth National Heat Transfer Conf.,* Atlanta, GA (1993).

43. Chung, M. and Catton, I., Steam Injection Into a Slow Water Flow Through Porous Media,(1993), *ASME J. Heat Transfer*, **115**, 734–743 (1993).

44. Cao, Y. and Faghri, A.,(1994), Conjugate Analysis of a Flat-Plate Type Evaporator for Capillary Pumped Loops With Three-Dimensional Vapor Flow in the Groove, *Int. J. Heat Mass Transfer*, **37**, No. 3, 401–409 (1994).

45. Dunn, P. D. and Reay, D. A.,(1982), *Heat Pipes,* (3rd Edn.), Pergamon Press, Oxford (1982)

46. Cao, Y., Beam, J.E., and Donovan, B., 1996, "Air-Cooling System for Metal Oxide Semiconductor Controlled Thyristors Employing Miniature Heat Pipes," *Journal of Thermophysics and Heat Transfer*, Vol. 10, No. 3, pp. 484 - 489..

47. North, M.T., and Avedisian, C.T., 1993. *Heat Pipes for Cooling High Flux/High Power Semiconductor Chips,* J. Elect. Pack., Vol. 115, pp. 112 - 117.

48. Hopkins, R., 1996, "Flat Miniature Heat Sinks and Heat Pipes with Micro Capillary Grooves: Manufacturing, Modeling and Experimental Study," *Masters Thesis,* The University of Connecticut.

49. Khrustalev, D., and Faghri, A., 1997, "Thick-Film Phenomenon During High-Heat-Flux Evaporation from Cylindrical Pores," *ASME Journal of Heat Transfer*, Vol. 119, pp. 272-278, 1997.

50. Bowers, M.B., and Mudawar, I., 1994, "High Flux Boiling in Low Flow Rate, Low Pressure Drop Mini-Channel and Micro-Channel Heat Sinks," *International Journal of Heat and Mass Transfer*, Vol. 37, No. 2, pp. 321-332.

144

51. Ravigururajan, T.S., Cuta, J., McDonald, C.E., and Drost, M.K., 1996, "Effects of Heat Flux on Two-Phase Flow Characteristics of Refrigerant Flows in a Micro-Channel Heat Exchanger," *Proc. of the 31st National Heat Transfer Conference.*, Houston, TX, HTD-Vol. 329, Vol. 7, pp. 167 - 178.

52. Takahashi, I., and Ishikava, E., 1995. "Microchannel Heat Sink Based on Boiling Heat Transfer," *Journal of the Japan Society of Mechanical Engineers* (B), Vol. 61, No. 584, pp. 282 - 293 (in Japanese).

53. Peng, X.F., and Wang, B.X., 1994, "Liquid Flow and Heat transfer in Microchannels With/Without Phase Change," *Proc. of the 10th International Heat Transfer Conf.*, Brighton, UK, Vol. 1, pp. 159 - 177.

54. Yang, C.Y., and Webb, R.L., 1996, "Friction Pressure Drop of R-12 in Small Hydraulic Diameter Extruded Aluminum Tubes With and Without Micro-Fins," *International Journal of Heat and Mass Transfer*, Vol. 39, No. 4, pp. 801-809.

55. Akers, W.W., Deans, H.A., Crosser, O.K., 1959, "Condensation Heat Transfer Within Horizontal Tubes," *Chem. Engng Prog. Symp. Ser.*, Vol. 59, No. 29, pp. 171-176.

56. Katto, Y., 1978, "A Generalized Correlation of Critical Heat Flux for the Forced Convection Boiling in Vertical Uniformly Heated Round Tubes," *Int. J. Heat Mass Transfer*, Vol. 21, pp. 1527 - 1542.

57. Schroeder-Richter, D., Yildiz, S., and Bartsch, G., 1996, "Effect of porous coating on Critical Heat Flux," *Int. Comm. Heat Mass Transfer*, Vol. 23, No. 4, pp. 463 - 471, 1996.

58. Bankston, C.A., and Smith, H.J., 1973, "Vapor Flow in Cylindrical Heat Pipes," *ASME J. Heat Transfer*, Vol. 95, pp. 371–376.

59. Bowman, W. J., and Hitchcock, J. E., 1938, "Transient, Compressible Heat-Pipe Vapor Dynamics," *Proc. ASME National Heal Transfer Conf.*, Houston, TX, Vol. 1, pp. 329–338.

60. Jang, J.H., Faghri, A., and Chang, W.S., 1991, "Analysis of the Transient Compressible Vapor Flow in Heat Pipes," *Int. J. Heat Mass Transfer*, Vol. 34, pp. 2029–2037.

61. Freggens, R. A.,(1968), Experimental determination of wick properties for heat pipe applications, *Proceedings of the 4th Intersociety Energy Conversion Conference*, Washington, D. C., 888–897 (1968).

62. Jacobs, H.R., and Hartnett, J.P., 1991, "Thermal Engineering: Emerging Technologies and Critical Phenomena," *Workshop Report*, NSF Grant No. CTS-91-04006, pp. 139-176.

63. Khrustalev, D., and Faghri, A., 1994b, "Evaporation and Condensation on Capillary-Grooved Structures of Heat Pipes," *Proceedings of 1994 Winter Annual ASME Meeting*, Chicago, HTD-Vol. 287, pp. 47-59.

64. Khrustalev, D. and Faghri, A., 1995, "Heat transfer in the inverted meniscus type evaporator at high heat fluxes", *Int. J. Heat Mass Transfer*, , Vol. 38, No. 16, pp.3091-3101.

65. Khrustalev, D., and Faghri, A., 1995, "Thermal Characteristics of Conventional and Flat Miniature Axially-Grooved Heat Pipes," *ASME Journal of Heat Transfer*, Vol. 117, November, No. 4, pp. 1048-1054.

66. Khrustalev, D., and Faghri, A., 1995, "Boiling Heat Transfer in the Miniature Axially-Grooved Rectangular Channel with Discrete Heat Sources," *Journal of Enhanced Heat Transfer*, in press, to appear in 1997

67. Khrustalev, D., and Faghri, A., 1996, "High Flux Evaporative Mini-Channel Heat Sink With Axial Capillary Grooves," *Journal of Enhanced Heat Transfer*, Vol. 3, No. 3, pp. 221-232 .

68. Lance, G.N., 1960, *Numerical Methods for High Speed Computers,* ILIFEE, London, pp. 134–138.

69. Stepanov, V.G., Volyak, L.D., and Tarlakov, Yu.V., 1977, "Wetting Contact Angles for Some Systems," *J. Engineering Physics and Thermophysics*, Vol. 32, No. 6, pp. 1000–1003.

70. Swanson and Peterson, 1994, "Evaporating Extended Meniscus in a V-Shaped Channel," *J. Thermophysics and Heat Transfer,* Vol. 8, No.1, pp. 172–180.

71. Thome, J. R., 1990, *Enhanced Boiling Heat Transfer* Hemisphere, 356 pp.

Chapter 6

APPENDIX A: Flat Miniature Heat Pipe Filling Procedure

The filling of the flat miniature heat pipes produced at The University of Connecticut (FMHP#3 and FMHP#4) was carried out with the heat pipe filling station located in the Heat Transfer Research Laboratory. The heat pipe filling station was developed and manufactured at Wright State University (Faghri, 1995) and transported to The University of Connecticut in the fall of 1994. The following is a description of the heat pipe filling stations' physical makeup and filling procedure followed. It will be noticed that the filling stations experimental setup and filling procedure was slightly altered in order to improve the filling of flat miniature heat pipes.

The heat pipe filling station shown schematically in Figure 6.1. was made from 1/4" O.D. copper refrigerant tubing soldered at the joints with copper sweat fittings. All valves (with the exception of the high vacuum valve and backing/roughing valve) were brass helium leak tested Nupro bellow type valves with 1/4" O.D. brass tube extensions that were connected to the copper refrigerant tubing with copper sweat fittings. The glass measurement burette had a total graduated volume of 100 ml. The burette was connected to the filling station by a rubber stopper at the mouth and a brass Cajun-Ultra Torr O-ring vacuum seal at the tip. The working fluid flask and water trap flask had total volumes of 2000 ml and were made of heavy walled Pyrex to ensure that the flasks would not implode under an interior vacuum. The flasks were connected to the copper lines by rubber stoppers. All connections were made to ensure that the filling station maintained vacuum integrity.

The filling station was attached to a mechanical low vacuum roughing pump and a high vacuum diffusion pump for use in the evacuation of the filling station and heat pipe. The pressure of the system was measured by Pirani ($1\text{x}10^{-3}$ torr) and Penning ($1\text{x}10^{-3}$) pressure gauges. All gauges and pumps were manufactured by Edwards Vacuum Technology.

The flat miniature heat pipe was attached between Valve 13 and Clamp 3 by a length of transparent tygon tubing on both sides of the flat miniature heat pipe connected to the 1/8" O.D. heat pipe filling tubes. Tygon tubing was chosen for the ability to see the working fluid as it entered and left the flat miniature heat pipe. This was necessary in order to approximate the amount of working fluid introduced to the flat miniature heat pipe. The flat miniature heat pipe was positioned with a positive inclination angle of at least 45 to insure that vapor

147
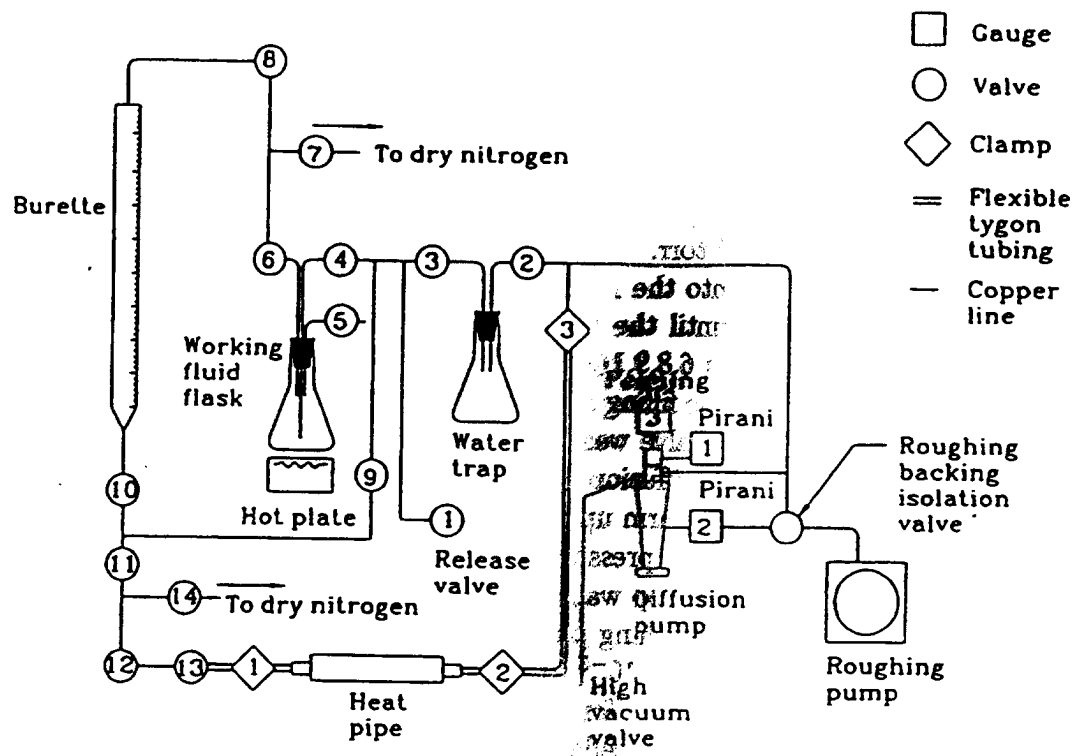
Figure 6.1: Schematic of miniature heat pipe filling station

could escape from the condenser end cap fill tube during the filling procedure detailed below. The flat miniature heat pipe was fitted with a minimum of four thermocouples along the full length of the heat pipe in order to investigate the isothermality of the total heat pipe length and condenser during the filling procedure. Also attached to the flat miniature heat pipe during the filling procedure were isothermal plates, mounted at the condenser, in order to help test the isothermality of the operating heat pipe during the filling procedure as described below. The isothermal plates were provided a constant temperature coolant flow from the Lauda RM-20 constant temperature bath/circulator as described in the Section 2.2 of Chapter Two.

The following steps were completed in a successful flat miniature heat pipe filling procedure. Initial evacuation of the filling station to a pressure of 5×10^{-5} torr, degassing of the working fluid, filling station drying, re-evacuation of the filling station to a pressure of 5×10^{-3} torr, evacuation of the miniature heat pipe to 5×10^{-3} torr, final evacuation of the filling station and miniature heat pipe to at least 1×10^{-5} torr, filling of the heat pipe with the working fluid and initial testing of the miniature heat pipe for an isothermal axial temperature drop.

Evacuation of filling station

Initially all valves were in the closed position and the backing/roughing valve was in the roughing position. The roughing pump was powered and the pressure monitored at gauge 2 until the pressure fell below 1×10^{-1} torr. Valve 2 was then slowly opened while the stopper in the water trap flask was drawn into the flask and became flush with the lip of the flask. Valves 3 and 4 were then opened until the stopper in the working fluid flask was drawn in the same manner. Finally Valves 6, 8, 10, 11 and 12 were opened in order to allow a vacuum to be achieved throughout the filling station up to Valve 13. Once gauge 2 reached 5×10^{-3} torr, the backing/roughing valve was switched to backing and the cooling line to the diffusion pump was opened. The diffusion pump was then turned on for a minimum of twenty minutes in order to allow it to warm up. After the warmup period, the high vacuum valve was slowly opened. The pressure at pressure gauge 3 should have dropped rapidly to at least 5×10^{-4} torr, if a rapid pressure drop was not registered at gauge 3, the filling station had to be evacuated further by the roughing pump. If it does drop rapidly, the system is left running until a pressure of at least 1×10^{-5} torr was reached which took upwards of two hours. After this pressure had been reached for at least thirty minutes all valves were closed and the degassing of the working fluid proceeded.

Working Fluid Degassing

The working fluid is initially placed in a clean beaker and the line from Valve 5 was positioned at the bottom of the beaker. Valve 5 was slowly opened and a specified amount of working fluid (1000 ml) was drawn into the evacuated flask along with any entrapped air in the liquid and the line leading to Valve 5. Valve 5 is then closed and the flask is heated by a variable adjusted hotplate. Heating continues until the working fluid is boiling vigorously and the stopper begins to rise from the flask signifying a higher pressure in the flask than the atmosphere. Valve 5 is opened to the atmosphere, and all trapped non-condensible gasses begin to escape to the environment. After 5 minutes of vigorous boiling with the flask opened to the atmosphere through Valve 5, Valve 5 is closed and the heat removed. The flask is allowed to cool and the stopper is drawn back into the flask as the interior pressure

149

decreases.

Entrapped air may still be found in the line from the flask to Valve 4. To remove this air, Valves 4 and 3 are slowly opened (all other valves are closed) until water appears in the water trap. Valves 3 and 4 are then closed and the degassing procedure is completed.

Filling station drying

Since the entrapped air that was forced through Valve 4 is still present in the filling station, the filling station must be re-evacuated. First, the filling station must be dried of all liquid that resides in the lines and liquid trap. This is necessary to avoid any liquid being evaporated and pulled into the diffusion pump where it will condense in the pumps oil during re-evacuation. This is undesirable since it effects the performance of the diffusion pump and may cause the diffusion pump to be unable to evacuate to the required pressures. This drying procedure was simply performed by blowing dry nitrogen through the system at valves 7 and 14 for a prolonged period of time. Two words of caution must be mentioned here. First, a significant amount of nitrogen in the air is undesirable because of safety concerns. Therefore, the room must be well ventilated during this procedure. Second, a pressure in the filling station above atmospheric must be avoided in order to ensure that the glass burette is not destroyed.

Evacuation of the filling station and miniature heat pipe All lines of the filling station, with the exception of the working fluid flask and the flat miniature heat pipe (Valve 13 to Clamp 3) were re-evacuated to 5×10^{-3} torr as described above. All valves were then closed. The miniature heat pipe and tygon tubing was then evacuated up through Valve 13 through Clamp 3, 2 and 1 (secondary line) to a pressure of 10^{-3} torr. Finally, the filling station and miniature heat pipe was brought to a pressure of approximately 1×10^{-5} torr at the same time employing the diffusion pump as described above. This final evacuation procedure was carried out overnight to guarantee that all trapped entrapped gases were removed from the system.

Filling of the heat pipe

Initially, all valves were closed and clamps opened. The line from the working fluid flask to the burette and up to Valve 13 was opened by slowly opening Valves 4, 9, 10, 11 and 12. The working fluid in the flask was then slowly heated to slightly increase the pressure in the flask. When the pressure increased sufficiently, the working fluid was observed to move into the burette. When enough liquid was introduced into the burette to fill the heat pipe completely, Valve 4 was closed and the heat was removed from the flask.

The flat miniature heat pipe was then filled completely with the working fluid by opening Valve 13, while Clamp 3 was closed (to ensure that no liquid is drawn into the vacuum pumps) and Clamps 1 and 2 were opened. When the working fluid appeared in the flexible tygon tubing at the heat pipe outlet, Clamp 1 was closed in order to stop the working fluid flow. Clamp 2 was also closed to isolate the heat pipe from the rest of the filling station. The location of the liquid-vapor front in the flexible tubing was then marked. At this point the miniature heat pipe was completely filled with the working fluid except for any entrapped vapor or air bubbles (that was carefully avoided). The calculated amount of working fluid that was desired to be removed from the miniature heat pipe was then converted to a length of liquid based on the interior diameter of the tygon tube. This length was then added to the position of the liquid-vapor front to indicate the position that the liquid-vapor front

150

should reach as water and entrapped air was forced from the completely filled heat pipe. To remove all excess liquid and entrapped gases, the heat pipe was brought to a temperature approaching 60°C in the adiabatic section using a combination of the heating element that supplies power to the evaporator and the constant temperature circulator that is used to maintain a constant operating temperature. Clamp 2 was then slightly opened to allow liquid and gas to escape from the condenser end of the heat pipe until the liquid-vapor front advanced the predetermined distance in the tygon tubing. Clamp 2 was then quickly closed again. The heat pipe was then tested at various evaporator power settings at a constant operating temperature (controlled by the isothermal plates) to determine whether the fill ratio was appropriate. If the measured temperature drop across the heat pipe length was sufficiently small, i.e. (T < 60°C for Q=40 W, and the condenser is isothermal (T < 1°C) signifying no entrapped non-condensable gases, the heat pipe filling tubes were crimped and soldered. If the temperature drop was too large, the above procedure was followed to allow more liquid and vapor to escape from the condenser fill tube. The heat pipe was then tested again until the above small temperature drops were obtained. It should be pointed out that too much liquid may be forced from the heat pipe, this is indicated if the observed temperature drop increases when extra liquid is forced out during the second or later iterations. If this happens, the heat pipe should be completely filled with water again and the above procedures followed until a good operational heat pipe is obtained.

The above procedure successfully obtained a good operational heat pipe, however, the working fluid amount introduced was not able to be measured accurately. As liquid and vapor is forced from the heat pipe, the tygon tube fills with both liquid slugs and droplets and vapor slugs and bubbles mixed in a very confusing manner (i.e the liquid/vapor length is not divided into homogenous slugs of vapor and liquid. The liquid may have vapor bubbles present and vice versa). Unfortunately, the calculated length of fluid to be removed is only based on the liquid density since the average vapor quality is impossible to measure, therefore, the length of liquid/vapor forced out was very approximate. It is approximated that the working fluid amount charged to the heat pipe was to 20% of the desired fill. This approximation was justified after the heat pipe testing was completed and the actual working fluid amount was found.